TROPOSPHERIC NITROGEN DIOXIDE FROM SATELLITE MEASUREMENTS: SCIAMACHY LIMB/NADIR MATCHING AND MULTI-INSTRUMENT TREND ANALYSIS

ANDREAS HILBOLL

Dissertation zur Erlangung des Grades *Doktor der Naturwissenschaften*

Institut für Umweltphysik
Fachbereich 1
Universität Bremen
November 2013

1. GUTACHTER	Prof. Dr. John P. Burrows
2. GUTACHTER	Prof. Dr. Thomas Wagner
BETREUER	Dr. Andreas Richter
DATUM DES KOLLOQUIUMS	5. Februar 2014

Für mich.

ABSTRACT

Tropospheric NO_2, a key air pollutant particularly in cities, has been measured from space since the mid-1990s by the GOME, SCIAMACHY, OMI, and GOME-2 instruments. These data provide a unique global long-term dataset of tropospheric pollution. The focus of this thesis is twofold:

When these satellite measurements are to be used for assessing tropospheric emissions and pollution, it is necessary to separate the stratospheric from the tropospheric signal. This thesis develops a new unique technique for this separation by using the measurements performed by SCIAMACHY in limb geometry. The stratospheric NO_2 measurements from SCIAMACHY are shown to be in very good agreement with NO_2 fields modeled by the Oslo CTM2. However, both stratospheric datasets need to be adjusted to the level of the nadir measurements, because a time- and latitude-dependent bias to the measured nadir columns can be observed over clean regions. By combining measurements of total and stratospheric air masses taken by the same instrument, the uncertainties commonly introduced by unjustified assumptions and spatial averaging and smoothing can be significantly reduced, leading to the best dataset of tropospheric NO_2 slant columns currently available.

The tropospheric columns can then be used to assess the level of air pollution on a regional and even local scale. However, the observations of the four instruments differ in spatial resolution, local time of measurement, viewing geometry, and other details, and all these factors can severely impact the retrieved NO_2 columns. Therefore, the analysis of temporal changes in troposheric NO_2 abundances using these measurements is challenging and not straightforward. In the second part of this thesis, several methods to account for these instrumental differences are developed and applied to the analysis of trends in tropospheric NO_2 columns over megacities. The first method is based on spatial averaging of the measured SCIAMACHY earthshine spectra and ex-

traction of a spatial pattern of the resolution effect. Furthermore, two empirical corrections, which summarize all instrumental differences by including instrument-dependent offsets in a fitted trend function, are developed. These methods are applied to data from GOME and SCIAMACHY separately, to the combined time series, and to an extended dataset comprising also OMI and GOME-2 measurements. All approaches show consistent trends of tropospheric NO_2 for a selection of areas on both regional and city scales, for the first time allowing consistent trend analysis of the full time series at high spatial resolution. Measured tropospheric NO_2 columns have been strongly increasing over China, the Middle East, and India, with values over east-central China tripling from 1996 to 2011. All parts of the developed world, including Western Europe, the United States, and Japan, show significantly decreasing NO_2 amounts in the same time period. On a megacity level, individual trends can be as large as +27.2 ± 3.9 $\%\,yr^{-1}$ and +20.7 ± 1.9 $\%\,yr^{-1}$ in Dhaka and Baghdad, respectively, while Los Angeles shows a very strong decrease of −6.00 ± 0.72 $\%\,yr^{-1}$. Most megacities in China, India, and the Middle East show NO_2 columns increasing by +5 to 10 $\%\,yr^{-1}$, which leads to a doubling to tripling within the study period.

ZUSAMMENFASSUNG

Stickstoffdioxid (NO_2) ist eine der Hauptkomponenten troposphärischer Luftverschmutzung, insbesondere in Städten. Die Bestimmung troposphärischer NO_2 Säulen mittels Satelliten-Instrumenten wie z.B. GOME, SCIAMACHY, OMI und GOME-2 ist seit Mitte der 1990er Jahre möglich. Diese Messungen ergeben einen einmaligen, globalen Langzeit-Datensatz troposphärischer Luftverschmutzung. Die vorliegende Arbeit gliedert sich in zwei Teile:

Um aus Satelliten-Messungen den Grad troposphärischer Luftverschmutzung zu bestimmen, muss zunächst das stratosphärische vom troposphärischen Signal getrennt werden. Im Rahmen dieser Dissertation wird eine neue Methode für die sogenannte Stratosphären-Korrek-

tur entwickelt, indem die Messungen, welche das SCIAMACHY-Instrument in Limb-Geometrie durchführt, für die Bestimmung des NO_2-Gehalts der Stratosphäre genutzt werden. Die von SCIAMACHY gemessenen stratosphärischen NO_2-Säulen stimmen zu einem hohen Grad mit den vom Oslo CTM2 Modell vorhergesagten NO_2 überein. Allerdings müssen beide Datensätze an die Nadir-Messungen über sauberen Ozean-Gebieten angeglichen werden, da ein Zeit- und Breitenabhängiger Unterschied zwischen den Datensätzen beobachtet werden kann. Die Kombination von NO_2-Messungen gesamt-atmosphärischer und stratosphärischer Luftmassen des gleichen Instruments kann die Probleme, unter denen troposphärische NO_2-Datensätze aufgrund ungerechtfertigter Annahmen und räumlicher Interpolations- und Glättungs-Prozesse normalerweise zu leiden haben, zu einem großen Teil vermeiden helfen. Am Ende dieses Prozesses steht der derzeit beste verfügbare Datensatz troposphärischer NO_2-Säulen.

Diese troposphärischen Daten können im Folgenden genutzt werden, um den Grad troposphärischer Luftverschmutzung auf regionalen und lokalen Skalen zu untersuchen. Die vier verfügbaren Instrumente unterscheiden sich jedoch unter anderem in räumlicher Auflösung, Lokalzeit der Messung und Beobachtungsgeometrie, und all diese Faktoren können die Messwerte stark beeinflussen. Daher ist eine Analyse von zeitlichen Änderungen des troposphärischen NO_2s unter Berücksichtigung aller Instrumente nicht-trivial. Im zweiten Teil dieser Dissertation werden Methoden entwickelt, die eine konsistente Analyse zeitlicher Änderungen von NO_2-Säulen über Großstädten erlauben. Die erste Methode basiert auf der räumlichen Mittelung der gemessenen Erdschein-Spektren und der Extraktion der räumlichen Verteilung des Effektes der instrumentalen räumlichen Auflösung. Weiterhin werden zwei empirische Korrekturen eingeführt, welche sämtliche instrumentalen Unterschiede zusammenfassen, indem Instrumenten-abhängige Parameter in dem benutzten Trend-Modell berücksichtigt werden. Diese Methode wird auf GOME- und SCIAMACHY-Messungen separat, auf die kombinierte GOME/SCIAMACHY-Zeitreihe, und letztendlich auch auf einen vollständigen Datensatz von Messungen aller vier Instrumente angewandt. Alle Herangehensweisen resultieren in

konsistenten Zeitreihen troposphärischen NO_2s für eine Reihe von regionalen und lokalen Gebieten; erstmalig wird so die konsistente Trend-Analyse troposphärischen NO_2s bei hoher räumlicher Auflösung möglich. Die gemessenen NO_2-Säulen zeigen sehr starke Wachstumsraten über China, Indien und im Mittleren Osten; die NO_2-Belastung über dem Osten Chinas hat sich zwischen 1996 und 2011 verdreifacht. Über der westlichen Welt, insbesondere im Westen Europas, den Vereinigten Staaten von Amerika und Japan, kommt es im gleichen Zeitraum zu stark sinkenden NO_2-Werten. Einzelne Ballungszentren stechen hervor, wie z.B. Dhaka, Bagdad und Los Angeles, wo Änderungsraten von $+27.2 \pm 3.9\ \%\,a^{-1}$, $+20.7 \pm 1.9\ \%\,a^{-1}$ und $-6.00 \pm 0.72\ \%\,a^{-1}$ gemessen wurden. Die meisten Ballungszentren in China, Indien und dem Mittleren Osten erleben einen starken Anstieg der NO_2-Belastung von +5–10 $\%\,a^{-1}$, was zu einer Verdoppelung bis Verdreifachung innerhalb des Beobachtungszeitraums führt.

PUBLICATIONS

Some ideas and figures have appeared previously in various publications, conference talks, and conference posters.

Those Sections of this thesis which are to large extent cited from one of these articles are labeled with a footnote to the Section's headline. Also, the abstract is to a large extent a combination of the abstracts in Hilboll et al. (2013a) and Hilboll et al. (2013c).

ARTICLES

- Yoon, J., Burrows, J. P., Vountas, M., von Hoyningen-Huene, W., Chang, D. Y., Richter, A., and **Hilboll, A.**: Changes in Atmospheric Aerosol Loading Retrieved from Space Based Measurements During the Past Decade. *Atmospheric Chemistry and Physics Discussions,* 13, 26001–26041, 2013.

- Vrekoussis, M., Richter, A., **Hilboll, A.**, Burrows, J. P., Gerasopoulos, E., Lelieveld, J., Barrie, L., Zerefos, C., and Mihalopoulos, N.: Economic Crisis Detected from Space: Air Quality observations over Athens/Greece, *Geophysical Research Letters*, 40, 458–463, 2013.

- **Hilboll, A.**, Richter, A., and Burrows, J. P.: Long-term changes of tropospheric NO_2 over megacities derived from multiple satellite instruments, *Atmospheric Chemistry and Physics*, 13, 4145–4169, 2013a.

- **Hilboll, A.**, Richter, A., Rozanov, A., Hodnebrog, Ø., Heckel, A., Solberg, S., Stordal, F., and Burrows, J. P.: Improvements to the retrieval of tropospheric NO_2 from satellite – stratospheric correction using SCIAMACHY limb/nadir matching and comparison to

Oslo CTM2 simulations, *Atmospheric Measurement Techniques*, 6, 565–584, 2013c.

- **Hilboll**, **A.**, Richter, A., and Burrows, J. P.: NO_2 pollution trends over megac- ities 1996-2010 from combined multiple satellite data sets, in: Earth System Sciences: Bridging the gaps between disciplines. A multi-disciplinary Helmholtz Graduate Research School., edited by Lohmann, G., Wolf- Gladrow, D., Notholt, J., Unnithan, V., Grosfeld, K., and Wegner, A., pp. 9–15, Springer, Heidelberg, 2013b.

- Hodnebrog, Ø., Solberg, S., Stordal, F., Svendby, T. M., Simpson, D., Gauss, M., **Hilboll**, **A.**, Pfister, G. G., Turquety, S., Richter, A., Burrows, J. P., and Denier van der Gon, H. A. C.: Impact of forest fires, biogenic emissions and high temperatures on the elevated Eastern Mediterranean ozone levels during the hot summer of 2007, *Atmospheric Chemistry and Physics*, 12, 8727–8750, 2012.

- Kim, S.-W., McKeen, S. A., Frost, G. J., Lee, S.-H., Trainer, M. K., Richter, A., Angevine, W. M., Atlas, E., Bianco, L., Boersma, K. F., Brioude, J., Burrows, J. P., de Gouw, J., Fried, A., Gleason, J. F., **Hilboll**, **A.**, Mellqvist, J., Peis- chl, J., Richter, D., Rivera, C., Ryerson, T., te Lintel Hekkert, S., Walega, J., Warneke, C., Weibring, P., and Williams, E.: Evaluations of NO_x and highly reactive VOC emission inventories in Texas and their implications for ozone plume simulations during the Texas Air Quality Study 2006, *Atmospheric Chemistry and Physics*, 11, 11 361–11 386, 2011.

- Noguchi, K., Richter, A., Bovensmann, H., **Hilboll**, **A.**, Burrows, J. P., Irie, H., Hayashida, S., and Morino, Y.: A feasibility study for the detection of the diurnal variation of tropospheric NO_2 over Tokyo from a geostationary orbit, *Advances in Space Research*, 48, 1551–1564, 2011.

- Richter, A., Begoin, M., **Hilboll**, **A.**, and Burrows, J. P.: An improved NO_2 retrieval for the GOME-2 satellite instrument, *Atmospheric Measurement Techniques*, 4, 1147–1159, 2011.

- Kanakidou, M., Mihalopoulos, N., Kindap, T., Im, U., Vrekoussis, M., Gerasopoulos, E., Dermitzaki, E., Unal, A., Koçak, M., Markakis, K., Melas, D., Kouvarakis, G., Youssef, A. F., Richter, A., Hatzianastassiou, N., **Hilboll, A.**, Ebojie, F., Wittrock, F., von Savigny, C., Burrows, J. P., Ladstaetter- Weissenmayer, A., and Moubasher, H.: Megacities as hot spots of air pollution in the East Mediterranean, *Atmospheric Environment*, 45, 1223–1235, 2011.

- Konovalov, I. B., Beekmann, M., Richter, A., Burrows, J. P., and **Hilboll, A.**: Multi-annual changes of NO_x emissions in megacity regions: nonlinear trend analysis of satellite measurement based estimates, *Atmospheric Chemistry and Physics*, 10, 8481–8498, 2010.

SELECTED PRESENTATIONS

- **Hilboll, A.**: Changes in tropospheric NO_2 over megacities: A mul-ti-instrument approach. Presented at the *PRESCRBE-Workshop*, Bremen, Germany, 15 May 2013.

- **Hilboll, A.**: NO_2 pollution trends in megacities 1996-2010: a multi-satellite approach. Presented at the *ACCENT+ Symposium*, Urbino, Italy, 14 Sep 2011.

- **Hilboll, A.**: Assessment of decadal trends in tropospheric nitrogen dioxide over large European agglomerations by combining satellite measurements and model data. Presented at the *EGU General Assembly*, Vienna, Austria, 4 Apr 2011.

- **Hilboll, A.**: Trends in tropospheric nitrogen dioxide (NO_2) over megacities and large conurbations in the Mediterranean and Middle East from GOME and SCIAMACHY. Presented at the *11th IGAC Science Conference*, Halifax, Canada, 14 Jul 2010.

- **Hilboll, A.**: Trends in tropospheric NO_2 over megacities in the Mediterranean and Middle East regions from GOME and SCIA-

MACHY. Presented at the *EGU General Assembly*, Vienna, Austria, 3 May 2010.

SELECTED POSTERS

- **Hilboll**, **A.**, Richter, A. Burrows, J. P.: Long-term changes of tropospheric NO2 over megacities derived from multiple satellite instruments. Presented at the *6th International DOAS Workshop*, Boulder, U.S., 2013.

- **Hilboll**, **A.**, Richter, A., Rozanov, A., Heckel, A., and Burrows, J. P.: Tropospheric NO_2 from SCIAMACHY limb/nadir matching. Presented at the *5th International DOAS Workshop*, Mainz, Germany, 2011.

- **Hilboll**, **A.**, Richter, A., and Burrows, J. P.: Intercomparison of different stratospheric correction schemes for the retrieval of tropospheric Nitrogen Dioxide columns from satellite. Presented at the *38th COSPAR Scientific Assembly*, Bremen, Germany, 2010.

- **Hilboll**, **A.**, Leitão, J., Vrekoussis, M., Richter, A., and Burrows, J. P.: Trends in tropospheric NO2 from SCIAMACHY over megacities in the Mediterranean and Middle East. Presented at the *ESA Atmospheric Science Conference*, Barcelona, Spain, 2009.

- **Hilboll**, **A.**, Wieters, N., Richter, A., Sinnhuber, B.-M., and Burrows, J. P.: The impact of the stratospheric correction on tropospheric NO_2 measurements from satellites. Presented at the *EGU General Assembly*, Vienna, Austria, 2009.

ACKNOWLEDGMENTS

I am deeply thankful for the opportunity to do my PhD at the *Institut für Umweltphysik* in Bremen. My appreciation goes to Prof. John P. Burrows for making me part of this stimulating, excellent research institute. Thank you for all your advice and support.

Prof. Dr. Thomas Wagner was kind enough to accept reviewing this dissertation as second examiner. He also served as board member in my PhD committee and gave many valuable impulses. Thank you for your time and efforts in accompanying my work.

Dr. Andreas Richter was the best thesis supervisor I could possibly have wished for. I am very thankful for the intense exchange you made possible, for the many things I could learn from you, and for always being there for me in times of ignorance and confusion.

The work on SCIAMACHY limb/nadir matching would not have been possible without the help of Alexei Rozanov, who was kind and patient enough to answer all my questions about the limb measurements made by SCIAMACHY. Thank you very much.

Discussions with many other people have made both research and life at IUP a brighter experience. Special thanks go to (in alphabetical order) Achim Zien, Alexei Rozanov, Alireza Sadeghi, Anja Schönhardt, Annette Ladstätter-Weißenmayer, Enno Peters, Folkard Wittrock, Jan Aschmann, Joana Leitão, Larysa Istomina, Leonardo Alvarado, Luca Lelli, Marco Vountas, Narges Khosravi, Sebastian Mieruch, Vladimir Rozanov, and Vladyslav Nenakhov.

I want to especially thank Heiko Schellhorn and Heiko Schröter, the two sysadmins at IUP, for providing a great, running IT infrastructure and always being helpful with my many questions and special requests.

The first three years of my work have been funded by the Earth System Science Research School (ESSReS), an initiative of the Helmholtz Association of German research centers (HGF) at the Alfred Wegener Institute for Polar and Marine Research. Thanks go to Klaus Grosfeld,

the ESSReS coordinator, for sharing his enthusiasm about interdisciplinary work in the Earth sciences, and for his endless energy to keep the school's morale high.

I was lucky to be part of the CityZen project, a European Union Seventh Framework Programme (FP7/2007-2013) project (Grant Agreement no. 212095) about air pollution issues in megacities. The CityZen project helped me broadening my views and making first steps on the international science stage. Special thanks go to Augustin Colette and Erika von Schneidemesser, who made working in the CityZen team interesting as well as fun.

Last but definitely not least, the IUP Bremen and the ESSReS research school are not only scientifically stimulating, but also comprise of wonderful people, some of whom have become great friends. A warm embrace goes to Joana, Anja, Franziska, and Mihalis, for giving warmth, sharing times of pain and joy, and most notably for being themselves.

CONTENTS

1 INTRODUCTION 1

2 SCIENTIFIC BACKGROUND 7

2.1 The Earth's atmosphere 7

2.2 Atmospheric pollution 9

2.3 Sources of atmospheric nitrogen dioxide 11

2.3.1 Sources of tropospheric nitrogen dioxide 11

2.3.2 Sources of nitrogen dioxide in the middle and upper atmosphere 14

2.4 Nitrogen dioxide in atmospheric chemistry 14

2.4.1 Distribution of NO_2 in the atmosphere 15

2.4.2 NO_2 in the troposphere 16

2.4.3 Troposphere-stratosphere exchange of NO_2 18

2.4.4 NO_2 in the stratosphere 19

2.5 Climate change 20

2.5.1 Interactions between air quality and climate change 21

2.6 The emergence and importance of megacities 23

2.7 Radiation and radiative transfer 24

2.7.1 Emission of photons 25

2.7.2 Absorption of photons 25

2.7.3 Scattering of photons 26

2.7.4 The solar spectrum 27

2.7.5 The Beer-Lambert law 28

2.7.6 The radiative transfer model SCIATRAN 28

2.8 Differential optical absorption spectroscopy 29

2.9 Retrieval of tropospheric nitrogen dioxide 30

2.9.1 Separation of stratospheric and tropospheric signals 30

2.9.2 Air mass factors 31

2.10 Satellite instruments measuring NO_2 32

2.10.1 GOME 33

2.10.2 SCIAMACHY 34
2.10.3 OMI 36
2.10.4 GOME-2 36
2.10.5 TROPOMI 37
2.10.6 Sentinel-4 37
2.10.7 Sentinel-5 38
3 SCIAMACHY LIMB/NADIR MATCHING 39
3.1 Introduction 39
3.1.1 Stratospheric NO_2 39
3.1.2 The reference sector method 41
3.1.3 Overview of existing methods to account for stratospheric NO_2 42
3.1.4 The importance of the stratospheric correction for analysis of tropospheric NO_2 pollution 45
3.1.5 Outline of this chapter 47
3.2 Datasets used in this study 47
3.2.1 SCIAMACHY limb profiles 47
3.2.2 SCIAMACHY nadir columns 48
3.2.3 Tropopause altitude 49
3.2.4 Bremen 3d CTM 49
3.2.5 Oslo CTM2 50
3.3 The limb/nadir matching algorithm 51
3.3.1 Calculating stratospheric NO_2 columns 52
3.3.2 Interpolation to nadir measurement location 54
3.3.3 Stratospheric air mass factor 56
3.3.4 Offset limb/nadir 58
3.3.5 Tropospheric background over the Pacific 59
3.3.6 Applying stratospheric correction 60
3.4 Results and discussion 61
3.4.1 Modeled and measured vertical profiles 61
3.4.2 Difference between limb and nadir measurements 62
3.4.3 Climatological comparison between measurements and model 64
3.4.4 Zonal variability of stratospheric NO_2 69

3.4.5 The effect of surface reflectance on stratospheric NO_2 73
3.4.6 Comparison of the day-to-day variability 76
3.4.7 Sensitivity study: impact of stratospheric air mass factors 79
3.4.8 Improvements to the tropospheric data product 81
3.4.9 Error analysis 87
3.5 Summary and conclusions 91
4 NITROGEN DIOXIDE TRENDS OVER MEGACITIES 95
4.1 Introduction 95
4.1.1 Previous studies of VCD_{trop} NO_2 trends 96
4.2 Instrument differences 100
4.2.1 Instrument spatial resolution 102
4.2.2 How previous trend studies approached the challenge of different spatial instrument resolution 104
4.3 Retrieval of VCD_{trop} NO_2 104
4.4 Observations of tropospheric NO_2 106
4.4.1 Temporal changes 106
4.4.2 Seasonal cycle 110
4.4.3 NO_2 measurements over megacities 113
4.5 Explicit resolution correction 115
4.5.1 Method 116
4.5.2 Expected goodness of Γ 118
4.5.3 Spatial variation of Γ 121
4.5.4 Temporal variation of Γ 124
4.5.5 Validation of the resolution correction 125
4.5.6 Discussion 127
4.6 Levelshift trend model 133
4.6.1 Method 133
4.6.2 Comparison with resolution correction 136
4.6.3 Global distribution 138
4.6.4 VCD_{trop} NO_2 over megacities 142
4.7 Multi-instrument fit model 147
4.7.1 Method description 147

4.7.2 Error analysis 148
4.7.3 Results and discussion 151
4.7.4 Extensions 154
4.8 Non-linear NO_2 trends 156
4.9 Co-evolution of NO_2 with other air pollutants 161
4.9.1 Correlations with aerosol optical depth 162
4.9.2 Formaldehyde (HCHO) 163
4.9.3 Carbon dioxide (CO_2) 164
4.9.4 Carbon monoxide (CO) 166
4.9.5 Ozone (O_3) 168
4.10 Summary 169
5 CONCLUSIONS AND OUTLOOK 173

Appendix:
Additional material 179
A STRATOSPHERIC CORRECTION 181
A.1 Comparison SCIAMACHY limb / Oslo CTM2 181
A.2 Daily maps of SCD_{trop} NO_2 181
A.3 Zonal variability of stratospheric NO_2 181
B TROPOSPHERIC NO_2 TRENDS 189
Bibliography 195

LIST OF FIGURES

Figure 2.1 Vertical structure of the atmosphere 8
Figure 2.2 NO_x emissions to the troposphere 12
Figure 2.3 Gridded NO_x emissions from the EDGAR database 13
Figure 2.4 Vertical NO_2 profile 15
Figure 2.5 Diurnal variation of stratospheric NO_2 20
Figure 2.6 Mean energy budget of the Earth 21
Figure 2.7 Radiative forcing by compound 22
Figure 2.8 Urban population per country 23
Figure 2.9 Percentage of urban population per continent, 2010 24
Figure 2.10 Solar irradiance spectrum 27
Figure 2.11 Satellite instrument timeline 33
Figure 3.1 VCD_{strat} from SCIAMACHY limb for June 2010 40
Figure 3.2 VCD_{trop} climatology over the Pacific from Oslo CTM2 43
Figure 3.3 VCD_{trop} NO_2 when using the reference sector method 46
Figure 3.4 Vertical sensitivity of limb retrievals 51
Figure 3.5 Stratospheric correction data flow 53
Figure 3.6 Spatial interpolation of VCD_{strat}^{limb} 55
Figure 3.7 Zonal variation of VCD_{strat} (60°–65° N, 2006/08) 58
Figure 3.8 Measured and modeled vertical NO_2 profiles 61
Figure 3.9 Offset between nadir and limb over the Pacific 63
Figure 3.10 Correlation between SCIAMACHY and Oslo CTM2 65
Figure 3.11 Correlation between SCIAMACHY and B3dCTM 65
Figure 3.12 Difference between SCIAMACHY limb and Oslo CTM2 67
Figure 3.13 Difference between SCIAMACHY limb and B3dCTM 67

Figure 3.14 Cloud influence on limb/model differences 68
Figure 3.15 Zonal variation of VCD_{strat} (60°–65° N, 2006/08) 70
Figure 3.16 Zonal variation of VCD_{strat} (50°–55° N, 2005/02) 71
Figure 3.17 Zonal variation of VCD_{strat} (50°–55° N, 2004/12) 72
Figure 3.18 Zonal variation of VCD_{strat} (30°–25° S, 2005/04) 73
Figure 3.19 VCD_{strat} NO_2 over Greenland 74
Figure 3.20 Cloud influence on VCD_{strat} NO_2 75
Figure 3.21 Daily time series of VCD_{strat} NO_2 77
Figure 3.22 Time series of relative VCD_{strat} residuals 78
Figure 3.23 Sensitivity of AMF_{strat} to NO_2 and T profiles 80
Figure 3.24 Gridded SCD_{trop} NO_2 for Feb 2005 82
Figure 3.25 Gridded SCD_{trop} NO_2 for 28 Jan 2006 82
Figure 3.26 Comparison of VCD_{trop} NO_2 83
Figure 3.27 SCD_{trop} NO_2 time series 84
Figure 3.28 Zonal variation of SCD_{trop} (50°–55° N) 86
Figure 4.1 Schematic view of ground pixel size influence 100
Figure 4.2 NO_2 columns over Europe at different spatial resolutions 101
Figure 4.3 GOME and SCIAMACHY measurements of VCD_{trop} NO_2 over Mexico City 101
Figure 4.4 Synthetic pollution sources of varying size, sampled at GOME, SCIAMACHY, OMI, and GOME-2 spatial resolutions. 102
Figure 4.5 Normalized NO_2 time series over continental regions 107
Figure 4.6 Normalized NO_x emission time series over continental regions 108
Figure 4.7 Temporal evolution of the distribution of VCD_{trop} NO_2 110
Figure 4.8 Seasonal variation of VCD_{trop} NO_2 111
Figure 4.9 VCD_{trop} NO_2 time series over megacities 114
Figure 4.10 Synthetic pollution sources, sampled at GOME, SCIAMACHY, and reduced SCIAMACHY resolutions 119
Figure 4.11 Global map of resolution correction factor Γ 121

Figure 4.12 Gridded resolution correction factor Γ over Europe and the U.S. 122
Figure 4.13 Resolution correction factor and possible NO_x sources 123
Figure 4.14 Temporal changes of Γ 126
Figure 4.15 Resolution correction results: megacity regions showing good results 128
Figure 4.16 Resolution correction results: megacity regions affected by overcorrection 129
Figure 4.17 Resolution correction results: continental regions 131
Figure 4.18 Original and resolution-corrected NO_2 time series 133
Figure 4.19 Autocorrelation of NO_2 time series 135
Figure 4.20 Comparison of resolution correction factor and levelshift offset 136
Figure 4.21 Levelshift offset δ for original and resolution-corrected GOME data 137
Figure 4.22 Gridded levelshift fit results 139
Figure 4.23 Gridded levelshift fit results from GOME, SCIAMACHY, and the combined dataset. 140
Figure 4.24 Absolute and relative NO_2 changes over China. 141
Figure 4.25 Levelshift fit results 145
Figure 4.26 Bootstrap confidence intervals 151
Figure 4.27 Multi-instrument fit results 152
Figure 4.28 Topography, population density, and NO_x emissions in New Delhi, New York, and Tehran. 153
Figure 4.29 STL decomposition of NO_2 time series. 157
Figure 4.30 Break-point regression of NO_2 time series. 159
Figure 4.31 Co-evolution of NO_2 and aerosol optical depth 163
Figure 4.32 Co-evolution of NO_2 and HCHO 165
Figure 4.33 Co-evolution of NO_2 and CO_2 166
Figure 4.34 Co-evolution of NO_2 and CO 167
Figure 4.35 Co-evolution of NO_2 and O_3 169

Figure A.1 Difference between SCIAMACHY limb and Oslo CTM2 182
Figure A.2 Difference between SCIAMACHY limb and B3dCTM 183
Figure A.3 Difference between SCIAMACHY nadir and SCIAMACHY limb 184
Figure A.4 Difference between SCIAMACHY nadir and Oslo CTM2 185
Figure A.5 Gridded SCD_{trop} NO_2 for three individual days 186
Figure A.6 Zonal variation of VCD_{strat}, 2006/01 187
Figure A.7 Zonal variation of VCD_{strat}, 2006/08 188

LIST OF TABLES

Table 2.1 Major gaseous constituents of the Earth's atmosphere 7
Table 2.2 Satellite platform characteristics 33
Table 3.1 Correlation of limb measurements and CTM 66
Table 3.2 Variability of stratospheric NO_2 79
Table 4.1 Literature review of megacity NO_2 trends 98
Table 4.2 Spatial sampling of a pollution point source 103
Table 4.3 Spatial sampling by original and corrected GOME measurements 118
Table 4.4 Relative difference of measured pollution signals 120
Table 4.5 Comparison of original and down-scaled SCIAMACHY SCDs 130
Table 4.6 Continental NO_2 trends: levelshift and multi-instrument fit 143
Table 4.7 Megacity NO_2 trends: levelshift and multi-instrument fit 144

Table B.1 Continental NO_2 trends: levelshift model, 1996–2011 189
Table B.2 Continental NO_2 trends: levelshift model, 1996–2006 190
Table B.3 Continental NO_2 trends: multi-instrument fit 190
Table B.4 Megacity NO_2 trends: levelshift model, 1996–2011 191
Table B.5 Megacity NO_2 trends: levelshift model, 1996–2006 192
Table B.6 Megacity NO_2 trends: multi-instrument fit 193

1 INTRODUCTION

Man has considerably changed the face of the Earth, especially since the onset of the industrial revolution in the second half of the 18th century. Intensified industrial activities and the accompanying large energy need have lead to an immense burning of fossil fuels, causing significant emissions of trace gases to the Earth's atmosphere, promoting air pollution from a very local to a global problem. Anthropogenic activities have an enormous impact on the development of the Earth system, which has lead Crutzen and Stoermer to propose using the term 'anthropocene' for the current geological epoch (2000). Stratospheric ozone loss leading to enhanced ultraviolet radiation penetrating the atmosphere to reach the Earth's surface, intensification of the greenhouse effect through the continuous combustion of fossil fuels causing the emission of carbon dioxide, nitrogen oxides, and volatile organic compounds leading to photochemical smog close to the surface, and acid rain, causing forest degeneration and ocean acidification, are only three examples where anthropogenic activities cause sustained changes to the Earth system.

While the human population changes the Earth system by its activities, it also in itself undergoes considerable changes. The entire Earth's population has increased from 100 million at the onset of the 18th century to approximately 7 billion (Encyclopædia Britannica), a growing proportion of which is living in cities (see Sect. 2.6). Especially the so-called megacities, urban agglomerations of more than 10 million inhabitants, are emerging in many places in South America, Africa, and Asia. Over the past 20 years, they have seen incredible growth rates, as large numbers of people formerly living in rural areas mainly from agriculture abandon their homes and migrate towards the large megacities in search for work and better living conditions (Saunders, 2010).

Due to the very high population densities in megacities, they are hot-spots in terms of air pollution, i. e., the release of compounds to the atmosphere which are harmful for humans and/or other parts of the Earth system (Molina and Molina, 2004). The most important factors are road traffic, electricity generation, and residential heating and burning. As many megacities are located in developing countries, and as they are inhabited to large extent by poor people, these often do not have access to modern heating and cooking facilities, which leads to inefficient and thus pollution-rich combustion. However, megacities are not only air pollution hot-spots; due to the very high population density the air quality in megacities affects a large number of people, making megacity air quality an important subject for study.

The combustion of fossil fuels leads to the emission of numerous air pollutant compounds. Apart from the greenhouse gases carbon dioxide (CO_2) and methane (CH_4), the nitrogen oxides (NO_x, the umbrella term for nitrogen oxide, NO, and nitrogen dioxide, NO_2) play an important role. They are produced everywhere in the atmosphere at high temperatures and play several important parts in tropospheric chemistry including (1) NO_x is a precursor for the production of ozone (O_3) which, in addition to being a strong greenhouse gas, causes respiratory illness in humans and impacts the oxidizing capacity of the atmosphere, and (2) enhanced NO_x concentrations can lead to wet deposition in the form of nitric acid, causing acid rain and thus leading to degeneration of forests and further ocean acidification (Finlayson-Pitts and Pitts, 1999; Doney et al., 2007).

The Earth's atmosphere has been probed by in-situ and remote sensing techniques first from the ground and later from airborne platforms (balloons, airplanes) since the 18th century, allowing valuable insight into its dynamical and chemical processes. The advance of space technology and the launch of satellite-borne remote-sensing instrumentation have added an important complement to these atmospheric sounding methods. Satellites are not constrained by topographical and political boundaries, and thus enable for the first time the investigation of the Earth's surface and atmosphere with consistent measurement conditions regardless of geolocation.

Satellite-based atmospheric sounding instruments are based on the analysis of electromagnetic radiation which has passed through the atmosphere. As all gaseous atmospheric constituents absorb radiation at characteristic energies, reflected in the so-called absorption cross-section, the electromagnetic radiation observed at the top of the atmosphere holds the signature of those parts of the atmosphere through which it has passed. The oldest heritage lies with those instruments analyzing solar radiation which is back-scattered and reflected in the Earth's atmosphere and at its surface, respectively; they can be used to infer the concentrations of species which absorb in the ultraviolet, visible, and infrared ranges of the electromagnetic spectrum by comparing the back-scattered to the direct solar measurements. More recent instruments use the emission of atmospheric constituents in the infrared and microwave spectral regions, or actively send out radiation whose reflected signal they then use to infer atmospheric properties.

Arguably the first fundamental contribution of satellite sensors to the understanding of atmospheric chemistry was the verification of the Antarctic ozone hole in the 1980s, when measurements by the TOMS and SBUV instruments were analyzed to yield evidence of stratospheric ozone depletion over the Antarctic during spring (Stolarski et al., 1986). Since then, the available instrumentation has improved in many aspects, most notably in accuracy and precision, the recorded spectral ranges, the spectral resolution, the spatial resolution of the measurements, and the surface coverage. With the launch of the Global Ozone Monitoring Instrument (GOME) in 1995, the first instrument enabling the retrieval of tropospheric NO_2 abundances became available (Burrows et al., 1999). The analysis is performed with the Differential Optical Absorption Spectroscopy (DOAS) technique, which is based on a least-squares fit of the differential absorption signal in a given wavelength range. After GOME, the SCIAMACHY, OMI, and GOME-2 instruments have been utilized to infer tropospheric NO_2 columns, providing a long-term, high-quality dataset. Using these measurements, the temporal evolution of tropospheric NO_2 abundances could be established on a global scale. Richter et al. (2005) could show that NO_2 columns over Eastern China have been vastly increasing since 1995,

while NO_2 columns over all developed countries like, e. g., the United States, Western Europe, and Japan, have been strongly decreasing. Recent studies have extended the analysis of tropospheric NO_2 trends to megacities, deriving strong rates of growth and decline for emerging and developed megacities, respectively (van der A et al., 2008).

The aim of this thesis is to improve the retrieval of tropospheric NO_2 from satellites and to investigate its temporal evolution, especially over megacities. As one important technical aspect about the retrieval of tropospheric NO_2 abundances is the determination of the stratospheric background signal, this 'stratospheric correction' will be improved by using SCIAMACHY's unique limb-geometry measurements to account for the contribution of stratospheric NO_2 to the observed total NO_2 signal. The results from this limb/nadir matching technique will be validated using results from chemistry and transport models (CTMs). The analysis of long time series spanning multiple satellite instruments is complicated by the various differences between measurements by the GOME, SCIAMACHY, OMI, and GOME-2 instruments, which make direct comparison of the retrieved NO_2 columns difficult. As the instruments' spatial resolution contributes most strongly to these differences, the main focus lies on the treatment of these differences to allow consistent analysis of all instruments' measurements. One such method is based on the re-distribution of the coarse measurements by the GOME instrument using the spatial structure of the finer resolved SCIAMACHY measurements, captured in a resolution correction factor Γ. The other two methods follow an empirical approach and are based on an idea by Mieruch et al. (2008), who suggested accounting for (additive) offsets between two different instruments' time series by using so-called levelshift parameters in the fit function. As this original 'resolution correction' method can only be directly applied to measurements by *two* instruments (in this case, GOME and SCIAMACHY), it will be generalized to allow for an arbitrary number of different instruments in the regression. These different approaches are then tested on time series of tropospheric NO_2 both on continental scale and over individual megacities.

This thesis is structured as follows: Important background information about the Earth's atmosphere, atmospheric chemistry, nitrogen oxides, megacities, climate change, and satellite remote sensing of atmospheric trace gases is presented in Chapter 2. The SCIAMACHY limb/nadir matching technique will be developed and validated in Chapter 3. Chapter 4 forms the main part of this thesis, namely the treatment of the differences in ground pixel size between the four analyzed satellite instruments and the investigation of the temporal changes of tropospheric NO_2 columns over megacities. Chapter 5, finally, summarizes the most important findings of this thesis; it further provides an outlook on how the analysis of changes of tropospheric NO_2 can be further improved and makes suggestions for future studies.

2

SCIENTIFIC BACKGROUND

2.1 THE EARTH'S ATMOSPHERE

Today's atmosphere is composed of a variety of different gases. However, only molecular nitrogen (N_2), molecular oxygen (O_2), Argon (Ar), and water vapor (H_2O) appear in larger quantities (see Tab. 2.1); all other gaseous constituents of the atmosphere occur in trace amounts only (hence the name *trace gas*). While the mixing ratios of the major

Table 2.1: Major gaseous constituents of the Earth's atmosphere, with respect to dry air, integrated from the surface to 105 km (from Wallace, 2006, p. 8).

Constituent	Molecular weight	Fractional concentration by volume
Nitrogen (N_2)	28.013	78.08 %
Oxygen (O_2)	32.000	20.95 %
Argon (Ar)	39.95	0.93 %
Water vapor (H_2O)	18.02	0–5 %
Carbon dioxide (CO_2)	44.01	380 ppm
Neon (Ne)	20.18	18 ppm
Helium (He)	4.00	5 ppm
Methane (CH_4)	16.04	1.75 ppm
Krypton (Kr)	83.80	1 ppm
Hydrogen (H_2)	2.02	0.5 ppm
Nitrous oxide (N_2O)	56.03	0.3 ppm
Ozone (O_3)	48.00	0–0.1 ppm

atmospheric components N_2, O_2, and Ar, as well as those of other long-

lived species, do not change significantly with altitude (vertically, the atmosphere is stable in most situations), most trace gases show very distinct vertical profiles due to the chemical reactions they undergo. Arguably one of the most important ones is ozone (O_3), as the absorption of UV radiation by the ozone layer is a necessary condition for life on Earth; it further leads to stratospheric heating and is responsible for the temperature maximum at $\sim$50 km, defining the stratopause (Wallace, 2006, p. 11).

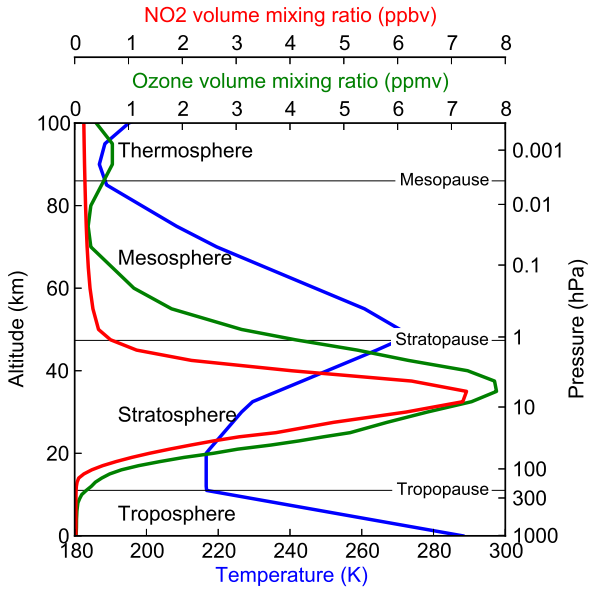

Figure 2.1: Vertical structure of the atmosphere (data taken from the U.S. Standard Atmosphere 1976, see U.S. Government Printing Office, 1976).

The atmosphere is commonly split into layers, namely the troposphere, stratosphere, mesosphere, thermosphere, and exosphere. These layers are defined by the vertical change rate of temperature; usually, temperature decreases with altitude. However, the stratosphere and thermosphere see a temperature inversion, i. e., an increase in temperature with altitude. In the stratosphere, this is caused by the absorption of ultraviolet radiation (and thus energy) by ozone molecules;

the temperature inversion in the thermosphere is caused by the extremely low density of air molecules. The exosphere, finally, is almost at vacuum, so that the notion of temperature loses its significance there. Fig. 2.1 shows the vertical temperature structure of the atmosphere, together with ozone and nitrogen dioxide concentrations, up to the thermosphere. Due to the exponential decrease of pressure with altitude, the bulk of the atmosphere's molecules are located in the troposphere. With the exception of the ozone layer in the stratosphere, which prevents UV radiation to penetrate to the Earth's surface, only the troposphere has direct impact on life on Earth.

2.2 ATMOSPHERIC POLLUTION

Air pollution is defined to be

> The presence of contaminants or pollutant substances in the air that interfere with human health or welfare, or produce other harmful environmental effects. (U.S. Environmental Protection Agency, 2009)

The polluting substances can be emitted both from anthropogenic and from natural sources. They can undergo several types of physical and chemical transformations, and contribute to a wide variety of environmental impacts (Gurjar et al., 2010). These include, among others, climate change, stratospheric ozone depletion, photooxidant formation (smog), eutrophication, acidification, toxicological stress on the health of humans and ecosystems, the depletion of resources, and noise (Pennington et al., 2004).

Contrary to common belief, air pollution is by no means a new phenomenon. The Roman philospher Seneca already wrote in 61 A.D.:

> As soon as I escaped from the oppressive atmosphere of the city, and from that awful odour of reeking kitchens which, when in use, pour forth a ruinous mess of steam and soot, I perceived at once that my health was mending. — (Seneca, 1917)

However, it was not until the second half of the twentieth century that air quality standards (i. e., upper bounds on air pollution) were developed and put into legislation (Vallero, 2007). At least since then, there have been large scientific efforts to assess and understand air pollution and its impact on the environment. For example, the concept of *total exposure* has been introduced as a measure for the integrated human exposure to air pollutants (see Smith, 1993, and references therein).

Undoubtedly, the pollutant with the largest direct impact on human health is particulate matter, or aerosols. Originating mostly from combustion processes, desert dust, and sea salt, they are harmful to the respiratory system of humans and responsible for numerous deaths. Current estimates for the number of deaths annually caused in Europe alone range up to 100 000 (World Health Organization, 2003, p. 14).

Other air pollutants cause more indirect effects to humans and the environment. The class of greenhouse gases (most notably CO_2, CH_4, and nitrous oxide, N_2O) are known to cause global warming, threatening ecosystem balances globally (see Sect. 2.5). Chlorofluorocarbons (CFCs), as a further example, are known to be the main cause of stratospheric ozone depletion (World Meteorological Organization, 2007), causing a dangerous increase of ultraviolet solar radiation at the Earth's surface. In the troposphere, on the other hand, ozone proves to be harmful to human health (World Health Organization, 2003, p. 30).

Ozone is formed in the troposphere in a catalytic cycle involving nitrogen oxides and photodissociation (see Sect. 2.4.2). Numerous studies have shown adverse health effects of NO_2 pollution, even though it is hard to distinguish between direct effects of NO_2 and health impacts of its reaction products (World Health Organization, 2003, p. 46). Therefore, detailed knowledge of NO_2 in the troposphere, its sources, and its temporal evolution, is important to the understanding of the effects of air pollution.

2.3 SOURCES OF ATMOSPHERIC NITROGEN DIOXIDE

2.3.1 *Sources of tropospheric nitrogen dioxide*

At high temperatures of more than ∼760℃, molecular nitrogen and oxygen undergo an endothermic reaction producing NO (U.S. Environmental Protection Agency, 1999, p. 3). This process leading to so-called 'thermal NO_x' is called the *Zeldovich mechanism*, and is described by the following reactions:

$$N_2 + O \longrightarrow NO + N \quad \text{(R 2.1)}$$

$$N + O_2 \longrightarrow NO + O \quad \text{(R 2.2)}$$

$$N + OH \longrightarrow NO + H \quad \text{(R 2.3)}$$

While thermal NO_x is by far the most important release mechanism in the troposphere, further NO_x emission pathways exist. 'Fuel NO_x' is emitted by the combustion of fuels which contain nitrogen through the oxidation of already-ionized nitrogen (U.S. Environmental Protection Agency, 1999, p. 5), while 'prompt NO_x' is created by the relatively fast reaction (hence, the name *prompt* NO_x) of nitrogen molecules in the combustion air with hydrocarbon radicals from the fuel (Office Of Air Quality Planning And Standards and Office Of Air And Radiation, 1995, p. 1.4-2).

In the troposphere, nitrogen oxides are emitted into the atmosphere mainly by the combustion of fossil fuels via these three pathways. Biomass burning and emissions from the biosphere also contribute to tropospheric NO_x sources, as does lightning. The estimates for the global NO_x emission budget are somewhat uncertain; Fig. 2.2a compiles an overview of the various anthropogenic and natural NO_x emission sources.

The spatial distribution of global NO_x emissions is shown in Fig. 2.3. Most NO_x emissions are closely located to anthropogenic activities, such as urban agglomerations, transport pathways (roads, shipping tracks, motorways), power generating stations, and industrial production centers.

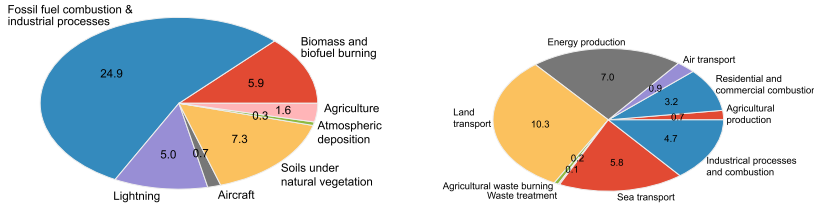

(a) Total NO_x emissions (b) Anthropogenic NO_x emissions

Figure 2.2: Sources of NO_x emissions to the troposphere, in $\mathrm{Tg\,N\,yr^{-1}}$. Total NO_x emissions are taken from (Solomon et al., 2007, p. 546); anthropogenic NO_x emissions are from the MACCity inventory (Granier et al., 2011).

Anthropogenic and industrial combustion

More than half of the tropospheric NO_x budget originates from anthropogenic and industrial combustion processes. Granier et al. (2011) compare several anthropogenic NO_x emission inventories. They report all considered inventories to show a slight increase since 1990, and they all agree to within 8 % in 2010. The MACCity inventory, e. g., states global anthropogenic NO_x emissions of $\sim$32.9 $\mathrm{Tg\,N\,yr^{-1}}$ for the year 2010 (Granier et al., 2011). Figure 2.2b shows the distribution among the different sectors.

Biomass burning

Biomass burning causes approx. 20 % of global NO_x emissions. Estimates differ by 50–80 % according to a recent intercomparison (Granier et al., 2011), depending on the year and season. The MACCity inventory, e. g., states global NO_x emissions from grassland/savanna and from forest fires of 3.4 and 1.5 $\mathrm{Tg\,N\,yr^{-1}}$ for the year 2010, respectively (Granier et al., 2011).

Emissions from the biosphere

A significant part of natural NO_x emissions originates from microbial processes in soils by numerous chemical pathways (Williams et al.,

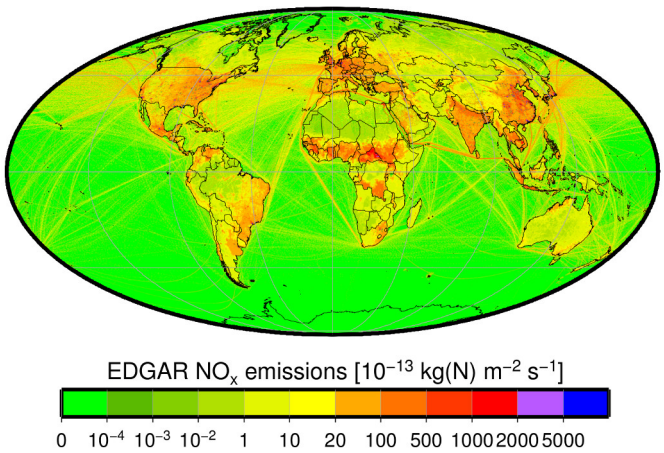

Figure 2.3: Gridded NO_x emissions for the year 2008 from the EDGAR database, version 4.2 (European Commission, Joint Research Centre and Netherlands Environmental Assessment Agency, 2011).

1992, and references therein). While these processes are basically natural processes, it has been shown that after the invention of the Haber-Bosch process, the application of fertilizer, i. e., agricultural activities, have significantly increased bacterial NO_x production (Bertram et al., 2005). In total, estimates for microbial NO_x emissions from natural and agricultural sources show a large uncertainty and vary widely, between 6 and 21 $\mathrm{Tg\,N\,yr^{-1}}$ (Ganzeveld et al., 2002); they estimate the total biogenic NO_x emissions from soils to be 12 and 3.8 $\mathrm{Tg\,N\,yr^{-1}}$, respectively.

Lightning

In the free troposphere, lightning can lead to significant production of NO_x, especially in the tropics. As is the case for biogenic emissions (see above), the estimation of lightning NO_x emission is highly uncertain; recent studies differ by more than one order of magnitude. Lee et al. (1997), e. g., give a range of 2–20 $\mathrm{Tg\,N\,yr^{-1}}$. Recently, satellite measurements have been used to infer the global lightning NO_x budget; Beirle et al. (2004b), e. g., use satellite measurements from the GOME

instrument (see Sect. 2.10.1) and yield an emission estimate of ∼2.8 $\mathrm{Tg\,N\,yr^{-1}}$.

2.3.2 *Sources of nitrogen dioxide in the middle and upper atmosphere*

The lifetime of tropospheric NO_2 is too short to allow for its transport into the stratosphere. However N_2O, which is emitted at the surface by both anthropogenic and natural processes, does not have significant sinks in the troposphere, leading to a very long lifetime of ∼ 120 years (Houghton et al., 2001). While anthropogenic emissions of N_2O originate mainly from agricultural soil management, animal manure management, and sewage treatment (Houghton et al., 2001), natural sources include a wide variety of biological processes in soil and water, particularly microbial action in wet tropical forests (Anderson et al., 2010). The very long tropospheric lifetime of N_2O molecules allows for their transport to the stratosphere, where the largest part of them is broken down to N_2 and $O(^1D)$ atoms by ultraviolet radiation (Brasseur et al., 1999). However, a fraction becomes the major source of stratospheric NO_2, via the reaction (see Seinfeld and Pandis, 2006, p. 151)

$$N_2O + O(^1D) \longrightarrow 2\,NO \qquad \text{(R 2.4)}$$

Since higher NO_x concentrations in the stratosphere lead to a net destruction of ozone (see Section 2.4.4), N_2O has recently started to be seen as an ozone depleting substance (Revell et al., 2012; Ravishankara et al., 2009). Consequently, there are efforts to have N_2O regulated under the Montreal Protocol (Kanter et al., 2013).

2.4 NITROGEN DIOXIDE IN ATMOSPHERIC CHEMISTRY

NO_2 appears as brownish, odorless gas and is hazardous to human health, causing irritations of the respiratory tract (Samet and Utell, 1990; Chauhan et al., 1998); typical surface concentrations are however too low to show significant direct effect on human health. Neverthe-

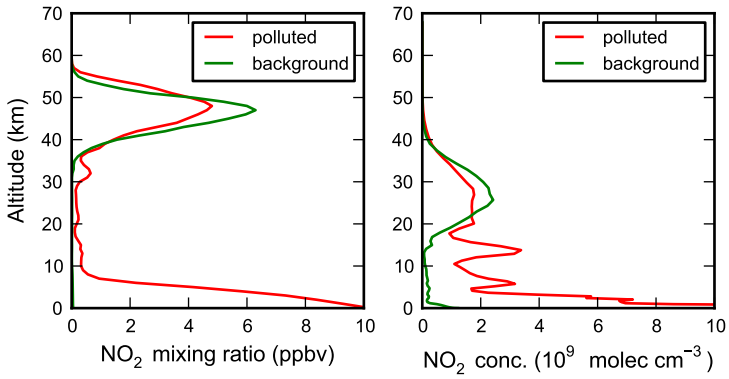

Figure 2.4: Vertical NO_2 profiles from the surface up to 70 km, both as volume mixing ratio (left) and as number concentration (right), from the Oslo CTM2, for 15 Jun 2005. The plots show cases of extremely polluted (32.1° N / 120.9° E, close to Shanghai, red) and background (32.1° N / 168.8° E, open Pacific Ocean, green) regions, each at 10:00 LT.

less, NO_2 plays a major role in atmospheric ozone chemistry, leading to ozone formation (destruction) in the troposphere (stratosphere).

Ozone is known to be damaging to human health; short-term effects include effects on mortality and respiratory morbidity, while long-term effects include lung damage and inflammatory responses (World Health Organization, 2003, and references therein). Therefore, enhanced NO_2 concentrations in in the lower troposphere can indirectly, i. e., via ozone production, severely impact human well-being.

2.4.1 *Distribution of* NO_2 *in the atmosphere*

In unpolluted regions, the bulk of the atmospheric NO_2 content can be found in the stratosphere, between 25 and 35 km altitude, where NO_x is formed by reaction R 2.4. In regions with high emissions of NO_2 to the troposphere, however, the maximum of atmospheric NO_2 concentrations is located close to the surface. Figure 2.4 shows typical atmospheric NO_2 profiles for both polluted and pristine regions,

derived from model calculations. It becomes obvious that, in order to correctly assess the tropospheric NO_2 content from satellite measurements, it is indispensable to accurately estimate the stratospheric NO_2 load.

2.4.2 NO_2 *in the troposphere*

Tropospheric NO_2 originates from a variety of sources, as outlined in Section 2.3. In the remote troposphere, i. e., in the absence of pollution, the nitrogen oxides NO and NO_2 constantly interchange by the set of reactions

$$NO_2 + \overset{\lambda \leq 420\,\mathrm{nm}}{h\nu} \longrightarrow NO + O \qquad \text{(R 2.5)}$$

$$O + O_2 + M \longrightarrow O_3 + M \qquad \text{(R 2.6)}$$

$$NO + O_3 \longrightarrow NO_2 + O_2 \qquad \text{(R 2.7)}$$

These three reactions effectively form a null cycle, as both NO_x and O_3 concentrations are conserved. Due to the photolysis reaction R 2.5, they are strongly dependent on the available sunlight, leading to a clear day-night contrast in NO_2 concentrations, with high (low) values during night (day), and dependencies on surface spectral reflectance and solar zenith angle.

When, however, hydroxyl radicals (OH) are available, a variety of oxidizable fuels can lead to ozone production. In the remote troposphere, both carbon monoxide (CO) and CH_4 are available as fuel, and can lead to photolytic production of O_3 molecules; in these cases, intermediate products in the CO and CH_4 oxidation cycles react with NO, rivaling reaction 2.7, which leads to net production of ozone. The maximum ozone yield of these cycles is given by the net reactions (see Seinfeld and Pandis, 2006, pp. 219 and 222)

$$\mathrm{CO} + 2\,\mathrm{O_2} + \overset{\lambda \leq 420\,\mathrm{nm}}{h\nu} \longrightarrow \mathrm{CO_2} + \mathrm{O_3} \qquad \text{(R 2.8)}$$

$$\mathrm{CH_4} + 4\,\mathrm{O_2} + \overset{\lambda \leq 420\,\mathrm{nm}}{2\,h\nu} \longrightarrow \mathrm{HCHO} + \mathrm{H_2O} + 2\,\mathrm{O_3} \qquad \text{(R 2.9)}$$

During nighttime, when it cannot be photolyzed, $\mathrm{NO_2}$ can, via the combination with the nitrate radical ($\mathrm{NO_3}$, see Wayne et al., 1991), lead to the formation of dinitrogen pentoxide ($\mathrm{N_2O_5}$), which acts as reservoir (Seinfeld and Pandis, 2006, p. 225):

$$\mathrm{NO_2} + \mathrm{O_3} \longrightarrow \mathrm{NO_3} + \mathrm{O_2} \qquad \text{(R 2.10)}$$

$$\mathrm{NO_2} + \mathrm{NO_3} + M \longrightarrow \mathrm{N_2O_5} + M \qquad \text{(R 2.11)}$$

This can only happen at night, because $\mathrm{NO_3}$ is quickly photolyzed during daytime. Another reservoir species is nitric acid ($\mathrm{HNO_3}$), which is the major tropospheric sink for $\mathrm{NO_2}$, via the reaction (Seinfeld and Pandis, 2006, p. 224)

$$\mathrm{OH} + \mathrm{NO_2} + M \longrightarrow \mathrm{HNO_3} + M \qquad \text{(R 2.12)}$$

The tropospheric lifetime of $\mathrm{NO_2}$ thus depends on the OH concentration and the $[\mathrm{NO}]/[\mathrm{NO_2}]$ ratio. At the surface, where OH concentrations can be high and the $[\mathrm{NO}]/[\mathrm{NO_2}]$ ratio is low, this leads to $\mathrm{NO_2}$ lifetimes of less than a day. In the free and upper troposphere, the usually lower OH concentrations and higher $[\mathrm{NO}]/[\mathrm{NO_2}]$ ratios yield longer lifetimes of 4-7 days (Brasseur et al., 1999, p. 255).

In the polluted continental troposphere, many reactions have considerably increased yields, due to the higher concentrations of available reactants. Various non-methane hydrocarbons (NMHC, also called volatile organic compounds, VOC) are available as additional oxidizable fuel, leading to increased $\mathrm{O_3}$ production via the following generalized oxidation cycle (Brasseur et al., 1999, p. 273):

$$\mathrm{OH} + R\mathrm{H} \longrightarrow R + \mathrm{H_2O} \tag{R 2.13}$$
$$R + \mathrm{O_2} + M \longrightarrow R\mathrm{O_2} + M \tag{R 2.14}$$
$$R\mathrm{O_2} + \mathrm{NO} \longrightarrow R\mathrm{O} + \mathrm{NO_2} \tag{R 2.15}$$
$$R\mathrm{O} + \mathrm{O_2} \longrightarrow \mathrm{HO_2} + R'\mathrm{CHO} \tag{R 2.16}$$
$$\mathrm{HO_2} + \mathrm{NO} \longrightarrow \mathrm{OH} + \mathrm{NO_2} \tag{R 2.17}$$
$$2\,(\mathrm{NO_2} + \overset{\lambda \leq 420\,\mathrm{nm}}{h\nu} \longrightarrow \mathrm{NO} + \mathrm{O}) \tag{R 2.18}$$
$$2\,(\mathrm{O} + \mathrm{O_2} + M \longrightarrow \mathrm{O_3} + M) \tag{R 2.19}$$

The net reaction cycle can be summarized as

$$R\mathrm{H} + 4\,\mathrm{O_2} + 2\,h\nu \longrightarrow R'\mathrm{CHO} + \mathrm{H_2O} + 2\,\mathrm{O_3} \tag{R 2.20}$$

Here, RH stands for a NMHC, and carbonyl products are denoted R'CHO, where R' is an organic fragment having one fewer carbon atom than R. The cycle is completely analogous to reaction R 2.9 and can lead to considerably increased ozone production, causing photochemical smog. Also, $\mathrm{HNO_3}$ concentrations can become so large that it becomes an important constituent of acidic precipitation.

2.4.3 *Troposphere-stratosphere exchange of* $\mathrm{NO_2}$

Exchange of $\mathrm{NO_2}$ containing air masses between troposphere and stratosphere can occur in both directions. Stratospheric intrusions, for example, can introduce $\mathrm{NO_2}$ enriched air masses into the upper troposphere, especially in polar conditions (Elbern et al., 1998; Sprenger and Wernli, 2003). While these air masses can show considerably enhanced $\mathrm{NO_2}$ concentrations of 75–110 pptv (Liang et al., 2011), these numbers are still very low compared to the $\mathrm{NO_2}$ rich layers close to the surface and in the middle stratosphere, and do not lead to significant changes in the tropospheric columns. On the other hand, deep convection has been reported to be able to introduce significant amounts of trace gases into the lowermost stratosphere, even at mid-latitudes (Hegglin et al., 2004).

However, as NO_2 concentrations in the upper troposphere and lower stratosphere are generally very low (see Fig. 2.4), these transport processes generally do not significantly influence atmospheric chemistry in these altitude regions.

2.4.4 NO_2 *in the stratosphere*

The main $NO-NO_2$ cycle (reactions R 2.5–R 2.7) is also taking place in the stratosphere. When, however, the concentration $[O]$ of single oxygen atoms becomes high enough (as is the case in the middle and upper stratosphere, where O_2 and O_3 can get photolyzed at wavelengths less than 242.4 nm and 310 nm, respectively; see Finlayson-Pitts and Pitts, 1999, pp. 89–95), the photodissociation of NO_2 (reaction R 2.5) becomes rivaled by the reaction

$$NO_2 + O \longrightarrow NO + O_2 \qquad \text{(R 2.21)}$$

leading to a net destruction of ozone (Crutzen, 1970; Hendrick et al., 2012):

$$O_3 + O \longrightarrow 2\,O_2 \qquad \text{(R 2.22)}$$

However, nitrogen oxides can also suppress ozone destruction by conversion of reactive hydrogen and chlorine species into reservoir species, e. g., chlorine nitrate ($ClONO_2$) and HNO_3 (Murphy et al., 1993).

At nighttime, the reaction of NO_2 with ozone becomes more important, leading to a build up of N_2O_5, which acts as NO_x reservoir (Wayne et al., 1991):

$$NO_2 + O_3 \longrightarrow NO_3 + O_2 \qquad \text{(R 2.10)}$$
$$NO_2 + NO_3 + M \longrightarrow N_2O_5 + M \qquad \text{(R 2.11)}$$

Other NO_x reservoirs include nitric acid (see reaction R 2.12), $ClONO_2$ and peroxynitric acid (HO_2NO_2). All three reservoir mechanisms lead to a two-fold slowing-down of ozone destruction through both the reduction of available NO_2 molecules and the sequestration of ClO_x and HO_x radicals.

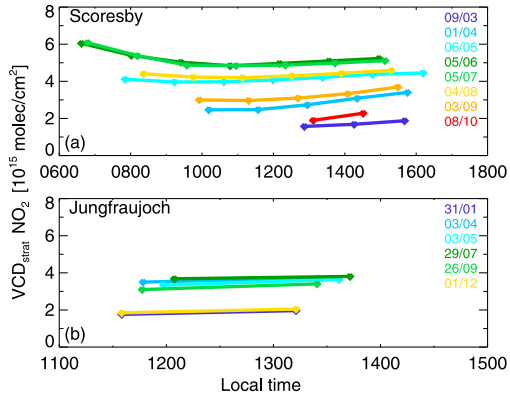

Figure 2.5: Diurnal variation of stratospheric NO_2 columns over Scoresby (70.5°N, 22°W) and Jungfraujoch (46.5°N, 8°E), measured by the OMI instrument, as a function of local time of observation (adapted from Dirksen et al., 2011, Fig. 11).

During daytime, the photochemical destruction of the reservoir species N_2O_5 leads to an increasing NO_2 concentration (Solomon and Keys, 1992; Brasseur and Solomon, 2005, p. 258). Both diurnal and seasonal cycles of stratospheric NO_2 are driven by this mechanism, leading to an almost linear increase in NO_2 concentrations during daytime, and to a clear seasonal cycle which gets more and more pronounced going polewards (see Fig. 2.5, Dirksen et al., 2011, and references therein).

When considering the lifetime of stratospheric NO_2, it makes most sense to talk of NO_x lifetime, due to the close coupling of the two molecules and their reservoir species. Depending on the altitude, the NO_x lifetime τ_{NO_x} varies between several days and several months (Brasseur and Solomon, 2005, p. 256).

2.5 CLIMATE CHANGE

At least since the third assessment report of the Intergovernmental Panel on Climate Change (IPCC, Houghton et al., 2001), the anthropogenic influence on current climate through the emission of green-

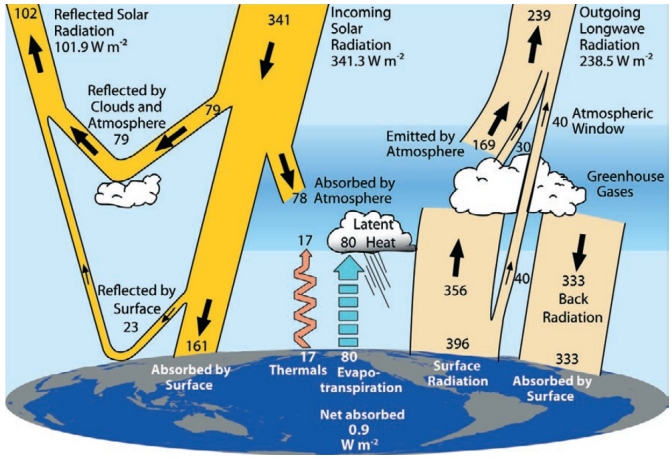

Figure 2.6: Global annual mean energy budget of the Earth, for the March 2000–May 2004 period (from Trenberth et al., 2009).

house gases like carbon dioxide, methane, nitrous oxide, and ozone, is scientifically undisputed. These greenhouse gases absorb part of the outgoing long-wave radiation and thus keep energy within the Earth system which would otherwise be radiated into space (see Fig. 2.6). The total net anthropogenic radiative forcing is estimated to be $1.6 \pm 0.8\,\mathrm{W\,m^{-2}}$ (Solomon et al., 2007). While the influence of the long-lived greenhouse gases CO_2, CH_4, N_2O, and of various halocarbons is quite accurately estimated, the individual uncertainties on the other compounds can be large (see Fig. 2.7). Through the mechanisms described in Sect. 2.4.2, tropospheric NO_2 directly influences ozone concentrations, showing that also in the light of climate change, accurate knowledge of NO_2 abundances and their temporal evolution are needed.

2.5.1 *Interactions between air quality and climate change*

An area which has received a lot of attention in current atmospheric research is the interactions between climate and air quality (Isaksen et al., 2009; Raes et al., 2010). A more thorough understanding of atmospheric oxidation processes, as well as ever increasing computa-

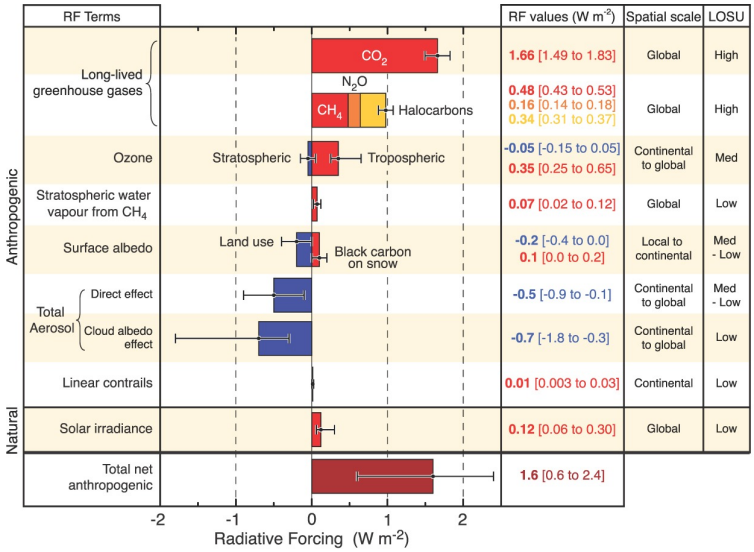

Figure 2.7: Radiative forcing of different climate-active compounds and their individual uncertainties (from Solomon et al., 2007).

tional power, have lead to growing interest in the feedback processes involving both atmospheric chemistry and the Earth's radiation balance. Chemically active atmospheric constituents like CH_4, O_3, sulfate and organic aerosols, are known to be driving factors in climate change. Atmospheric pollution by these compounds and their precursors thus change the atmospheric composition, contributing to climate change. Reciprocally, climate change directly influences atmospheric composition and oxidation processes through changes in temperature, dynamics, hydrological cycle, atmospheric stability, and biosphere-atmosphere interactions (Isaksen et al., 2009). Some examples for these interaction processes are enhanced stratosphere-tropo-sphere exchange of O_3, increased biogenic emissions due to enhanced temperature, release of CH_4 from thawing permafrost, and decreasing carbon sinks due to reduced biospheric uptake (see Isaksen et al., 2009, and references therein). As integrated modeling systems of atmospheric chemistry and climate are being developed (Raes et al., 2010), detailed understanding of at-

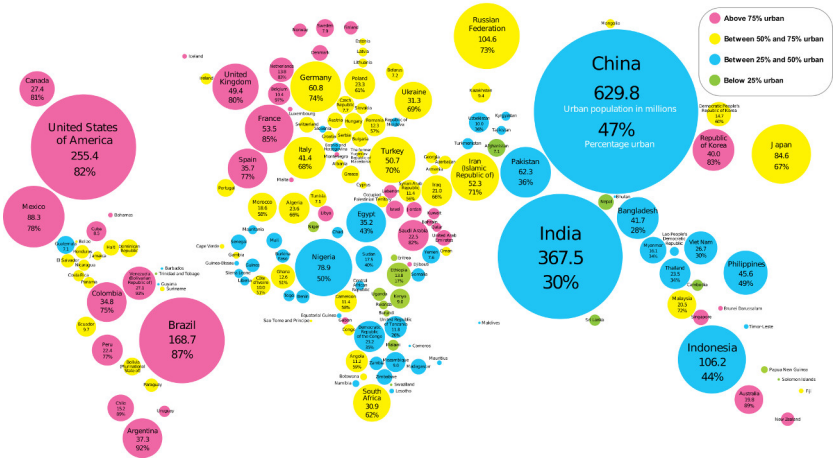

Figure 2.8: Countries and territories with urban populations exceeding 100,000. Circles are scaled in proportion to urban population size. Where space allows, numbers within circles show urban population (in millions) and urban percentage of the country's total population (from United Nations Children's Fund, 2012).

mospheric oxidation processes becomes ever more important, showing the need for ongoing observations of atmospheric pollutants like NO_2.

2.6 THE EMERGENCE AND IMPORTANCE OF MEGACITIES

A large proportion of the human population lives in urban agglomerations (see Fig. 2.8). This proportion has been increasing for a long time and exceeded 50% in 2008 (United Nations, Department of Economic and Social Affairs, Population Division, 2012). Figure 2.9 shows that, while the growth rate of urbanization has slowed down in Europe and the Americas, Asia and Africa still show strongly increasing urbanization. The very high population densities inherent to such agglomerations provide a challenging environment to its inhabitants. The high traffic, energy use, and pollution lead to a strongly enhanced total exposure to harmful pollutants for the megacity population (Gurjar et al.,

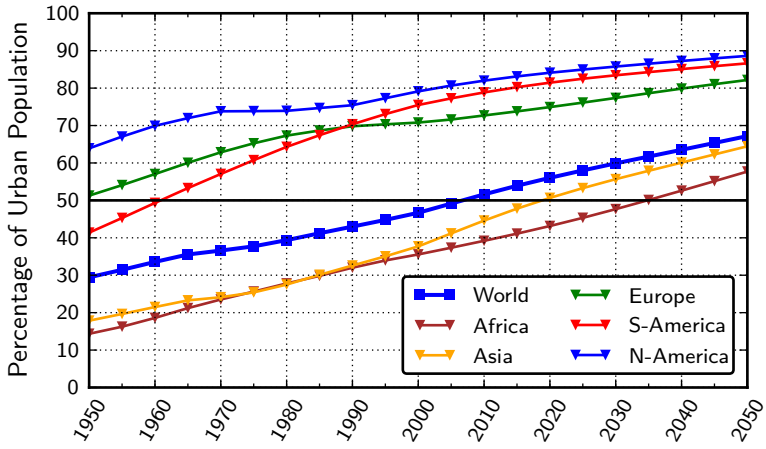

Figure 2.9: Percentage of urban population per continent, as of 2010 (data from United Nations, Department of Economic and Social Affairs, Population Division, 2012).

2008; Molina and Molina, 2004; Mage et al., 1996; Lelieveld et al., 2013). On the other hand, shorter distances leading to less transport, reduced land use, and generally better availability of technology are indicators that in a global sense, the environmental impact of megacities might not be as unfavorable as it may seem. Finally, one has to remember that the high rate of urbanization is rooted in the extremely hard living conditions in the developing world's rural areas, which generally leads to a significant increase in quality of life for the recently migrated megacity population, in spite of the hardships they have to endure (Saunders, 2010).

2.7 RADIATION AND RADIATIVE TRANSFER

Electromagnetic radiation is energy propagating through space in the form of coupled electric and magnetic fields. At the same time, it exhibits particle-like behavior; these particles are called photons. The

photon's energy depends on the wavelength of the electromagnetic field; the two quantities are coupled via the equation

$$E = h\nu$$

where $h \approx 6.626 \times 10^{-34}$ Js is the Planck constant and ν is the frequency of the electromagnetic field (the value for the Planck constant is taken from Mohr et al., 2012).

2.7.1 *Emission of photons*

All matter emits electromagnetic radiation in the form of photons. This emission is driven by a molecule's transition from a higher energy state to a lower energy state; the emitted photon's energy is determined by the energy difference between the two states (Haken and Wolf, 2001, p. 60). For atoms, the energy states are determined by its electronic configuration; in the case of molecules, the configuration also includes rotational and vibrational oscillations of its nuclei (Haken and Wolf, 2006, pp. 179 ff.). At equilibrium (of radiation and matter), the photon wavelengths are distributed according to the *Planck distribution* (Bohren and Clothiaux, 2006, p. 9):

$$P_e(\lambda) = \frac{2\pi hc^2}{\lambda^5} \frac{1}{\exp\left(\frac{hc}{\lambda k_B T}\right) - 1} \tag{E 2.1}$$

Here, λ denotes the wavelength, T the temperature, and h is the Planck constant, $c \approx 2.998 \times 10^8$ ms^{-1} is the speed of light, $k_b \approx 1.381 \times 10^{-23}$ JK^{-1} is the Boltzmann constant (all physical constants are taken from Mohr et al., 2012).

2.7.2 *Absorption of photons*

Inversely, a photon can be absorbed by a molecule if the former's energy equals the energy difference between a higher and a lower energy state of the molecule. Consequently, any given molecule can absorb

radiation of specific wavelengths only, which are determined by the molecule's configuration.

The absorption at wavelength λ by a molecule can be described by its absorption cross-section $\sigma^a(\lambda)$, which has the unit of length squared (i. e., area) and can be viewed as the effective area of the molecule for removing energy from incident radiation; it depends on temperature and pressure, as both have influence on the molecule's configuration (Bohren and Clothiaux, 2006, p. 61).

2.7.3 *Scattering of photons*

When photons are forced to deviate from their path by localized inhomogeneities in the medium through which they travel, one commonly speaks of scattering. In the case of photons traveling through a gaseous mixture, scattering can occur on single gas molecules and small particles. Depending on the ratio of the particle's circumference and the photon's wavelength, i. e., the dimensionless size parameter $\alpha = \frac{\pi \cdot D_p}{\lambda}$, one speaks of Rayleigh ($\alpha \ll 1$), Mie ($\alpha \approx 1$), and geometric ($\alpha \gg 1$) scattering.

The scattering of ultraviolet and visible solar radiation on the gaseous molecules of the Earth's atmosphere happens in the Rayleigh regime. According to the first scattering law derived by Rayleigh in 1871, the scattering efficiency is proportional to the inverse fourth power of the wavelength, which is the reason why clear sky appears blue: the blue part of the visible spectrum has shorter wavelength and is therefore much more likely to be scattered towards the surface; the redder parts of solar radiation are more likely to pass through the atmosphere without being scattered (Bohren and Clothiaux, 2006, p. 128). Scattering of sunlight on atmospheric particles, or aerosols, happens in the Mie regime. Here, the scattering efficiency strongly depends on the shape of the scattering particle, the wavelength, and also on the direction of the incident photon. Due to these complexities, accounting for the influence of atmospheric aerosols in radiative transfer simulations is extremely challenging, because the scattering characteristics of the

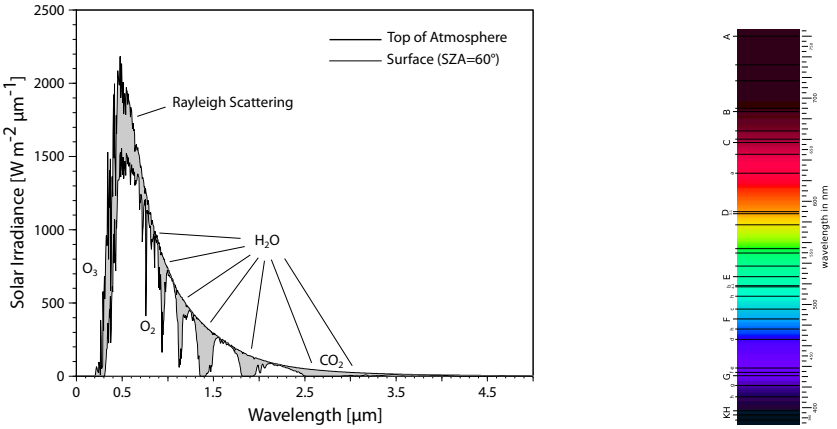

Figure 2.10: (left) Solar irradiance curve at the top of the atmosphere and at the surface for a solar zenith angle of 60° in an atmosphere without aerosols or clouds. Absorption and scattering regions are indicated (after Liou, 2002). (right) Fraunhofer lines in the solar spectrum (from `http://en.wikipedia.org/wiki/File:Fraunhofer_lines.svg`).

aerosols need to be known precisely. Geometric scattering, finally, can be observed as rainbows which are caused by rain drops and ice crystals. In clear-sky conditions, it is irrelevant to atmospheric radiative transfer, as the scattering molecules and particles in the atmosphere are rather small.

2.7.4 *The solar spectrum*

The wavelength-dependence of emission, absorption, and scattering processes can be shown using the example of the spectral characteristics of solar radiation. Figure 2.10 shows the solar irradiance at the Earth's surface and at the top of the atmosphere. The shape of the solar irradiance spectrum at the top of the atmosphere is approximately the energy distribution of a black body (i. e., an idealized physical body absorbing all incident electromagnetic radiation) of temperature 5800 K, as determined by Eq. E 2.1. In reality, the solar spectrum prominently

shows a number of so-called *Fraunhofer lines*, which are caused by molecular absorption within the sun's atmosphere (see Fig. 2.10).

The attenuation of the sun's radiation in the Earth's atmosphere can be seen in the gray-shaded difference between the top of atmosphere and surface spectra. In the visible wavelength range, the largest part of attenuation is due to Rayleigh scattering; in the UV and IR ranges, the observed attenuation can be mostly attributed to absorption processes due to ozone, water vapor, and carbon dioxide.

2.7.5 *The Beer-Lambert law*

The combined attenuation effect of absorption and scattering is often called extinction. When traveling through any medium, the transmission of radiation decreases exponentially with the medium's extinction cross-section and the path length. This fact has become known as the Beer-Lambert-Bouguer law and can be written as

$$I(\lambda) = I_0(\lambda) \cdot \exp(-\rho s \sigma^e(\lambda)), \tag{E 2.2}$$

where $I_0(\lambda)$ is the unattenuated intensity, ρ is the absorber/scatterer density, s is the path length, and $\sigma^e(\lambda)$ is the extinction cross-section (Bohren and Clothiaux, 2006, p. 53).

2.7.6 *The radiative transfer model SCIATRAN*

The effective simulation of radiative transfer, i. e., the passage of photons through the Earth's atmosphere, is indispensable for the analysis of hyperspectral measurements and the subsequent retrieval of meaningful quantities. At the Institut für Umweltphysik of the Universität Bremen, the radiative transfer model SCIATRAN has been developed (Rozanov et al., 2013). SCIATRAN is a modular system which can be employed in multiple tasks, e. g., the simulation of radiances at given atmospheric conditions, the calculation of air mass factors (see Sect. 2.9.2), or the retrieval of absorber profiles from hyperspectral measurements (see 3.2.1).

2.8 DIFFERENTIAL OPTICAL ABSORPTION SPECTROSCOPY

As stated in Sect. 2.7.5, the effect of absorption of radiation is summarized by the Beer-Lambert law (Eq. E 2.2). For solar radiation passing through the Earth's atmosphere, usually J different absorbers have to be considered, and the individual absorption cross-sections $\sigma_j(\lambda)$ depend on temperature and pressure. In the case of clear-sky measurements and optically thin absorbers, the atmospheric attenuation is dominated by scattering processes, which slowly vary with wavelength (see Sect. 2.7.3); it is thus possible to separate the optical thickness spectrum $\ln \frac{I(\lambda)}{I_0(\lambda)}$ into a low-frequency and a high-frequency part.[1] The low-frequency variations can then be approximated by a low-order (usually 3–6) polynomial. In the case of space-borne instruments, the Beer-Lambert law thus leads to the following equation, called the DOAS equation:

$$\ln \frac{I_0(\lambda)}{I(\lambda)} = \sum_{j=1}^{J} \sigma'_j(\lambda) \cdot \mathrm{SCD}_j + \sum_{p=0}^{P} a_p \cdot \lambda^p \qquad \text{(E 2.3)}$$

Here, $I_0(\lambda)$ and $I(\lambda)$ are the measured solar and Earthshine spectra, respectively;

$$\sigma'_j = \sigma_j - \sum_{p=0}^{P} b_p \cdot \lambda^p$$

are the high-frequency parts of the absorption spectrum of absorber j, while SCD_j is the integrated concentration of absorber j along the light path,

$$\mathrm{SCD}_j = \int \rho_j(s) ds.$$

a_p are the coefficients of the polynomial covering the low-frequency features in the measured spectra (Platt and Stutz, 2008).

In practice, Eq. E 2.3 needs to be extended to account for various atmospheric processes, e. g., the filling-in of Fraunhofer and molecular

[1] This cannot be done with the intensities themselves, because the solar spectrum is dominated by high-frequency Fraunhofer lines.

absorption lines called *Ring effect* (Vountas et al., 1998), which is included as a pseudo-absorber. Equation E 2.3 can then be solved for the integrated absorber concentrations SCD_j, which can subsequently be further analyzed to yield meaningful atmospheric quantities. Within this study, the DOAS analysis has been carried out using the software package `NLIN_D` (Richter, 1997).

2.9 RETRIEVAL OF TROPOSPHERIC NITROGEN DIOXIDE

The DOAS method yields atmospheric slant columns, i. e., the integrated number of molecules along the average light path reaching the detector. In order to use the measurements to assess tropospheric NO_2 loads, these total slant columns have to be corrected for the influence of the stratospheric NO_2 field. Furthermore, the resulting tropospheric slant column densities (SCD) must be converted to vertical column densities (VCD), i. e., the integrated number of molecules above a given ground location.

2.9.1 *Separation of stratospheric and tropospheric signals*

The determination of the stratospheric background signal to the measured NO_2 slant columns often relies on the assumption of longitudinal homogeneity. As NO_2 in the stratosphere is mainly driven by the solar radiation available for photolysis, and is dependent on ozone concentrations and temperature only to a lesser extent, this assumption is more or less satisfied, at least in low and mid-latitudes. Usually, a meridional band over the Pacific Ocean is then assumed to be clean of tropospheric NO_2, and the instrument's measurements over this region are then assumed to be representative of the stratospheric contribution to the measured signal; this is approximately true because the satellite's sun-sunchronous orbit leads to identical photochemical states within a zonal band around the globe. While this second assumption is generally correct (see, e. g., Schultz et al., 1999, and references therein), the lifetime of tropospheric NO_2 in boreal winter can be long

enough for significant amounts of pollution from East Asia and North America to be transported over the open Pacific Ocean.[1] As part of this thesis, an alternative method to correct for the stratospheric influence on measured slant columns will be developed (see Chapter 3).

2.9.2 *Air mass factors*

The slant column density is strongly influenced by the measurement geometry and the sun's elevation above the horizon. To yield a quantity which is independent of the measurement geometry and to relate this quantity to geographic location, the SCD needs to be converted to vertical column densities.

Under the assumption that slant and vertical columns are proportional to each other for equivalent measurement conditions, this conversion is performed with the so-called 'air mass factor' (AMF), which relates the measured and desired quantities via

$$\mathrm{AMF} = \frac{\mathrm{SCD}}{\mathrm{VCD}}.$$

The AMF depends on measurement geometry (solar zenith, viewing azimuth, and relative azimuth angles), wavelength, surface spectral reflectance (albedo), surface pressure, and the vertical distributions of aerosols, clouds, and absorbing trace gases. It is calculated using radiative transfer simulations (see Sect. 2.7.6).

Since the dependence of the AMF on these quantities is relatively smooth, it is possible to pre-calculate lookup-tables so that the computationally expensive radiative transfer simulations do not have to be performed for each individual measurement (Nüß, 2005). However, the radiative transfer heavily depends on the measurement conditions, especially albedo and aerosol profiles (Leitão et al., 2010). As independent measurements of vertical absorber and aerosol profiles and surface spectral reflectance are non-existent for most satellite measurements, these data have to be assumed a-priori or taken from climatological datasets. This introduces the largest contribution to the total

[1] This will be shown using model simulations in Chapter 3.3.5.

uncertainty of the retrieval of vertical absorber columns; it can reach values of 50% and more (Boersma et al., 2004). To minimize the uncertainty introduced by clouds, often cloudy scenes are excluded from the analysis.

The formulation of the air mass factor can be generalized to the altitude-dependent *block air mass factor* (BAMF) concept. The BAMF is defined as the ratio of slant and vertical partial columns within individual atmospheric layers,

$$\mathrm{BAMF_i} = \frac{\mathrm{SCD_i}}{\mathrm{VCD_i}},$$

and yields the total AMF by weighting with the absorber profile (Palmer et al., 2001):

$$\mathrm{AMF} = \frac{\sum \mathrm{BAMF_i} \times \mathrm{VCD_i}}{\sum \mathrm{VCD_i}}.$$

This formulation has the advantage that the calculated AMFs no longer depend on the vertical absorber profile; they can rather be applied to various different a-priori profiles, e. g., from atmospheric chemistry models.

2.10 SATELLITE INSTRUMENTS MEASURING NO_2

Satellites provide the unique possibility to observe the whole globe under consistent measurement conditions. While their spatial resolution is several orders of magnitude lower than that of ground-based or airborne instrumentation, they provide the advantage of allowing for global measurements, especially over regions where ground-based measurements are not possible due to their remoteness (e. g., remote ocean areas) or political constraints.

Using the DOAS method to retrieve atmospheric trace gas concentrations necessitates hyper-spectral measurements of both direct and scattered solar radiation. Appropriate satellite instruments have been available since the mid-1990s. Table 2.2 gives an overview of the past, present, and future low-Earth orbit satellite instruments allowing the retrieval of atmospheric NO_2 abundances from nadir geometry. A

Table 2.2: Characteristics of selected past, present, and future satellite platforms used to study tropospheric NO_2.

Instrument	GOME	SCIAMACHY	OMI	GOME-2	TROPOMI
Equator crossing	10:30 LT	10:00 LT	13:45 LT	09:30 LT	13:45 LT
Global coverage	3 days	6 days	1 day	~1 day	1 day
Availability period	1995/10–2003/06	2002/08–2012/04	2004/10–	2007/01–	(2015–)
Pixel size at nadir [km^2]	40×320	30×60*	13×24*	40×80	7×7

*The spatial resolution depends on wavelength and measurement scene.

timeline visualizing the availability of the individual instruments' datasets is given in Fig. 2.11.

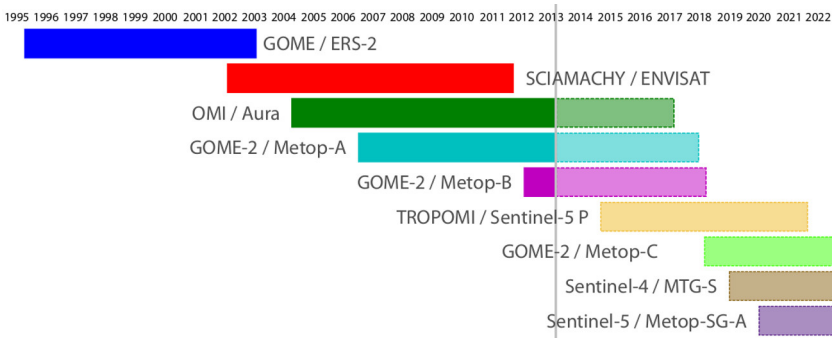

Figure 2.11: Timeline of past, present, and future space-borne spectrometers measuring tropospheric NO_2 columns.

2.10.1 *GOME*

The Global Ozone Monitoring Experiment (GOME) on board the European research satellite ERS-2 was launched on April 21, 1995. It was a nadir-looking grating spectrometer performing hyperspectral measurements of the Earth's atmosphere in the 240–790 nm wavelength region, at a spectral resolution of between 0.2 nm and 0.4 nm. The spatial resolution of a standard GOME ground pixel was 40×320 km^2 and allowed global coverage at the equator within 3 days. ERS-2 circled the

Earth in a near-polar sun-synchronous orbit with a descending-node equator crossing local time of 10:30 (Burrows et al., 1999).

After June 1997, the GOME instrument was operated in a narrow-swath mode three days per month. In this mode, the instrument's scan angle was reduced from $\pm 31.0°$ to $\pm 8.7°$, leading to an increased spatial resolution of 40×80 km^2 at the expense of reduced coverage (Beirle et al., 2004a).

Following a failure of the ERS-2 satellite's on-board tape recorder in June 2003, the instrument was switched to an 'online-only' mode, i. e., measurement data were directly transferred to a satellite ground station. This lead to data gaps over the Pacific Ocean due to lacking ground stations in that area (ESA Earthnet Online, 2003). Unfortunately, this meant that from then onwards, retrieving tropospheric NO_2 columns from GOME measurements was impossible, as measurements over the remote Pacific Ocean are needed in the process of stratospheric correction (see Sects. 2.9.1 and 3.3.4). The ERS-2 satellite was decommissioned on 5 Sep 2011 (ESA Earthnet Online, 2011).

2.10.2 *SCIAMACHY*

The SCanning Imaging Absorption spectroMeter for Atmospheric CartograpHY (SCIAMACHY, Burrows et al., 1995) was one of ten instruments on board the European research satellite ENVISAT. Its name stems from the greek word *σκιάμάχη*, meaning "fighting shadows". SCIAMACHY provided measurements starting August 2002, several months after ENVISAT's launch on 1 Mar 2002. Communication with the satellite was lost on 8 Apr 2012, after the satellite's estimated life span had been exceeded by five years.

ENVISAT circled the Earth in a near-polar sun-synchronous orbit with an equator crossing local time of 10:00; the satellite's altitude was 799.8 km, the inclination angle 98.6°, and it had a repeat cycle of 35 days (501 orbits per cycle). In late October 2010, the orbit was lowered by 17.4 km, leading to a repeat cycle of 30 days (431 orbits per cycle; ESA Earthnet Online, 2010) .

The spectrometer covered the wavelength range from ultraviolet (214 nm) to near-infrared (2384 nm) in eight channels. The spectral resolution depended on the channel and ranged between 0.21 nm and 1.56 nm; the resolution in channel 3, which is used for retrieving NO_2 via the DOAS technique (see Chapter 2.8), was 0.47 nm.

SCIAMACHY was unique amongst the various space-borne Earth observation spectrometers in that it offered measurements in three different viewing geometries: nadir, limb, and occultation. In nadir geometry, the instrument operated in a whisk broom fashion; it was directed towards the Earth's surface, covering a swath width of 960 km. While the forward scan (left-to-right) was performed in 4 s, the backward scan took only 1 s. Combined with the instrument's integration time of 0.25 s, this lead to across-track extents of 60 km and 240 km for the forward and backward scan pixels, respectively (Gottwald and Bovensmann, 2011), while the along-track extents of the measured pixel were constant at 30 km.

In limb geometry, the instrument operated forward-looking, scanning the atmosphere from the surface to a tangent height of 92 km (Gottwald and Bovensmann, 2011), thereby allowing the retrieval of vertical absorber profiles, using scattered light only. The ground scene of a limb scan is defined by the geolocation of the line of sight tangent point at the start and end of the state; the measurement cycles in synchronized such that both nadir and limb measurements cover approximately the same area with a time gap of 7 minutes (Heckel, 2007). In every limb state, four distinct vertical profiles were recorded, each covering a ground area 240 km wide. Due to the elevation steps executed by the instrument, the tangent point of the line of sight moved towards the spacecraft as the platform proceeded along the orbit. The satellite's movement around the Earth thus lead to a rather narrow appearance of the along-track extent of the limb pixels (Gottwald and Bovensmann, 2011).

In occultation mode, finally, SCIAMACHY directly measured the radiation of the rising sun and moon, and its attenuation by the Earth's atmosphere at the line-of-sight tangent point. These measurements al-

low for the retrieval of absorber vertical profiles (Gottwald and Bovensmann, 2011).

2.10.3 *OMI*

The Ozone Monitoring Instrument (OMI) is a UV/vis imaging spectrometer flying on NASAs EOS AURA satellite, which was launched in July 2004. It provides nearly global coverage within one day, at a spatial resolution of 13×24 km^2 at the nadir point. The spatial resolution becomes coarser towards the edges of the swath due to its large width; this effect is even increased by the Earth's curvature. The AURA satellite circles the Earth in an ascending node near-polar sun-synchronous orbit with an equator crossing local time of 13:45 (Levelt et al., 2006).

Over the years, instrumental problems have contributed to what has become known as 'row anomaly' of the OMI instrument. The row anomaly is a temporally varying malfunction caused by something blocking the field-of-view; it affects single rows on the CCD detector, leading to erroneous measured spectra in single viewing directions. Especially after January 2009, this has lead to a significant decrease in the ground coverage of the OMI instrument (Koninklijk Nederlands Meteorologisch Instituut, 2012). While originally, the Aura mission was supposed to last for only five years, a mission extension until 2017 is likely to be implemented (Ritchie et al., 2013, and Anne R. Douglass, NASA, *pers. comm.*).

2.10.4 *GOME-2*

The GOME-2 instruments on board the Metop satellite series are nadir looking UV/vis spectrometers (240–790 nm) with a spectral resolution of between 0.24–0.53 nm, depending on channel (Callies et al., 2000). The instruments' footprint is 40×80 km^2. Metop is a series of identically equipped European operational meteorological satellites; the first two satellites were launched on 19 Oct 2006 and 17 Sep 2012, respectively. The instruments' swath width of 1920 km leads to nearly global

coverage during one day, and the satellites' near-polar , sun-synchronous orbit crosses the equator descending-node at 09:30 local time (EUMETSAT, 2012). On 15 Jul 2013, operations of the GOME-2 instrument on board Metop-A were switched to a 'narrow swath' mode, enabling a swath width of 960 km, yielding a horizontal resolution of 40×40 km^2 (O3M SAF - EUMETSAT Satellite Application Facility on Ozone and Atmospheric Chemistry Monitoring, 2013). Each satellite has a projected mission lifetime of six years; the Metop-A mission has however been extended until mid-2018. Metop-C is scheduled to launch in August 2018 (Eumetsat, *pers. comm.*).

2.10.5 *TROPOMI*

The TROPOspheric Monitoring Instrument (TROPOMI) will be the single payload of the Sentinel-5 Precursor satellite, which is to be launched in March 2015. It will be an imaging spectrometer measuring the the ultraviolet, visible, near-infrared, and shortwave infrared spectral regions (Veefkind et al., 2012). Compared to the spectrometers available today, TROPOMI will feature a considerably improved spatial resolution of 7×7 km^2, while the spectral resolution in the visible range will be 0.2 nm. The satellite will fly in an early afternoon orbit, comparable to that of OMI; the projected mission lifetime is 7 yrs (Veefkind et al., 2012).

2.10.6 *Sentinel-4*

The near-polar, sun-synchronous orbits of the GOME, SCIAMACHY, OMI, GOME-2, and TROPOMI instruments does not allow for the investigation of diurnal variations of the observed trace gases, except in polar regions. A geostationary UV/vis mission has been proposed to close this measurement gap about a decade ago (Bovensmann et al., 2002; Burrows et al., 2004; Bovensmann et al., 2004). This proposal will be realized in the upcoming Sentinel-4 instrument on the Meteosat Third Generation (MTG)-Sounder satellite, which is to be launched in 2019

(European Space Agency, 2013b). The instrument will feature the UV, visible, and near-infrared spectral bands and allow the retrieval of atmospheric trace gases at a spatial and temporal resolution of 8 km and 60 min, respectively. The satellite's view will cover Europe and North Africa, and operations are supposed to run for 8.5 yrs (European Space Agency, 2013a).

2.10.7 *Sentinel-5*

The Metop Second Generation satellite platform, whose first satellite is to be launched in 2020, will carry the Sentinel-5 instrument, a spectrometer covering the UV, visible, near-infrared, and shortwave-infrared spectral regions (European Space Agency, 2013b). The satellite's projected mission lifetime is 8.5 yrs (European Space Agency, 2011), enabling Sentinel-5 measurements of tropospheric composition well into the 2020s.

3

IMPROVING THE STRATOSPHERIC CORRECTION IN THE RETRIEVAL OF TROPOSPHERIC NO_2

3.1 INTRODUCTION

As outlined in Sect. 2.9.1, the NO_2 slant column as retrieved using the DOAS technique still contains information from the stratosphere. In regions not affected by tropospheric pollution, the stratospheric NO_2 column is actually considerably larger than the tropospheric one (see Fig. 2.4). As the main interest in NO_2 lies in the troposphere, the stratospheric contribution to the retrieved slant columns has to be accounted for.

3.1.1 *Stratospheric* NO_2

The global distribution of stratospheric NO_2 depends mainly on latitude (or rather the amount of sunlight during one day, see Sect. 2.4.4). Stratospheric NO_2 columns derived from SCIAMACHY limb measurements for June 2010 are shown in Fig. 3.1.

On regional to local scales, variations in the stratospheric NO_2 content are determined mainly by transport processes. However, Cook and Roscoe (2009) show that the NO_x partitioning and thus the NO_2 concentration also depends on temperature; they report a linear increase of the modeled NO_2 vertical column with temperature of 0.5%/K.

The stratospheric N_2O burden has been reported to increase by approx. 2.5% per decade (World Meteorological Organization, 2007). Given that N_2O is the main source of stratospheric NO_2 (see Sect. 2.3.2), one should expect an according increase in VCD_{strat} NO_2. However, Hendrick et al. (2012) found decreasing stratospheric NO_2 columns using ground-based measurements from 1990–2009 over the NDACC station at Jungfraujoch (located in the German Alps, i. e., in northern mid-

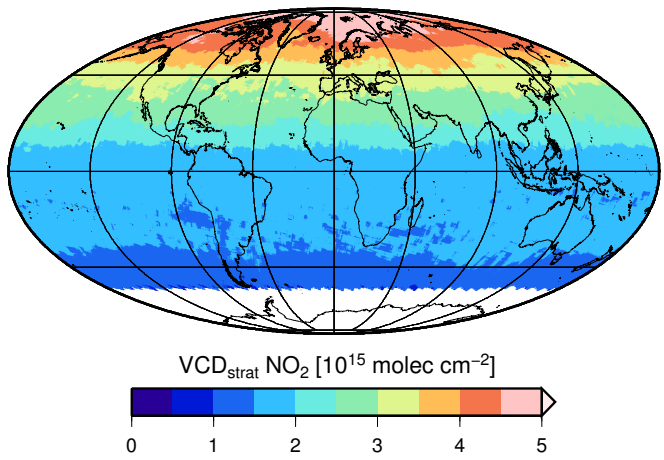

Figure 3.1: Monthly averages of VCD_{strat}^{limb} from SCIAMACHY limb measurements for June 2010, interpolated to the locations of the SCIAMACHY nadir measurements, and binned to 0.125° (from Hilboll et al., 2013c).

latitudes). After accounting for 'external' effects, i. e., QBO, the solar cycle, and stratospheric aerosols (mainly following the eruption of Mount Pinatubo in 1991), they derive a statistically significant decline of stratospheric NO_2 columns of ∼3.5% per decade. Hendrick et al. (2012) attribute this reduction to a change in the NO/NO_2 partitioning, driven by stratospheric cooling. For the southern hemisphere, Liley et al. (2000) and Dirksen et al. (2011) evaluated measurements of stratospheric NO_2 columns over Lauder (New Zealand, i. e., in the southern mid-latitudes) using ground-based and OMI observations, respectively. There, the stratospheric NO_2 load has been reported to be moderately increasing, by 5% per decade (Liley et al., 2000, statistically significant, for 1981–1999) and a moderate 0.5% per decade (Dirksen et al., 2011, not statistically significant, for 2004–2010), which is more in line with the expectations. In high latitudes, the stratospheric NO_2 content can also be influenced by changes in transport patterns, e. g., the Brewer-Dobson circulation. For Antarctica, Cook and Roscoe (2009) evaluated 18 years of data (1990–2007) from a zenith-sky spectrometer. However, they do not ob-

serve a significant trend but report large inter-annual variability, with a maximum in 2000.

3.1.2 *The reference sector method*

Originally, the separation of the stratospheric signal has been done using the so-called *reference sector method*, where measurements over a meridional band over the remote Pacific Ocean (the reference sector) are subtracted from all measurements globally (Burrows et al., 1999; Richter and Burrows, 2002; Martin et al., 2002). This is done for each latitudinal band separately, and is made feasible by the sun-synchronous orbit of the satellites, as this ensures that the measurements at a given latitude are representative of the same local time (and thus, photochemical state) throughout the globe.

Previously, this has already been applied to ozone measurements from the TOMS instrument (Hudson and Thompson, 1998; Kim et al., 1996); however, the method works better on NO_2 due to its shorter lifetime and thus lesser dependency on transport processes.

The reference sector method relies on two assumption: that the reference sector does not contain significant amounts of tropospheric NO_2, and that the stratospheric NO_2 field is zonally homogeneous. While previous studies have achieved reasonable results using this approach, both assumptions are known not to be correct.

Zonal homogeneity

For NO_2, the assumption of zonally constant stratospheric columns can be justified with the characteristic shape of the vertical profile, which shows the maximum concentrations at altitudes of around 30km (Rozanov et al., 2005a; Gordley et al., 1996, see Fig. 2.4). At these altitudes, zonal variability in transport processes is very low compared to the lower stratosphere (Brasseur and Solomon, 2005, p. 38); likewise, tropopause dynamics do not interfere with the layers of elevated NO_2 concentrations. However, the limb-mode observations of stratospheric NO_2 by the SCIAMACHY instrument have shown that there is some

meridional variability in stratospheric NO_2 (see Fig. 3.1), so the assumption of zonally homogeneous VCD_{strat} NO_2 is not fulfilled. This is particularly the case in high latitudes during winter, when the polar vortex introduces air masses which are often depleted from NO_2 and reservoir species like N_2O_5 to lower latitudes.

Tropospheric NO_2 content over the remote Pacific Ocean

Under favorable meteorological conditions and when the tropospheric lifetime of the NO_2 molecule is long enough, NO_2 plumes originating from the large industrial areas of east Asia can reach the remote Pacific Ocean. This is especially the case in winter months, when the NO/NO_2 ratio is shifted more towards NO_2 due to the shortage of sunlight available for photodissociation. Unfortunately, measurements of the tropospheric NO_2 load in the reference sector are extremely sparse. While existing studies suggest NO_2 mixing ratios in the free troposphere of less than 100ppt (see, e. g., Noxon, 1981 for first direct-sun measurements, Schultz et al., 1999 for results from the PEM-Tropics aircraft campaign, and Peters et al., 2012 for a recent ship-borne MAXDOAS study), one has to keep in mind that these studies do not represent the whole seasonal cycle; no measurements exist in northern hemisphere winter mid-latitudes. However, global chemistry and transport model (CTM) simulations can be used to estimate tropospheric NO_2 concentrations. As shown in Fig. 3.2, modeled tropospheric NO_2 columns over the reference sector are below 3×10^{14} molec cm^{-2} in the climatological mean, except in northern mid-latitudes, where values can reach up to 9×10^{14} molec cm^{-2} on average in winter.

3.1.3 *Overview of existing methods to account for stratospheric NO_2*

Several retrievals of tropospheric NO_2 columns from satellite measurements tried to improve the reference sector method by defining remote ocean areas as reference region globally and not only over the remote Pacific.

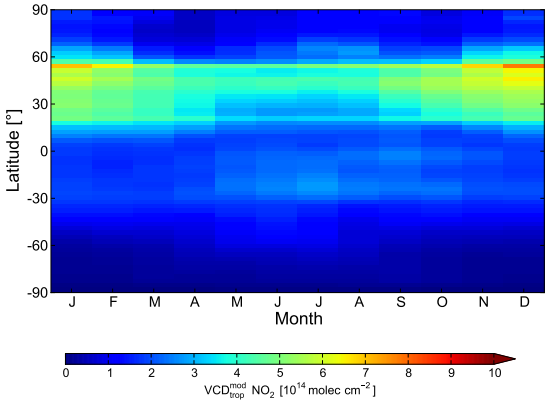

Figure 3.2: Climatology of VCD_{trop} over the Pacific Ocean (180° W–150° W) for the years 1998–2007, computed from Oslo CTM2 simulations (from Hilboll et al., 2013c).

Velders et al. (2001), e. g., defined every oceanic region more than approx. 200km away from the coast as unpolluted and applied an image processing technique to yield the global stratospheric NO_2 field. However, as it becomes clear from Plate 1b in the study by Velders et al., this method fails in instances of unexpected tropospheric NO_2 amounts, as, e. g., in the case of long-range transport from the North-American east coast across the north Atlantic, and over the highly polluted regions of eastern China.

This image processing technique was subsequently improved by Leue et al. (2001), who additionally applied a cloud criterion; they only selected GOME pixels with a measured cloud fraction of more than 50% for estimating the stratospheric NO_2 columns, assuming that any NO_2 below clouds is effectively shielded from being detected by the instrument.

The reference sector method was first used by Richter and Burrows (2002). Martin et al. (2002) also used the reference sector method, but use almost all of the open Pacific Ocean as reference region; they use the GEOS-CHEM model to ensure their selected area is not influenced by pollution from nearby land masses. Additionally, Martin et al. ac-

counted for the presence of tropospheric NO_2 over the reference sector using the same model simulations. For July 1996, they find latitudinally varying tropospheric slant columns (SCD_{trop}) of between 7×10^{14} molec cm^{-2} and 3×10^{14} molec cm^{-2}, with minima in the tropics and southern mid-latitudes, and maxima around 30°S and between 25° and 40°N.

Later, Richter et al. (2005) used CTM simulations with the SLIMCAT model to account for the stratospheric NO_2 field. While in principle, one could expect modeled stratospheric NO_2 fields to well represent the true state of the atmosphere and thus be a good correction method, Richter et al. found a systematic offset between the modeled and measured NO_2 over presumably clean regions; they accounted for this bias by applying a zonal offset to the modeled NO_2 columns to match those measured over the remote Pacific.

A more elaborate version of the image processing technique has been introduced by Bucsela et al. (2006). Operating on the gridded daily SCD_{trop} measurements, they mask polluted regions in a two-step process. After applying a global a-priori mask, they use planetary wave analysis to derive a preliminary stratospheric NO_2 field. To account for possible contamination of this field due to tropospheric pollution, in a second step those regions with a high difference between the original masked and the preliminary NO_2 fields are masked out. The remaining data points are then analyzed again to yield the final set of planetary waves (Bucsela et al., 2006). While evaluating several parameter sets, the optimal results were achieved by using $VCD_{trop} > 5 \times 10^{14}$ molec cm^{-2} as pollution criterion (derived from the GEOS-CHEM model), and a wave-2 fit for the planetary wave analysis.

Boersma et al. (2007) use the TM4 model in a data assimilation scenario. Using averaging kernels, stratospheric slant columns as would have been observed by the sensor if the model represented the true atmosphere are calculated. Then, the NO_2 concentrations in the model are being forced towards the observed slant column. This assimilation, based on the Kalman filter approach, occurs mainly in the stratosphere and at places where tropospheric NO_2 concentrations are comparatively low, avoiding a possible contamination of the stratospheric model

state by tropospheric NO_2 signals. This is achieved by weighting modeled and observed columns with weighting factors dependent on observation representativeness and model errors (Boersma et al., 2007). The stratospheric contribution to the individual measurements is then estimated using a forecast run based on this reanalysis. As a result, Boersma et al. estimate the uncertainty of their stratospheric correction scheme to be lower than 2×10^{14} molec cm^{-2} for the slant columns in most cases.

The potential of SCIAMACHY's unique measurements in both nadir and limb geometry to assess tropospheric trace gas abundances was first evaluated by Sierk et al. (2006). Both stratospheric and tropospheric columns are measured using the exact same instrumentation, and was one of the driving ideas behind the SCIAMACHY instrument (Burrows et al., 1995). Beirle et al. (2010) first implemented this idea into a scientific data product. They used Gaussian functions to create a smoothed global field from the individual limb measurements. To minimize the effect of the relatively low spatial coverage of the limb observations, they included measurements from the previous and following days (with 50% weight) in the smoothing procedure. Similarly to the studies using modeled stratospheric NO_2 fields, Beirle et al. found a systematic, latitude-dependent bias between limb and nadir measurements, which they accounted for with an additive offset, using values over the reference sector.

Bucsela et al. (2013), finally, subtract climatological CTM output of tropospheric NO_2 columns from the measured total vertical columns (derived using a stratospheric AMF) to get an initial stratospheric NO_2 field. They then mask out those regions where the modeled tropospheric climatology exceeds a threshold value of 3×10^{15} molec cm^{-2}, and fill these gaps by interpolation.

3.1.4 *The importance of the stratospheric correction for analysis of tropospheric NO_2 pollution*

The uncertainty which is introduced into tropospheric NO_2 columns by the stratospheric correction has been estimated in several studies;

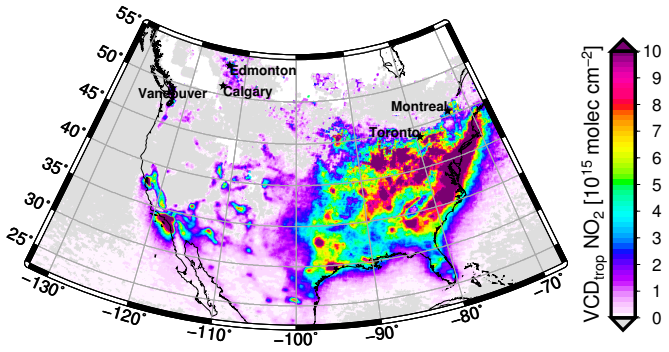

Figure 3.3: Multi-year average of the winter months December, January, and February 2002–2011, of VCD_{trop} NO_2 from SCIAMACHY, using the reference sector method as stratospheric correction. Negative VCD_{trop} are shown in gray, while missing data (due to constant cloud/snow cover) is marked in white.

all of them state a value of less than 5×10^{14} molec cm^{-2} (Boersma et al., 2004). As this is about two orders of magnitude lower than typical tropospheric NO_2 columns over the megacities in eastern China, one could draw the conclusion that traditionally used methods such as the reference sector technique are 'good enough' for any study estimating the inter-annual evolution of megacity NO_2 levels. While this may be true for the extremely polluted cities in eastern China, the stratospheric correction can indeed severely influence the observation of anthropogenic urban NO_2 signals, especially of those cities which do not formally qualify as 'megacity' but still are important pollution hot spots.

To illustrate this point, Fig. 3.3 shows a multi-year average of tropospheric NO_2 over North America, retrieved using the reference sector method, during the winter months December–February. Most of the North American continent shows negative tropospheric NO_2 columns, which is an artifact introduced by the reference sector method. It is clearly visible that the large Canadian urban and industrial centers like, e. g., Montréal and Calgary, exhibit only mildly enhanced NO_2 columns; notably, there is no significant NO_2 plume in the surrounding

areas, like around the cities in the western U.S. This clearly shows that an accurate estimation of the stratospheric contribution to the measured NO_2 absorption signal is vital also for the study of the NO_2 load over densely populated, urban agglomerations.

3.1.5 *Outline of this chapter*

In this chapter, the limb-mode measurements by the SCIAMACHY instrument are used to infer the stratospheric contribution to the measured NO_2 fields. An interpolation scheme is developed which allows for the determination of the stratospheric NO_2 influence for every single SCIAMACHY nadir measurement, avoiding the construction of a smoothed global daily stratospheric NO_2 field as in Beirle et al. (2010). While this means this stratospheric correction technique is only applicable to SCIAMACHY measurements, the spatio-temporal accuracy of the used interpolation scheme is expected to be superior to that global analysis by Beirle et al., leading to more representative tropospheric NO_2 columns. This limb/nadir matching technique is compared to the original reference sector method, and to stratospheric NO_2 fields modeled by the Oslo CTM2 and the Bremen 3d CTM, and the suitability of both models as stratospheric correction scheme is evaluated.

3.2 DATASETS USED IN THIS STUDY

3.2.1 *SCIAMACHY limb profiles**

The limb-mode measurements made by SCIAMACHY are the most elaborate global assessment of stratospheric NO_2 available today. The instrument operates forward-looking and scans the atmosphere from the surface to a tangent height of 92 km (Gottwald and Bovensmann, 2011), thereby allowing the retrieval of vertical absorber profiles, using scattered light only. The ground scene of a limb scan is defined by the geolocation of the line of sight tangent point at the start and end of the

*This subsection has been previously published as part of Hilboll et al. (2013c).

state. In every limb state, four distinct vertical profiles are recorded, each covering a ground area 240 km wide. Due to the elevation steps executed by the instrument, the tangent point of the line of sight moves slightly towards the spacecraft as the platform moves along the orbit. The satellite's movement around the Earth thus leads to a rather narrow appearance of the along-track extent of the limb pixels (Gottwald and Bovensmann, 2011). About 100 limb NO_2 profiles are taken by SCIAMACHY each orbit.

This study employs the NO_2 concentration profiles from the IUP Bremen scientific retrieval, version 3.1. The software package SCIATRAN (Rozanov et al., 2005b) is used for the retrieval of these absorber concentrations. The retrieval is performed in the $420 - 470$ nm wavelength range, after all measured limb radiances have been normalized with respect to the radiance at tangent height 43 km, in order to eliminate spectral features emerging from solar Fraunhofer lines. Stratospheric absorber concentrations are then inverted from the measured spectra using the information operator approach (Bauer et al., 2012). Apart from NO_2, O_3 and O_4 are included in the forward model, and the temperature dependence of the cross-sections is considered using ECMWF data. The retrieved profiles yield NO_2 concentrations for tangent heights from $\approx 10 - 40$ km, with a vertical sampling of 1 km and a vertical resolution of $3 - 5$ km. This dataset has been validated by Bauer et al. (2012). For those measurements where the tropopause lies below the lower boundary of the retrieved SCIAMACHY limb profiles, the profiles were extended down towards the tropopause by NO_2 concentration profiles derived from a monthly climatology created from the Oslo CTM2 model run (see Sect. 3.2.5).

3.2.2 *SCIAMACHY nadir columns*

Total slant columns SCD_{tot} NO_2 are retrieved from SCIAMACHY nadir measurements using the DOAS technique, as described in Sect. 2.8.

3.2.3 *Tropopause altitude**

The tropopause height was computed on a latitude/longitude grid of 1.5° resolution, using the ECMWF ERA-Interim reanalysis (Dee et al., 2011). The location of the tropopause was obtained by applying both dynamical (potential vorticity) and thermal (lapse rate) definitions, following an approach similar to the one discussed in Hoinka (1998). The combination of the dynamical and thermal criteria enables a clear definition of the boundary between the troposphere and the stratosphere. For the tropics, the thermal criterion was used, and from the mid-latitudes to the poles the dynamical criterion using a potential vorticity of 3 PVU (1 PVU $= 10^{-6}\,\mathrm{km^2\,s^{-1}\,kg^{-1}}$). In the transition region between the two regimes, both criteria were used and weighted with the distance from the regime boundaries. This method is further described in Ebojie et al..

3.2.4 *Bremen 3d CTM*

The Bremen 3d CTM is a combination of the *Bremen transport model* (Sinnhuber et al., 2003a) with the chemistry code of the *Bremen two-dimensional model of the stratosphere and mesosphere* (Sinnhuber et al., 2003b; Winkler et al., 2008), which evolved from SLIMCAT (Chipperfield, 1999). The model is driven by ECMWF ERA-Interim meteorological reanalysis fields (Dee et al., 2011) and runs on a combined 30 min / 15 min time-scale for transport and chemistry, respectively. Vertical transport is included in the dynamics using the advection scheme developed in Prather (1986). While the horizontal resolution is constant at 2.5°× 3.75°, the vertical resolution varies from $\sim$ 1 km at the lower stratosphere to $\sim$ 4 km at $\sim$ 60 km altitude. The model runs on 28 isentropic surfaces from 330 K to 3402 K (about 10 km–65 km). Stratospheric vertical columns $\mathrm{VCD_{strat}}$ for each satellite measurement were interpolated in space and time using smoothing spline and linear interpolation, respectively.

*This subsection has been previously published as part of Hilboll et al. (2013c).

3.2.5 *Oslo CTM2**

Oslo CTM2 is a chemistry and transport model developed at the University of Oslo, Norway (Søvde et al., 2008). The model is driven by meteorological data from the ECMWF Integrated Forecast System (IFS). Both tropospheric (Berntsen and Isaksen, 1997) and stratospheric (Stordal et al., 1985) chemistry have been included. The simulation has been run for the period 1997–2007, whereof the latter ten years have been used in the analysis (1997 was considered as spin-up). The model domain extends from the surface to 0.1 hPa in 60 vertical layers, and spans the whole globe with a horizontal resolution of 2.8125×2.8125; the time step is 60 minutes. Anthropogenic and biogenic emissions are taken from the MACCity (Granier et al., 2011) and POET (Granier et al., 2005) inventories, respectively. Biomass burning emissions are from the RETRO inventory (Schultz et al., 2008) for the 1997–2000 period, and and from GFEDv2 (van der Werf et al., 2006) for the remaining period (World Meteorological Organization, 2007). Lightning emissions are re-distributed according to lightning frequencies, based on (Price et al., 1997); the procedure is described in detail in Søvde et al. (2008). Advection is incorporated in Oslo CTM2 using the second order moment scheme (Prather, 1986), convection is based on the Tiedtke mass flux parametrisation (Tiedtke, 1989), and boundary layer mixing is treated according to the Holtslag K-profile method (Holtslag et al., 1990). For the numerical solution of the chemistry scheme, the Quasi Steady-State Approximation (Hesstvedt et al., 1978) is used, and photodissociation is performed on-line using the FAST-J2 method (Wild et al., 2000; Bian and Prather, 2002). The tropopause height is fixed to the layer interface which is closest to the 'real' tropopause altitude calculated using the 2.5 PVU criterion, and vertical tropospheric NO_2 columns are calculated by integrating the modeled concentrations from the surface to this layer interface.

*This subsection has been previously published as part of Hilboll et al. (2013c).

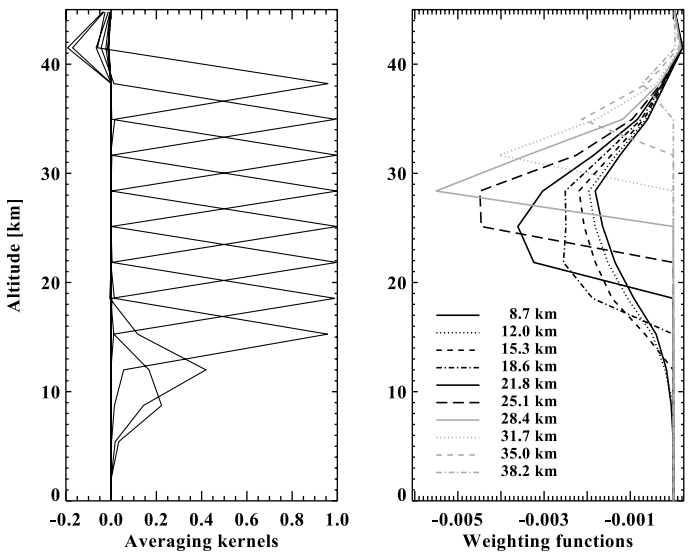

Figure 3.4: Vertical sensitivity of limb NO_2 retrievals from SCIAMACHY (from Rozanov et al., 2005a).

3.3 THE LIMB/NADIR MATCHING ALGORITHM*

This study concentrates on converting total slant columns to tropospheric slant columns by using stratospheric NO_2 profiles retrieved from SCIAMACHY limb measurements as described in Sect. 3.2.1. First, as the SCIAMCHY limb retrieval is sensitive down to approximately 11 km (see the respective averaging kernel in Fig. 3.4 and the discussion in Rozanov et al., 2005a), the stratospheric NO_2 profiles must be extrapolated downward to the tropopause. The resulting vertical profiles are then integrated into VCD_{strat} (Sect. 3.3.1). In a next step, the limb measurements are geographically matched to the nadir measurements (Sect. 3.3.2). While the limb pixels' small extent probably does not optimally reproduce the actual volume observed by the instrument, the definition via the line-of-sight tangent point is still the

*This section has been previously published as part of Hilboll et al. (2013c).

most plausible description not needing computationally expensive 3-D radiative transfer calculations (Pukite et al., 2010). The small pixel sizes in along-track direction lead to relatively low global coverage, making the derivation of global fields from these measurements a challenging task.

In this study, one stratospheric NO_2 column for every single SCIAMACHY nadir measurement is calculated. Whilst having the disadvantage of not attaining global coverage with the resulting stratospheric data product, this has the advantage of avoiding the need to average over several days of measurements, as, for example, in Beirle et al. (2010). The interpolated VCD_{strat} are then converted to slant columns using stratospheric air mass factors (Sect. 3.3.3). Following this step, the limb stratospheric slant columns are adjusted to the level of the SCD_{tot} from nadir measurements using an additive offset (Sect. 3.3.4), taking into account the tropospheric contribution to the measured signal (Sect. 3.3.5). The full procedure is depicted in Fig. 3.5.

3.3.1 *Calculating stratospheric NO_2 columns**

For the limb measurements, the following procedure was used: Based on the measured and modeled (using the Oslo CTM2) number concentration profiles $n^{\mathrm{limb}}(t,h,\varphi,\psi)$ [molec cm^{-3}] and $n^{\mathrm{mod}}(t,h,\varphi,\psi)$ [molec cm^{-3}], respectively, and on the tropopause heights $h_{\mathrm{trop}}(t,\varphi,\psi)$ [m], stratospheric NO_2 profiles are calculated for time t, latitude φ, and longitude ψ as follows: The modelled NO_2 profiles are compiled into a monthly climatology $\overline{n^{\mathrm{mod}}}(m(t),h,\varphi,\psi)$. Let $h^{\mathrm{limb}}_{\mathrm{min}}(t,\varphi,\psi)$ the minimum altitude above surface for which a reliable number concentration has been retrieved from the limb radiances. The combined stratospheric profile is defined as

*This subsection has been previously published as part of Hilboll et al. (2013c).

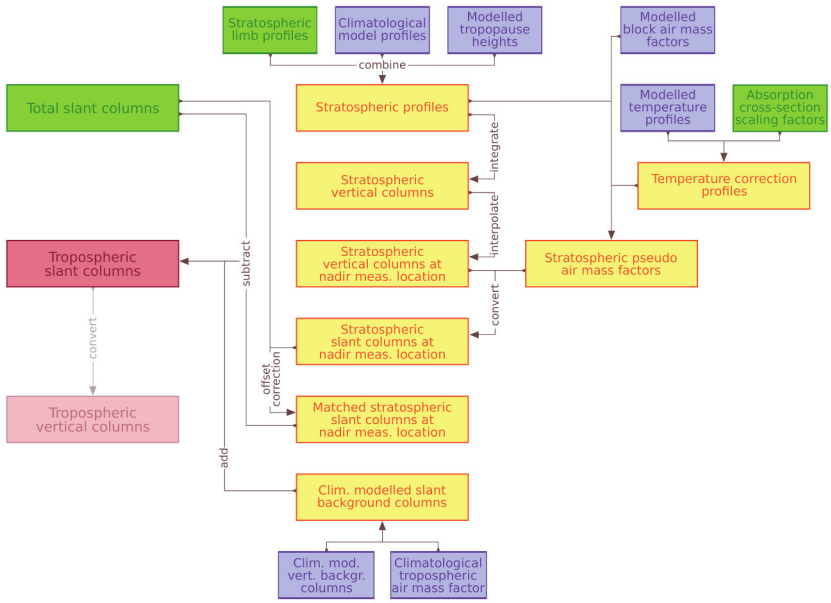

Figure 3.5: Data flow of calculating tropospheric columns from SCIAMACHY measurements. Measured and modeled quantities are shown in green and purple, respectively, while intermediate results are marked in yellow. Conversion of SCD_{trop} to VCD_{trop} involves calculation of tropospheric air mass factors, the discussion of which is beyond the scope of this study (from Hilboll et al., 2013c).

$$n^{\text{limb}}_{\text{strat}}(t,h,\varphi,\psi) = \begin{cases} 0 & \text{if } h < h_{\text{trop}}(t,\varphi,\psi) \\ \overline{n^{\text{mod}}}(m(t),h,\varphi,\psi) & \text{if } h_{\text{trop}}(t,\varphi,\psi) \leq h < h^{\text{limb}}_{\text{min}}(t,\varphi,\psi) \\ n^{\text{limb}}(t,h,\varphi,\psi) & \text{if } h \geq h^{\text{limb}}_{\text{min}}(t,\varphi,\psi). \end{cases} \tag{E 3.1}$$

The combined limb/model number density profiles are then vertically integrated into stratospheric columns:

$$\text{VCD}^{\text{limb}}_{\text{strat}}(t,\varphi,\psi) = \int_{h=h_{\text{trop}}(t,\varphi,\psi)}^{TOA} n^{\text{limb}}_{\text{strat}}(t,h,\varphi,\psi)dh. \tag{E 3.2}$$

For the Oslo CTM2 and the B3dCTM, vertical stratospheric columns $\text{VCD}^{\text{o2m}}_{\text{strat}}(t,\varphi,\psi)$ and $\text{VCD}^{\text{b3d}}_{\text{strat}}(t,\varphi,\psi)$ are calculated by integrating from the model tropopause layer to the model top, respectively.

3.3.2 *Interpolation to nadir measurement location**

Both the model and the limb stratospheric NO_2 column products used in this study are only available on a horizontal resolution which is much coarser than the spatial extents of individual SCIAMACHY nadir measurements (usually $60 \times 30\,\text{km}^2$). Therefore, these coarse stratospheric columns need to be interpolated to the locations of each SCIAMACHY nadir measurement, to ensure the best possible spatial matching.

For SCIAMACHY limb measurements, several steps are required in order to calculate stratospheric NO_2 columns for each nadir measurement, processing each orbit separately. This procedure is illustrated in Fig. 3.6. First, a fixed azimuth angle is assigned to each of the four discrete limb line-of-sight directions, namely -25°, -8°, 10°, and 27°. These angles are chosen to be the mean viewing azimuth angles of those nadir pixels which fall into the field of view of the respective limb state.[1]

*This subsection has been previously published as part of Hilboll et al. (2013c).

[1]In this case a negative angle describes a point west of the nadir point, while a

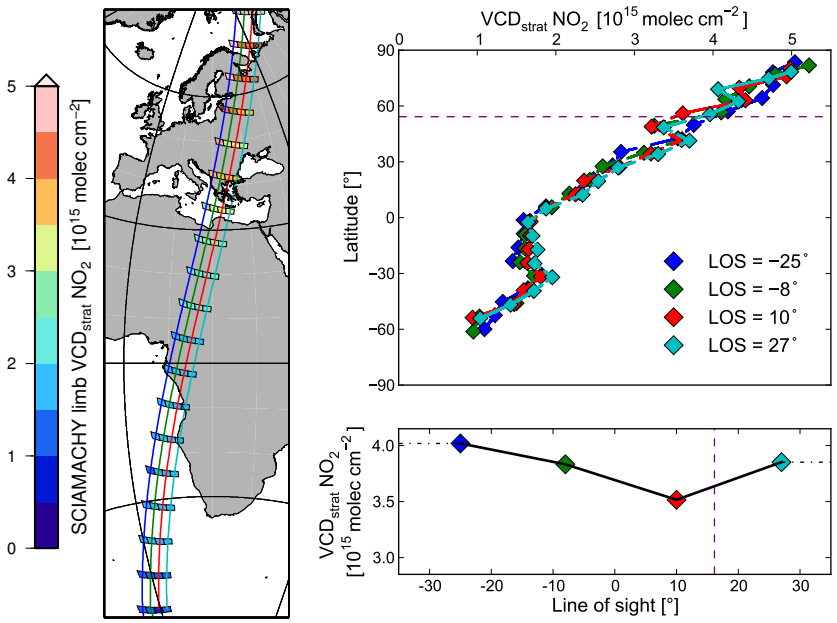

Figure 3.6: Interpolation of stratospheric columns from SCIAMACHY limb measurements to the location of the same orbit's nadir measurements. This example shows the procedure for the nadir measurement located at 54.25° N / 32.25° E from SCIAMACHY orbit no. 32984 (21 June 2008). In a first step, each limb state is treated independently. For each state, is considered to be a function of latitude only (left). To calculate a value for one single nadir measurement, at first, one per state is calculated by linear interpolation in latitude (right). Finally, the value corresponding to the nadir measurement of interest is calculated by linear interpolation in the line of sight angle (right) (from Hilboll et al., 2013c).

Next, the stratospheric NO_2 column density along each line-of-sight is considered as depending only on latitude. For each nadir pixel at time t, latitude φ, and longitude ψ, four stratospheric vertical columns $\mathrm{VCD}^{\mathrm{i}}_{\mathrm{strat}}(t, \varphi, \psi)$ are calculated by linearly interpolating along-track, that is along each viewing direction i. For both limb and nadir measurements, only the descending parts of the orbit are taken into account to avoid complications from measurements taken at different local times and therefore photochemical states. Finally, for all nadir pixels, the stratospheric NO_2 column is considered to be a function of the line of sight, and the correct column density is linearly interpolated from the four column densities $\mathrm{VCD}^{\mathrm{i}}_{\mathrm{strat}}(t, \varphi, \psi)$. As an example the global map of monthly averaged $\mathrm{VCD}^{\mathrm{limb}}_{\mathrm{strat}}(t, \varphi, \psi)$ for June 2010, gridded to 0.125°, are shown in Fig. 3.1.

In the case of Oslo CTM2 and Bremen 3d CTM simulations, the modeled NO_2 columns are interpolated to the location and time of the individual nadir measurements using smoothing cubic splines and linear interpolation, respectively.

For ease of notation, the interpolated NO_2 columns will again be called $\mathrm{VCD}^{\mathrm{limb}}_{\mathrm{strat}}(t, \varphi, \psi)$, $\mathrm{VCD}^{\mathrm{o2m}}_{\mathrm{strat}}(t, \varphi, \psi)$, and $\mathrm{VCD}^{\mathrm{b3d}}_{\mathrm{strat}}(t, \varphi, \psi)$ for SCIAMACHY limb, Oslo CTM2, and Bremen 3d CTM, respectively.

3.3.3 *Stratospheric air mass factor**

The radiative transfer model SCIATRAN (Rozanov et al., 2005b) is used to calculate a lookup table of block air mass factors (BAMF, see Sect. 2.9.2) for 31 solar zenith angles ϑ (SZA) between 10° and 92°, and for 101 uniformly spaced altitude layers h from sea level (0 km) to 100 km.

The NO_2 absorption cross-section has a well-known dependence on temperature (Burrows et al., 1998). Boersma et al. (2004) have suggested a simple linear approach to correct for this effect in the retrieval of tropospheric NO_2 columns. The NO_2 absorption cross-section used in the DOAS fit was measured at a fixed temperature of 243 K. At very low

*This subsection has been previously published as part of Hilboll et al. (2013c).

positive angle describes a location east of the nadir point.

stratospheric temperatures, the cross-section representing the actual atmospheric conditions is therefore larger than the one used in the retrieval, leading to an overestimation of the stratospheric NO_2 column. This will subsequently be corrected for by an increased air mass factor.[1] Following, the correction function $f_{tcorr}(T)$, based on the idea presented in Boersma et al. (2004), is defined as

$$f_{tcorr}(T) = \frac{3.826 \times 10^{-3} \times T + 0.1372}{3.826 \times 10^{-3} \times T_0 + 0.1372}. \qquad \text{(E 3.3)}$$

This correction function has been derived by comparing differential cross-sections measured at four distinct temperatures between 221 K and 293 K and is described by Nüß et al. (2006). T_0 is the temperature at which the cross-section used in the fit has been measured; in our case, $T_0 = 243$ K. The stratospheric air mass factor at time t, latitude φ, longitude ψ, SZA ϑ and viewing zenith angle α is then calculated as

$$\mathrm{AMF}_{\mathrm{strat}}^{\mathrm{limb}} = \frac{1}{\cos\alpha} - 1 + \int_{h=h_{\mathrm{trop}}}^{TOA} \frac{\mathrm{BAMF} \times \mathrm{n}_{\mathrm{strat}}^{\mathrm{limb}}}{f_{tcorr}(T) \times \mathrm{VCD}_{\mathrm{strat}}^{\mathrm{limb}}} dh \qquad \text{(E 3.4)}$$

and accordingly $\mathrm{AMF}_{\mathrm{strat}}^{\mathrm{o2m}}$ and $\mathrm{AMF}_{\mathrm{strat}}^{\mathrm{b3d}}$ for Oslo CTM2 and Bremen 3d CTM, respectively. Here, the summand $\frac{1}{\cos\alpha} - 1$ represents a geometric line-of-sight correction, assuming that the total light path enhancement (as compared to an exactly nadir-viewing instrument) expected from the point of last scattering is purely geometric to first order, and that profile shape, relative azimuth, and other second order processes can be ignored (Richter, 2004). Temporal and spatial interpolation to the measurement geolocation is then done as described in Sect. 3.3.2, while the SZA interpolation is linear.[1]

[1] To be precise, one should speak of pseudo air mass factors when they incorporate the temperature correction.

[1] For SZAs <10°, the BAMF values for 10° are used. As in near-zenith sun situations, the length of the average lightpath almost does not vary with the SZA, this does not introduce any significant error.

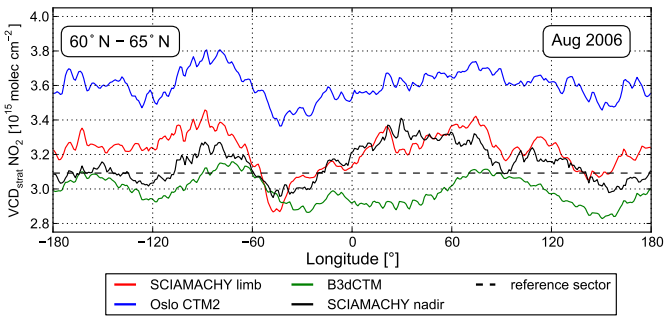

Figure 3.7: Zonal variation of VCD_{strat}^{limb} from SCIAMACHY limb measurements (red), VCD_{strat}^{mod} from Oslo CTM2 (blue) and Bremen 3d CTM (green) simulations, and of VCD_{strat}^{nadir} from SCIAMACHY nadir measurements. Monthly mean values for August 2006, between 60° and 65° N (after Hilboll et al., 2013c).

3.3.4 *Offset between limb and nadir measurements**

The stratospheric vertical columns derived from SCIAMACHY limb measurements and Oslo CTM2 or B3dCTM simulations differ considerably from total vertical columns obtained over the clean Pacific region from SCIAMACHY nadir measurements by applying a stratospheric air mass factor, VCD_{strat}^{nadir}.[2] In this study, the Pacific region between longitudes 180°W and 150°W are used to correct for this effect. This region will subsequently be called 'reference sector'. The latitude- and time-dependent offset is shown exemplarily in Fig. 3.7 for northern latitudes in August 2006.

In order to account for these systematic biases, a daily, latitude-dependent offset is applied to all limb and modeled stratospheric slant columns to force them to the base level of the nadir measurements over the reference sector.

*This subsection has been previously published as part of Hilboll et al. (2013c).

[2] VCD_{strat}^{nadir} still contains the tropospheric contribution to the measured signal.

3.3.5 *Tropospheric background over the Pacific**

Before the stratospheric columns from SCIAMACHY, Oslo CTM2, and Bremen 3d CTM can be adjusted to the level of the total nadir columns over the Pacific, the latter must be corrected for possible tropospheric NO_2 signals. As independent, appropriate measurements over the Pacific Ocean are extremely sparse, climatological NO_2 data derived from the same run of the Oslo CTM2 model as used for the stratospheric columns (see Sect. 3.2.5) are used. The data show that the tropospheric NO_2 content over the Pacific Ocean is negligibly small most of the time. Only in northern mid-latitudes, and there especially during winter, significant amounts of tropospheric NO_2 are predicted by the model (see Fig. 3.2). These enhanced NO_2 columns can most probably be attributed to exported pollution from Eastern Asia and North America, as the lifetime of tropospheric NO_2 is strongly enhanced during winter.

Similar corrections have been previously performed by Martin et al. (2002).

From the modeled NO_2 fields $n^{\mathrm{o2m}}(t, h, \varphi, \psi)$ [molec cm^{-3}], vertical tropospheric columns over the reference sector are calculated as

$$\mathrm{VCD}_{\mathrm{trop}}^{\mathrm{mod}}(t, \varphi, \psi) = \int_{h=0}^{h_{\mathrm{trop}}(t,\varphi,\psi)} n^{\mathrm{o2m}}(t, h, \varphi, \psi)\, dh. \qquad \text{(E 3.5)}$$

These columns are then compiled into a monthly climatology over the reference sector, $\mathrm{VCR}_{\mathrm{trop}}^{\mathrm{mod}}(m, \varphi)$.

As tropospheric air mass factors, the dataset developed by Nüß (2005), which was derived using the radiative transfer model SCIATRAN (Rozanov et al., 2005b) and NO_2 profiles from the MOZART4 model, was used. A monthly climatology of air mass factors over the reference sector $\mathrm{AMFR}_{\mathrm{trop}}(m, \varphi)$ was compiled by zonally averaging over the $\mathrm{AMF}_{\mathrm{trop}}$ for all SCIAMACHY nadir measurements in month m and at latitude φ over the reference sector during the 2003–2011 time period.

*This subsection has been previously published as part of Hilboll et al. (2013c).

The monthly climatology of modeled tropospheric background columns is then converted to slant columns via

$$\mathrm{SCR}^{\mathrm{mod}}_{\mathrm{trop}}(m,\varphi) = \mathrm{VCR}^{\mathrm{mod}}_{\mathrm{trop}}(m,\varphi) \times \mathrm{AMFR}_{\mathrm{trop}}(m,\varphi). \qquad \text{(E 3.6)}$$

3.3.6 *Applying stratospheric correction**

The stratospheric slant columns are calculated on a daily basis. The limb, nadir, and modeled datasets are compiled into zonally averaged daily aggregates over the reference sector, yielding $\mathrm{SCR}^{\mathrm{limb}}_{\mathrm{strat}}(t,\varphi)$, $\mathrm{SCR}^{\mathrm{nadir}}_{\mathrm{strat}}(t,\varphi)$, and $\mathrm{SCR}^{\mathrm{mod}}_{\mathrm{strat}}(t,\varphi)$, respectively. These daily averages are then linearly interpolated (to fill latitudes with missing values over the reference sector in case of measured columns) and smoothed in latitude to account for latitudes with missing measurements and to make the stratospheric correction less sensitive to measurement noise over the Pacific Ocean. The resulting quantities are called $\mathrm{SCR}^{\mathrm{limb}}_{\mathrm{strat}}(d,\varphi)$, $\mathrm{SCR}^{\mathrm{nadir}}_{\mathrm{strat}}(d,\varphi)$, and $\mathrm{SCR}^{\mathrm{mod}}_{\mathrm{strat}}(d,\varphi)$.

The desired stratospheric slant columns are then calculated by applying the additive offset, derived from the averaged limb (or model) and nadir columns over the reference sector, and forcing the resulting tropospheric slant columns to equal the modeled background columns $\mathrm{SCR}^{\mathrm{mod}}_{\mathrm{trop}}(m,\varphi)$:

$$\begin{aligned} \mathrm{SCD}^{\mathrm{limb}}_{\mathrm{strat}} \quad = \quad & \mathrm{VCD}^{\mathrm{limb}}_{\mathrm{strat}} \times \mathrm{AMF}^{\mathrm{limb}}_{\mathrm{strat}} + \\ & \mathrm{SCR}^{\mathrm{nadir}}_{\mathrm{tot}} - \mathrm{SCR}^{\mathrm{limb}}_{\mathrm{strat}} - \mathrm{SCR}^{\mathrm{mod}}_{\mathrm{trop}} \end{aligned} \qquad \text{(E 3.7)}$$

and accordingly $\mathrm{SCD}^{\mathrm{o2m}}_{\mathrm{strat}}$ and $\mathrm{SCD}^{\mathrm{b3d}}_{\mathrm{strat}}$ for Oslo CTM2 and Bremen 3d CTM, respectively.

These $\mathrm{SCD}^{\mathrm{limb/o2m/b3d}}_{\mathrm{strat}}(t,\varphi,\psi)$ are the final output of the stratospheric correction algorithm. They can be directly subtracted from retrieved nadir total slant columns to yield tropospheric slant columns.

*This subsection has been previously published as part of Hilboll et al. (2013c).

3.4 RESULTS AND DISCUSSION

3.4.1 *Modeled and measured vertical profiles**

As described in Sect. 3.3.1, the measured SCIAMACHY limb profiles are extended down to the tropopause, using climatological profiles from the Oslo CTM2 simulations for the years 1998–2007. Figure 3.8 illus-

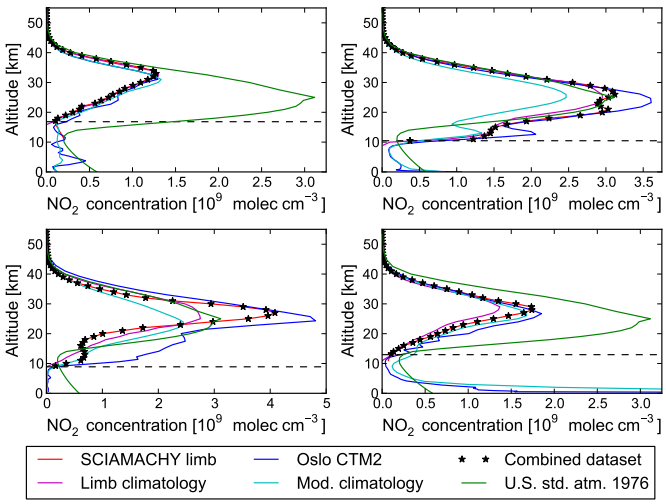

Figure 3.8: Vertical NO_2 profiles from SCIAMACHY limb (actual measurement: red, climatology: magenta), Oslo CTM2 (actual value: blue, climatology: cyan), and U.S. Standard Atmosphere 1976 (green) for 1 June 2007, at 3.48°W, 58.66°N (top left), 2 July 2007, at 58.54°W, 63.7°N (top right), 18 February 2007, at 70.54°W, 75.50°S (bottom left), and 27 March 2006, at 5.17°E, 40.65°N (bottom right). The tropopause altitude is shown as a black dashed line, while the combined limb measurements/model climatology profile used for the column and air mass factor calculations in this study are marked as black stars (from Hilboll et al., 2013c).

trates that this approach is valid: the profiles measured by SCIAMACHY are sufficiently similar to the climatology of those modeled by

*This subsection has been previously published as part of Hilboll et al. (2013c).

Oslo CTM2, especially in the altitude regions between the tropopause and 11 km, where NO_2 concentrations are relatively small.

In some cases, however, the modeled profiles show additional detail in the $10 - 15$ km altitude range, which is not detected by the SCIAMACHY sensor. The top right profile in Fig. 3.8 for example shows a layer of increased NO_2 concentrations around 14 km altitude. This is not a random fluctuation, as the feature is also seen in the climatological model profiles; on the other hand, such sharp peaks are not visible to the SCIAMACHY instrument due to vertical smoothing. At that time of year (early July) and in those latitude regions (65°N), the ECMWF-IFS temperature fields show a layer of enhanced temperature around 14 km (Ø. Hodnebrog, *pers. comm.*). This could drive the decomposition of N_2O_5 and HO_2NO_2, two reservoir species which are especially sensitive to temperature changes, leading to increased NO_2 concentrations. Since this feature can be observed at all longitudes, the increased temperature and NO_2 are unlikely to be caused by terrain effects. In these situations, the stratospheric columns resulting from SCIAMACHY observations will be a few percent smaller than those from the model.

3.4.2 *Difference between limb and nadir measurements**

As described in Sect. 3.3.4, the NO_2 columns retrieved from SCIAMACHY nadir and limb measurements show a systematic offset. This offset has already been observed previously (Beirle et al., 2010). Figure 3.9 (top) shows the magnitude of this offset over the Pacific Ocean (180°W–150°W). It ranges from $+3 \times 10^{14}$ molec cm^{-2} in near-polar latitudes in December to -4×10^{14} molec cm^{-2} in polar latitudes in austral winter. In the tropics and mid-latitudes, the offset varies between -1×10^{14} and -3×10^{14} molec cm^{-2}, with a minimum in June/July. The same annual cycle can be observed in all latitude bands, with minima in June and July, and maxima in December and January. In the months October to March, outside the tropics, nadir columns can be larger than limb columns by about $5 - 6 \times 10^{14}$ molec cm^{-2} in individual months.

*This subsection has been previously published as part of Hilboll et al. (2013c).

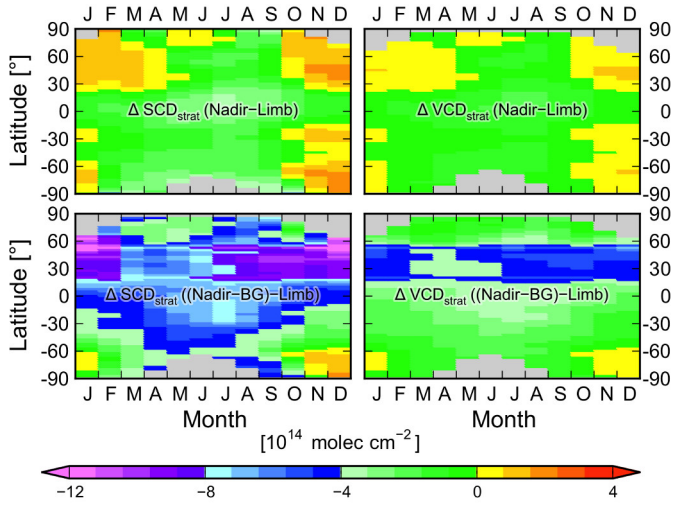

Figure 3.9: Monthly climatology of the difference between SCIAMACHY nadir and limb measurements over the Pacific Ocean (180°W–150°W), averaged from the years 2004–2010 and gridded into 2.5° latitude bins. ΔVCD_{strat} (left) and ΔSCD_{strat} (right), 'raw' columns (top) and after subtracting the tropospheric influence from the Oslo CTM2 climatology (bottom) (after Hilboll et al., 2013c).

However, the measured nadir columns still contain a tropospheric contribution. After subtracting this modeled background signal (see Sect. 3.3.5), the stratospheric NO_2 from limb measurements is higher than from nadir geometry almost globally. Only in austral summer, nadir measurements show larger NO_2 values than limb (Fig. 3.9, bottom). This could point to possible issues in the nadir retrieval from SCIAMACHY measurements, as (Richter et al., 2011) reported that over clean background regions, vertical NO_2 columns from SCIAMACHY are smaller than those from GOME-2 by $2 - 3 \times 10^{14}$ molec cm^{-2}— too much to be solely explained by diurnal differences caused by the local measurement time. Another possible explanation might lie in the different wavelength windows used for the retrievals (425 − 450 nm vs. 420 − 470 nm for nadir and limb, respectively); however this seems unlikely to be the only cause. The offset shows both a clear seasonal

cycle and strong meridional variation. The seasonal variation suggests that in regions where frontal systems are modulating the tropopause height, a varying systematic difference between limb and nadir measurements might be observed. The latitudinal variability of the offset looks very similar to that of the modeled background climatology, suggesting that the Oslo CTM2 overestimates the lifetime of tropospheric NO_2, especially in winter.

While generally, the observed differences are small in absolute numbers and are well within the expected uncertainties of the two measurements, they do have a significant effect on the retrieved tropospheric columns and therefore need to be corrected for. Overall, further work is needed to investigate this phenomenon in more detail. In the study of tropospheric NO_2, which is dominated by lower atmospheric sources and chemical removal of NO_x, the taken approach for empirically removing its effect is however appropriate.

3.4.3 *Climatological comparison between measurements and model**

As a first step in comparing two independent datasets, correlation analysis using scatter plots can be very helpful. Here, a total of four correlation plots is shown, comparing both Oslo CTM2 and B3dCTM to SCIAMACHY limb measurements, in- and excluding high latitudes (polewards from 60°). The Oslo CTM2 analysis comprises the years 2003–2007, while the B3dCTM comparison goes from 2003–2010. Figures 3.10 and 3.11 show the comparison of the monthly mean values of the VCD_{strat} NO_2, interpolated to the locations (and, for the model data, times) of the nadir measurements, and gridded to 0.125°. The Pearson correlation coefficients as well as the slopes of the regression lines are given in Table 3.1.

*This subsection has been adapted from Hilboll et al. (2013c).

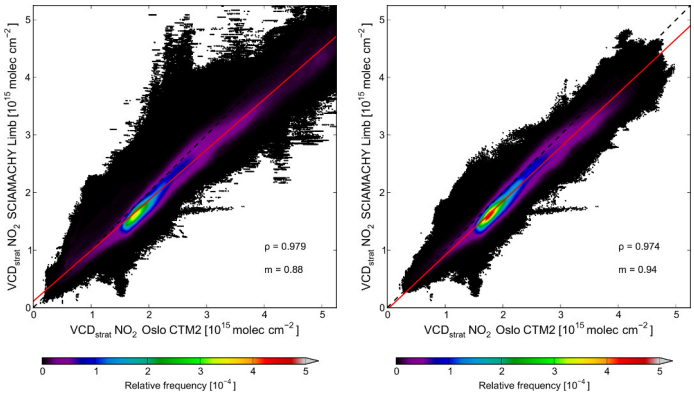

(a) all latitudes (b) latitudes between 60°S and 60°N

Figure 3.10: Scatter plot of monthly mean values for VCD_{strat} NO_2 from SCIAMACHY limb measurements and Oslo CTM2 simulations for the 2003–2007 time period. The red line marks the linear regression fit. Both the Pearson correlation coefficient ρ and the slope of the regression line m are shown (from Hilboll et al., 2013c).

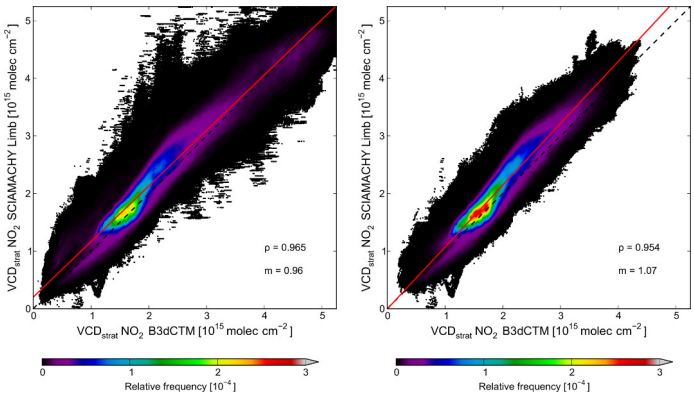

(a) all latitudes (b) latitudes between 60°S and 60°N

Figure 3.11: Same as Fig. 3.10, but for the Bremen 3d CTM, for the 2003–2010 time period.

Table 3.1: Pearson correlation coefficient ρ and slope of regression line m between SCIAMACHY limb measurements and Oslo CTM2/B3dCTM simulations.

	ρ		m	
	Oslo CTM2	B3dCTM	Oslo CTM2	B3dCTM
60°S–60°N	0.974	0.954	0.94	1.07
90°S–90°N	0.979	0.965	0.88	0.96

For all considered datasets, the correlation coefficient ρ is larger than 0.95, showing excellent correlation. However, both CTMs have trouble with the magnitude of the stratospheric NO_2 columns. The Oslo CTM2 consistently overestimates the measured NO_2 columns by several percent, especially at high latitudes. From the comparison of the measured and modeled vertical profiles, it becomes apparent that the systematic overestimation is mostly coming from altitudes lower than 30 km (see Sect. 3.4.1). The Bremen 3d CTM on the other hand consistently underestimates the measured VCDstrat at low and mid-latitudes; at high latitudes, however, this changes to a strong overestimation.

The spatial patterns in VCD_{strat} NO_2 from SCIAMACHY limb measurements and the CTM simulations agree remarkably well, after removing an offset between the datasets. Figures 3.12 and 3.13 show the average difference between measured SCIAMACHY limb columns and those modeled using the Oslo CTM2 and the B3dCTM, respectively, for the 2003–2007 and 2003–2010 periods and for three selected climatological monthly means.[1]The differences of the five-year averages have been offset so that they amount to 0 over the reference sector (180°W–150°W).

Systematic differences in the vertical columns are smaller than 5×10^{13} molec cm^{-2}. The spatial pattern of these differences is interesting, showing a clear seasonality and, in some regions, e. g., the South American West coast, a strong land-sea contrast. One possible explanation might be an orographic effect stemming from the comparably low

[1]See the Appendix A.1 for plots of the months not shown in Figs. 3.12 and 3.13.

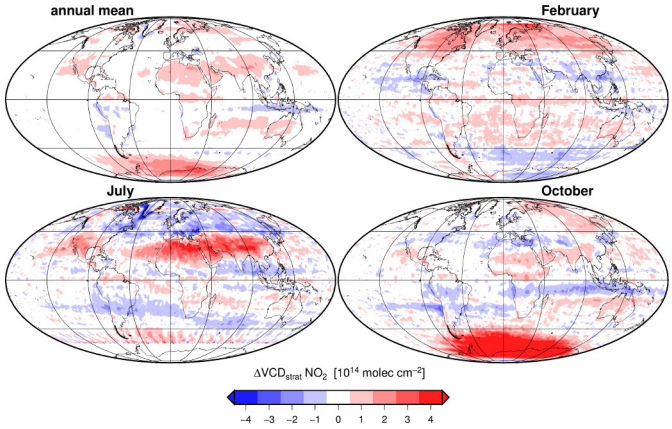

Figure 3.12: The difference ΔVCD_{strat} NO_2 between SCIAMACHY limb and Oslo CTM2 for the 2003–2007 time period. Red and blue areas correspond to regions where SCIAMACHY limb measurements are larger and smaller than Oslo CTM2 simulations, respectively. Top left: average difference over all months. Top right: average difference of all Februaries. Bottom left: average difference of all Julies. Bottom right: average difference of all Octobers. An additive offset has been applied to force the difference to equal zero over the reference sector (180°W–150°W) (from Hilboll et al., 2013c).

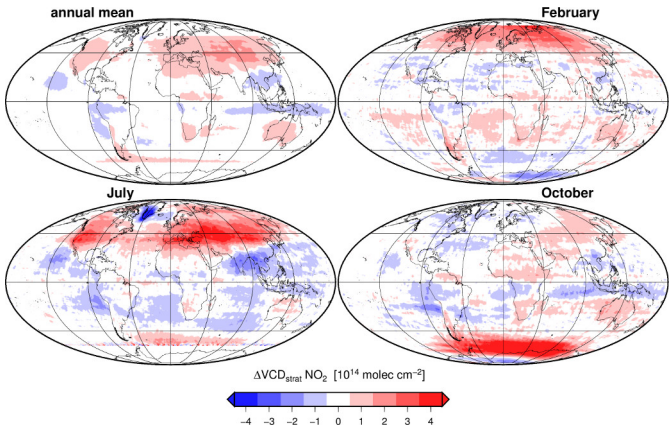

Figure 3.13: Same as Fig. 3.12, but for the Bremen 3d CTM, for the 2003–2010 time period.

resolution of the CTMs. Another possible source for the observed spatial patterns might be the models' treatment of clouds and their influence on photochemistry; however, the photochemistry is mostly determined by the short wavelengths which usually do not penetrate deep enough to be affected by clouds, especially at high latitudes. It must also be noted that the seasonal variation of the measurement/model bias is not the same for the Oslo CTM2 and the B3dCTM. While the climatological differences in spring and fall look remarkably similar, values for July differ considerably, especially over the Eurasian continent and over Greenland. While the B3dCTM's overestimation of the stratospheric NO_2 load over Greenland will be discussed in Section 3.4.5, reasons for the obvious differences over Eurasia remain unclear.

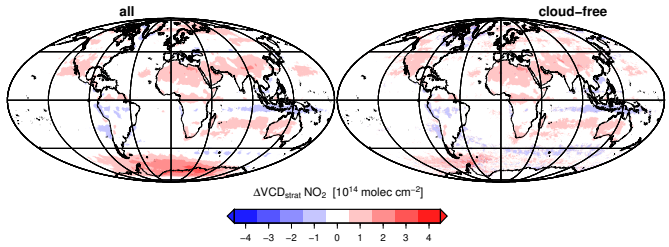

Figure 3.14: Influence of clouds on the climatological difference between SCIAMACHY limb measurements and Oslo CTM2 simulations. The left map shows the climatological difference $\Delta VCD_{strat}\ NO_2$ between SCIAMACHY limb and Oslo CTM2 for the 2003–2007 time period; it is the same as the upper left plot in Fig. 3.12. For the right map, only those pixels with a cloud fraction <20 % (according to the FRESCO+ algorithm, see Wang et al., 2008), are used.

The possible influence of clouds has been investigated for Oslo CTM2 simulations by filtering for scenes with less than 20 % cloud cover from the FRESCO+ dataset (Wang et al., 2008). In general, clouds cannot be made responsible for the observed spatial patterns, as seen in Fig. 3.14. The only exceptions are the Antarctic coast, where the cloud-screened data lack the large area of positive differences seen in the full dataset, and the Canadian Hudson Bay area, where the difference in the cloud-

screened data turns negative from the positive values in the full dataset. In the case of the Antarctic coast, the large positive differences come mostly from austral spring (September and October). Both effects can, most probably, be attributed to the FRESCO+ cloud algorithm having difficulties in identifying clouds over bright surfaces, which in turn leads to an under-representation of winter values in the climatological average.

The impact of clouds should be explored further, because the understanding of the systematic differences between limb retrievals and model simulations can improve our knowledge of the influence of clouds and surface spectral reflectance on atmospheric photochemistry. A first step in this direction will be discussed in Sect. 3.4.5.

3.4.4 *Zonal variability of stratospheric* NO_2 *

A detailed comparison between the offset-corrected stratospheric datasets has been carried out on monthly averages. Gridded data points have been binned into boxes of 1° longitude × 5° latitude. Here, the results of the correction algorithm presented in Sect. 3.3 are compared, namely stratospheric vertical columns NO_2 derived from the offset-corrected SCD^{limb}_{strat} and SCD^{mod}_{strat} (from both Oslo CTM2 and B3dCTM) via

$$
\begin{aligned}
VCD'^{limb}_{strat} &= \frac{SCD^{limb}_{strat}}{AMF^{limb}_{strat}} \\
VCD'^{o2m}_{strat} &= \frac{SCD^{o2m}_{strat}}{AMF^{o2m}_{strat}} \\
VCD'^{b3d}_{strat} &= \frac{SCD^{b3d}_{strat}}{AMF^{b3d}_{strat}}.
\end{aligned}
$$

As comparison, the figures include the 'stratospheric' vertical column derived from SCIAMACHY nadir measurements via

$$
VCD'^{nadir}_{strat} = \frac{SCD^{nadir}_{tot} - SCR^{mod}_{trop}}{AMF^{limb}_{strat}}.
$$

*This subsection has been adapted from Hilboll et al. (2013c).

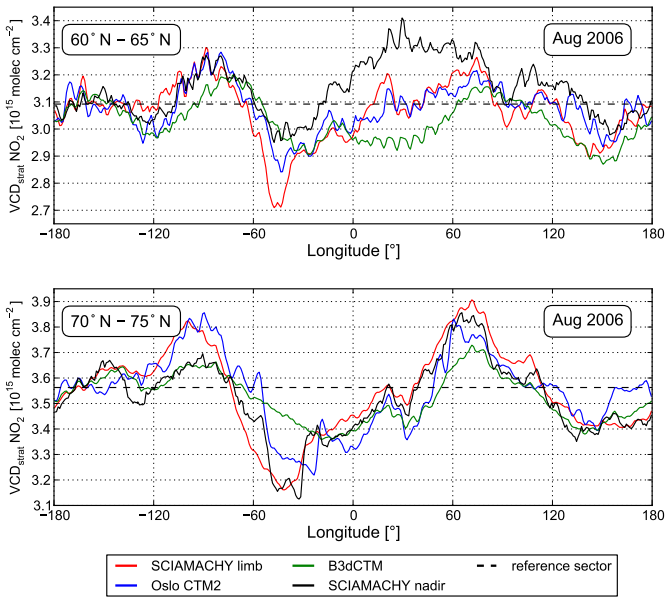

Figure 3.15: Zonal variation of VCD'^{limb}_{strat}, VCD'^{mod}_{strat}, and VCD'^{nadir}_{strat}. The nadir measurements' value over the reference sector is marked as dashed black line. Monthly mean values for August 2006, between 60° and 65°N (top) and between 70° and 75°N (bottom) (after Hilboll et al., 2013c).

First, it is noticeable that the zonal variability of SCIAMACHY limb measurements and Oslo CTM2 simulations is remarkably similar (see Fig. 3.15, top). However, the simulated stratospheric columns are often larger than the measured values, which is also shown by the linear regression of the two datasets (cf. Fig. 3.10). The two stratospheric datasets agree reasonably well with the nadir measurements in unpolluted regions (see Fig. 3.15, top). In contrast, values from the B3dCTM do not agree as well with the measured VCD_{strat}. They are often lower than the values from the Oslo model or the limb measurements, and seem to show slightly less spatial detail. The latter is probably caused by the B3dCTM's zonal resolution of 3.75°, compared to the 2.8125° of the Oslo CTM2.

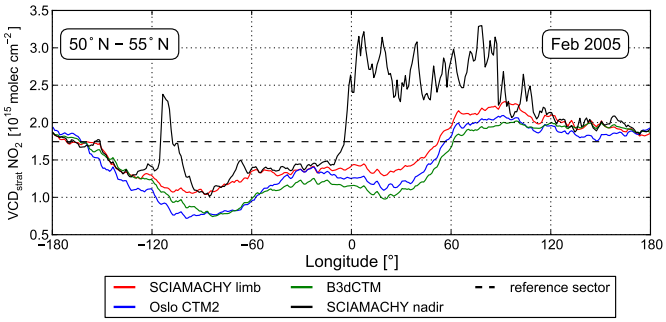

Figure 3.16: Zonal variation of VCD'^{limb}_{strat}, VCD'^{mod}_{strat}, and VCD'^{nadir}_{strat}. The nadir measurements' value over the reference sector is marked as dashed black line. Monthly mean values for February 2005, between 50° and 55°N (after Hilboll et al., 2013c).

While, generally, the shape of the zonal variation is very similar between SCIAMACHY limb and the two CTMs, in some cases, the amplitudes can differ significantly. An example is shown in Fig. 3.16, where, after applying the offset, the agreement between nadir and limb measurements is mostly excellent in those regions without tropospheric pollution. The simulated VCD'^{mod}_{strat}, however, are lower than the measured ones, indicating that the models might be overestimating the stratospheric NO_2 over the Pacific Ocean, leading to an exaggerated bias correction.

In the Northern hemisphere, the maxima of stratospheric NO_2 abundances are often located over the Pacific Ocean. Reasons for this can be found in the unique geographical conditions: in northern latitudes, it is located over the open ocean and surrounded by the Rocky Mountains in North America and the mountain ranges in East Siberia. This pronounced land-sea contrast strongly influences tropospheric circulation, which in turn might drive stratospheric conditions. The source of the systematic difference between limb and nadir columns might thus be related to NO_2 in the upper troposphere/lower stratosphere (UT/LS) and the tropopause height being modulated by Lee waves which are generated by the wind system and the topography. It seems that the ECMWF meteorological models (which drive the meteorol-

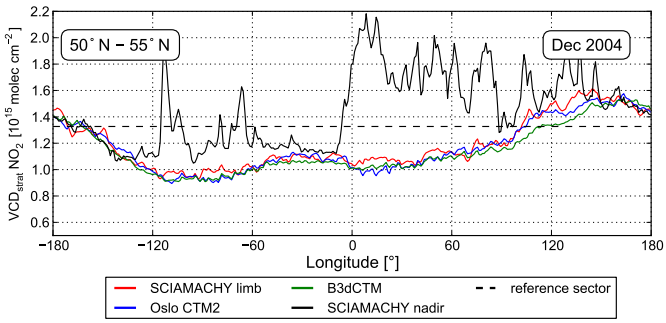

Figure 3.17: Zonal variation of $\mathrm{VCD}'^{\mathrm{limb}}_{\mathrm{strat}}$, $\mathrm{VCD}'^{\mathrm{mod}}_{\mathrm{strat}}$, and $\mathrm{VCD}'^{\mathrm{nadir}}_{\mathrm{strat}}$. The nadir measurements' value over the reference sector is marked as dashed black line. Monthly mean values for December 2004, between 50° and 55°N (after Hilboll et al., 2013c).

ogy in Oslo CTM2 and B3dCTM) sometimes fail to correctly capture the actual extent of these effects, leading to a slightly overestimated stratospheric NO_2 column over the Pacific Ocean, which in turn would lead to an overestimated tropospheric NO_2 burden over North America when using the modeled NO_2 fields as stratospheric correction.

In cases like this, the assessment of tropospheric pollution can be severely influenced by the used stratospheric correction, especially over North America. Figure 3.17 shows another example (January 2005, 50°–55°N), when using the reference sector method, only the pollution signals of the cities Montréal, Toronto, and Edmonton would be visible as positive tropospheric columns, but the actual $\mathrm{VCD}_{\mathrm{trop}}$ would be underestimated by more than 50 %. This is again caused by the fact that the Pacific Ocean stratosphere often contains larger NO_2 columns than the zonally adjacent areas.

Finally, an interesting issue regarding the nadir measurements can be identified by comparing them to limb measurements. In many months, the retrieved nadir columns seem to be lower than the integrated limb stratospheric measurements off the Chilean coast in the East Pacific (∼75°–80°W). As it can be seen in Fig. 3.18, the $\mathrm{VCD}'^{\mathrm{nadir}}_{\mathrm{strat}}$ from nadir measurements are lower than those from limb measurements and model simulations by about 1×10^{14} molec cm^{-2}. In this case, it seems

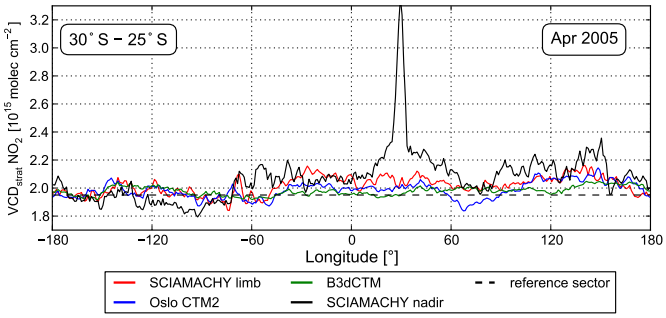

Figure 3.18: Zonal variation of $\mathrm{VCD}'^{\mathrm{limb}}_{\mathrm{strat}}$, $\mathrm{VCD}'^{\mathrm{mod}}_{\mathrm{strat}}$, and $\mathrm{VCD}'^{\mathrm{nadir}}_{\mathrm{strat}}$. The nadir measurements' value over the reference sector is marked as dashed black line. Monthly mean values for April 2005, between 30° and 25°S (after Hilboll et al., 2013c).

not to be an artifact originating from the reference sector offset, as the nadir measurements are significantly higher than the limb measurements at many other longitudes. This might be a hint leading to issues in the nadir retrieval over clean ocean waters. While these might come from liquid water absorption or vibrational Raman scattering in water (Vountas et al., 2003; Lerot et al., 2010), first investigation of monthly mean liquid water 'slant columns' shows no spatial correlation with the observed differences between SCIAMACHY nadir and limb stratospheric NO_2 columns (Peters, 2013, Fig. 7.33c).

3.4.5 *The effect of surface reflectance on stratospheric* NO_2

One noticeable feature in limb measurements and Oslo CTM2 simulations is a systematic low in the observed $\mathrm{VCD}_{\mathrm{strat}}$ NO_2 over Greenland (∼50°W) in summer (June–September), a pattern which can be seen in all years 2003–2011 (see Fig. 3.15 for Aug 2006). Since this feature is present in both datasets and persistent over the years, it seems unlikely to be both a retrieval and modeling artifact. The area of Southern Greenland is known to be special for multiple reasons. There exists strong tropopause folding activity (Elbern et al., 1998) and thus troposphere-stratosphere exchange (Sprenger and Wernli, 2003). Furthermore, a lo-

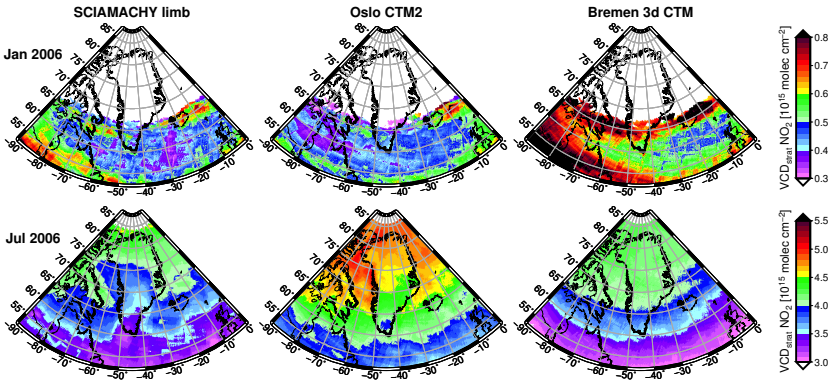

Figure 3.19: VCD_{strat} NO_2 over Greenland from SCIAMACHY limb measurements (left), Oslo CTM2 (center), and Bremen 3d CTM (right), for January (top) and July (bottom) 2006.

cal maximum in the density of polar low pressure systems exists to its East (see Zahn and Storch, 2008), and Greenland's high surface altitude and high surface reflectance (due to ice cover) stand in clear contrast to the surrounding Atlantic Ocean. While all these factors might contribute to the observed summer lows in VCD_{strat} NO_2, the underlying mechanism remains unclear at the moment, and it is hard to clearly attribute this phenomenon to one of them.

However, it is interesting to note that the Bremen 3d CTM does not show these reduced NO_2 columns over Greenland in summer (see Fig. 3.19). This draws attention to a different possible explanation for the phenomenon observed in SCIAMACHY limb measurements and Oslo CTM2 simulations, as the B3dCTM assumes a globally constant surface reflectivity of 0.30. The Oslo CTM2, on the other hand, uses the ECMWF IFS surface brightness and cloud coverage forecasts, leading to a more realistic representation of the upwelling radiance in the stratosphere, which in turn causes an increased photon flux. This could result in the NO/NO_2 partitioning being shifted more towards NO, as more radiation is available for photochemistry. On the other hand, over very bright surfaces, the Bremen 3d CTM would then, by assuming a ground

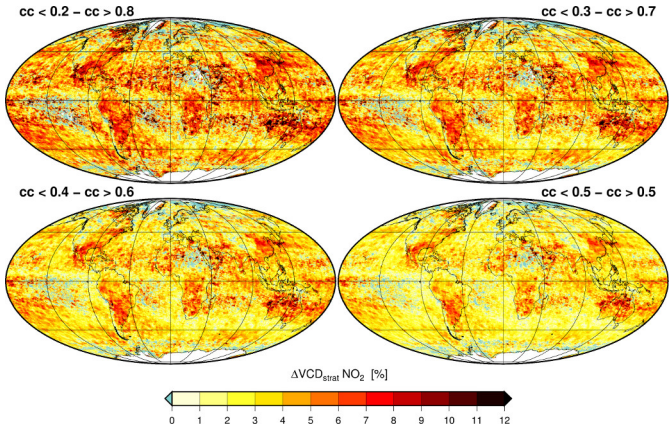

Figure 3.20: Relative difference of VCD_{strat} NO_2 from SCIAMACHY limb measurements, interpolated to the locations of the SCIAMACHY nadir pixels, over cloud-free vs. cloudy ground scenes. The plots show the climatological average of the years 2003–2010.

reflectivity of 0.3, underestimate the upwelling radiance, leading to an overestimation of the stratospheric NO_2 amount.

This hypothesis can be further investigated by comparing the stratospheric NO_2 content over cloudy and cloud-free ground scenes. If there is significant influence of the upwelling radiance on stratospheric NO_2 levels, this should result in lower VCD_{strat} NO_2 over cloudy ground scenes, due to the increased amount of radiation in the atmosphere above clouds. Using the FRESCO+ cloud algorithm (Wang et al., 2008), the relative difference of SCIAMACHY limb VCD_{strat} NO_2 over cloudy and cloud-free ground scenes is shown in Fig. 3.20. The plots show a clear indication for reduced stratospheric NO_2 columns over cloudy ground scenes. The effect varies with the cloud cover selection criterion; when comparing cloud fractions < 20% with those > 80%, the relative difference in VCD_{strat} NO_2 lies between 5% and 10%. When comparing cloud fractions < 50% and > 50%, significant differences in stratospheric NO_2 columns are still visible around the globe, mostly between 1% and 5%. It should be noted that almost in no places, VCD_{strat} NO_2 over cloud-free ground is lower than over cloudy scenes.

It should be noted that these differences between cloud-free and cloudy NO_2 columns are approximately a factor of 2 smaller than expected from the observed spatial patterns over Greenland as shown in Fig. 3.19. There, stratospheric NO_2 columns of the same latitude differ by approximately 10–20% between Greenland and the open ocean. However, this section can only provide a very first glance at the interesting issue of the dependency of stratospheric NO_2 on the upwelling radiation. A thorough investigation, including appropriate model studies, calculation of photochemical efficiencies ("j-values"), and radiative transfer simulations, is out of scope for this study.

3.4.6 *Comparison of the day-to-day variability**

Particular attention needs to be paid to the variability of the different stratospheric datasets. The very sparse spatial coverage of the limb measurements could lead to large variability of the interpolated data product. As this would severely interfere with its usability for stratospheric correction, this issue is investigated by comparing the variability of the stratospheric vertical columns.

For 2005, daily averages of all data points (measurement pixel centers / model grid cell centers) within $2.5° \times 2.5°$ boxes, located at 180° longitude and nine different latitudes, are calculated. Figure 3.21 shows the daily time series. Both limb measurements and modeled columns are taken from the 'raw' datasets, i.e. neither spatial interpolation nor offset correction have been applied. The modeled values at very high latitudes in winter are unrepresentative since at SCIAMACHY measurement time (to which the modeled data have been interpolated), the sun is still below the horizon, and the model state therefore represents nighttime chemistry. SCIAMACHY limb measurements generally yield higher VCD_{strat} NO_2 than the other datasets at low and mid-latitudes. At very low solar zenith angles however, Oslo CTM2 simulations show considerably higher NO_2 values, especially in the Southern hemisphere. This is most probably due to the difficult determination of the average

*This subsection has been adapted from Hilboll et al. (2013c).

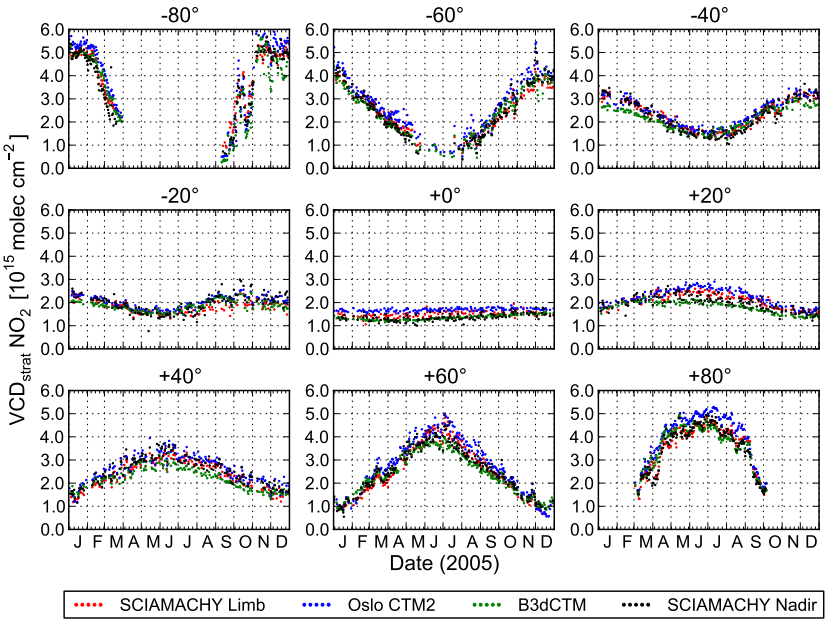

Figure 3.21: Daily time series for the year 2005 of VCD_{strat} NO_2 from SCIAMACHY limb (red), Oslo CTM2 (blue), B3dCTM (green), and of VCD_{tot} from SCIAMACHY nadir (stratospheric air mass factor applied, black) for nine $2.5° \times 2.5°$ grid boxes. The centres of the grid boxes are located at 180° longitude and the latitudes are given in the plot titles (after Hilboll et al., 2013c).

overpass time of one model grid cell at such high latitudes, which might cause significant errors when the overpass time can vary considerably within one model grid cell. A similar effect can be seen in the B3dCTM data, which are generally considerably lower than the other datasets; at high latitudes, however, they tend to over-estimate the measured limb columns (see also the correlation analysis in Sect. 3.4.3).

As a measure to compare the variabilities of the three data sets, the coefficients of variation c_v are computed. Daily residuals are calculated by subtracting a centered 31-day moving average from the daily time series (see Fig.3.22), and c_v is then defined as the ratio of their standard deviation and sample mean (see Table 3.2).

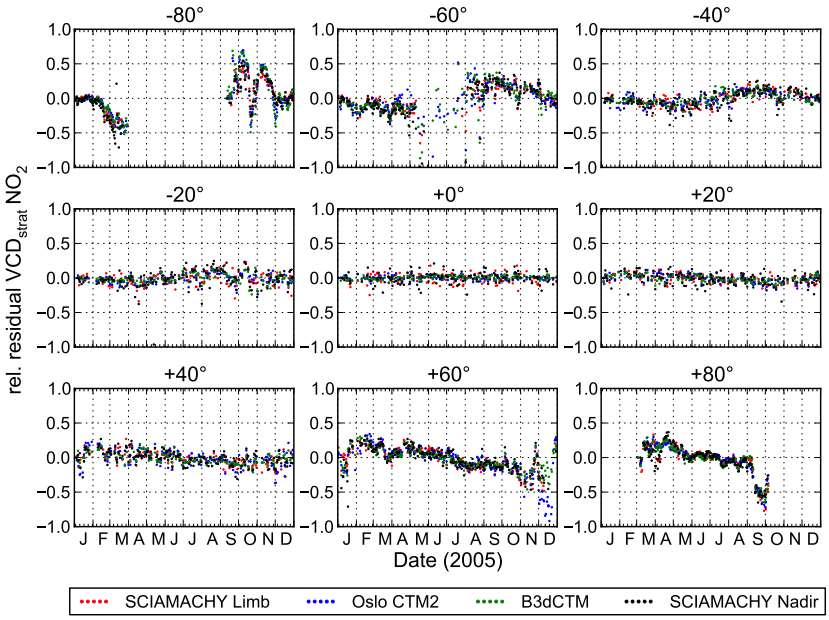

Figure 3.22: Time series for the year 2005 of the relative residuals of VCD_{strat} NO_2 from SCIAMACHY limb (red), Oslo CTM2 (blue), B3dCTM (green), and of VCD_{tot} from SCIAMACHY nadir (stratospheric air mass factor applied; black) for nine $2.5° \times 2.5°$ grid boxes. The centres of the grid boxes are located at 180° longitude and the latitudes are given in the plot titles. The residuals have been computed by subtracting a centred 31-day moving average from the daily dataset (after Hilboll et al., 2013c).

In most latitude bands, the variability of limb measurements and modeled columns is quite comparable. SCIAMACHY nadir measurements have a higher c_v than the three purely stratospheric datasets at low latitudes, while at mid- and high latitudes (with the exception of Antarctica), the variability of the four datasets does not differ by more than 20%. Still, the coefficient of variation c_v of the nadir measurements is larger than that of the limb measurements at almost all latitudes, hinting to higher random errors in the nadir retrieval as compared to the limb retrieval. In conclusion, one can say that the measurement noise in

Table 3.2: Coefficients of variation $c_v = \frac{\sigma}{\mu}$ (σ being the standard deviation, and μ being the sample mean) of daily VCD_{strat} NO_2 for nine $2.5° \times 2.5°$ grid boxes located at 180° longitude for the year 2005.

Latitude	SCIA limb	Oslo CTM2	B3dCTM	SCIA nadir
-80°	0.290	0.417	0.420	0.344
-60°	0.377	0.409	0.431	0.444
-40°	0.261	0.250	0.232	0.305
-20°	0.142	0.132	0.120	0.204
0°	0.083	0.040	0.079	0.113
20°	0.155	0.165	0.137	0.162
40°	0.253	0.232	0.213	0.237
60°	0.420	0.432	0.377	0.376
80°	0.271	0.262	0.249	0.284

the individual limb columns, while being significant, does not severely impact the retrieval of tropospheric NO_2 columns.

3.4.7 *Sensitivity study: impact of stratospheric air mass factors**

As described in Sect. 3.3.3, the integrated and interpolated VCD_{strat} need to be converted to slant columns. The simplest approach is to use an air mass factor based on a single atmospheric profile, like, e. g., the climatological stratospheric NO_2 profile from the U.S. Standard Atmosphere 1976 (U.S. Government Printing Office, 1976), and to assume a constant surface reflectivity, e. g., 0.05. The influence of the surface reflectivity on the stratospheric AMF is reported to be very low (Wenig et al., 2004), which is why this effect is not further investigated within this study. Figure 3.23 (bottom left) shows the relative change of the stratospheric AMF introduced by using the actual stratospheric NO_2 profile as measured by SCIAMACHY. In virtually all cases, the influence of the assumed NO_2 profile on the stratospheric air mass factors

*This subsection has been previously published as part of Hilboll et al. (2013c).

is negligible. Only in polar latitudes in winter, assuming the stratospheric NO_2 profile from the U.S. Standard Atmosphere leads to an overestimation of stratospheric AMFs by up to 4.5%.

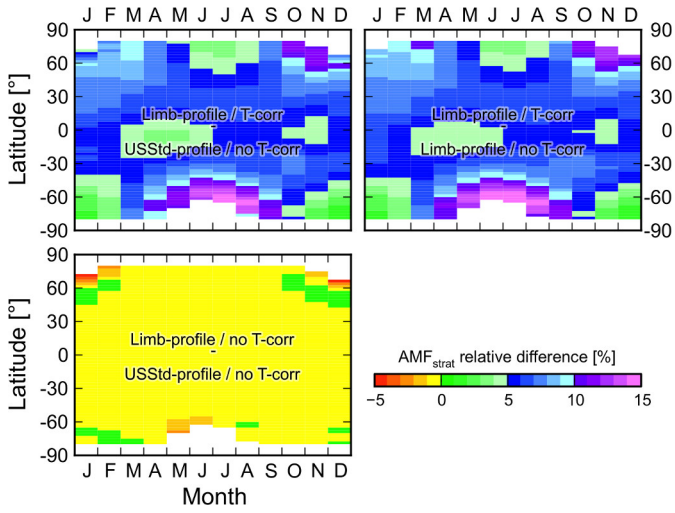

Figure 3.23: Monthly climatologies of the influence of stratospheric NO_2 profiles and temperature correction on stratospheric air mass factors. The plots show the influence of both profiles and temperature correction (top left), temperature correction alone (top right), and vertical profiles alone (bottom left). The climatologies are calculated for the years 2003–2010, using all retrieved limb profiles from the descending part of the SCIAMACHY orbit. The influence of the vertical profile is derived by comparing to AMFs calculated using the U.S. Standard Atmosphere's NO_2 profile. Stratospheric temperature profiles are taken from the ECMWF forecast (the same profiles used in the limb retrieval). The geometric line-of-sight correction (the summand $\frac{1}{\cos\alpha} - 1$) has been ignored in this comparison, and the relative difference of two datasets is computed as $\frac{2\cdot(a-b)}{(a+b)}$ (after Hilboll et al., 2013c).

To assess the influence of the temperature-dependence of the NO_2 absorption cross-section on the stratospheric NO_2 correction (see Sect. 3.3.3), a sensitivity study on eight years of data from 2003 until 2010 was performed, based on the same ECMWF forecast temperature pro-

files which were used in the limb retrieval. The results show that the temperature dependence of the NO_2 absorption cross-section actually does have significant influence on stratospheric air mass factors. As it can be seen in Fig. 3.23 (top right), the temperature dependence influences the stratospheric air mass factors by between 5 % and 15 %; using a fixed temperature of 243 K leads to an underestimation of the AMF. The influence is highest for the winter months and can reach up to 15 % at polar latitudes in the climatological mean. Combined, the two effects cancel out to some degree. When comparing the most accurate AMF_{strat} (derived using SCIAMACHY profiles and ECMWF temperatures) with the most simple one (using a U.S. Standard Atmosphere profile and disregarding the temperature dependence), the simple AMF underestimates the accurate one by ca. 2–14 % (Fig. 3.23, top left).

3.4.8 *Improvements to the tropospheric data product**

When using modeled or measured NO_2 fields as stratospheric correction scheme instead of the reference sector method, the data quality of the resulting fields of tropospheric slant columns improves considerably. Figure 3.24 shows monthly mean SCD_{trop} NO_2 for February 2005, using the reference sector method, SCIAMACHY limb measurements, and simulations made with the Oslo CTM2 and the B3dCTM as stratospheric corrections. Compared to using the reference sector method, the other stratospheric corrections considerably reduce the number of negative tropospheric NO_2 columns. On the other hand, it seems that the Bremen 3d CTM under-estimates the stratospheric NO_2 content over the northern Atlantic Ocean, leading to unexpectedly high tropospheric slant columns in this region in winter.

*Parts of this subsection have been previously published as part of Hilboll et al. (2013c).

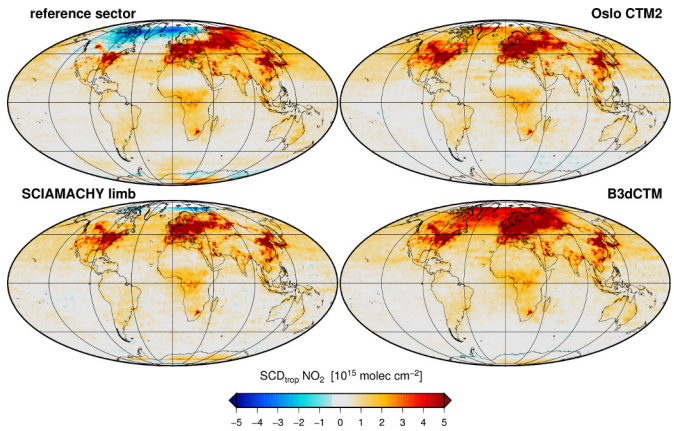

Figure 3.24: Monthly average of SCD_{trop} NO_2 from SCIAMACHY for February 2005, using the reference sector method (top left), SCIAMACHY limb measurements (bottom left), and Oslo CTM2 (top right) and B3dCTM (bottom right) simulations as stratospheric correction (after Hilboll et al., 2013c).

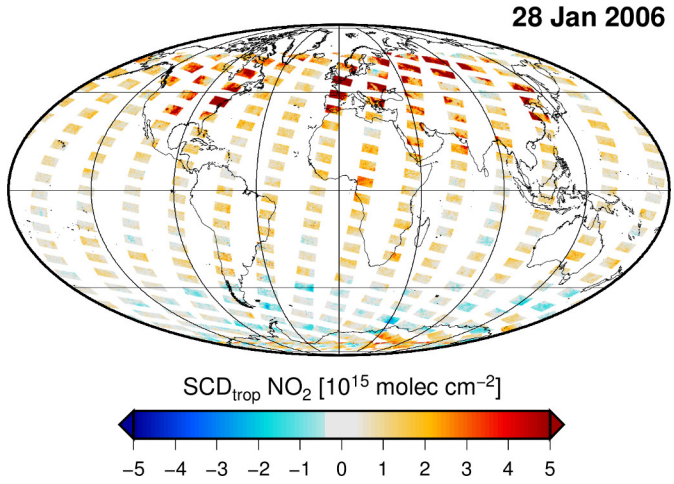

Figure 3.25: SCD_{trop} NO_2 from SCIAMACHY for 28 Jan 2006, using SCIAMACHY limb measurements as stratospheric correction (from Hilboll et al., 2013c).

The SCD_{trop}^{limb} for a single day (28 Jan 2006) are shown in Fig. 3.25.[1] Compared to the data shown by Beirle et al. (2010), the results of this

[1]Additional days are shown in the Appendix in Sect. A.5. All days have been cho-

study appear to be slightly less noisy. This might be because this study's approach accounts for possible small-scale variability in stratospheric NO_2 abundances using the interpolation scheme discussed in Sect. 3.3.2. The most striking difference, however, is the almost complete lack of significantly negative tropospheric NO_2 columns in the new data product. This is mostly due to the fact that here, the NO_2 content of the Pacific troposphere is accounted for, contrary to the 'relative limb correction' of Beirle et al. (2010).

The improved data quality of the tropospheric NO_2 fields is further illustrated in Fig. 3.26, where the multi-year winter average of VCD_{trop} NO_2 is shown for the four different correction methods. Compared to

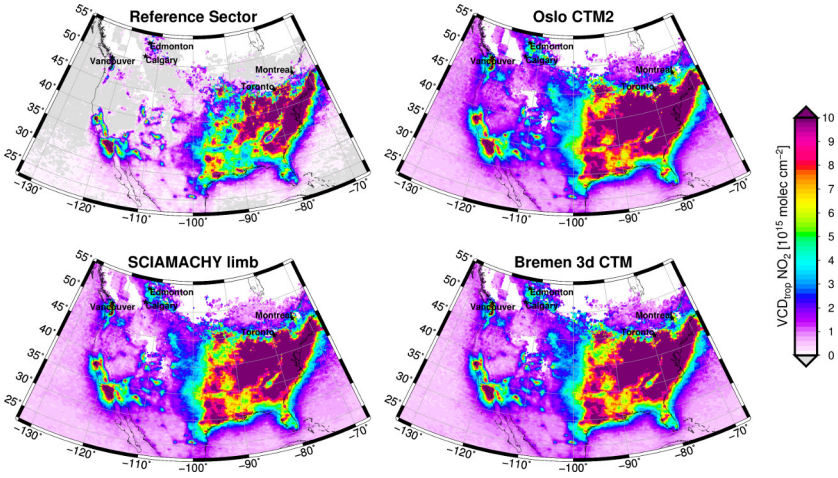

Figure 3.26: Multi-year averages of the winter months December, January, and February from Dec 2002–Feb 2007, of VCD_{trop} NO_2 from SCIAMACHY, using the reference sector method (top left), SCIAMACHY limb measurements (bottom left), and Oslo CTM2 (top right) and B3dCTM (bottom right) simulations as stratospheric correction. Negative VCD_{trop} are shown in gray, while missing data (due to constant cloud/snow cover) is marked in white.

the reference sector method, which leads to negative NO_2 columns over large part of the western U.S., the SCIAMACY limb measurements as

sen to allow easy comparison to the results of Beirle et al. (2010).

well as the modeled stratospheric NO_2 fields lead to a considerably improved tropospheric data product.

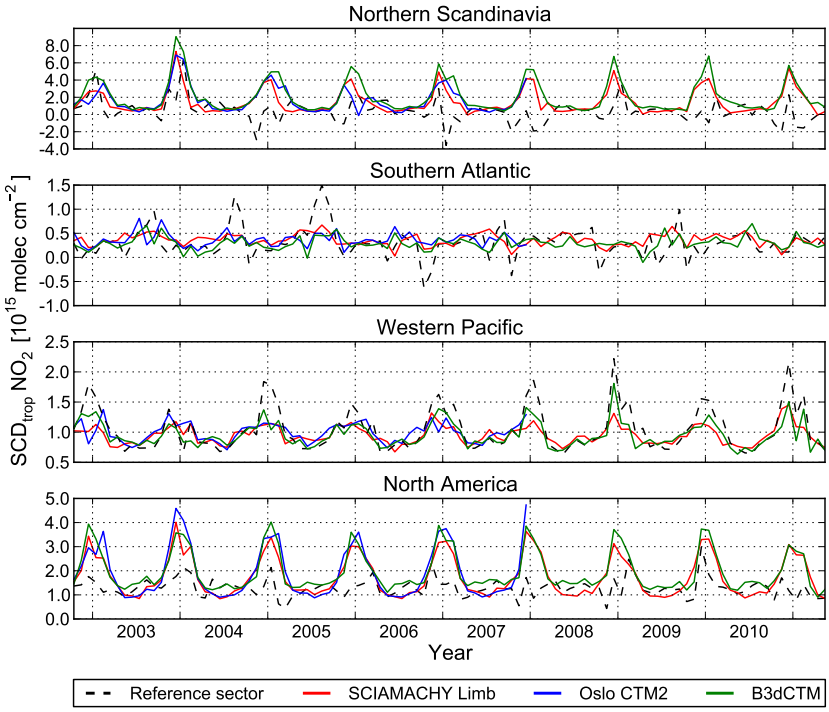

Figure 3.27: Time series of monthly mean values of SCD_{trop} NO_2 for the regions Northern Scandinavia (60°N–75°N, 0°–40°E), Southern Atlantic (50°S–30°S, 45°W–15°E), Western Pacific (25°N–50°N, 148°E–178°E), and North America (40°N–60°N, 120°W–90°W). Three different stratospheric corrections have been used: SCIAMACHY limb measurements (red), Oslo CTM2 simulations (blue, only until 2007), and the reference sector method (black) (after Hilboll et al., 2013c).

Another way to evaluate possible improvements to the tropospheric data product is to analyze time series over regions where the reference sector method leads to problematic results. Figure 3.27 shows time series of SCD_{trop} for the period from October 2002 until May 2011 over four regions with different characteristics. When using the reference

sector method as stratospheric correction, the Northern Scandinavia region shows a very clear seasonal cycle, with large negative values in winter. While the large amplitude of the oscillations is mostly due to the varying measurement geometry, the fact that the monthly mean values are consistently negative results from the observation already made in Sect. 3.4.4, where it was shown that, especially in polar winter, stratospheric NO_2 fields are far from being zonally homogeneous. Most often, stratospheric NO_2 between 60°N and 75°N seems to peak over the reference sector—a result which is backed by investigation of the zonal variability of the stratospheric NO_2 products (see Sect. 3.4.4). When using SCIAMACHY limb measurements or CTM simulations as stratospheric correction, these issues appear to be solved. The retrieved slant columns show a clear seasonal cycle with large winter maxima, as it is to be expected from measurement geometry and enhanced lifetime of tropospheric NO_2 in winter, due to photochemistry. The curves for SCIAMACHY limb and Oslo CTM2 qualitatively agree very well throughout the year, and during summer months, also with the reference sector method. As already noted earlier, the B3dCTM leads to higher winter values at high northern latitudes, which points to either an underestimation of VCD_{strat} over the Pacific Ocean as compared to the north Atlantic.

In the Southern Atlantic region, results are similar. The large amplitudes of the reference sector time series in spring are gone when using limb measurements or Oslo CTM2 / B3dCTM simulations as stratospheric correction. However, the SCIAMACHY limb and the modeled datasets do not seem to agree as well. This might be due to the fact that the overall magnitude of the tropospheric slant columns is considerably smaller in this region, leading to a higher relative influence of the uncertainty in the stratospheric columns on the time series.

In the Western Pacific region, a clear seasonal cycle can be seen independently of the used stratospheric correction. During the summer months, all four datasets agree very well. During winter, however, the tropospheric slant columns retrieved using the reference sector method are considerably larger than the other three datasets, by as much as 60 %. This interesting feature might hint towards higher

stratospheric NO_2 columns in this region compared to the reference sector, which is directly neighboring to the East. While this observation is supported by the plots of zonal variability in Sect. 3.4.4, the reason for this repeating pattern is unclear.

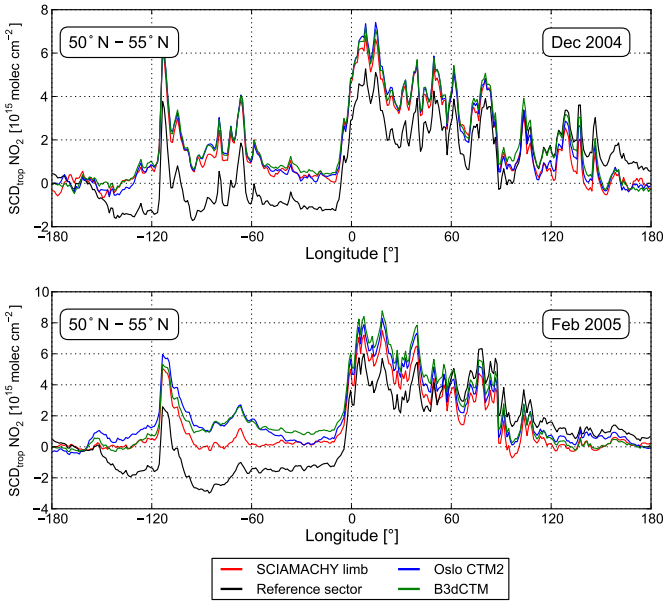

Figure 3.28: Longitudinal variation of SCD_{trop} NO_2 between 50° and 55° N for December 2004 (top, see 3.17) and February 2005 (bottom, see 3.16). Vertical tropospheric excess columns are calculated with SCIAMACHY limb measurements (red), the reference sector method (black), and the Oslo CTM2 (blue) and B3dCTM (green) models; these vertical columns have been converted to tropospheric slant columns using a climatological stratospheric air mass factor, assuming a solar zenith angle $\vartheta = 79.77°$ (top, representative for 52.5° N on 15 Dec 2004, 10:00 LT) and $\vartheta = 71.14°$ (bottom, representative for 52.5° N on 15 Dec 2004, 10:00 LT) (after Hilboll et al., 2013c).

Over North America, finally, the reference sector method leads to a clear underestimation of tropospheric pollution levels in winter. When either SCIAMACHY limb measurements or model simulations are used

as stratospheric correction, however, the seasonal cycle becomes a lot more pronounced. The tropospheric columns in winter more than double in many years, while the summer lows remain almost unchanged.

Finally, the improvements to the tropospheric data product can be illustrated by showing the zonal variation of tropospheric slant columns derived with the different stratospheric correction schemes. Figure 3.28 shows, analogously to Figs. 3.16 and 3.17, the SCD_{trop} for the latitude band from 50°–55° N, for December 2004 and February 2005. It is clearly visible that the reference sector method leads to unphysical negative tropospheric NO_2 values over the Atlantic Ocean. SCIAMACHY limb measurements and the modeled NO_2 fields mostly lead to quite similar results; only over the Atlantic Ocean in February, the modeled NO_2 fields lead to considerably higher tropospheric NO_2 abundances. As it seems unlikely that long-range transport of pollution can lead to such high tropospheric NO_2 columns over the open ocean (A. Zien, *pers. comm.*), one can conclude that probably the SCIAMACHY limb measurements lead to an even better tropospheric data product than the modeled stratospheric NO_2 fields.

3.4.9 *Error analysis**

Errors in the nadir measurements

Several different sources contribute to the total error in the slant columns measured by SCIAMACHY in nadir geometry. The uncertainties in the measured radiances lead to a random error in the DOAS fitting procedure. Systematic errors can be introduced by the absorption cross-sections used in the DOAS fit. Inaccuracies in the fitting procedure, like e.g. errors in the estimation of water leaving radiance, lead to retrieval errors. One issue could be identified off the Chilean coast, where nadir measurements are lower than limb measurements by approximately 10^{14} molec cm^{-2}. In total, the retrieval errors amount to approximately 4×10^{14} molec cm^{-2} for the retrieved slant columns, which is less than 5 % (Richter et al., 1998; Boersma et al., 2004; Wenig

*This subsection has been previously published as part of Hilboll et al. (2013c).

et al., 2004). Additionally, the nadir columns are subject to errors introduced by air mass factor calculations. For tropospheric columns over polluted regions, this is the dominating error source, which has been discussed elsewhere (Boersma et al., 2004; Leitão et al., 2010; Heckel et al., 2011). Here, only the uncertainties introduced into the stratospheric contribution of the signal are of interest. The vertical NO_2 profiles (taken from the limb measurements) as well as the temperatures from the ERA-Interim reanalysis both contribute to these errors, but are hard to quantify. The sensitivities of the resulting air mass factors to changes in the vertical absorber profile and to the temperature profile are given in Fig. 3.23, showing that uncertainties in these two quantities do not contribute significantly to the total error in most cases.

Errors in the limb measurements

Random errors in the measured radiances and systematic errors due to inaccuracies in the used absorption cross-sections can influence the limb retrieval as well as the nadir retrieval. Instrument pointing errors can impact on the vertical resolution and position of the measured profiles, and the retrieval sensitivity decreases at lower altitudes. These error sources are discussed in detail in Bauer et al. (2012) and Rozanov et al. (2005a), and are expected to add up to less than 15 % of the VCD_{strat} in most cases.

In those cases when the tropopause layer lies below the lower boundary of the limb profiles at 11 km, the measured limb profiles are extended with climatological profiles derived from Oslo CTM2 simulations (see Sect. 3.3.1). Errors in the climatological modeled vertical profiles can thus contribute to the total error of the stratospheric columns. However, the comparison of modeled and measured profiles shows that this effect can generally be neglected, as NO_2 number concentrations in the UT/LS region are very low (see Fig. 3.8).

One further uncertainty comes from the radiative transfer modeling. Air masses from far away can contribute to the limb signal reaching the satellite, and spatial gradients can further complicate the situation. This effect has been studied in great detail in Pukite et al. (2010). De-

pending on the tangent height, the errors introduced to the retrieved NO_2 concentrations can be as large as 20 %. Pukite et al. show that these errors can be avoided by using a tomographic 2-D approach in the radiative transfer calculations. It is however not applicable in an operational data product, as it is only improving the profile retrieval in the case of reduced distance between the individual SCIAMACHY measurements (3.3°) obtained in dedicated limb-only orbits. Based on the findings of Pukite et al., the upper bound of the error on the retrieved stratospheric columns is estimated to be 30 % in some rare extreme cases of low absolute values, while in most situations, the associated error should not exceed 10 % of the VCD_{strat}.

Errors in the resulting tropospheric slant columns

Uncertainties in the tropospheric slant columns derived by the limb/nadir matching approach are determined by the uncertainties in both the nadir and limb observations as well as the model background added over the Pacific Ocean. This study suggests that the random error in the stratospheric columns retrieved from limb measurements is of the same magnitude as the one for nadir measurements (see Table 3.2), leading to an increase of the random errors in the resulting tropospheric slant columns by a factor of approx. $\sqrt{2}$. Assuming a 10 % random uncertainty in the limb columns, and maximum stratospheric slant columns of about 1×10^{16} molec cm^{-2} at latitudes below 60°, errors of up to 1×10^{15} molec cm^{-2} can be introduced. Systematic errors are to a large extent removed by adjusting the limb columns over the reference sector, but longitude-dependent offsets between limb and nadir measurements might still exist. Also, it must be noted that in cases when the visibility of tropospheric NO_2 is reduced by cloud coverage in the reference sector, the offset correction might lead to an underestimation of the stratospheric slant columns and thus yield too high tropospheric columns. The resulting uncertainty in the tropospheric slant columns is bounded by the NO_2 content of the Pacific troposphere and thus on the order of $2 - 4 \times 10^{14}$ molec cm^{-2} in most regions and times; only in Northern hemisphere winter, considerable amounts

of NO_2 are predicted by the Oslo CTM2 model, leading to possibly larger errors. However, it must be noted that currently, accepting this uncertainty seems to be unavoidable. While excluding cloudy pixels from the calculation of SCD_{tot}^{nadir} would avoid the systematic underestimation of stratospheric slant columns, the cloud filter would remove a large amount of all measurements over the Pacific, considerably increasing the influence of random errors and noise (which would cancel out to a large extent with a higher number of measurements) on the data product. On the other hand, explicitly accounting for clouds in the calculation of AMF_{trop} is almost impossible, because both NO_2 and clouds are mostly found in the free troposphere and no measurements of their relative vertical distribution exist on a regular and global scale.

While it is difficult to quantify such uncertainties, a careful study of the climatological differences between measured and modeled stratospheric columns can lead towards a better understanding of problematic regions (see Fig. 3.12). In early boreal spring, the measured vertical columns are significantly higher than the modeled columns in northern high and mid-latitudes by approx. 3×10^{14} molec cm^{-2}. In July, on the other hand, the measured columns are lower than the modeled ones over almost all of the Eurasian continent by up to 2×10^{14} molec cm^{-2} when using the Oslo CTM2; the Bremen 3d CTM however predicts considerably lower stratospheric NO_2 columns. Furthermore, the systematic differences exhibit a stripe structure in the subtropics and mid-latitudes between South America and Australia. Likewise, in July, modeled stratospheric columns are significantly higher than measured ones along the western coast of Greenland. This feature can clearly be attributed to the limb measurements, because the systematic underestimation of the limb-measured columns is also visible in the climatological difference between SCIAMACHY limb and nadir columns (see the Supplement). In October, stratospheric columns modeled by Oslo CTM2 and B3dCTM are considerably lower in the southern polar region than SCIAMACHY's limb columns. This is in accordance with Beirle et al. (2010) (Fig. S16), who show that at the same time and region, their SCIAMACHY limb columns are considerably higher than their nadir columns, using their SCD_{trop}. This feature is also present

in our data (not shown) and points towards an overestimation of stratospheric NO2 columns of the Antarctic coast in austral spring. It is hard to clearly attribute these differences to either of the datasets; however, they must be considered in the estimation of the uncertainties. Also in October, a streaky pattern similar to the one observed in July can be seen over the Indian Ocean; the sign of the differences is however reversed, and their magnitude amounts to up to 2×10^{14} molec cm^{-2}.

The impact of these differences on the tropospheric slant columns depends on the corresponding stratospheric air mass factors, which are typically of the order of 2–3 over low and mid-latitudes, but can be as large as 9 at 85° SZA (high latitudes in winter). The systematic differences highlighted above therefore correspond to tropospheric slant column uncertainties of usually up to 5×10^{14} molec cm^{-2}, but can be as large as 2.5×10^{15} molec cm^{-2} at high latitudes in winter.

Over polluted regions, the bulk of tropospheric NO_2 abundances is located in the boundary layer, leading to a one-to-one translation of these systematic errors in the slant columns to errors in the vertical columns, because the tropospheric air mass factor is close to one. In these cases, the uncertainties in the vertical columns only contribute a small relative fraction to the large measured quantities. In cleaner regions, the tropospheric air mass factor is larger than one and approaching the stratospheric AMF, leading to smaller absolute contributions of the stratospheric correction scheme to the total errors in the tropospheric vertical columns. In conclusion, the relative importance of the error introduced by the limb stratospheric correction is rather small in most polluted cases, but care must be taken over clean regions and those areas highlighted above, where model and measurements show larger deviations.

3.5 SUMMARY AND CONCLUSIONS*

This chapter presents the implementation of the direct limb/nadir matching method to correct for the stratospheric contribution to total slant columns of NO_2 retrieved using the DOAS technique from SCIAMA-

*Parts of this section have been previously published as part of Hilboll

CHY nadir measurements. The use of SCIAMACHY limb measurements was compared to the simple reference sector method and to using stratospheric NO_2 columns modeled with the Oslo CTM2 and the Bremen 3d CTM. In contrast to previous studies, one stratospheric NO_2 value for every single nadir-mode measurement made by SCIAMACHY is being interpolated, using only the limb measurements from the same orbit. This leads to a very accurate representation of the zonal variability of stratospheric NO_2, avoiding the problems arising from spatio-temporal averaging. However, this advantage comes at the cost of creating a stratospheric correction method tailor-made for SCIAMACHY nadir measurements—the interpolation scheme described in this study cannot be applied to other satellite sensors like, e.g. GOME-2.

Both SCIAMACHY limb measurements and CTM simulations provide a significant and important improvement compared to the reference sector method. However, none of the datasets can be applied as an absolute correction. They all need to be corrected for a systematic bias by shifting them to the level of the nadir measurements over a clean region in the Pacific Ocean. After this offset correction, the measured and modeled datasets are found to agree surprisingly well. For SCIAMACHY limb measurements, Beirle et al. (2010) also had to apply an offset correction. In the case of the CTM simulations, this offset is in principle a very simplistic assimilation scheme. In contrast to the TM4 assimilation used in the retrievals at KNMI (Boersma et al., 2007), the approach shown here is different in that the 'assimilation' is not performed online during the model calculations but rather afterwards. On the other hand, both Oslo CTM2 and Bremen 3d CTM feature a full chemistry scheme compared to the simpler mechanisms found in TM4 (Dirksen et al., 2011). While measurements of tropospheric NO_2 over the Pacific Ocean are sparse, tropospheric NO_2 abundances must be accounted for in this bias correction. Results from the Oslo CTM2 show that tropospheric NO_2 columns over the reference sector are generally very low, but can reach significant amounts in northern mid-latitudes

et al. (2013c).

in winter. Therefore, a climatology based on data from this model was used to account for the tropospheric background in the data.

The sensitivity of stratospheric air mass factors to actual atmospheric conditions has been analyzed as well as the importance of the temperature dependence of the NO_2 absorption cross-section. In most regions, using climatological vertical profiles for the air mass factor calculations does not introduce significant errors. Only during the winter months, applying the U.S. Standard Atmosphere climatological NO_2 profiles results in a slight overestimation of stratospheric AMFs, which can reach up to 4 %. The influence of the temperature dependence of the NO_2 absorption cross-section is more substantial. Using a fixed temperature of 243 K in the DOAS fit leads to an overestimation of stratospheric NO_2 abundances by 6.4 % on average. During winter months, the influence can be as large as 15 % in the climatological means.

This present study reveals many details on the interpretation of the involved datasets, which were found to be in very good agreement with each other. In several cases, shortcomings of the reference sector method can be made up for by applying either the limb or the model correction, significantly improving the consistency of the resulting tropospheric columns. For example, during winter, tropospheric columns are underestimated by a factor of 2 over the urban centers of North America when using the reference sector method.

While it is hard to give a quantification of the error of the resulting tropospheric slant columns, one can conclude that the discussed stratospheric correction schemes, while leading to an increase of the random error component by approx. $\sqrt{2}$, minimize the error due to the zonal variability of stratospheric NO_2 fields. When accounting for a systematic bias between the stratospheric datasets by forcing their difference to be zero over the Pacific Ocean, SCIAMACHY limb measurements and Oslo CTM2/B3dCTM simulations exhibit very good agreement. Climatological differences between the two vertical column datasets are smaller than 2×10^{14} molec cm^{-2} on an annual basis, and in most cases smaller than 3×10^{14} molec cm^{-2} on a monthly basis. However, the lack of independent measurements and thorough validation makes it impossible to say which of the datasets is more correct. In most cases,

uncertainties of the order of magnitude deduced from the observed differences between the stratospheric corrections result in tropospheric slant column uncertainties of less than 5×10^{14} molec cm^{-2}, but in some rare cases can be as large as 2.5×10^{15} molec cm^{-2}. While over polluted regions, the stratospheric contribution to the uncertainties can usually be neglected when applying the limb/nadir matching technique, it has to be considered over clean regions, in particular where the agreement between model and measurement is found to be less good.

The limb/nadir matching technique described in this chapter will be tested for implementation as operational SCIAMACHY NO_2 product in the near future. This approach leads to a significant improvement of the stratospheric correction in the retrieval of tropospheric NO_2 abundances from SCIAMACHY measurements.

As modeled stratospheric NO_2 columns from the Oslo CTM2 and the Bremen 3d CTM agree very well with the measured quantities after correcting for a systematic bias, they prove to be a feasible stratospheric correction scheme in cases where limb/nadir matching cannot be applied, e. g., with other satellite sensors. This is especially important for multi-sensor analysis (see Ch. 4), where it is indispensable that all datasets are retrieved in a comparable way. Also, it should be noted that the need for an offset correction will introduce difficulties when trying to apply model data for the upcoming geostationary satellite missions which have only limited spatial coverage.

Finally, this study shows the importance of measuring stratospheric NO_2 accurately for both the interpretation of total column NO_2 and the derivation of tropospheric NO_2 as proposed for SCIAMACHY, and points out limitations of the nadir-only observations of GOME, GOME-2, OMI, and related instruments. Limb and occultation measurements of NO_2 are needed to complement the nadir observations to generate an adequate global observing system.

4

THE TEMPORAL EVOLUTION OF TROPOSPHERIC NO_2 OVER MEGACITIES SINCE 1996

4.1 INTRODUCTION

As described in Sect. 2.6, an increasingly important percentage of the Earth's human population is affected by the air quality in urban agglomerations. While anthropogenic activity, especially from the combustion of fossil fuels, leads to the emission of a variety of pollutants (see Sect. 2.2), ozone takes up a key position due to its harmfulness for human health and its role in smog formation.

In spite of its importance, the derivation of tropospheric ozone abundances from space-borne instrumentation is very challenging, since it exists in such large quantities throughout the atmosphere that it cannot be considered as optically thin in the main ozone absorption bands which lie in the ultraviolet spectral range, which, in combination with the strong Rayleigh scattering in these bands, leads to low sensitivity of the measurements close to the surface (Valks et al., 2003). However, the nitrogen oxides are closely coupled to O_3, as discussed in Sect. 2.4.2. Of these, NO_2 is especially suited for space-borne retrievals because of its distinct absorption lines, which do not interfere with any other major atmospheric absorbers (see Sect. 2.7.2), and its relatively large quantities in the troposphere. NO_2 is emitted by various different anthropogenic and naturally occurring processes (see Sect. 2.3.1) and, due to its short lifetime, allows the identification of source regions from space-borne measurements. Remote sensing of tropospheric nitric oxide (NO) from space is not feasible as its only absorption lines lie in the short- and mid-wavelength infrared and suffer from interference from mostly water vapor (Rothman et al., 2009). Also, emissions of NO_2 are strongly regulated in most countries. All this makes NO_2 a very suit-

able proxy species to assess megacity air quality from space on a global scale.

For these reasons, a lot of scientific effort has been undertaken to determine tropospheric abundances of nitrogen dioxide from space. With the launch of the GOME instrument in 1995, the first satellite-based instrument became available to retrieve tropospheric NO_2 levels at a global scale (Burrows et al., 1999). The first scientific data products of tropospheric NO_2 were developed by Leue et al. (2001), Richter and Burrows (2002), and Martin et al. (2002).

Since the beginning of the GOME measurements, more than a decade has passed, and thus the analysis of the measured time series becomes a promising target for scientific investigation.

4.1.1 *Previous studies of* VCD_{trop} NO_2 *trends**

GLOBAL STUDIES Richter et al. (2005) and Irie et al. (2005) reported on the increase of tropospheric NO_2 columns over China since 1996 already in 2005. They analyzed measurements from the GOME (and, in Richter et al., SCIAMACHY) instrument, averaged over large regions, e. g., eastern China, and reported a strong annual growth rate of 4 to 20 % and 7% annually over the county's industrialized central East (Richter et al., 2005 and Irie et al., 2005, respectively).

INVERSE MODELLING The ultimate goal of the observation of the tropospheric NO_2 burden is usually the inference of NO_x emissions from the measurments. Konovalov et al. (2006) undertook one of the first attempts to infer NO_x emissions from satellite measurements on a continental scale, using the CTM Chimere and EMEP emission data in an inverse modelling approach. They were able to significantly reduce the uncertainties in the a-priori emission data using their approach, and could identify several regions in Western Europe where EMEP emissions seem to be persistently biased.

*Parts of this subsection have been previously published as part of Hilboll et al. (2013a).

Further inverse modeling studies have been carried out, e. g., by Stavrakou et al. (2008). They used measurements from GOME and SCIAMACHY to infer anthropogenic NO_x emissions on a global scale, gridding the measurements to the coarse resolution of the used IMAGES model ($5^\circ \times 5^\circ$). Stavrakou et al. (2008) were able to estimate annual changes in NO_x emissions for the 1997–2006 period, with strongly increasing values of +7.3% in China, while emissions in all industrialized countries of North America and Western Europe were declining.

MEGACITIES The NO_2 observations of individual megacities came into focus shortly thereafter. van der A et al. (2008) fitted a seasonal trend model to ten years of GOME and SCIAMACHY data. They analyzed measurements globally on a $1^\circ \times 1^\circ$ grid, providing trend estimates for the 22 largest megacities. The seasonal variation of tropospheric NO_2 columns was modeled by using one sinus component. Over China, van der A et al. (2008) retrieve trend estimates up to 50% higher than Richter et al. (2005). van der A et al. attribute this difference to possible exponential growth of NO_2 emissions in the highly polluted Chinese East, proposing that "[t]he extra years (2003–2006) in [their] fit will therefore increase the trend found in China."

Recently, Nine years of SCIAMACHY measurements were analyzed by Schneider and van der A (2012), focusing on China and Europe on a country level. Using global SCIAMACHY measurements gridded to $0.25^\circ \times 0.25^\circ$, they were able to find positive tropospheric NO_2 trends over China of $7.3 \pm 3.1\%$ annually on average, with the strongest relative increases of 15% to 19% annually in a wide-spread area close to Huolin Gol in Inner Mongolia. Schneider and van der A attribute these strong relative increases to the construction of coal-fired power stations. Furthermore, they were able to identify the Bangladesh capital Dhaka as the megacity with the strongest growth rates globally, namely $+9.50 \pm 1.66\%$ annually.

In addition to these global studies, a number of further studies with a regional focus have been published for several regions of the world like China (He et al., 2007; Zhang et al., 2009a, 2007b), India (Ghude et al., 2008), the megacity Moscow (Sitnov, 2010), and coal power sta-

Table 4.1: Relative trend estimates for selected megacities, in % per year, compiled from the available literature (He et al., 2007; Ghude et al., 2008; Russell et al., 2012; van der A et al., 2008; Schneider and van der A, 2012). The strongly different relative trends for the individual studies are to a large extent caused by the different reference years. However, absolute trend estimates are not available for all studies.

	Beijing	Dhaka	Los Angeles	Moscow	Mumbai	New Delhi	New York	Shanghai
He et al. (1996–2000)	+10.5							+5
He et al. (2000–2005)	+23.1							+27.5
Ghude et al. (1996–2006)					+2.1	+2.4		
Russell et al. (2005–2011)			-6.72				-7.91	
van der A et al. (1996–2006)	+11	+1.4	-0.9	+2.1	+3	+7.4	-0.3	+29
Schneider and van der A (2002–2011)	+2.48	+9.5	-5.07	-1.7	+2.72	+2.72	-5.31	+3.26

tions in the United States (Kim et al., 2006); additionally, the NO_2 columns present over international shipping lines have been studied by Richter et al. (2004) and Franke et al. (2009). Recent studies have been focusing on the impact of NO_x emission reductions due to the global economic crisis and air quality legislation in the United States (Russell et al., 2012), Europe (Castellanos and Boersma, 2012), Greece (Vrekoussis et al., 2013), China (Lin and McElroy, 2011), and for shipping emissions (de Ruyter de Wildt et al., 2012).

A summary of these findings for some selected megacities is presented in Table 4.1.

IMPROVED METHODOLOGY Several studies tried to improve the underlying methodology of these trend studies, to be able to, e. g., investi-

gate the importance of different factors for tropospheric NO_2 columns (Zhou et al., 2012; Hayn et al., 2009; Voulgarakis et al., 2010), or to assess the potentially non-linear nature of tropospheric NO_2 column changes (Konovalov et al., 2010). Hayn et al. (2009) and Zhou et al. (2012) performed an extensive study on the impact of annual and weekly cycles on observed NO_2 columns over Europe, using a generalized additive regression model. They were able to reproduce the weekday-effect first reported by Beirle et al. (2003) (later, also Kim et al., 2009 studied this effect), showing clear minima in VCD_{trop} NO_2 during weekend in Western Europe. Additionally, the studies reproduced the typical seasonal cycle with high values in winter and low values in summer, and showed that, e. g., over the North Sea, NO_2 columns are highest when the wind blows from Southerly directions (Hayn et al., 2009).

Voulgarakis et al. (2010) studied the importance of meteorological variability for tropospheric NO_2 column changes. Their study showed that on timescales of approx. 5 years, meteorological variability is the key factor driving changes in tropospheric NO_2 columns. While this is especially true for the oceans, Voulgarakis et al. (2010) claim that also most areas on land are stronger influenced by meteorological changes than by varying NO_x emissions. However, one has to keep in mind that they focused on a global assessment of the importance of meteorological variability, and did not focus on regions dominated by anthropogenic emissions, like megacities. While in these regions, the influence of varying NO_x emissions is most probably stronger, the study by Voulgarakis et al. still shows that meteorological variability is a key driver of varying VCD_{trop} NO_2, notably that 86% of the inter-annual NO_2 variability over Europe between 1996-2000 was caused by meteorology.

As the available time series of tropospheric NO_2 columns from satellite measurements becomes longer, the assumption of linearly varying VCD_{trop} NO_2 becomes more and more questionable. One method to overcome this issue is non-linear trend analysis. Konovalov et al. (2010) applied non-linear trend analysis to 13 years of summer measurements from GOME and SCIAMACHY of European urban centers, finding indication of non-linear NO_2 changes in the cities Baghdad, Madrid, Mi-

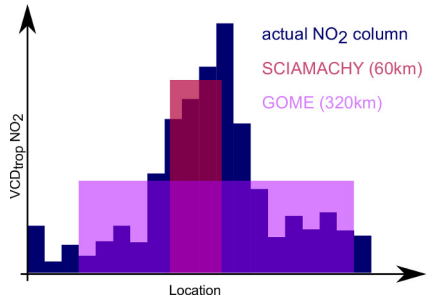

Figure 4.1: Schematic view of the effect of the instrument's ground pixel size on the measured VCD_{trop} NO_2 (from Hilboll et al., 2013a).

lan, Moscow, and Paris. Non-linear approaches will be discussed later in Section 4.8 on page 156.

4.2 TROPOSPHERIC NO_2 DIFFERENCES BETWEEN SATELLITE INSTRUMENTS

Whilst over large areas of relatively homogeneous NO_2 signals coincident GOME and SCIAMACHY observations agree very well (Richter et al., 2005), they show considerable differences for ground scenes with steep gradients in the tropospheric NO_2 columns. This is the result of spatial smoothing, which differs depending on the ground resolution of the instruments. A schematic diagram illustrating this resolution effect is shown in Fig. 4.1, and Figs. 4.2a and 4.2b show mean VCD_{trop} NO_2 from GOME and SCIAMACHY measurements as an example. SCIAMACHY measurements show considerably more spatial detail and yield higher NO_2 columns over pollution hot-spots than GOME measurements. As example, Fig. 4.3 shows the GOME and SCIAMACHY time series of monthly NO_2 columns from 1996–2011. Measurements by SCIAMACHY are considerably higher than those by GOME; the two time series differ by a factor of between 2 in summer and 4 in winter. Clearly, the inherent spatial heterogeneity of the NO_2 fields must be considered when investigating their temporal evolution over small, localized areas.

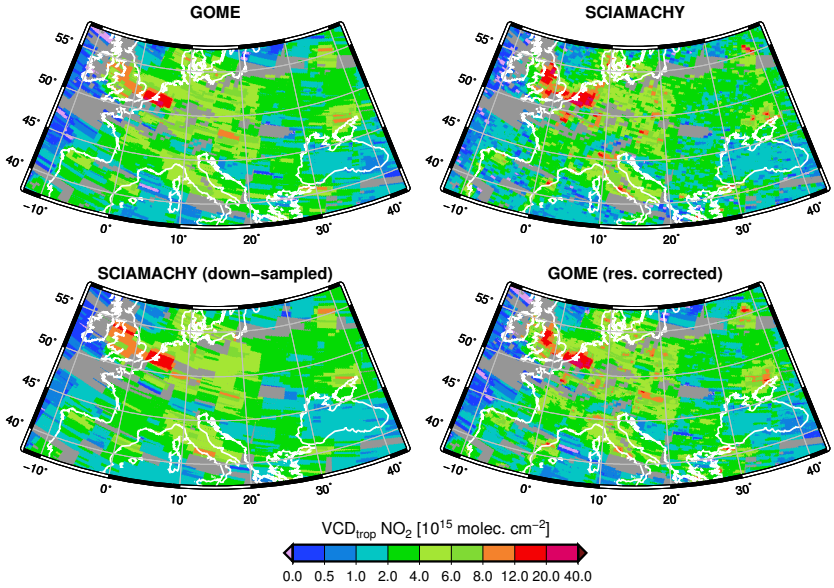

Figure 4.2: Tropospheric NO_2 columns from GOME (top left), SCIAMACHY (top right), down-sampled SCIAMACHY (bottom left; see Sect. 4.5.1), and resolution-corrected GOME (bottom right; see Sect. 4.5.1) measurements for May 2003, gridded to $1/16° \times 1/16°$. The effect of spatial smoothing can be seen in the original GOME and the down-sampled SCIAMACHY measurements for all point-like sources like cities, as the signal becomes smeared out (from Hilboll et al., 2013a).

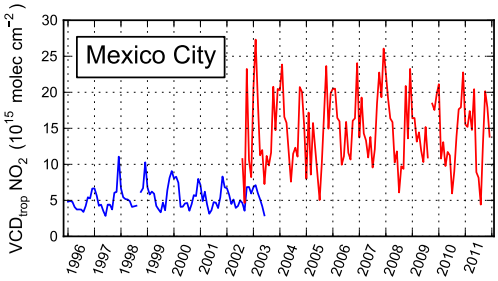

Figure 4.3: GOME (blue) and SCIAMACHY (red) measurements of tropospheric NO_2 columns over Mexico City.

4.2.1 *Impact of the instrument's spatial resolution on retrieved NO_2*

To investigate the impact of the instrument's spatial resolution on the retrieved NO_2 columns, one can sample a synthetic pollution signal using the different pixel sizes. In this study, the pollution signal was chosen to have Gaussian shape with six different full width at half maximum (FWHM) values between 15 km and 300 km, to cover the range from point sources (like individual coal power stations) to large cities. These synthetic pollution signals were then sampled with the spatial resolutions of the four satellite instruments (see Sect. 2.10).

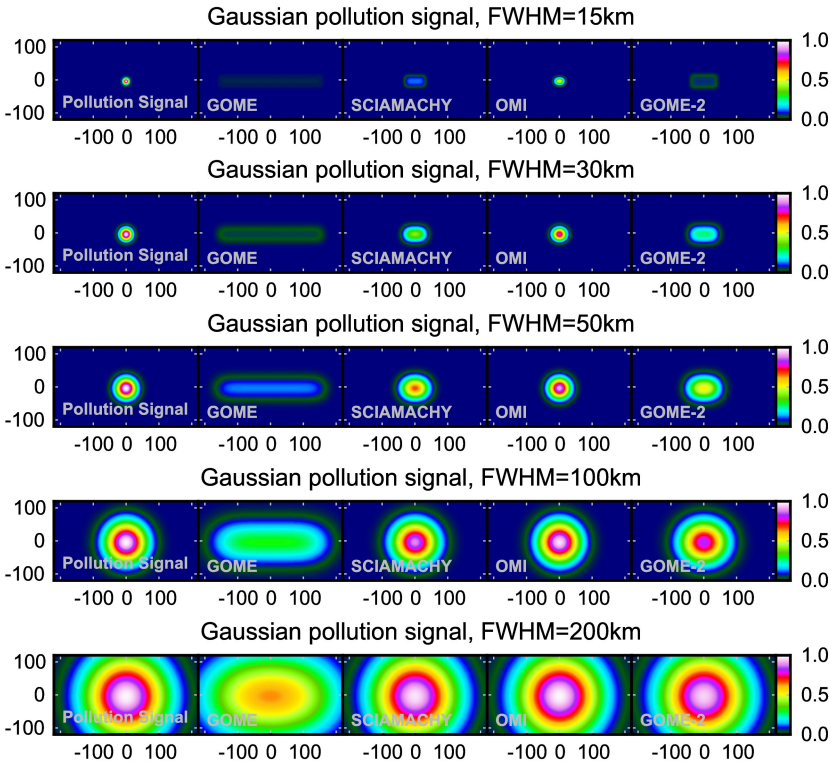

Figure 4.4: Synthetic pollution sources of varying size, sampled at GOME, SCIAMACHY, OMI, and GOME-2 spatial resolutions.

Table 4.2: Fraction of a pollution signal with strength 1.0 and different spatial extent (given by its FWHM), as observed when sampled with the footprint of the GOME, SCIAMACHY, OMI, and GOME-2 instruments.

FWHM [km]	VCD^{GOME}	VCD^{SCIA}	VCD^{OMI}	VCD^{GOME-2}
15	0.020	0.139	0.520	0.080
30	0.070	0.423	0.828	0.281
50	0.145	0.690	0.932	0.544
60	0.181	0.766	0.952	0.639
100	0.321	0.904	0.983	0.839
200	0.652	0.985	1.000	0.969
300	0.878	1.000	1.000	1.000

The results of the simulated measurements are shown in Figure 4.4. Table 4.2 summarizes the pollution signals sampled by the individual instruments. It is clearly visible that only the OMI instrument is able to properly resolve the spatial pollution patterns of typical megacities. SCIAMACHY can capture signals from areas larger than 100km, while for GOME-2, the source region should be rather 150km large in order to be properly resolved.

It should be noted, however, that when considering monthly averaged NO_2 column measurements, the effective ground pixel size of the instruments slightly increases due to spatial sampling effects: over the course of one month, each location gets measured several times, and the exact extents of the measurements vary due to the orbit repeat cycle of the satellite. It is however difficult to quantify this effect because in practice it is not possible to clearly attribute different NO_2 signals to either spatial sampling or temporal changes, or both.

4.2.2 *How previous trend studies approached the challenge of different spatial instrument resolution*

While early studies had data from only one instrument available (Richter et al., 2005; Irie et al., 2005), the individual instruments' datasets are becoming long enough to facilitate their sole analysis (Zhou et al., 2012; Schneider and van der A, 2012). Those studies investigating data from more than one instrument have usually either ignored the different ground pixel sizes of the GOME and SCIAMACHY instruments, or they artificially reduced the spatial resolution of SCIAMACHY measurements. While this latter approach potentially solves the problems arising from the differing pixel sizes, it discards the considerably better spatial resolution of the SCIAMACHY instrument.

van der A et al. (2008) down-graded the SCIAMACHY resolution by convolving over three horizontally adjacent $1^\circ \times 1^\circ$ grid cells (about 300 km). Similarly, Konovalov et al. (2010) convolved SCIAMACHY measurements to the spatial resolution of GOME. Konovalov et al. (2006) convoluted SCIAMACHY measurements, gridded to $1^\circ \times 1^\circ$, to calculate correction factors by which GOME measurements were multiplied, yielding a consistent combined GOME/SCIAMACHY dataset.

Other studies, such as Stavrakou et al. (2008), used such a coarse resolution ($5^\circ \times 5^\circ$) that they did not see the need to especially consider the different pixels sizes. For a discussion of this assumption, see Sect. 4.5.6 on page 129.

4.3 RETRIEVAL OF TROPOSPHERIC NO_2 COLUMNS*

The retrieval of tropospheric NO_2 with the DOAS technique is based on measuring spectra of extraterrestrial solar irradiance and the upwelling earthshine radiance at the top of the atmosphere. Within this study, spectra from the GOME, SCIAMACHY, and GOME-2 instruments are subsequently analyzed using differential optical absorption spec-

*Parts of this section have been previously published as part of Hilboll et al. (2013a).

troscopy (Platt and Stutz, 2008) in the 425–450 nm wavelength window (Richter and Burrows, 2002). Absorption cross-sections for O_3, NO_2 (both Bogumil et al., 2003), O_4 (Greenblatt et al., 1990), and H_2O (Rothman et al., 1992) are included in the fitting process, as well as the infilling of Fraunhofer lines and molecular absorption known as the Ring Effect (Vountas et al., 1998), an under-sampling correction (Chance, 1998), and, for GOME and SCIAMACHY, a calibration function accounting for the polarization dependency of the instrument's spectral response (Richter and Burrows, 2002). For the determination of the tropospheric NO_2 column amount from the measurements of the OMI instrument, slant columns from NASA's *OMI/Aura Nitrogen Dioxide (NO_2) Total & Tropospheric Column1-orbit L2 Swath 13x24 km (Version 3)* dataset are used.

The stratospheric contribution to the measured total slant columns SCD_{tot} has been accounted for using simulated stratospheric NO_2 fields from the Bremen 3d CTM (B3dCTM; see Sect. 3.2.4). The algorithm for separating tropospheric and stratospheric NO_2 loads is described in Sect. 3.3.

Tropospheric AMFs have been calculated with the radiative transfer model SCIATRAN (Rozanov et al., 2005b). The vertical distribution of tropospheric NO_2 has been taken from a climatology of NO_2 mixing ratios from the MOZART2 model (Horowitz et al., 2003), and surface spectral reflectance from GOME measurements (Koelemeijer et al., 2003). Both aspects are explained in detail in Nüß (2005). The AMFs have then been spatially interpolated to a 0.125° grid, using cubic splines. Measurements with a cloud coverage exceeding 20% have been filtered out using the FRESCO+ algorithm (version 6; Wang et al., 2008). Additionally, an intensity filter has been applied to discard scenes with very large surface reflectivity. This is necessary as the used albedo or surface spectral reflectance climatology (Koelemeijer et al., 2003) does not account for short-term changes in reflectivity for example from snow; in addition, the FRESCO+ cloud fractions have large uncertainties over bright surfaces.

4.4 TROPOSPHERIC NITROGEN DIOXIDE AS OBSERVED BY THE INDIVIDUAL INSTRUMENTS

4.4.1 *Changes in tropospheric NO_2 columns as observed by GOME and SCIAMACHY**

When concatenating annual mean VCD_{trop} NO_2 from GOME (1996–2002) and SCIAMACHY (2003–2011) measurements into one 16-year time series, many areas of the World show persistent changes. Figure 4.5 shows this for seven selected regions[1], the time series all normalized to the 1996 value to make relative changes comparable. This figure extends the approach used to determine Fig. 1 in Richter et al. (2005), but uses a slightly updated data analysis (e.g. FRESCO+ v6 cloud screening for both instruments, a more recent version of the stratospheric correction model, and a higher spatial resolution of the gridding). All the selected spatial regions show persistent trends, which are downward in case of Western industrialized countries (United States, Europe, and Japan), and upwards for countries with developing economies like Chi-na, India, and in the Middle East. East Central China, for example, has seen a triplication of tropospheric NO_2 columns over the whole time period, while NO_2 values over the central East coast of the United States have receded by more than 40%. These changes are explained by two behaviors, which have opposite impacts: continuing success in the reduction of NO_x emissions, in particular from cars and power plants, and increasing emissions from intensified use of the combustion of fossil fuels for energy. In rapidly developing regions such as China, any reductions in specific emissions are overwhelmed by the absolute increase of energy use. In the case of east central China, Fig. 4.5 clearly proves that NO_2 columns do indeed show signs of exponential growth,

*This subsection has been previously published as part of Hilboll et al. (2013a).

[1]The North Central Indian industrial region extending between the cities of New Delhi and Lahore lies partly within an area for which GOME measurements are not available because of platform calibration made by ERS-2 in this region. Therefore, this region had to be selected quite small.

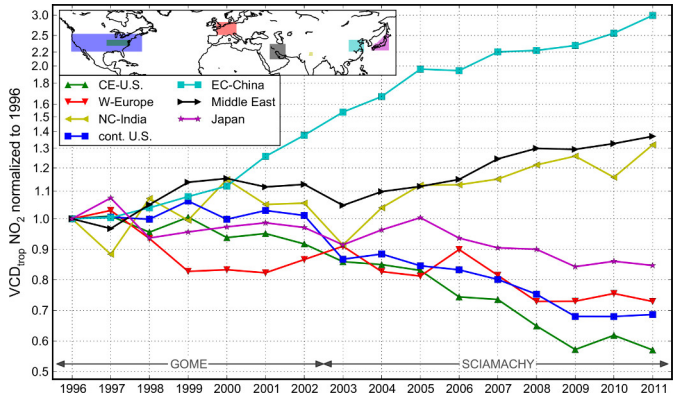

Figure 4.5: Mean annual VCD_{trop} NO_2 normalized to 1996, for the regions Central East coast U.S., Western Europe, U.S., East Central China, Japan, Middle East, and North Central India. Values for 1996–2002 are from GOME, values from 2003–2011 from SCIAMACHY measurements. The first five regions are defined as in Richter et al. (2005). The y-axis has been modified to make relative changes above and below 1 more comparable (values larger than one have been scaled to $y \mapsto 2 - \frac{1}{y}$) (from Hilboll et al., 2013a).

at least until 2005. This is in agreement with the conclusions by van der A et al. (2008) (see Sect. 4.1.1).

It is important to note, however, that even though the selected areas are all quite large, some of them appear to show small discontinuities in 2003 where the two time series are connected.

The regional trends in satellite observed NO_2 columns are compared to EDGAR NO_x emission data (European Commission, Joint Research Centre and Netherlands Environmental Assessment Agency, 2011) integrated over the same regions (Fig. 4.6).[1] First comparison shows that the sign of direction of changes is the same for all regions in EDGAR and satellite observations. While generally, the trend observed in the measured NO_2 columns is more pronounced than in the EDGAR emis-

[1] As the published version 4.2 of the EDGAR database contains erroneous emission data for the year 2008 in Iran, this plot uses an updated, so far unpublished version (G. Maenhout, personal communication, 2012) for the Middle East

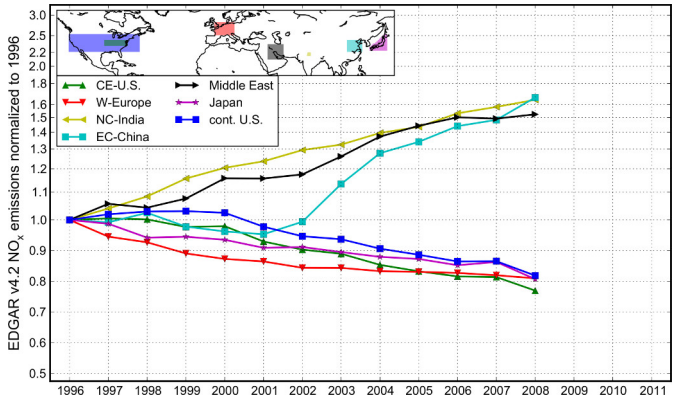

Figure 4.6: NO_x emissions from the EDGAR v4.2 database, normalized to 1996. The regions and y-axis scaling are defined as in Fig. 4.5 (from Hilboll et al., 2013a).

sion inventory, this is not the case for the Middle East and North Central India, which show smaller trends in the data than in the inventory. For East Central China, it is interesting to note that until 2002, the inventory does not significantly increase. Only from 2003 onward, it shows a strong positive trend. This is in contrast to the satellite observations, which show increasing NO_2 values over East Central China from the start of the observation period onwards. It must be noted, however, that this failure to reproduce the satellite observations before 2003 might be inherent to the EDGAR inventory. While it is out of the scope of this study to compile information about all available emission inventories, at least Zhang et al. (2007a) present an emission inventory which is very consistent with GOME/SCIAMACHY satellite measurements. This is especially true in summer, but also in winter, their inventory is only about 20% lower than the observations.

A further point comparing EDGAR emission with measurements is the temporal variability of the NO_x emissions, which is considerably lower than that of the observed NO_2 columns. This could either be the result of measurement uncertainties, mostly related to year-to-year changes in spatial and temporal sampling of the observations, or indicate inappropriate or inadequate assumptions in the bottom-up inven-

tory. One possible issue in the direct comparison of emission inventories and satellite measurements might be found in the way emission inventories are compiled. Often, country-level emission estimates are spatially redistributed based on activity data. In regions where only limited activity data are available, this might lead to inaccuracies in the spatial distribution of the emissions. On the other hand, changes in NO_2 columns and NO_x emissions are not necessarily related to each other in a linear way, particularly if changes are large (Stavrakou et al., 2008; Lamsal et al., 2011; Konovalov et al., 2010). One also needs to keep in mind that the inter-annual variability of observed columns stems to a large part from meteorological variability (Voulgarakis et al., 2010; Hayn et al., 2009). In spite of the qualitative agreement between emission inventory and satellite observations, the unusual behaviour of bottom-up emissions in China before 2003 and the discrepancy between the onset of the consequences of the development in China and India apparent in the measurements but not the inventory need further investigation to identify unambiguously their origin.

In many regions, NO_2 pollution remains a local problem, as is apparent from plotting histograms of VCD_{trop}. Figure 4.7 shows the temporal evolution of the histograms for some selected regions for the SCIAMACHY time series (2003–2011). For all regions with the exception of East Central China, a large part of the area is characterized by low and moderate NO_2 levels, and only relatively small areas are affected by intense pollution. Comparing the distributions in different years, it is clearly visible that economic growth and emission control measures and the resulting increases and decreases in the observed VCD_{trop} impact not only on pollution hotspots, but on regional scales as a whole. Over East Central China, for example, the fraction of areas with exceptionally high NO_2 levels has been significantly increasing during the observing period, leading to a shrinking area which can be considered as being polluted at lower levels. Over the same period, the Central Eastern U.S. have seen systematic increases in the fraction of low or moderately polluted areas.

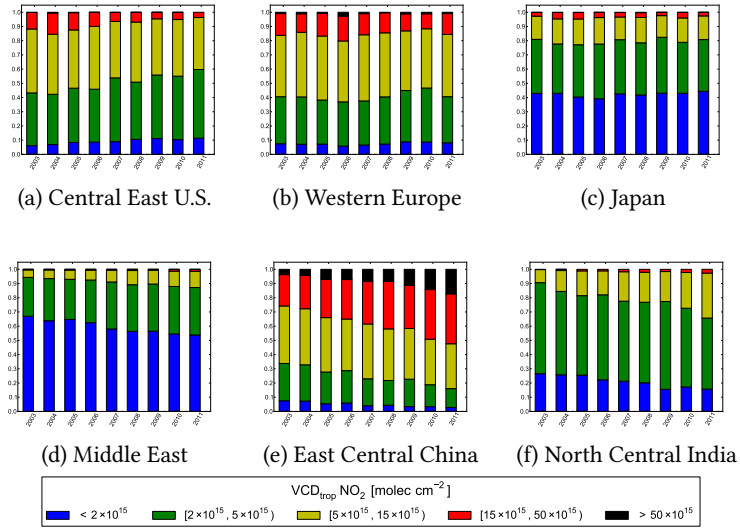

(a) Central East U.S. (b) Western Europe (c) Japan

(d) Middle East (e) East Central China (f) North Central India

Figure 4.7: Histogram of $VCD_{trop}\,NO_2$ from SCIAMACHY over the regions from Fig. 4.5 for the years 2003-2011. The plot shows the relative counts of background (blue), moderately polluted (green), polluted (yellow), very polluted (red), and extremely polluted (black) $1^\circ \times 1^\circ$ grid cells per region (from Hilboll et al., 2013a).

4.4.2 *Investigating the seasonal cycle of tropospheric* NO_2 *columns from GOME and SCIAMACHY*

Tropospheric NO_2 concentrations generally undergo a strong seasonal variation, which is under natural conditions determined by the availability of sunlight for photochemical reactions (see Reaction R 2.5) and by the temperature, which both influence the NO_2 lifetime. In areas dominated by anthropogenic pollution, this seasonal cycle is enhanced by the intra-annual variation of the NO_2 emissions, mainly due to increased heating in winter. Feedbacks with the hydroxyl radical OH can increase the amplitude of the seasonal cycle; in cases of extremely strong NO_x pollution, as in East China in winter, the very high NO_2 concentrations lead to a decrease of OH, which in turn slows down

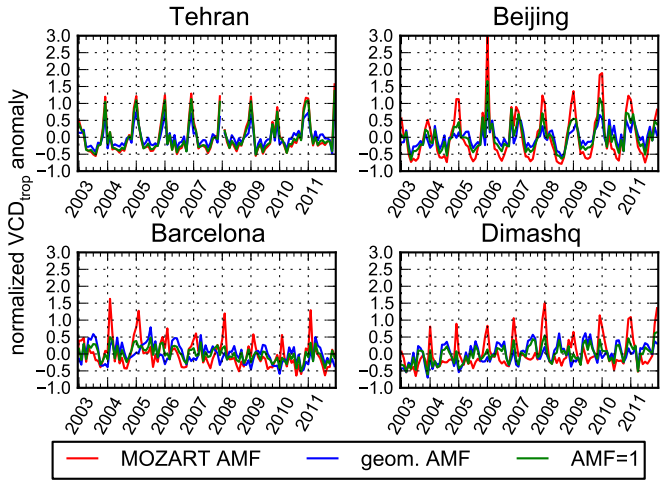

Figure 4.8: Seasonal variation (defined as $\frac{\mathrm{VCD}_{\mathrm{trop}} - <VCD_{trop}>}{<VCD_{trop}>}$) of $\mathrm{VCD}_{\mathrm{trop}}$ NO_2 from the SCIAMACHY instrument in four selected megacities. NO_2 columns from the standard data product, using a geometric AMF approximation of $1 + \frac{1}{cos(\vartheta)}$ (ϑ being the solar zenith angle), and using a constant AMF of 1 (effectively yielding $\mathrm{SCD}_{\mathrm{trop}}$) are shown in red, blue, and green, respectively.

NO_2 decomposition and increases the lifetime of the NO_2 molecule (Stavrakou et al., 2008).

The seasonal cycle of the retrieved tropospheric NO_2 columns thus also depends on the assumed seasonality in the a-priori data, namely the air mass factor climatology. In order to check if the retrieved seasonal cycle is mainly driven by actual NO_2 concentrations or is rather a consequence of the used AMFs, Fig. 4.8 compares the tropospheric vertical columns retrieved using three different air mass factors: the regular AMF[1], a geometric approximation of $1 + \frac{1}{cos(\vartheta)}$ (ϑ being the solar zenith angle), and 1 (effectively yielding tropospheric slant columns).

[1]In this context, the standard or regular AMF refers to the tropospheric air mass factor described in Sect. 4.3.

In most cases, the choice of air mass factor has only little effect on the retrieved vertical columns. Figure 4.8 shows the examples of Tehran, where the agreement is almost perfect, and Beijing, where using the standard AMF intensifies the seasonal cycle, but does not affect if qualitatively. Here, the seasonal cycle is amplified by the local meteorology: in summer, prevailing winds transport oceanic air masses to the Beijing area, diluting the tropospheric NO_2. Furthermore, precipitation in Beijing has a very strong peak in the summer months, leading to an increased scouring of the troposphere (Huang et al., in preparation).

In some cases, however, the direct comparison shows discrepancies between the NO_2 columns, indicating areas in need of further investigation. In Barcelona, for example, the NO_2 columns from the standard data product show a very pronounced seasonality, with high winter peaks in February each year. The AMFs without a-priori information show a different picture; the winter peaks are considerably lower than using MOZART AMFs, and also the annual maxima are not in February but some months later, between February and May, depending on year. As the geometric AMF approximation consistently yields higher NO_2 columns in spring as compared to winter, it seems that NO_x emissions in Barcelona then might be higher than assumed for the MOZART run; an alternative cause might be that the seasonal cycle in aerosol optical properties (see, e. g., Kosmopoulos et al., 2008 and von Hoyningen-Huene et al., 2011) is not accounted for in the standard AMF climatology.

A further city where the seasonal cycles of tropospheric NO_2 do not agree between the three different air mass factors is the Syrian capital Dimashq. There, both the geometric approximation and a constant AMF of 1 result in a second peak in the intra-annual cycle in summer. Often, this summer peak is even higher than the winter peak. This is in clear contrast to the standard AMF, which leads to a clear minimum in tropospheric NO_2 columns in summer. Possible explanations for the summer peaks include hugely increased electricity consumption due to air conditioning use and largely increased traffic emissions due to tourism, or a considerable under-estimation of surface spectral reflectance. However, without having reliable ground measurements

from the city, interpretation of the influence of the different air mass factors remains speculative.

These findings clearly show that the choice of tropospheric air mass factor strongly influences the retrieved NO_2 columns (which has already been discussed in great detail, e. g., in Leitão et al., 2010 and Nüß, 2005). While the climatological AMFs from the standard data product lead to reasonable results in many cases, there are cities where comparison with a-priori-free AMFs gives some indication of inconsistencies in the seasonal cycle. If these differences were caused by inacurracies in the climatological AMFs, this might be due to, e. g., local meteorological conditions, the spatial averaging, or inaccurate NO_x emissions in the MOZART model. While the shape of the seasonal variation can differ between the used AMFs, in virtually all cases the year-to-year variability of the seasonal cycle seems to be quite low. This shows that using a climatological air mass factor database per se does not introduce strong biases, and means that evaluation of temporal changes is most probably not strongly influenced by this issue. However, in the future, the spatial resolution of the AMF database should be improved. While factors as terrain height and albedo do play a role (see, e. g., Heckel et al., 2011 and Zhou et al., 2009), the most crucial point seems to be the intra-annual variability of NO_x emissions. Unfortunately, this point is also the hardest to improve on, because in many cases, especially outside the western industrialized world, detailed information on NO_x emission data is not available at high spatial and temporal resolution. Therefore, it will remain imperative to always remember that the choice of AMF greatly influences the resulting tropospheric NO_2 columns.

4.4.3 *Tropospheric NO_2 columns over megacities observed by GOME, SCIAMACHY, OMI, and GOME-2**

The 'raw' NO_2 measurements from GOME, SCIAMACHY, OMI, and GOME-2 are shown for selected megacity regions in Fig. 4.9. Several

*This subsection has been previously published as part of Hilboll et al. (2013a).

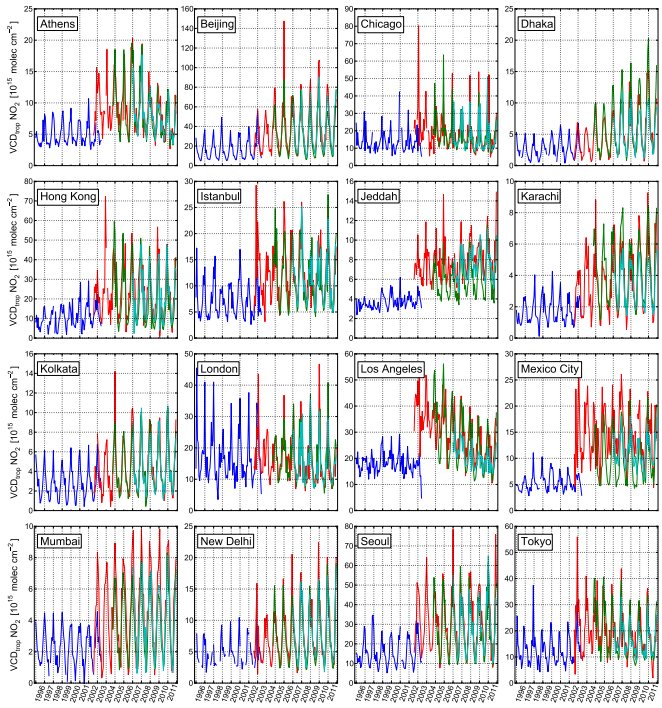

Figure 4.9: Time series of monthly mean VCD_{trop} NO_2 from GOME (blue), SCIAMACHY (red), OMI (green), and GOME-2 (cyan) (from Hilboll et al., 2013a).

interesting features can be observed from these plots. In Athens, for example, NO_2 columns seem to be increasing until about 2004, followed by some years of stagnation, which turn into a rapid downward trend 2008/2009 Vrekoussis et al. (2013). This can be attributed to the deep economic crisis affecting Greece since that time. Similarly, Chicago and Los Angeles both see downward trends, starting from stagnating and even increasing NO_2 columns before 2000, and leading to significant NO_2 decreases in following years, with the most recent years showing some sign of slowdown of the decreases. Reasons for this include increasingly efficient emission control measures and a slowdown of economic activity, as has been reported by Russell et al. (2012).

In Beijing, summer minima in 2008 are clearly lower than in the preceding and following years. This effect has been linked to the pollution control measures taken for the 2008 summer Olympic Games and has been studied e.g. by Mijling et al. (2009). Over Jeddah and Mexico City, the NO_2 columns derived from the OMI instrument are significantly lower than those from SCIAMACHY and GOME-2, especially during the summer minima. This might be an effect of the different measurement time, as OMI measures in the early afternoon as opposed to the morning for all other instruments (Boersma et al., 2007). For Mexico City, Zhang et al. (2009b) studied the diurnal cycle of NO_2 surface concentrations, and showed that 10:00 LT morning values were about three times higher than 13:45 LT values.

It is clearly visible from Fig. 4.9 that the four instruments yield considerably different NO_2 measurements over localized megacity regions, and that these differences also strongly depend on the megacity. Therefore, methods have to be developed to allow for quantitative analysis of the different time series by taking into account the differences of the four instruments.

4.5 EXPLICITLY CORRECTING FOR THE DIFFERENT PIXEL SIZES OF GOME AND SCIAMACHY *

In order to create a consistent data set of NO_2 measurements at high spatial resolution, the difference in the area of the ground scene or spatial footprint of the measurements made by the GOME and SCIAMACHY instruments needs to be accounted for. Previous studies have either degraded the resolution of both data sets to a level where differences can be ignored or applied an ad hoc deconvolution of gridded GOME data (Konovalov et al., 2006). Building on this idea, in this study, high spatial resolution SCIAMACHY spectra have been averaged to cover a similar area as individual GOME observations. Comparison of the high and low resolution analysis then provides an empirical correc-

*This section has been previously published as part of Hilboll et al. (2013a).

tion function or factor, which can be applied to GOME data. For this, it is assumed that the difference between GOME and SCIAMACHY measurements of VCD_{trop} only depends on the size difference between the two instruments' ground pixels and on season. This allows the simulation of measurements with GOME's spatial resolution using SCIAMACHY measurements by averaging over five adjacent spectra. A similar approach has previously been introduced by Beirle et al. (2004a), who applied this methodology to GOME measurements, using the instrument's narrow swath mode.

4.5.1 *Method**

Based on these assumptions, a monthly climatology of correction factors, which describe the difference between the two instruments, is calculated. To approximately match the GOME pixel size of $320 \times 40\,km^2$, the measured spectra are averaged from five adjacent SCIAMACHY forward scan ground pixels with an effective size of $300 \times 30\,km^2$, which yields three enlarged ground pixels per forward scan. On these enlarged ground pixels, a regular DOAS fitting procedure was performed with the same settings as used for the regular retrieval to obtain a dataset of SCD_{tot} from reduced resolution. This dataset was further processed in a fashion identical to that used for the original SCD_{tot}, which in the end yields a set of VCD_{trop} NO_2 from SCIAMACHY measurements with reduced resolution.

This approach has the advantage of providing an appropriate end-to-end simulation of the effects of spatial resolution change, including the impact of change in cloud statistics on the fit, the specific orientation of the satellite ground pixels and the details of the a priori data bases used. The only issue which could not fully be simulated is the change in FRESCO+ cloud fraction which was approximated by using the average of the individual cloud fraction values. As this value is only used for screening of cloudy scenes, the impact of this approximation is assumed to be small.

*This subsection has been previously published as part of Hilboll et al. (2013a).

Both datasets (regular and reduced resolution) of $\mathrm{VCD}_{\mathrm{trop}}$ are then gridded globally to a $\frac{1}{16}^\circ \times \frac{1}{16}^\circ$ grid and compiled into monthly averages for the months t' from January 2003 to December 2011. From these two monthly datasets, the climatological means $\mathrm{VCD}^{\mathrm{SCIA}}(t, \vartheta, \varphi)$ and $\mathrm{VCD}^{\mathrm{SCIA}}_{\mathrm{red.res.}}(t, \vartheta, \varphi)$ were calculated, where $t = 1, \ldots, 12$ are the months from January to December, and ϑ and φ are latitudes and longitudes, respectively. From these monthly climatologies, the climatological correction factors (ratios) were derived:

$$\Gamma(t, \vartheta, \varphi) = \frac{\mathrm{VCD}^{\mathrm{SCIA}}(t, \vartheta, \varphi)}{\mathrm{VCD}^{\mathrm{SCIA}}_{\mathrm{red.res.}}(t, \vartheta, \varphi)}. \tag{E 4.1}$$

The gridded monthly averages of the GOME measurements are subsequently multiplied with the appropriate ratio grid of correction factors to yield the resolution-corrected GOME $\mathrm{VCD}_{\mathrm{trop}}\,\mathrm{NO}_2$:

$$\mathrm{VCD}^{\mathrm{GOME}}_{\mathrm{corr.}}(t', \vartheta, \varphi) = \Gamma(t(t'), \vartheta, \varphi) \times \mathrm{VCD}^{\mathrm{GOME}}(t', \vartheta, \varphi) \tag{E 4.2}$$

It should be noted that in principle, this correction for ground pixel size could also be applied to measurements from other satellite instruments. This would however only be of limited use in the analysis of long-term time series: Firstly, correcting GOME measurements to have the spatial resolution of the GOME-2 instrument would leave a gap of 3.5 years (from 2003–2006) in the combined timeseries. Furthermore, with larger temporal gaps between the individual instruments' measurement periods, the influence of temporal changes to the spatial distribution of tropospheric NO_2 would increase the uncertainties of the resulting, resolution-corrected columns. Furthermore, in the case of OMI, the ground pixel size is not uniform for all measurements; as OMI is an imaging instrument, the pixels are considerably larger towards the edges of the scan. Moreover, the influence of the difference in local measurement time would blend with the effects of the different spatial resolutions.

Table 4.3: Spatial sampling by original and corrected GOME measurements. Fraction of a pollution signal with strength 1.0 and different spatial extent (given by its FWHM), as observed when sampled with the footprint of the GOME and SCIAMACHY instruments, and with the reduced SCIAMACHY resolution.

FWHM [km]	VCD^{GOME}	VCD^{SCIA}	$VCD^{SCIA}_{red.res.}$
15	0.020	0.139	0.028
30	0.070	0.423	0.086
50	0.145	0.690	0.164
60	0.181	0.766	0.201
100	0.321	0.904	0.347
200	0.620	0.975	0.652
300	0.793	0.989	0.814

4.5.2 *Expected goodness of* Γ^*

Even after averaging over five adjacent SCIAMACHY nadir pixels, the attained spatial extents do not perfectly match the larger pixels of the GOME instrument. Therefore, one cannot expect the proposed resolution correction to account for all observed differences between GOME and SCIAMACHY measurements. This is illustrated by repeating the synthetic study presented in Section 4.2.1 for the footprint of five averaged SCIAMACHY pixels. Figure 4.10 compares synthetic same pollution signals, sampled at the spatial resolutions of GOME, down-scaled SCIAMACHY, and SCIAMACHY measurements ($40 \times 320\,km^2$, $5 \times 30 \times 60\,km^2$, and $30 \times 60\,km^2$).

The fraction of the actual pollution signal which is observed at the three different resolutions is given in Table 4.3. It is apparent that for pollution signals smaller than 100 km, all three measurements significantly underestimate the pollution peak, while they considerably overestimate the signal in surrounding areas (see Fig. 4.10). Only when the instrument resolution gets as low as 50% of the spatial extents of

*This subsection has been previously published as part of Hilboll et al. (2013a).

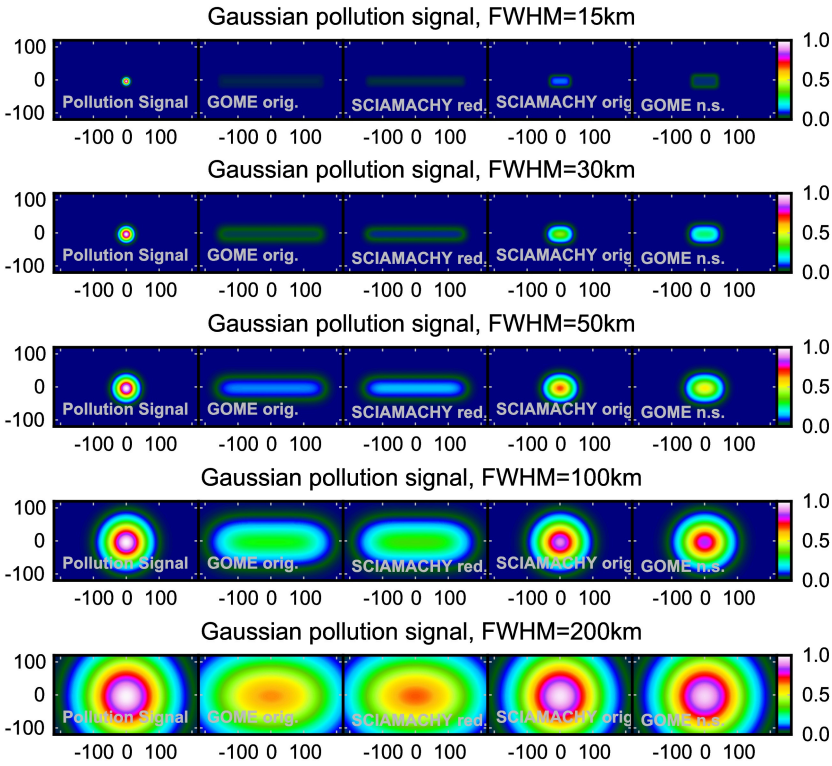

Figure 4.10: Illustration of the instruments' spatial resolution on the retrieved pollution signals. A given pollution distribution (top left), assumed to be Gaussian with different FWHM, is sampled with the spatial resolutions of the GOME and SCIAMACHY instruments, and with the resolution of the artificially down-graded SCIAMACHY resolution.

Table 4.4: Ratios of the measured pollution signals as given in Table 4.3

FWHM [km]	$\frac{\mathrm{VCD}^{\mathrm{SCIA}}}{\mathrm{VCD}^{\mathrm{GOME}}}$	$\frac{\mathrm{VCD}^{\mathrm{SCIA}}}{\mathrm{VCD}^{\mathrm{SCIA}}_{\mathrm{red.res.}}}$	$\frac{\mathrm{VCD}^{\mathrm{SCIA}}_{\mathrm{red.res.}}}{\mathrm{VCD}^{\mathrm{GOME}}}$
15	6.992	5.000	1.398
30	6.011	4.907	1.225
50	4.765	4.212	1.131
60	4.233	3.805	1.113
100	2.819	2.602	1.083
200	1.571	1.496	1.051
300	1.248	1.215	1.027

the pollution signal, the instruments start to well represent the actual NO_2 distribution. These results are in good agreement with Beirle et al. (2004a), who studied the difference between GOME narrow swath and standard measuring mode.

Table 4.4 finally summarizes the ratios of the different measurements to each other. The column $\mathrm{VCD}^{\mathrm{SCIA}}_{\mathrm{trop}}/\mathrm{VCD}^{\mathrm{GOME}}_{\mathrm{trop}}$ shows the actual relation of the two instruments' measurements and is an indicator for the offset one should expect to see in the GOME and SCIAMACHY time series. $\mathrm{VCD}^{\mathrm{SCIA}}/\mathrm{VCD}^{\mathrm{SCIA}}_{\mathrm{red.res.}}$ is the resolution correction factor Γ, theoretically derived for the different pollution signals. Finally, the difference which has to be expected to remain visible in the combined time series of resolution-corrected GOME and original SCIAMACHY measurements is labeled $\mathrm{VCD}^{\mathrm{SCIA}}_{\mathrm{red.res.}}/\mathrm{VCD}^{\mathrm{GOME}}$.

The results show that the proposed resolution correction works accurate to within a few percent only for large, spread out pollution sources. In the case of isolated point sources, like individual large coal power plants, the application of the resolution correction factor Γ will bring a significant improvement in the agreement of the two time series, but still a remaining under-correction of up to 40% has to be expected.

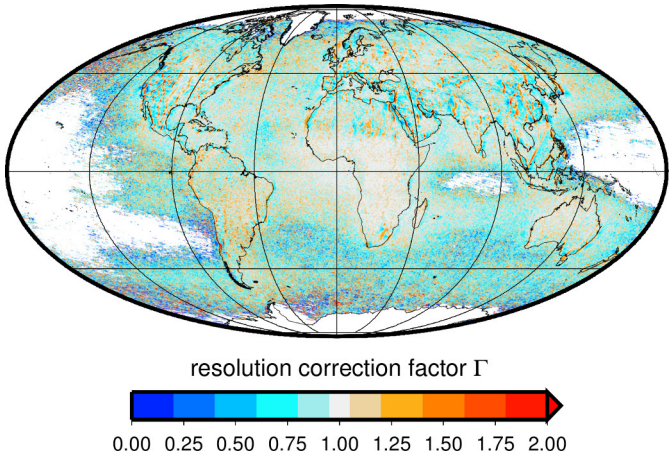

Figure 4.11: Annual mean $\bar{\Gamma}$ of the resolution correction factor climatology (2003–2011). Pixels with a mean $\mathrm{VCD}^{\mathrm{SCIA}}_{\mathrm{red.res.}}$ significantly lower than the instrument precision (estimated to be 10^{14} molec cm^{-2}) have been excluded from the plot (from Hilboll et al., 2013a).

4.5.3 *Spatial variation of* Γ *

The resolution correction factor Γ is a measure for the spatial heterogeneity of the observed NO_2 signal. Values of Γ larger than 1 indicate that typically observed NO_2 columns at a location are higher than in the surrounding area. Figure 4.11 shows the global distribution of the annual mean $\bar{\Gamma}(\vartheta, \varphi) = \frac{1}{12}\sum_t \Gamma(t, \vartheta, \varphi)$ of the resolution correction factor climatology. Over the open oceans, the signal of $\bar{\Gamma}$ is noisy. This is related to the large relative errors of the very low measured $\mathrm{VCD}_{\mathrm{trop}}$ NO_2 over the oceans, which are close to or below the instrument's detection limit. Over land, however, and especially in regions with high spatial gradients in NO_2 emissions, such as the United States and Europe, the maxima in the gridded values for $\bar{\Gamma}$ clearly coincide with urban agglomerations or conurbations (see Fig. 4.12). While noisy, a line of enhanced values of $\bar{\Gamma}$ can be distinguished over the Atlantic Ocean, running from the tip of North-Western France to North-Western Spain.

*This subsection has been previously published as part of Hilboll et al. (2013a).

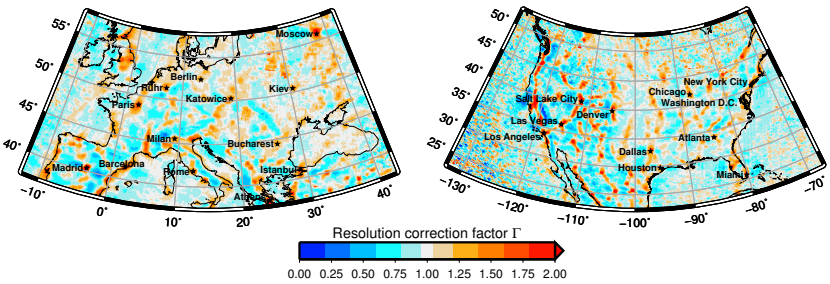

Figure 4.12: Annual mean $\bar{\Gamma}$ of the resolution correction factor over the United States (right) and Europe (left) (from Hilboll et al., 2013a).

This coincides with a major shipping line, whose NO_2 emissions have previously been discovered in satellite imagery (Richter et al., 2004; Franke et al., 2009; de Ruyter de Wildt et al., 2012).

SPATIAL PATTERN OF Γ IN THE WESTERN U.S. Especially in the Western U.S., where NO_x emissions tend to be very sparsely distributed, local maxima in $\bar{\Gamma}$ can be attributed to individual sources like coal power stations. As it is to be expected, local minima of the correction factor are visible longitudinally adjacent to these peaks (see Fig. 4.12), which is in good agreement with the findings by Beirle et al. (2004a).

The spatial distribution of the resolution correction factor $\bar{\Gamma}$ can reveal rich structures, most of which can be readily explained. Figure 4.13 shows the western part of the United States, where the low population density and subsequently low NO_x background signal in most parts of the country allow for easy identification of localized sources.

All major urban settlements clearly show $\bar{\Gamma}$ values larger than 1. Furthermore, along almost all major highways in the Western U.S., enhanced values of $\bar{\Gamma}$ can be observed, indicating that road traffic significantly contributes to measured NO_2 columns in most areas. Additionally, many local maxima in $\bar{\Gamma}$ coincide with the locations of large coal power stations, which are known to considerably contribute to anthropogenic NO_x pollution (Kim et al., 2006; Zhang et al., 2009a). In some cases, however, clearly visible local $\bar{\Gamma}$ maxima do not correspond to

power plants. Some of these could be identified as places of open-pit coal mining.

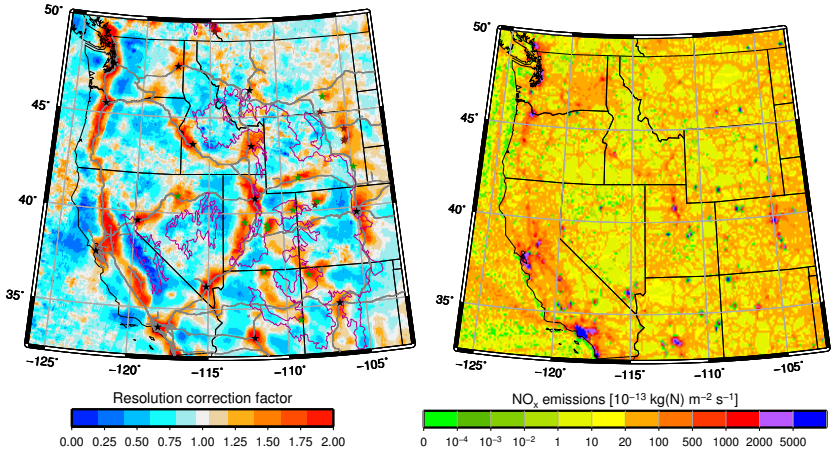

Figure 4.13: Resolution correction factor $\bar{\Gamma}$ (left) and NO_x emissions (right) over the western United States. On the left, major cities are designated by black stars. Primary roads are marked as grey lines (U.S. Census Bureau, 2012). The purple line marks the 1900m elevation isoline (data from the GTOPO30 dataset, see U.S. Geological Survey, 2004). The locations of the strongest polluting coal power stations are marked as green stars (data from the CARMA project, see Wheeler and Ummel, 2008 and Ummel, 2012). Red stars mark the locations of major open-pit coal mines (see InfoMine Inc., 2012). NO_xemissions for the year 2008 (right figure) are taken from the EDGAR database (European Commission, Joint Research Centre and Netherlands Environmental Assessment Agency, 2011).

As already observed by Beirle et al. (2004a), the topography also heavily influences local NO_2 distributions. From Figure 4.13 it is clearly visible that regions with high surface altitudes correspond to $\bar{\Gamma}$ values of less than 1 in most cases. The few exceptions to this rule are caused by the high NO_2 emissions from power plants, as in the case of the North Valmy and Jim Bridger power stations, located at 117.1542° W, 40.8831° N and 108.8° W, 41.75° N, respectively. In some places, locally

high $\bar{\Gamma}$ values in absence of extended pollution sources can also be attributed to the topography, when NO_2 emitted from e.g. a coal power station stays confined to valleys, as is the case over the Painted Desert between the Springerville and Navajo power stations, which are located at 109.1636° W, 34.3186° N and 111.3917° W, 36.9125° N, respectively.

In summary, the mapped resolution correction factor provides a very detailed view of the spatial structure of tropospheric NO_2 columns. Since $\bar{\Gamma}$ is a relative measure, it is able to pick up and enhance even structures which would normally be lost in retrieval noise. Together, cities, power stations, mines, topography, and roads account for basically all visible features in the mapped resolution correction factor; these visible features are all in excellent agreement with NO_x emission data from the EDGAR database (European Commission, Joint Research Centre and Netherlands Environmental Assessment Agency, 2011).

4.5.4 *Temporal variation of* Γ

As the resolution correction factor Γ is a measure of the relative NO_2 abundance compared to a location's surroundings, increasing NO_2 columns at a point source should in principle lead to decreasing Γ at the same location, given that NO_2 columns in the surrounding areas remain constant. This claim can be tested by performing a simple linear regression of the annual means of the resolution correction factors Γ. As the signal of Γ is relatively noisy, significant results can only be obtained for few selected cities. Figure 4.14 shows the significant temporal changes of both Γ and VCD_{trop} NO_2 for the surroundings of the two megacities Tehran and Beijing.

For Beijing, positive trends in VCD_{trop} NO_2 in regions surrounding the city clearly coincide with negative trends in Γ over the city itself. As the NO_2 load in surrounding areas increases faster than over the city itself, the ratio of NO_2 in and around the city decreases, which shows in negative trends in Γ. While at first sight it might be surprising that the center of Beijing does not show significant NO_2 trends, this is in agreement with Schneider and van der A (2012), who also

do not see significant NO_2 trends in Beijing itself for the 2003–2011 time period. However, it should be expected that the bulk of the visible NO_2 increases comes from growth of the emitting area, and not of the emissions in the city center. Further possible reasons include the severe emission control measures during the 2008 Olympic Games, which lead to a decrease in NO_2 concentrations of up to 60% (Mijling et al., 2009). Even though NO_2 columns over Beijing have quickly regained their original high values, this 'dent' can influence the significance level of the trend calculations. While MAXDOAS measurements have shown increasing NO_2 columns over Beijing after 2008 (Ma et al., 2013), it is possible that progress in emission control technology has lead to a slowdown of emission increases, leading to a signifance level below 95%. Also, it must be considered that Beijing suffers severely from very high aerosol levels. These strongly scattering and absorbing aerosol layers can be mistaken for clouds by the FRESCO algorithm, which in turn leads to the measurements being mistakenly flagged as cloudy. As the number of available measurements from SCIAMACHY is already quite low (only up to six measurements per month), this can have significant impact on the random error of the monthly mean NO_2 columns, increasing the trend uncertainty.

In the case of Tehran, the increasing NO_2 columns over the city and its sister town Karaj are accompanied by significantly decreasing Γ over the neighboring Alborz mountains. As the NO_2 pollution over the urban areas increases, the ratio of NO_2 around and in the city decreases.

These two examples show that in principle, the spatial distribution of the temporal changes of Γ is consistent with the retrieved VCD_{trop} NO_2 themselves. However, as the time series is relatively short, most places do not show statistically significant temporal changes.

4.5.5 *Validation of the resolution correction**

In many cases, the resolution correction works extremely well. This can be evaluated using data from the period of overlapping measure-

*This subsection has been previously published as part of Hilboll et al. (2013a).

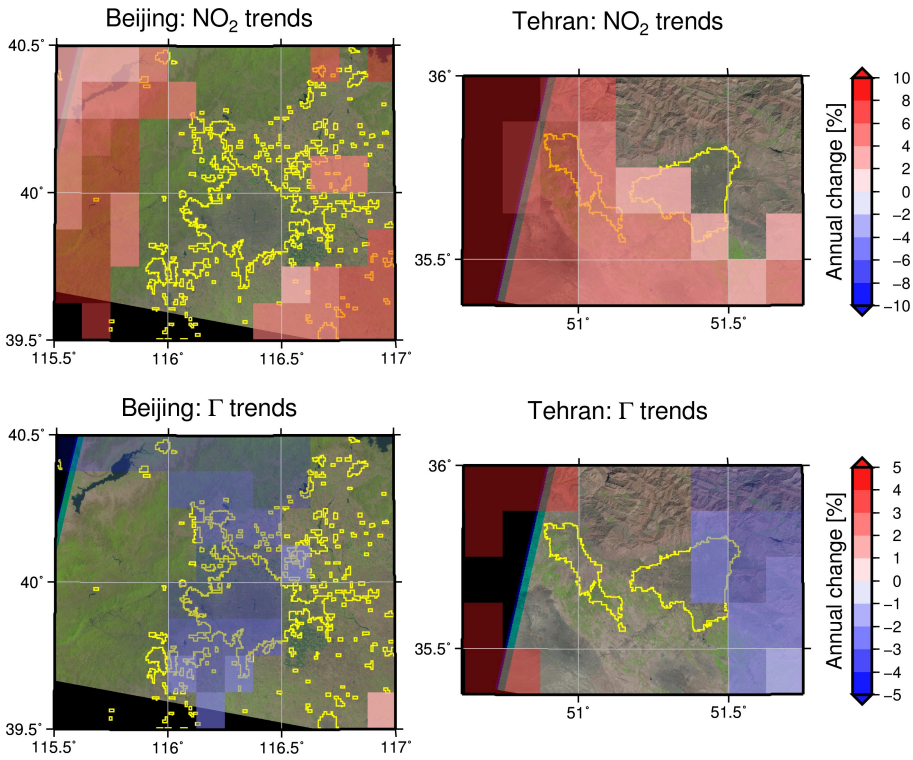

Figure 4.14: Temporal changes of resolution correction factor Γ and NO_2 measurements, for the Beijing and Tehran areas, gridded to 0.125°. All trends have been calculated from SCIAMACHY measurements in the 2003–2011 period. NO_2 trends are calculated with the trend model from Eq. 4.3 (without the levelshift terms $\delta U(t)$ and $(\gamma - 1)U(t)$), and the changes in Γ are estimated using a linear regression of the annual means. Only trends significant at the 5% level are plotted. The background shows LANDSAT imagery (U.S. Geological Survey). Urban areas, as classified by the GLOBCOVER database (European Space Agency, 2009) , are enclosed in yellow.

ments of the GOME and SCIAMACHY instruments (August 2002–June 2003). To reduce the impact of temporal sampling, only data points for which both instruments have measurements on the same day are in-

cluded in the validation. For Europe, Fig. 4.2 compares original GOME and SCIAMACHY measurements to spatially down-sampled SCIAMACHY and resolution-corrected GOME measurements. The spatial distribution of GOME measurements is well approximated by the down-sampled SCIAMACHY measurements. Furthermore, the greater spatial detail inherent to the gridded SCIAMACHY measurements is obviously well transferred to the resolution-corrected GOME measurements.

A more detailed comparison over pollution hot spots is provided in Figure 4.15, which shows the monthly mean values of VCD_{trop} NO_2 for the four cities Mumbai, Seoul, Mexico City, and Rome[1]. While in the direct comparison, there are differences of up to a factor of two, most of the corrected GOME data agree with SCIAMACHY data within 10%, independent of season. Quite often, however, the correction method actually overshoots, which leads to unreasonably high VCD_{trop} NO_2 for the corrected GOME measurements, especially over urban areas. As an example, the four cities Houston, Baghdad, Cairo, and Karachi are shown in Figure 4.16. When performed over larger areas, a small over-correction is also observable in some months (see Figure 4.17).

4.5.6 *Discussion**

The apparent overcorrection in some situations is initially at least unexpected, as from the approximations made, one would expect the correction to underestimate the resolution effect, because the SCIAMACHY pixels with reduced resolution still only cover about 70% of the ground area of a GOME measurement. There are several possible reasons for the observed differences: A problem with the approach used for resolution correction, a bias in one or both of the data sets, or real NO_2 differences, for example from the different overpass times of the two satellites, which could lead to systematically different NO_2 columns.

*This subsection has been previously published as part of Hilboll et al. (2013a).

[1]Depending on the extent of the urban sprawl, the individual city regions have been defined as rectangles with edge lengths between 0.5°and 1.0°.

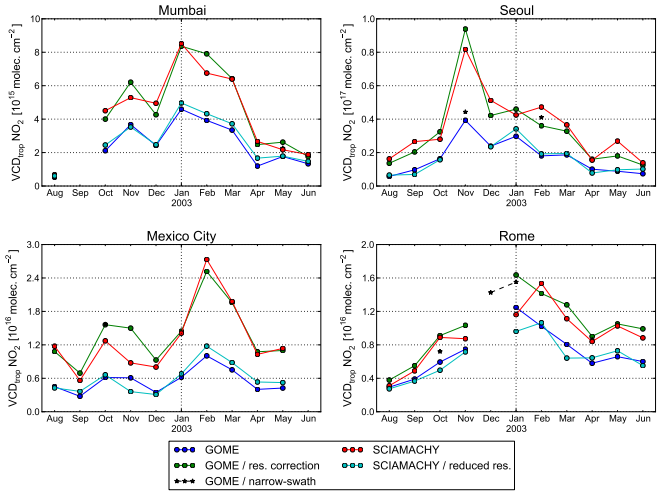

Figure 4.15: Monthly averages of VCD_{trop} NO_2 over four exemplary areas showing very good agreement between corrected GOME and original SCIAMACHY measurements, for the time period August 2002 - June 2003. Only those days for which both GOME and SCIAMACHY measurements for a city are available are taken into account (from Hilboll et al., 2013a).

For most investigated areas, down-sampled SCIAMACHY measurements agree extremely well with original GOME measurements (see Figs. 4.15–4.17), showing that the derived resolution correction factor Γ should in principle well capture the differences between the two instruments which are due to their respective spatial resolutions.

Possible biases between the two instruments could in principle be evaluated using GOME's narrow-swath mode. However, as this mode was operating only every 12 days, temporal coverage is extremely sparse. While this does not prevent the analysis of spatial patterns (see, e. g., Beirle et al. (2004a)), time series of VCD_{trop} from the narrow-swath mode are subject to large influence of measurement variability (see Fig. 4.17).

As a next check, it was investigated whether DOAS analysis of the spatially averaged SCIAMACHY spectra actually yields the same mean

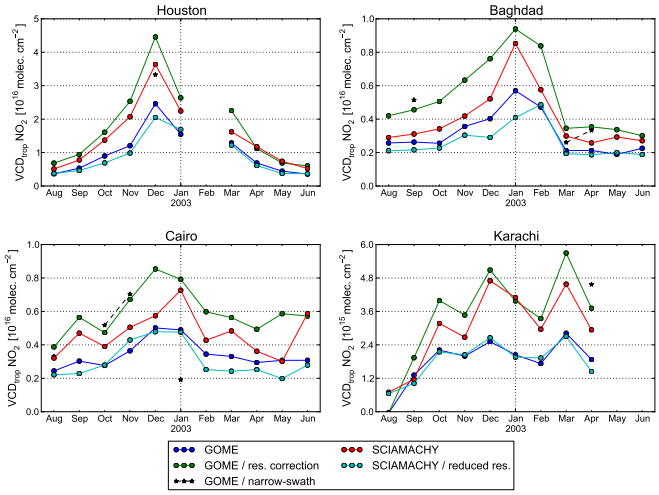

Figure 4.16: Monthly averages of VCD_{trop} NO_2 over four exemplary areas showing a significant over-correction, for the time period August 2002 – June 2003. Only those days for which both GOME and SCIAMACHY measurements for a city are available are taken into account (from Hilboll et al., 2013a).

SCD_{tot} NO_2 as from the regular measurements. The results for 4 exemplary orbits from the year 2011 are shown in Tab. 4.5. The open Pacific Ocean was chosen for this first test because in this pristine region, spatially homogeneous NO_2 measurements can be expected. As the measured slant columns agree almost perfectly in most cases, one can conclude that for homogeneous scenes, the spatial averaging of the measured spectra does not influence the magnitude of the retrieved VCD_{trop}.

When repeating the same test for regions affected by the over-correction, e.g. the relatively isolated pollution hot spot formed by the city of Cairo in Northern Egypt, original SCIAMACHY measurements give an up to 10% higher average than those with down-sampled spatial resolution, even when considering an area as large as $4° \times 5°$. This suggests that for heterogeneous ground scenes, an averaging of the measured

Table 4.5: Relative difference of original SCIAMACHY measurements $\mathrm{SCD}^{\mathrm{SCIA}}(\vartheta, \varphi)$ and reduced-resolution SCIAMACHY measurements $\mathrm{SCD}^{\mathrm{SCIA}}_{\mathrm{red.res.}}(\vartheta, \varphi)$ for four exemplary orbits from the year 2011.

	relative difference $\frac{\mathrm{SCD}^{\mathrm{SCIA}}(\vartheta,\varphi)}{\mathrm{SCD}^{\mathrm{SCIA}}_{\mathrm{red.res.}}(\vartheta,\varphi)} - 1$ [%]			
orbit number	46222	47514	48821	50143
Latitude range	01 Jan 2011	01 Apr 2011	01 Jul 2011	01 Oct 2011
90°S - 80°S	-0.15	+0.00	n/a	+0.75
80°S - 70°S	+4.1	-16.	n/a	+2.6
70°S - 60°S	+1.0	+2.7	-6.1	+0.68
60°S - 50°S	+0.90	+0.87	+2.3	+0.44
50°S - 40°S	+0.75	+2.2	+1.7	+0.49
40°S - 30°S	+0.12	+0.59	+0.92	+2.3
30°S - 20°S	-0.32	+0.23	+1.2	+0.59
20°S - 10°S	-0.34	+0.29	-0.54	+0.51
10°S - 0°	+0.28	-0.29	-0.051	+0.35
0° - 10°N	+0.75	+1.1	+0.054	+0.062
10°N - 20°N	+0.47	+0.056	+0.063	+0.62
20°N - 30°N	+0.12	+0.086	-0.11	+0.36
30°N - 40°N	+0.51	+0.11	+0.080	+0.62
40°N - 50°N	+0.61	-0.014	+0.38	+0.25
50°N - 60°N	+0.29	+0.33	+0.66	+0.64
60°N - 70°N	-16.	+1.2	+0.90	+0.22
70°N - 80°N	+3.8	-1.0	+2.3	-6.3
80°N - 90°N	n/a	-2.4	+0.83	-17.

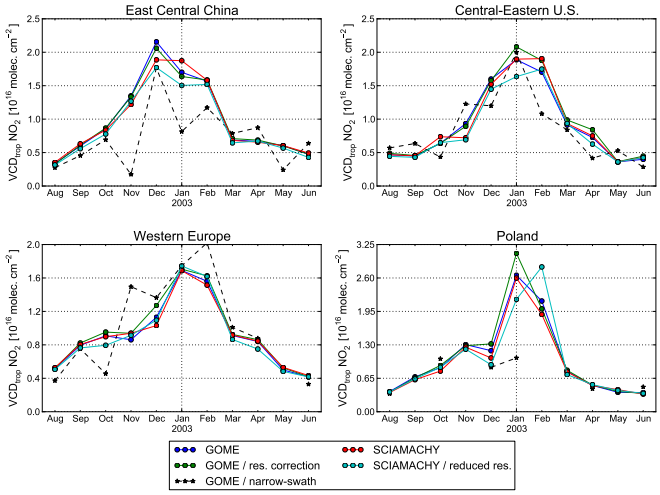

Figure 4.17: Monthly averages of VCD_{trop} NO_2 over four country to continental scale areas, for the time period August 2002 – June 2003. The regions are the same as used in Richter et al. (2005). Only those days for which both GOME and SCIAMACHY measurements for a city are available are taken into account (from Hilboll et al., 2013a).

spectra is not always equivalent to an averaging of the actual NO_2 columns, and hints towards possible non-linearities in the approach.

As this effect is most often observed for cities in desert-like areas, one could also speculate that the spectral signature of bare soil, which was shown to influence NO_2 DOAS retrievals by Richter et al. (2011), is differently captured by the GOME and SCIAMACHY instruments and thus leads to the observed over-correction. One reason for this could be the different local overpass times of the two instruments: as GOME measures approx. 30 minutes later than SCIAMACHY, the measurements are at lower solar zenith angle, which leads to differences in the upwelling radiance, possibly influencing the soil signal.

Since the resolution correction factors are calculated from the NO_2 columns measured by SCIAMACHY during the years 2003–2011, they represent the average spatial distribution of this time period. For cities

with large temporal NO_2 changes, this can potentially lead to inaccuracies when the average spatial structure of 2003–2011 is superimposed on measurements from 2002/2003 and before. Rapid changes, such as construction of new power plants, growth of cities, or implementation of NO_x reduction technologies may change the spatial pattern of NO_2 on the scales resolved by SCIAMACHY (see Sect. 4.5.4), leading to biases in the GOME resolution correction. However, analysis of annual (instead of climatologically averaged) resolution correction factors did not yield firm evidence for such systematic effects, at least not within the uncertainty of the values.

The potential influence of the difference in measurement times could in principle be investigated using GOME measurements from the instrument's narrow swath mode. In practice, the small number of such measurements and the different temporal sampling compared to normal instrument operation make an interpretation of the results very challenging.

For most investigated cities, the resolution correction factor is a valuable tool to combine NO_2 measurements from GOME and SCIAMACHY consistently, as it is able to capture the impact of the different instrumental resolutions very well. After applying it to GOME measurements, combined time series of tropospheric NO_2 columns do not show instrumental differences any more in many cases (Fig. 4.18), allowing for the first time the evaluation of long-term NO_2 trends over local hotspots. However, it has to be noted that especially over small, localized regions, the resolution correction does not work perfectly well; especially for quantitative trend analysis with corresponding error analysis, a different approach should be developed.

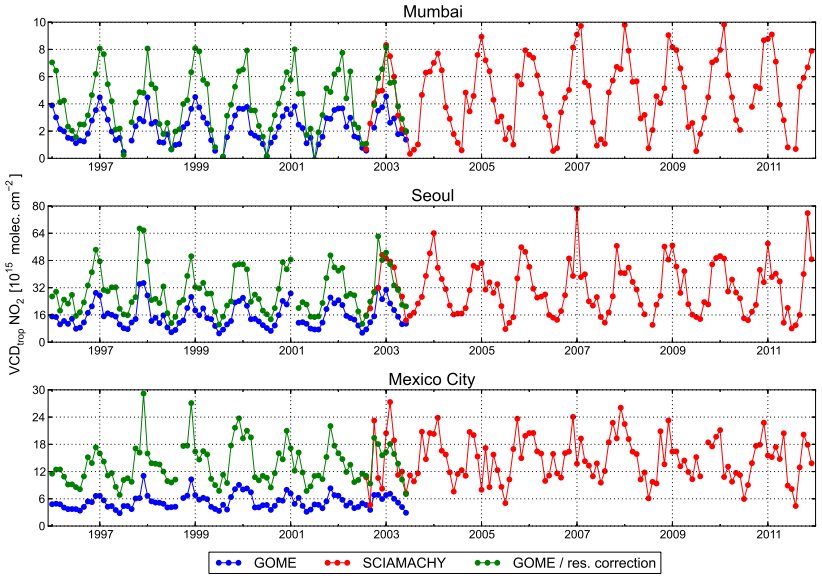

Figure 4.18: Time series of original GOME (blue), resolution-corrected GOME (green), and SCIAMACHY (red) measurements of tropospheric NO_2 for the three selected megacities Mumbai, Seoul, and Mexico City (from Hilboll et al., 2013a).

4.6 FITTING A TREND MODEL TO ACCOUNT FOR THE DIFFERENCE BETWEEN GOME AND SCIAMACHY MEASUREMENTS

4.6.1 *Method**

An alternative approach to evaluate the combined time series for temporal changes is to use a trend model which includes a parameter allowing for adjustments between the two data sets. Such an analysis is not based on modelling the physical process of spatial averaging but has the advantage of accounting also for other differences between the datasets and of providing a more rigorous error assessment. In order

*This subsection has been previously published as part of Hilboll et al. (2013a).

to account for the systematic difference between GOME and SCIAMACHY measurements, the approach proposed by Mieruch et al. (2008) for the analysis of global water vapour trends was followed. The method is based on the work of Weatherhead et al. (1998) and Tiao et al. (1990), and explicitly accounts for the instrumental difference with a levelshift parameter in the fitting procedure.

In addition to a linear change and an annual cycle in the observed NO_2 columns, the trend model explicitly accounts for a) a levelshift between the two instruments and b) for a change in the amplitude of the seasonal variation. In brief, the time series of monthly averages of NO_2 measurements $Y(t)$ is described by the equation

$$Y(t) = \mu + \omega t + \delta U(t) + S(t) + N(t) \tag{E 4.3}$$

where μ is the VCD_{trop} measurement at time $t = 0$, ω is the monthly trend component, and t is the time in months since January 1996. δ is the levelshift between GOME and SCIAMACHY measurements occurring at time $t = T_0$ (which was set to January 2003), and $U(t)$ is the step function

$$U(t) = \begin{cases} 0 & t < T_0 \\ 1 & t \geq T_0 \end{cases} \tag{E 4.4}$$

The seasonal component $S(t)$ has the same shape (represented by harmonic functions) and varying amplitude for the two instruments, and is modelled by

$$S(t) = (1 + (\gamma - 1)\, U(t)) \sum_{j=1}^{4} \left(\beta_{1,j} \sin\left(\frac{2\pi j t}{12}\right) + \beta_{2,j} \cos\left(\frac{2\pi j t}{12}\right) \right) \tag{E 4.5}$$

where the term $(\gamma - 1)U(t)$ describes the amplitude change of the seasonality component at the change between the instruments. $N(t)$, finally, is the noise component, i.e. the part of the time series which cannot be explained by the underlying model.

The trend estimator $\hat{\omega}$ is calculated in a two-step procedure: First, the noise components $N(t)$ are derived by solving Eq. 4.3 for those es-

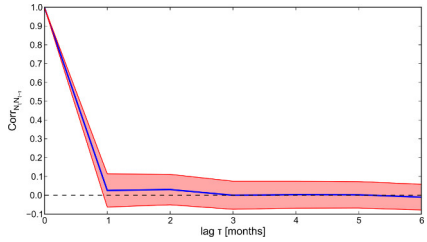

Figure 4.19: Autocorrelation coefficient of the noise process $N(t)$ (blue) with 1σ-variability (red) for all global timeseries, gridded to $0.25° \times 0.25°$.

timators $\hat{\mu}$, $\hat{\omega}$, $\hat{\delta}$, and $\hat{\gamma}$ which lead to minimal $N(t)$. After subtracting the seasonal component $S(t)$, which usually has negligible effect on the estimation of the other trend parameters (Weatherhead et al., 1998), the autocorrelations are accounted for using a linear matrix transformation. Finally, linear regression is applied to derive the estimators $\hat{\mu}$, $\hat{\omega}$, $\hat{\delta}$, and $\hat{\gamma}$ (Mieruch et al., 2008).

For the estimation of the trend error, it is assumed that the noise process $N(t)$ is AR(1), i. e., autoregressive with lag 1, an assumption which is clearly valid in the present case (see Fig. 4.19). The autocorrelation in the noise is accounted for in the error calculation as detailed in Mieruch et al. (2008). The trend is assumed to be significant if and only if

$$P_{H_0}\left(|\hat{\omega}| > 2\sigma_{\hat{\omega}}\right) = \mathrm{erf}\left(\frac{|\hat{\omega}|}{\sigma_{\hat{\omega}}\sqrt{2}}\right) > 95\% \qquad \text{(E 4.6)}$$

with

$$\mathrm{erf}(x) = \frac{2}{\sqrt{\pi}} \int_0^x e^{-t^2} dt \qquad \text{(E 4.7)}$$

being the Gauss error function.

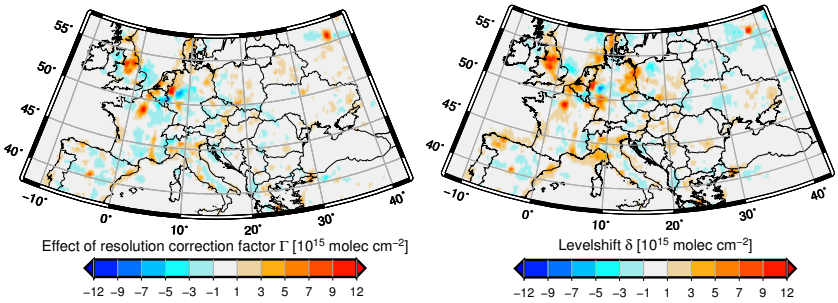

(a) Resolution correction factor Γ (b) Levelshift offset δ

Figure 4.20: Comparison of resolution correction factor and levelshift offset (from Hilboll et al., 2013a).

4.6.2 *Comparison of resolution correction factor* Γ *and levelshift parameter* δ *

As both the resolution correction factor Γ and the levelshift parameter δ are measures for how large the tropospheric NO_2 content at a given point is compared to its surrounding area, the two datasets should show large similarities. Indeed, as shown in Fig. 4.20, the maps of the respective impacts of Γ and δ are in very good agreement. For example, large urban agglomerations, such as Madrid, Paris, Moscow, and Istanbul, are clearly visible in both datasets. As the two methods are unconnected and only depend on the satellite measurements, one can conclude that both techniques are legitimate approaches to overcome the issue of varying pixel sizes when combining measurements from GOME and SCIAMACHY. However, the levelshift can also account for other, not resolution related differences between the two datasets.

If the resolution correction method described in Sect. 4.5 worked perfectly well, the application of the levelshift trend model (Eq. 4.3) to resolution-corrected GOME measurements VCD_{corr}^{GOME} and SCIAMACHY measurements VCD_{trop}^{SCIA} should yield a levelshift δ equivalent to the instrumental bias between GOME and SCIAMACHY mea-

*This subsection has been previously published as part of Hilboll et al. (2013a).

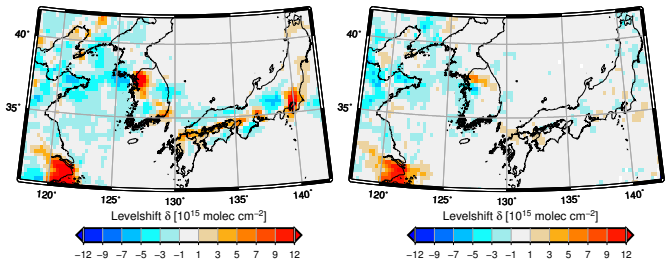

Figure 4.21: Comparison of levelshift offset δ between the original (left) and resolution-corrected (right) GOME measurements and the SCIAMACHY dataset (from Hilboll et al., 2013a).

surements, which is assumed to be negligibly small. In practice, the resolution correction only produces valid results when the actual tropospheric NO_2 column is considerably larger than the instrument's detection limit, as pointed out in Sect. 4.5.3. Figure 4.21 compares the spatial distribution of the levelshift offset δ calculated for the original and the resolution-corrected GOME datasets. As expected, the original data show a characteristic pattern of positive and negative levelshifts δ over and adjacent to pollution hot spots, respectively, along the East and South coasts of the Japanese main island Honshū and over South Korea. These patterns dissolve when the levelshift model is applied to resolution-corrected GOME measurements. However, the levelshift does not totally vanish. While over Japan and the Korean peninsula, δ is reduced significantly and close to zero in the resolution-corrected dataset, the area around Shanghai in Eastern China still shows enhanced levelshifts of $10 - 14 \times 10^{15}\,\mathrm{molec\,cm^{-2}}$, which is about 40% lower than in the original dataset. One possible explanation is the temporal changes in the spatial NO_2 patterns, which cannot be accounted for using the resolution correction factor (see Sect. 4.5.6). As it can be seen from Fig. 4.24, the largest changes in tropospheric NO_2 columns in the Shanghai area do not happen in the city itself, but rather North-West of Shanghai. Most of these changes are due to a steep increase in the years 2002–2005. This results in a decrease of the spatial NO_2 gradient over time, and consequently, the resolution correction factor

calculated from the 2003–2011 climatology is too low for the stronger spatial gradients of the 1996–2002 period. As a result, a clearly visible gap between GOME and SCIAMACHY measurements remains in the time series for Shanghai, which results in the large levelshift which can be observed.

4.6.3 *Global distribution of tropospheric* NO_2 *changes**

The levelshift model has been applied to the combined dataset of GOME (Jan 1996 – Dec 2002) and SCIAMACHY (Jan 2003 – Dec 2011) measurements. The results show strong and significant changes in tropospheric NO_2 columns for large areas in North America, Europe, the Middle East, China, Japan, and India (see Fig. 4.22). While Western countries have experienced strongly decreasing VCD_{trop} NO_2 during the past 16 years, developing countries like India, China, and in the Middle East, show strongly increasing NO_2 columns. Over the United States, large decreases can be observed for the Los Angeles metropolitan area and for large parts of the Eastern U.S. There, the areas with the largest reductions coincide with those areas already shown to be strongly affected by power plant emission reductions (see Kim et al., 2006). In the Middle East, the large increases are limited to large urban agglomerations, like the cities of Dimashq, Baghdad, Kuwait, Tehran, Isfahan, Riyadh, Jeddah, Cairo, Doha, and Dubai. For the regions defined in Fig. 4.5, the results are summarised in Tab. 4.6. All these observations are in good agreement with the general findings presented in Sect. 4.4, and are backed by Granier et al. (2011), who report according trends in NO_x emissions in all major emission inventories.

The results from the combined GOME/SCIAMACHY dataset can be compared to trends which are derived from GOME or SCIAMACHY measurements alone, as shown in Fig. 4.23. Obvious differences can be identified for North America, Europe, and China. Over the East coast of the U.S., the largest annual decreases in tropospheric NO_2 columns can be observed in the SCIAMACHY time series. In Europe, the GOME

*This subsection has been previously published as part of Hilboll et al. (2013a).

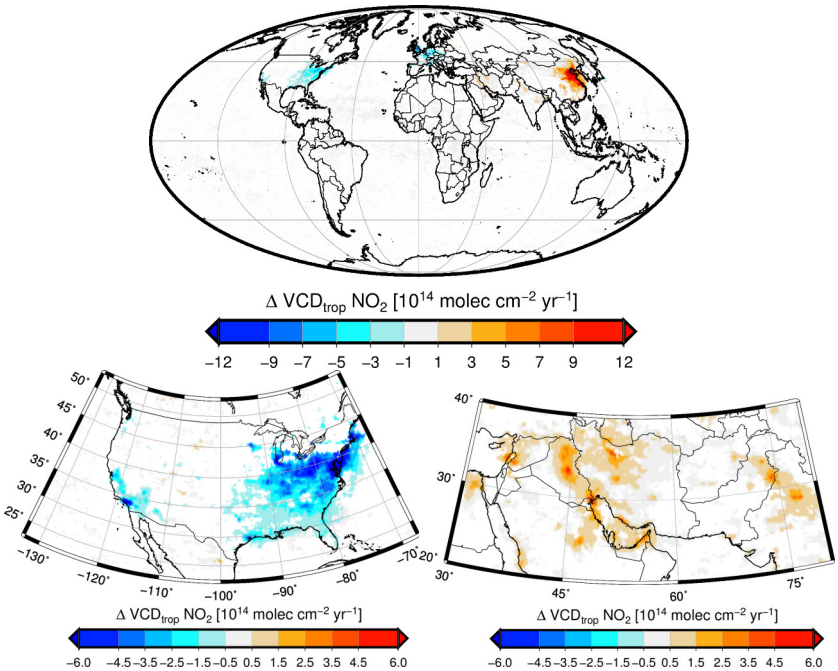

Figure 4.22: Slope ω of the linear trend component of the levelshift trend model (Eq. 4.3), applied to monthly averages of GOME and SCIAMACHY measurements from 1996–2011, gridded to 0.25°. Those grid cells where the two-sided p-value for a hypothesis test whose null hypothesis is that the slope is zero is larger than 0.05 are excluded from the plot (from Hilboll et al., 2013a).

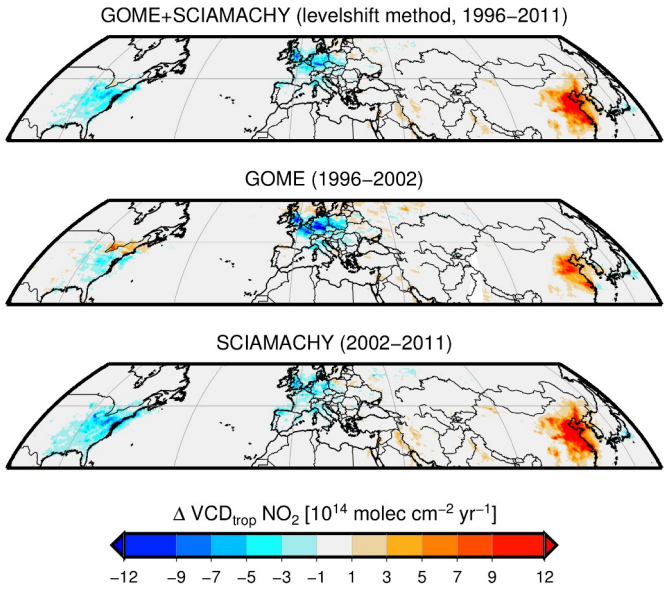

Figure 4.23: Slope ω of the seasonality model (Eq. 4.3 without the levelshift terms $\delta U(t)$ and $(\gamma - 1)U(t)$), applied to monthly averages of GOME (top) and SCIAMACHY (bottom) measurements alone. All data have been gridded to 0.25° before performing the model fit. Contrary to Fig. 4.22, insignificant trends have not been masked out (from Hilboll et al., 2013a).

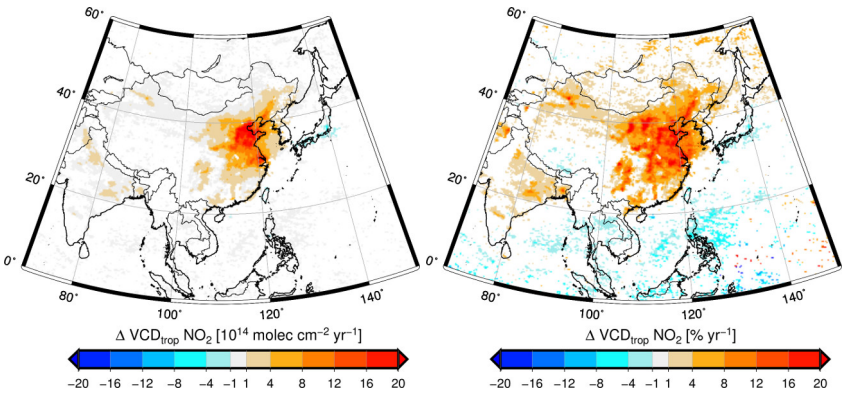

(a) absolute changes (b) relative changes (base year 1996)

Figure 4.24: Annual change in VCD_{trop} NO_2 over China derived from the levelshift trend model for the years 1996–2011. The maps show the significant values of the linear trend component ω from the levelshift model (Eq. 4.3) in absolute values (left) and relative changes (right) (from Hilboll et al., 2013a).

time series shows considerably larger decreases in VCD_{trop} NO_2 than both the SCIAMACHY and the combined time series. At the Chinese East coast, finally, the area showing large annual increases is considerably larger in the SCIAMACHY period than in the GOME time series. This observation is consistent with the observed increase in the fraction of highly polluted areas in China (see Fig. 4.7), and is backed by a comparison of absolute to relative changes, as shown in Fig. 4.24. While in the absolute changes, the well known area of East Central China shows the largest upward trend, the spatial distribution of the relative changes is more homogeneous, and the largest relative increases are actually seen at the margins of the area with highest NO_2 columns. Large annual increases of 10% and more can be observed in extended areas. Apart from the Chinese coastal area, which hosts the bulk of the nation's economic activities and is known for its high levels of air pollution, other regions show large relative trends as well. Especially in Inner Mongolia and Xingjiang, and in the Ningxia, Shaanxi, and Gansu

regions of central China, large relative growth rates in tropospheric NO_2 columns can be observed. As these areas still show relatively low VCD_{trop} NO_2, they do not stand out in the absolute annual increases. It should however be noted that especially in these regions of large economic growth, new point sources (like e.g. power plants) can be constructed, and their new emissions will show up as large non-linear relative growth rates. Another interesting aspect in Fig. 4.24 is the large increase of NO_2 over the ocean between China and Korea. This NO_2 is attributed to transport of air from the polluted regions on land and gives an idea of the impact of transport on the NO_2 fields observed in countries downwind of China. Any increases in emissions from shipping also need to be considered. It is noteworthy to also point out that the effect of transport of air pollution also limits the spatial resolution of the satellite NO_2 maps, in particular in winter.

The differences between the trends in the GOME and SCIAMACHY time periods indicates an overall problem with the assumption of linear trends in NO_x emissions and NO_2 columns. As emissions are controlled by technological, political, and economic factors, rapid, non-linear changes have to be expected. This issue has already been raised by Konovalov et al. (2010), but for most regions, the length of the time series in combination with the uncertainties of the individual values does not yet allow for reliable detection of the non-linear component of the observed changes. However, for individual time series over selected regions (i.e. Los Angeles and Athens), the non-linearity is obvious and has to be taken into account when interpreting the data.

4.6.4 VCD_{trop} NO_2 *over megacities**

The levelshift trend model enables the development of individual pollution hot spots' NO_2 abundances to be investigated. As it does not require the spatial down-sampling applied in previous studies (van der A et al., 2008; Konovalov et al., 2010), accurate estimation of the tem-

*Parts of this subsection have been previously published as part of Hilboll et al. (2013a).

Table 4.6: Annual growth rate ΔVCD_{trop} NO_2 from the levelshift model (Eq. 4.3) and the multi-instrument fit (Eq. 4.8) for the regions shown in Fig. 4.5. The relative trends have been computed relative to the 1996 annual mean.

Region	Levelshift-model (orig. GOME data)		Multi-instrument fit	
	[10^{14} molec cm^{-2} yr^{-1}]	[% yr^{-1}]	[10^{14} molec cm^{-2} yr^{-1}]	[% yr^{-1}]
Continental U.S.	-0.82 ± 0.14	-1.72 ± 0.30	-0.78 ± 0.20	-1.66 ± 0.42
Central-Eastern U.S.	-2.94 ± 0.38	-2.96 ± 0.38	-2.65 ± 0.47	-2.69 ± 0.48
Western Europe	-2.94 ± 0.63	-2.61 ± 0.56	-2.63 ± 0.85	-2.35 ± 0.76
Japan	-0.49 ± 0.13	-1.24 ± 0.33	-0.49 ± 0.17	-1.24 ± 0.42
Middle East	+0.779 ± 0.082	+4.00 ± 0.42	+0.727 ± 0.093	+3.70 ± 0.47
East Central China	+10.1 ± 1.1	+20.5 ± 2.2	+8.7 ± 1.2	+16.3 ± 2.2
North Central India	+1.30 ± 0.27	+4.05 ± 0.84	+1.05 ± 0.32	+3.23 ± 0.98

poral evolution of NO_2 pollution of localized sources becomes feasible. The trend estimates for a variety of megacities are summarized in Tab. 4.7. The strongest relative upward trends are visible over the cities of Dhaka in Bangladesh and Baghdad in Iraq, at and, respectively, which is in agreement with Schneider and van der A (2012). The apparent difference between our trend estimates and those published in Schneider and van der A (2012) can be explained with the different reference year (1996 vs. 2002).

The retrieved NO_2 trend is comparable using original and resolution-corrected GOME measurements in the levelshift fit; in virtually all cases the absolute growth rates between the two datasets agree within the assumed uncertainty (see Tab. 4.7). The respective relative trends, however, differ considerably, mainly because the data in the reference year 1996 are systematically higher in the resolution-corrected GOME than in the original dataset. Exemplary, time series for New York, Tehran, Mumbai, and Beijing are shown in Figure 4.25.

For all four cities, the gridded VCD_{trop} NO_2 (on a $\frac{1}{16}^\circ \times \frac{1}{16}^\circ$ grid) have been averaged over an area of $1.0^\circ \times 0.5^\circ$ ($1.0^\circ \times 0.75^\circ$ in the case of Mumbai). In all cases, it is clearly visible that a) there are significant differences between GOME and SCIAMACHY measurements which must not be ignored, and that b) these differences are being addressed by the levelshift method very well. New York shows a strongly decreas-

Table 4.7: Annual growth rate ΔVCD_{trop} NO_2 from the levelshift model (Eq. 4.3) and the multi-instrument fit (Eq. 4.8) for a list of megacities. The relative trends have been computed relative to the 1996 annual mean. Non-significant trends (see Eq. 4.6) are shown *in italics*.

City	Levelshift-model (orig. GOME data)		Multi-instrument fit	
	[10^{14} molec cm^{-2} yr^{-1}]	[% yr^{-1}]	[10^{14} molec cm^{-2} yr^{-1}]	[% yr^{-1}]
Algiers	+0.74 ± 0.14	+3.64±0.69	+0.60 ± 0.18	+2.89 ± 0.88
Athens	-2.33 ± 0.70	-4.1±1.2	-2.09 ± 0.83	-3.7 ± 1.5
Baghdad	+3.54 ± 0.33	+20.7±1.9	+3.24 ± 0.37	+18.0 ± 2.1
Beijing	+8.8 ± 2.5	+6.7±1.9	+9.5 ± 2.9	+7.3 ± 2.2
Buenos Aires	+1.14 ± 0.48	+3.9±1.6	*+0.55 ± 0.51*	*+1.7 ± 1.6*
Cairo	+1.91 ± 0.25	+7.21±0.93	+1.73 ± 0.28	+6.4 ± 1.0
Chicago	-6.7 ± 1.8	-4.1±1.1	-6.2 ± 2.2	-3.9 ± 1.4
Dhaka	+3.66 ± 0.52	+27.2±3.9	+3.41 ± 0.54	+24.0 ± 3.8
Dimashq	+3.44 ± 0.54	+10.2±1.6	+2.62 ± 0.53	+7.2 ± 1.4
Guangzhou	*+1.2 ± 2.0*	*1.3±2.0*	*+0.2 ± 2.6*	*+0.2 ± 2.6*
Hong Kong	*-2.6 ± 1.8*	*-2.3±1.6*	*-1.1 ± 2.3*	*-1.0 ± 2.1*
Istanbul	*-0.5 ± 1.1*	*-0.7±1.5*	*-0.4 ± 1.1*	*-0.5 ± 1.5*
Jakarta	-1.45 ± 0.42	-3.9±1.1	-1.19 ± 0.41	3.3 ± 1.1
Jeddah	+1.30 ± 0.29	+4.07±0.92	+1.4 2± 0.36	+4.5 ± 1.2
Karachi	+0.94 ± 0.22	+6.8±1.6	+0.85 ± 0.25	+6.0 ± 1.8
Kolkata	+0.75 ± 0.22	+2.98±0.89	+0.80 ± 0.26	+3.2 ± 1.0
Lagos	+0.41 ± 0.10	+3.41±0.83	+0.33 ± 0.12	+2.68 ± 0.95
Lima	+0.99 ± 0.40	+7.1±2.9	+1.06 ± 0.36	+7.9 ± 2.7
London	-4.4 ± 1.3	-2.40±0.71	*-3.0 ± 1.6*	*-1.66 ± 0.91*
Los Angeles	-13.7 ± 1.7	-6.00±0.72	-13.2 ± 2.6	-5.8 ± 1.2
Manila	-1.13 ± 0.18	-5.32±0.85	-1.03 ± 0.20	-4.93 ± 0.95
Mexico City	*-0.65 ± 0.83*	*-1.2± 1.5*	*+0.51 ± 0.82*	*+1.0 ± 1.6*
Moscow	*-0.2 ± 1.5*	*-0.3± 1.9*	*-1.4 ± 1.6*	*-1.6 ± 1.9*
Mumbai	+0.82 ± 0.17	4.31±0.91	+0.70 ± 0.21	+3.6 ± 1.1
New Delhi	+3.07 ± 0.53	+9.3±1.6	+2.57 ± 0.60	+7.4 ± 1.7
New York	-5.3 ± 1.7	-2.45±0.80	-5.7 ± 2.3	-2.6 ± 1.0
Osaka	-1.94 ± 0.98	-1.74±0.88	-2.54 ± 0.98	-2.23 ± 0.86
Paris	-4.6 ± 2.0	-3.0±1.3	*-5.2 ± 2.5*	*-3.3 ± 1.6*
Riyadh	+2.01 ± 0.39	+6.7±1.3	+2.05 ± 0.38	+6.9 ± 1.3
São Paolo	*+0.52 ± 0.46*	*-1.3± 1.2*	*+0.37 ± 0.52*	*+0.9 ± 1.3*
Seoul	*+0.6± 1.7*	*0.4± 1.1*	*+1.0 ± 1.8*	*+0.7 ± 1.2*
Shanghai	+11.9 ± 3.1	+12.8±3.3	+9.4 ± 3.0	+9.2 ± 2.9
Shenzhen	*-2.4 ± 1.6*	*-1.9± 1.3*	*-2.2 ± 1.7*	*-1.8 ± 1.3*
Tehran	+2.08 ± 0.68	+5.7±1.9	+2.68 ± 0.93	+7.8 ± 2.7
Tokyo	-5.2 ± 1.1	-3.61±0.79	-5.4 ± 1.4	-3.77 ± 0.97

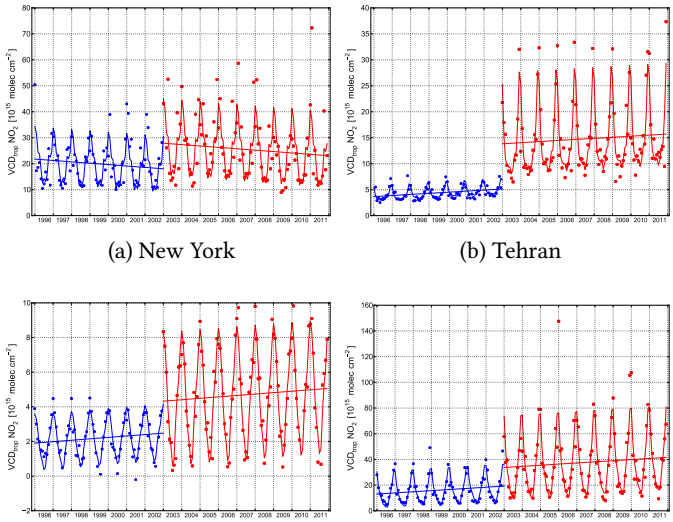

(a) New York (b) Tehran

(c) Mumbai (d) Beijing

Figure 4.25: Time series of monthly VCD_{trop} NO_2 (dots), fitted levelshift trend model (thick line), and linear component of the fit (straight line) for the time periods 1996–2002 (GOME, blue) and 2003–2011 (SCIAMACHY, red) (from Hilboll et al., 2013a).

ing trend of $-5.3 \pm 1.7 \times 10^{14}$ molec cm^{-2} yr^{-1}. This is considerably stronger than the $-0.3 \pm 1.7 \times 10^{14}$ molec cm^{-2} yr^{-1} reported for the 1996–2006 time period by van der A et al. (2008). However, one has to note the differences, namely that our study period is five years longer, and that van der A et al. did not account for instrumental differences between GOME and SCIAMACHY measurements. Figure 4.25 shows that VCD_{trop} measured by SCIAMACHY are significantly higher than those retrieved from GOME measurements, which leads to an underestimation of a downward trend if not accounted for. Tehran, Mumbai, and Beijing all show very pronounced upward trends of $+2.1 \pm 0.68 \times 10^{14}$, $+8.2 \pm 1.7 \times 10^{14}$, and $+8.8 \pm 2.5 \times 10^{14}$ molec cm^{-2} yr^{-1}, respectively. These results compare well to those reported by van der A et al. (2008), who quote $+2.6 \pm 0.5 \times 10^{14}$, $+7 \pm 3 \times 10^{13}$, and $+12 \pm 2.9 \times 10^{14}$ molec cm^{-2} yr^{-1}. When repeated for the 1996–2006

period, the results of the trend calculation become similar to those by van der A et al. (2008) both in magnitude an in uncertainty (see Table B.5). Here, I derive trends of $+1.9 \pm 0.82 \times 10^{14}$ molec cm^{-2} yr^{-1} and $+8.8 \pm 3.6 \times 10^{14}$ molec cm^{-2} yr^{-1}, for Tehran and Beijing, respectively. The larger trends by van der A et al. might partly be caused by them not accounting for the offset between GOME and SCIAMACHY measurements, as the jump in NO_2 values between the two instruments biases a standard trend model towards higher growth rates. Generally, one can observe a convincing reduction of the trend uncertainties by using our levelshift model, as compared to the estimates presented in van der A et al. (2008), which leads to significant trends in most of the regions considered in this study. However, this reduction in uncertainty is mostly due to the longer study period.

Comparing the trend results from the two study periods 1996–2006 and 1996–2011 further illustrates that, e. g., the North American megacities New York City and Los Angeles show very pronounced downward NO_2 trends in the longer period, while the trend analysis does not yield any significant trends for 1996-2006 alone. This is due to an interplay between changes in economic activity, emission control measures, and nonlinear chemistry, which can lead to non-linear NO_2 changes, as already observed by Russell et al. (2012).

In China, it is interesting to note that the cities in the Pearl River Delta (Guangzhou, Shenzhen, and Hong Kong) do not show significant trends. While this might be expected in Hong Kong, which industrialised earlier and has an advanced level of economic development, it seems surprising that NO_2 pollution in Shenzhen, whose population has more than doubled since 1995 (O'Donnell, 2011), has not increased. However, the regional government of Hong Kong has established effective vehicle emission control measures during the 2000s, leading to a significant decrease of 28% in roadside NO_x concentrations between 1999 and 2011, with concentrations slowly starting to increase again since 2009 (Air Science Group, Environmental Protection Department, The Government of Hong Kong Special Administrative Region, 2012). Furthermore, the regional governments of Hong Kong and the Guangdong province have in 2003 agreed on the Pearl River Delta Re-

gional Air Quality Management Plan (Environmental Protection Department, The Government of the Hong Kong Special Administrative Region‘, 2004), which seems to have considerably slowed the increase of air pollutant emissions (Environmental Protection Department, The Government of the Hong Kong Special Administrative Region‘, 2012), effectively counteracting the huge increase in population and industrial activity.

4.7 COMBINING ALL FOUR INSTRUMENTS INTO A LEVELSHIFT-LIKE TREND MODEL*

As measurements of tropospheric NO_2 from different satellite instruments are becoming available, it is necessary to find ways to analyse these data in an integrated consistent and consolidated manner. The levelshift model presented in Sect. 4.6 has the limitation that it can only account for one measurement per time step. Therefore, the method was evolved to be able to use measurements from all four available instruments by developing a non-linear trend model accounting for the differences in the measured VCD_{trop} from GOME, SCIAMACHY, OMI, and GOME-2 (Hilboll et al., 2013b).

4.7.1 *Method description***

The time series $Y(t,i)$ of average NO_2 measurements made by instrument i in month t is modeled as

$$\begin{aligned} Y(t,i) &= \mu_i + \omega t + \eta_i \times S(t) + N(t,i) \qquad \text{(E 4.8)} \\ S(t) &= \sum_{j=1}^{4} \left(\beta_{1,j} \sin\left(\frac{2\pi j t}{12}\right) + \beta_{2,j} \cos\left(\frac{2\pi j t}{12}\right) \right). \end{aligned}$$

ω is the linear trend component, which is assumed to be common among all four instruments. μ_i are the offsets of the linear trend per

*This section has been previously published as part of Hilboll et al. (2013a).

**This subsection has been previously published as part of Hilboll et al. (2013a).

instrument, and η_i gives the relative amplitude of the seasonality component (with $\eta_1 \equiv 1$). The optimal trend estimators $(\hat{\omega}, \ldots)$ are then calculated by minimizing the sum of the squared noise components $N(t,i)$, applying weights to the individual monthly averages $Y(t,i)$ to account for the varying number of instruments providing $\mathrm{VCD}_{\mathrm{trop}}$ at time t.

4.7.2 *Error analysis**

As the multi-instrument trend model allows more than one measurement at each point in time, an analytical derivation of the resulting uncertainties is not easily possible. Therefore, the uncertainties of the trend estimators have been calculated using the bootstrap technique (Efron and Tibshirani, 1993). The main idea of the bootstrap is to randomly reorder the random parts of the data (the whole right-hand side of Eq. 4.8 apart from the term $N(t,i)$) and repeat the model fit with these resampled data to yield a replication of the trend estimators $(\hat{\omega}, \ldots)$. This process is repeated a large number of times, and then the standard error of the trend estimators can be derived from the distributions of the replications.

To apply the bootstrap technique to Eq. 4.8, the trend model is first solved for the set of optimal estimators $(\hat{\omega}, \ldots)$. Then it is necessary to create a timeseries of the total residuals,

$$\left\{\tilde{N}(t)\right\}_{t=1}^{n} = \left\{\sum_i \frac{1}{m(t)} N(t,i)\right\}_{t=1}^{n},$$

where $m(t)$ is the number of measurements at time t. Since the NO_2 timeseries show a seasonal cycle, the resampling must try to preserve this temporal autocorrelation. Here, the nonparametric moving block bootstrap (MBB) algorithm is used (Mudelsee, 2010): The timeseries of residuals $\left\{\tilde{N}(t)\right\}_{t=1}^{n}$is cut into $n - l + 1$ consecutive blocks of length l, which are allowed to overlap. The block length l has been calculated

*Parts of this subsection have been previously published as part of Hilboll et al.

using the algorithm by Bühlmann and Künsch (1999), which is driven purely by the data. The MBB algorithm randomly draws (with replacement) $\lceil \frac{n}{l} \rceil$ blocks and concatenates them to form a new resampled timeseries $\left\{ \tilde{N}(t^{*b})_{t^*=1}^{n} \right\}$. From these resampled total residuals, a new series of residuals $\tilde{N}(t^{*b}, i)$ is constructed by drawing $m(t)$ random numbers from a normal distribution with mean $\tilde{N}(t^*)$ and standard variation Σ, where Σ is the standard deviation of all $N(t, i)$.

A new timeseries of measurements $\tilde{Y}(t, i)$ is then calculated from the trend estimators $(\hat{\omega}, \ldots)$ and the resampled residuals $\tilde{N}(t^*, i)$. The trend model is then fitted to these resampled timeseries $\tilde{Y}(t, i)$ to yield a replication of the trend estimators $\hat{\theta}^{*b} = (\hat{\omega}^{*b}, \ldots)$.

These steps (the resampling of the residuals and the calculation of the resulting replications of the trend estimators) is repeated B times. In this study, $B = 2000$ was used as this number of replications has shown to be large enough yield reasonably consistent results (Efron and Tibshirani, 1993; Mudelsee and Alkio, 2007; Mudelsee, 2010). The bootstrap standard error of the trend estimators is then calculated, following Mudelsee (2010), by

$$\hat{se}_{\hat{\theta}^*} = \sqrt{\sum_{b=1}^{B} \frac{\left(\theta^{*\hat{b}} - \left\langle \hat{\theta}^{*b} \right\rangle \right)^2}{B-1}}. \tag{E 4.9}$$

For determining the significance of the retrieved trends, confidence intervals for the trend estimators $\hat{\theta}$ have been calculated. To take into account possible biases and scale effects, bootstrap bias-corrected and accelerated (BCa) confidence intervals at the 95% are used (Efron and Tibshirani, 1993; Mudelsee, 2010). They are defined as

$$CI_{\hat{\theta},1-2\alpha} = \left[\hat{\theta}^*(\alpha 1); \hat{\theta}^*(\alpha 2) \right], \tag{E 4.10}$$

where the notation $\hat{\theta}^*(x)$ signifies the value of the $\hat{\theta}^*$ distribution at the percentile x. The percentiles $\alpha 1$ and $\alpha 2$ are defined, using the standard normal distribution function

$$F(x) = \int_{-\infty}^{x} f(x')dx',$$

(2013a).

by

$$\alpha 1 = F\left(\hat{z}_0 + \frac{\hat{z}_0 + z(\alpha)}{1 - \hat{a}(\hat{z}_0 + z(\alpha)}\right)$$

and

$$\alpha 2 = F\left(\hat{z}_0 + \frac{\hat{z}_0 + z(1-\alpha)}{1 - \hat{a}(\hat{z}_0 + z(1-\alpha)}\right).$$

With $\hat{z}_0 = \hat{a} = 0$, this definition yields $\alpha 1 = \alpha$ and $\alpha 2 = 1 - \alpha$ and leads to the usual confidence interval. The correction for the median estimation bias, $\hat{z}_0$, is defined by

$$\hat{z}_0 = F^{-1}\left(\frac{\#\left(\hat{\theta}^{*b} < \hat{\theta}\right)}{B}\right).$$

The acceleration $\hat{a}$ measures the rate of change of the standard error of $\hat{\theta}$ with respect to the true parameter value θ, and takes possible scale effects into account. It is defined as

$$\hat{a} = \frac{\sum_{j=1}^{n}\left(\left\langle\hat{\theta}_{(j)}\right\rangle - \hat{\theta}_{(j)}\right)^3}{6\sqrt{\sum_{j=1}^{n}\left(\left\langle\hat{\theta}_{(j)}\right\rangle - \hat{\theta}_{(j)}\right)^2}^3}.$$

$\hat{\theta}_{(j)}$, the jackknife value of $\hat{\theta}$, is defined as the estimator $\hat{\theta}$ which is computed from a sample of reduced size where the jth value has been removed . A trend estimator $\hat{\theta}$ is then considered significant if and only if the value 0 lies outside the BCa confidence interval $CI_{\hat{\theta},1-2\alpha}$. As an example, the distribution of the replications $\hat{\omega}$ for the NO_2 measurements over Istanbul, Tehran, and Tokyo are shown in Fig. 4.26. It is clearly visible that even in cases when the different methods of trend analysis do not yield significant results, the trend estimator $\hat{\omega}$ almost perfectly coincides with the mean of the bootstrap distribution, indicating that the chosen method to estimate the uncertainties is well suited to the task.

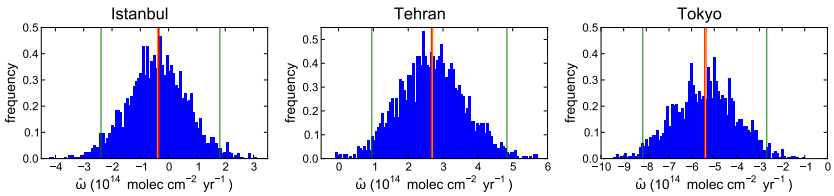

Figure 4.26: Distribution of the $B = 2000$ replications of the estimator for the linear trend component, $\hat{\omega}$, for Istanbul, Tehran, and Tokyo. The 'true' trend estimator $\hat{\omega}$ is marked in red. Then mean of the replications is marked in orange, and the edges of the BCa confidence interval are marked in green.

4.7.3 *Results and discussion**

As is apparent from Tabs. 4.6 and 4.7, the linear trend estimates $\hat{\omega}$ from the multi-instrument fit generally agree very well with those derived from the levelshift model.

Many regions do not show large differences between the instruments (e.g. New Delhi), while in other regions, these differences are strongly pronounced, as in Tehran (see Fig. 4.27). Reasons for this include differing spatial distributions of both the NO_2 columns themselves and other factors influencing the NO_2 retrieval, as e.g. aerosol load, surface altitude, and surface spectral reflectance. All these quantities influence the retrieved NO_2 columns, as the differing spatial resolutions of the satellite measurements lead to instrument-dependent spatial sampling, which in turn has a significant effect on the observed NO_2 amounts or levels and their seasonality. A further issue is the different local times of the satellite measurements. As OMI measures in the early afternoon, diurnal cycles of NO_2 (which can lead to large differences between morning and noon, see, e. g., Huijnen et al., 2010) and aerosols, as well as the different angular sampling of spectral surface reflectance, can lead to offsets between the instruments.

This can result in varying ground amounts of retrieved NO_2 columns and varying seasonal cycles between the four instruments. For

*This subsection has been previously published as part of Hilboll et al. (2013a).

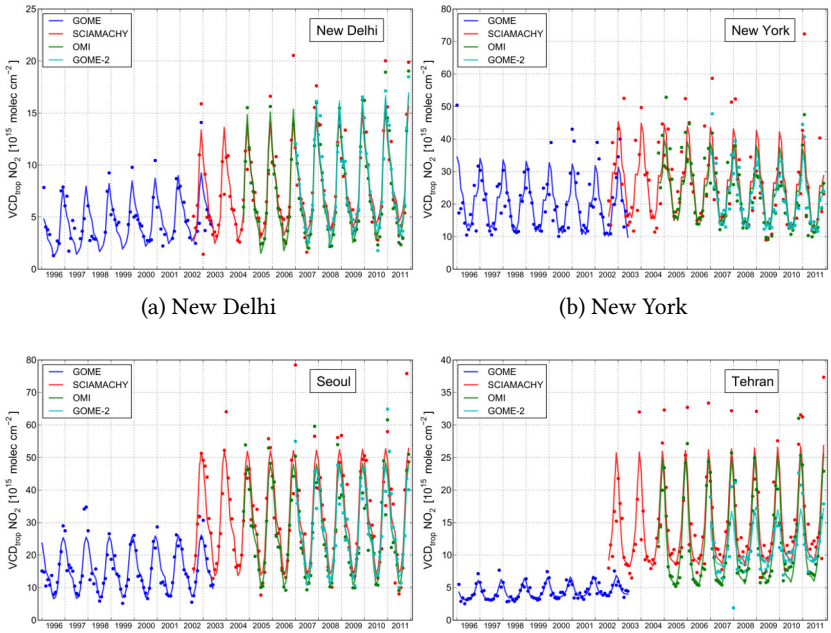

(a) New Delhi (b) New York

(c) Seoul (d) Tehran

Figure 4.27: Measured monthly average VCD_{trop} NO_2 (dots) and fitted trend function from the multi-instrument trend model (lines) for the four instruments GOME (blue), SCIAMACHY (red), OMI (green), and GOME-2 (cyan) (from Hilboll et al., 2013a).

large ground scenes, the NO_2 columns will be more inhomogeneous than in small ones, leading to a stronger smearing of the high pollution peaks of e.g. megacities. This is shown exemplarily for the three cities New Delhi, New York, and Tehran, using topography (Hastings et al., 1998), population density (Center for International Earth Science Information Network, Columbia University et al., 2011), and NO_x emission (European Commission, Joint Research Centre and Netherlands Environmental Assessment Agency, 2011) data (see Fig. 4.28). In New Delhi, which lies in a topographically flat region with homogeneously high population density and NO_x emissions, virtually no difference between the four instruments can be observed. Under these

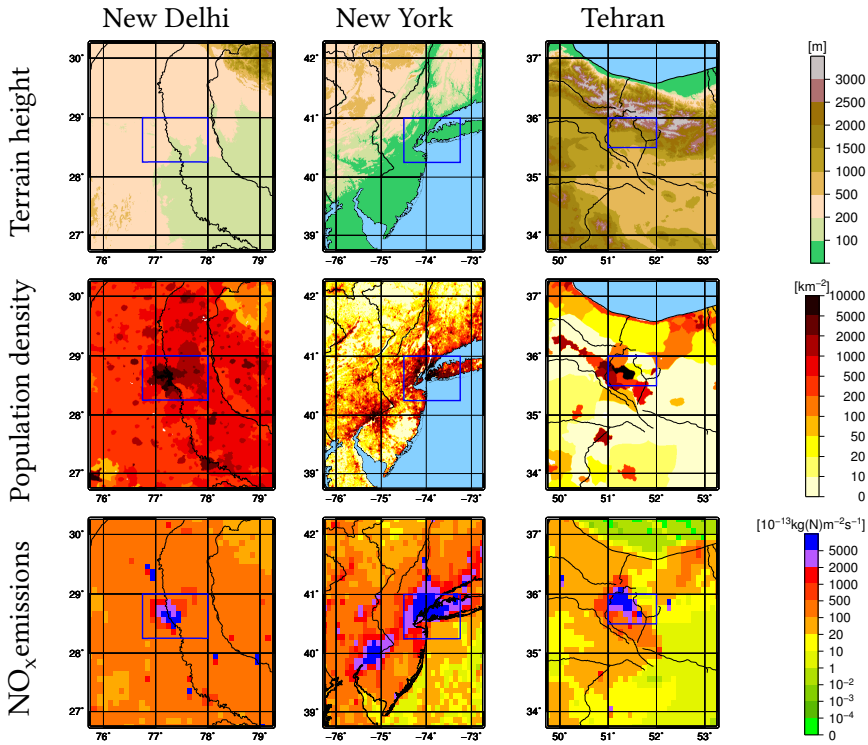

Figure 4.28: Topography, population density, and NO_x emissions for the three selected megacity regions New Delhi (India), New York (United States), and Tehran (Iran). Topographic data is from the GLOBE project (Hastings et al., 1998), population density data from the GRUMP dataset (Center for International Earth Science Information Network, Columbia University et al., 2011), and NO_x emission values are from the EDGAR database (European Commission, Joint Research Centre and Netherlands Environmental Assessment Agency, 2011) (from Hilboll et al., 2013a).

conditions, NO_2 can spread without barriers. The area around New York City is also topographically flat, but the NO_x emissions are mostly constrained to land, with the exception of shipping routes and aircraft corridors, land being only $\frac{2}{3}$ of the whole area. This leads to inhomogeneities in the observed region, as emissions only happen in part of the area, while the rest only shows the effect of transported NO_x. This NO_2 gradient between megacity and open ocean leads to the noticeable impact of the instruments' pixel size on retrieved VCD_{trop} values. In the case of Tehran, emissions are mostly confined to the city's boundaries. Moreover, the emitted NO_2 cannot spread evenly throughout the area, because Tehran is bordered by the Alborz mountain range towards the North and East, leading to inhomogeneous NO_2 pollution in the observed area and thus to lower NO_2 columns in the case of large pixel sizes. Therefore, the NO_2 time series over Tehran show a very strong dependence on the instrument's spatial resolution.

The multi-instrument trend model presented in this section has the advantage of being suitable for the later inclusion of measurements from future satellite instruments. Under the assumption that the growth rate of the linear trend component is constant among all instruments, the model is therefore an excellent tool to assess the temporal evolution of the measured quantity. In the trend calculation, each month has the same weight, while at the same time a maximum of the available measurement data is included in the fitting procedure, and instrumental differences are accounted for to some extent.

4.7.4 *Extensions to the multi-instrument trend model**

As a result of the multitude of factors contributing to the magnitude and changes in tropospheric NO_2 column densities, it is well possible that change rates are not constant throughout the seasons. An example are changes in the relative importance of emission sources with large seasonality (heating) and others which are rather constant (transportation). One way to account for this is to link temporal changes to the

*This subsection has been previously published as part of Hilboll et al. (2013a).

amplitude of the seasonality component of Eq. 4.8. The effect of such a model extension requires the introduction of a parameter ξ representing the rate of change of the seasonality component:

$$\begin{aligned} Y_i(t,i) &= \mu_i + \omega t + (1+\xi t) \times \eta_i \times S(t) + N(t,i) \quad \text{(E 4.11)} \\ S(t) &= \sum_{j=1}^{4} \left(\beta_{1,j} \sin\left(\frac{2\pi j t}{12}\right) + \beta_{2,j} \cos\left(\frac{2\pi j t}{12}\right) \right) \end{aligned}$$

The resulting trend estimators are shown in Tables B.3 and B.6. The trend estimator $\hat{\omega}$ is found to be of smaller magnitude than when the seasonality is kept at a fixed amplitude. The increasing (decreasing) NO_2 values are partly absorbed by a changing amplitude of the seasonality signal, which in turn leads to lower linear trend estimators $\hat{\omega}$.

In virtually all cases the signs of the linear and harmonic trend estimators $\hat{\omega}$ and $\hat{\xi}$ coincide. The observed magnitude of $\hat{\xi}$ however varies widely, depending on the region of interest. While for many regions the two estimators are similar in (relative) magnitude (e.g. Beijing, Hong Kong, New York, Po Valley), often the harmonic component $\hat{\xi}$ is significantly larger than $\hat{\omega}$, as e.g., in Athens, Baghdad, Barcelona, and Cairo. As summer NO_2 values often show slower rates of change than winter values, this is averaged out when assessing the linear growth rates. The seasonal cycle however is strengthened by this effect, as the difference between summer and winter values becomes larger. Both methods, treating the increase in the amplitude of the seasonal cycle separately from the general NO_2 column increase and including both into one change rate, work well; the choice which trend model to use thus depends on the research question to be asked.

In a further step, the trend model should be extended to account for the different noise levels of the individual instruments' time series. This is common in climate time series analysis (see Mudelsee (2010) and assures that instruments with more stable measurements have more weight in the fitting process. Usually, this is achieved by minimizing the variability-weighted squared noise components $\frac{N(t,i)}{S(i)}$ where $S(i)$

denotes the standard deviation of all measurements of instrument i. In practice, this common correction leads to a slight reduction of the retrieved linear trend estimates for many regions. As a result of the relatively high variability of SCIAMACHY measurements (when compared to OMI and GOME-2, mostly caused by the significantly lower spatial and temporal coverage), the instrument has lower relative weight in the trend calculation. Since most regions show the strongest relative NO_2 changes for SCIAMACHY observations (see e.g. Fig. 4.9), the instrument's lower relative weight thus leads to a slight reduction of the calculated trend estimates. For the results shown in Tabs. 4.6 and 4.7, this correction was not applied so as to make the results more comparable to those retrieved from the resolution correction factor and levelshift methods.

4.8 INVESTIGATING NON-LINEAR TROPOSPHERIC NO_2 CHANGES

Tropospheric NO_2 concentrations depend mainly on anthropogenic use of fossil fuels, on meteorological conditions, and on the availability of sunlight for photochemical reactions. While this generally leads to a clear seasonal cycle, the first two sources can vary independently, which can lead to irregularities in the observed annual cycle. In a study of megacity NO_2 pollution, anthropogenic emissions obviously play the dominant role. For time series as short as the available time span of satellite measurements of tropospheric NO_2, linearly fitting the data most commonly yields a reasonable picture of the underlying interannual changes. However, as anthropogenic emissions are strongly dependent on economic development and also on meteorological conditions (e. g., heating emissions for a specific region are almost fully determined by winter temperatures), the actual NO_2 concentrations might not be strictly following a linear pattern. Moreover, Voulgarakis et al. (2010) have pointed out that meteorological variability also plays a major role for tropospheric NO_2 year-to-year variability, possibly through one or more of the factors lightning activity, humidity, cloud optical depth, and transport processes. This further reduces the probability of a strictly linear evolution of tropospheric columns, especially

as the available time series become even longer. An additional point is that economic growth, which at least in developing economies can be considered as a good approximation of the changes in air pollutant emissions, is often exponential; e. g., China has seen an average GDP increase of 9.7% annually from 1996–2012 (International Monetary Fund, 2012).

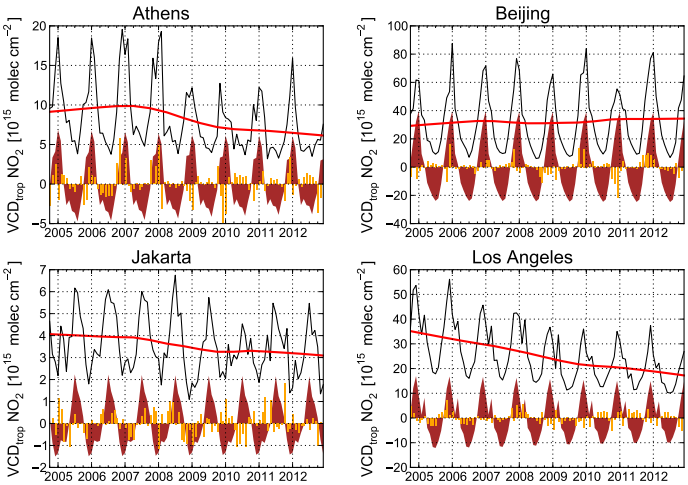

Figure 4.29: STL decomposition of NO_2 time series over Athens, Beijing, Jakarta, and Los Angeles, as retrieved from the OMI instrument. The actual measurements of VCD_{trop} NO_2 are shown as black lines. A seasonal trend decomposition has been performed, using the seasonality and smoothing parameters $s = 13$ and $t = 51$, respectively (see Cleveland et al., 1990). The trend, seasonality, and residual components is marked in red, brown, and orange, respectively.

Unfortunately, there is no common, general standard methodology for the analysis of non-linear changes in time series. The choice of non-linear regression method strongly depends on the observed and expected patterns in the underlying data. It is thus helpful to investigate the data by the naked eye. In the case of tropospheric NO_2 time series, this is complicated by an often strong seasonal cycle, which can conceal non-linear changes. Non-parametric decomposition of the time

series can be one method to overcome this issue. One such method is the 'Seasonal-Trend decomposition based on LOESS (STL)' (Cleveland et al., 1990), which is a local regression method being applied to smoothed subsets of the time series. Exemplary, the decompositions is shown for four megacities in Fig. 4.29. The clearly non-linear nature of the trend component shows the shortcomings of assuming a linearly changing NO_2 column over the full study period.

Among the easiest non-linear regression models are piecewise linear models, like a 'ramp' or 'break-point' (Mudelsee, 2010; Reinsel et al., 2005; Vyushin et al., 2007). Spectral analysis provides a more elaborate analysis of non-linear changes (Moore et al., 2005; Mudelsee, 2010, and references therein); however, spectral methods cannot be applied in the context of this study, as the available time series of tropospheric NO_2 columns is too short (Konovalov et al., 2010). As an example for non-linear regression analysis, Fig. 4.30 shows break-point regressions for six megacity regions, derived from SCIAMACHY measurements. The measured NO_2 columns are fitted against the trend model defined by

$$Y_{break}(T) = \begin{cases} x_1 + (t - t_1)\,(y_2 - y) \,/\, (t_2 - t_1) & t \leq t_2 \\ x_2 + (t - t_2)\,(y_3 - y_2) \,/\, (t_3 - t_2) & t > t_2 \end{cases} \tag{E 4.12}$$

Here, y_1, y_2, and y_3 mean the NO_2 columns at times t_1, t_2, and t_3, respectively. t_1 and t_3 are the beginning and the end of the NO_2 time series, and t_2 is the break-point. The time steps have been weighted with the variability of the measurements S(t), which is defined as $S(t) = \sigma\left(Y(t')\Big|_{m(t')=m(t)}\right)$, where σ denotes the standard deviation, and $m(t)$ means the month of time step t. The weighting somewhat reduces the influence of the seasonal cycle on the regression results. Considering the seasonality in the break-point regression has not yet been established in the statistical literature.[1] The parameters y_1, y_2, y_3, and t_2 have been calculated by minimizing the weighted sum of squared

[1] Reinsel et al. (2002) have explicitly accounted for the seasonal cycle using a similar methodology as Weatherhead et al. (1998); however, Reinsel et al. (2002) did not include the time t_2 of the break-point in the model but instead defined t_2 a-priori.

residuals using the L-BFGS-B algorithm (Byrd et al., 1995, in the implementation from Zhu et al., 1997, used via Jones et al., 2001).

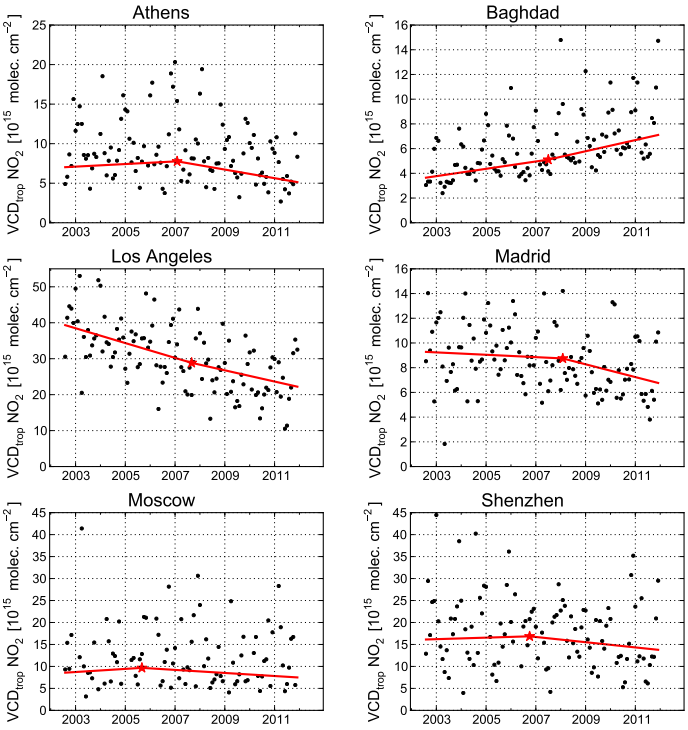

Figure 4.30: Break-point regression of NO_2 time series over Athens, Baghdad, Los Angeles, Madrid, Moscow, and Shenzhen, derived from SCIAMACHY measurements. The actual measurements of VCD_{trop} NO_2 are shown as black dots. The piecewise linear fits are shown in red lines, whereas the break-point is marked as red star.

Athens shows increasing NO_2 columns until the beginning of 2007, reflecting the considerable economic growth seen in most East-Mediterranean cities. In more recent years, however, the effects of the economic crisis show clearly (see Vrekoussis et al., 2013). The situation is similar in the case of Madrid, where a slight decrease in NO_2 columns until the beginning of 2008, owed mostly to emission reduction measures, strongly intensifies after that, also caused by the economic crisis.

In Baghdad, where NO_2 columns have more than doubled in the past 10 years, the rate of change has increased; the break-point has been detected by the regression in Spring 2008. The cities Shenzhen and Hong Kong (not shown), both located in the Pearl River Delta of South-East China, show a break-point in the winter 2006/2007, when NO_2 trends become more negative. This is in line with the air quality measures introduced by local authorities since the year 2000, as discussed in Sect. 4.6.4. In Moscow, the regression finds a breakpoint in late 2005, when the NO_2 trend changes from positive to negative. This is in line with Sitnov (2010), who report a trend change in spring 2006. Los Angeles, finally, shows a continuous decrease in NO_2 columns, but the decrease slowed down after mid-2007. This can probably be attributed to a lessening influence of air quality legislation as the implemented emission reduction technology becomes more and more efficient (Russell et al., 2012).

The only quantitative study of non-linear changes in tropospheric NO_2 columns has been performed by Konovalov et al. (2010) and Russell et al. (2012). Konovalov et al. (2010) investigated GOME and SCIAMACHY measurements of the 1996–2008 time period. They based their analysis on using an artificial neural network for approximating non-linear changes, employing a probabilistic Bayesian approach for constraining the optimal fit and estimating the random fluctuations in the measured data (Konovalov et al., 2010). In spite of the complexity of their methodology, the algorithm was only able to detect significant non-linear trends in five of the 12 investigated megacity regions, namely in Baghdad, Madrid, Milan, Moscow, and Paris—even though they used gridded data at $1^\circ \times 1^\circ$ resolution and smoothed SCIAMACHY measurements to simulate the spatial sampling of the GOME instrument (Konovalov et al., 2010). Russell et al. (2012), on the other hand, conducted piecewise linear regression of NO_2 columns derived from OMI measurements, considering the time periods 2005–2007, 2007–2009, and 2009-2011 separately, approximately capturing the available OMI measurements before, during, and after the economic recession in the United States. They generally find continuously decreasing NO_2 values, with the strongest decrease occurring during the recession. The

results by Russell et al. (2012) are consistent and according to expectations, but the fixed break-points 2007 and 2009, as well as the very short individual segments of 3 years each, hinder the detection of possible differences in the onset of the stronger NO_2 decrease due to the recession, and lead to statistically significant results only in some cases (Russell et al., 2012). However, when adapting the breakpoint regression model (Eq. 4.8) to allow for two breakpoints in the time series, the breakpoints are found in late 2007 and mid-2010 (not shown), and the qualitative trends during the individual periods agree well with those reported by Russell et al. (2012) (not shown).

Concluding, one can establish that currently, the available time series of tropospheric NO_2 measurements is still too short to conduct meaningful analyses of non-linear changes at high spatial resolution. While for larger regions, innovative methods can in principle yield interesting results, preserving the relatively high spatial resolution of modern satellite spectrometers when analysing data from multiple instruments and significant non-linear trend analysis seems to be mutually exclusive.

4.9 CO-EVOLUTION OF NO_2 WITH OTHER AIR POLLUTANTS

It can be potentially interesting to compare the temporal evolutions of tropospheric NO_2 columns to measurements of other air pollutants. Over urban and industrialized regions, fossil fuel burning caused by anthropogenic activity is the main NO_2 emission source; this is also true for other atmospheric pollutants to some extent. However, the individual emissions strongly depend on fuel type, and therefore differing temporal changes can possibly point towards a changing fuel partitioning, making it possible to attribute emissions to different sources. This analysis is however made more challenging because most other air pollutants which can be measured from space have either significant emission sources not linked to anthropogenic activity, or long tropospheric lifetimes, leading to high background concentrations and therefore low temporal variability, or both. Furthermore, the retrieval of tropospheric NO_2 columns from satellite measurement is compara-

tively easy as compared to other components, so that not always the retrieved concentrations have a low enough uncertainty to yield meaningful results.

4.9.1 *Correlations with aerosol optical depth*

For a number of reasons, the retrieval of aerosol optical depth (AOD) from space is very challenging; especially the analysis of temporal changes is made difficult by the very variable number of measurements per month (see, e. g., Yoon et al., 2013). Also, it is important to note that the AOD trends are quite inconsistent between the available instruments MISR, MODIS (on board the Aqua and Terra satellites), and SeaWifs (Alpert et al., 2012; Yoon et al., 2013). Here, MISR AOD measurements were used because they have the largest temporal overlap with SCIAMACHY measurements, and because MODIS data might be inaccurate over land (Levy et al., 2010; Zhang and Reid, 2010).

An additional challenge for such a comparison of NO_2 columns and AODs, especially in the Middle East and in China, comes from the high importance of desert dust aerosols for the retrieved AOD values. There, it must be remembered that a considerable fraction of the observed AODs might originate from desert dust and be unrelated to anthropogenic emissions.

Monthly mean aerosol optical depth (AOD) from the Multi-angle Imaging SpectroRadiometer (MISR; Diner et al., 1998) were used for a quick comparison to SCIAMACHY tropospheric NO_2 columns. In this context, the MISR Lv3 AOD product[1] was used. Both datasets were compiled into annual means and horizonzally gridded to $1^\circ \times 1^\circ$.

Only few of the investigated megacity regions show continuous behavior in both NO_2 and AOD values. Figure 4.31 shows the temporal co-evolution of tropospheric NO_2 columns and aerosol optical depth, for the years 2003–2011, for five exemplary cities.

[1]The MISR data product is available at https://eosweb.larc.nasa.gov/project/misr/mil3mae_table

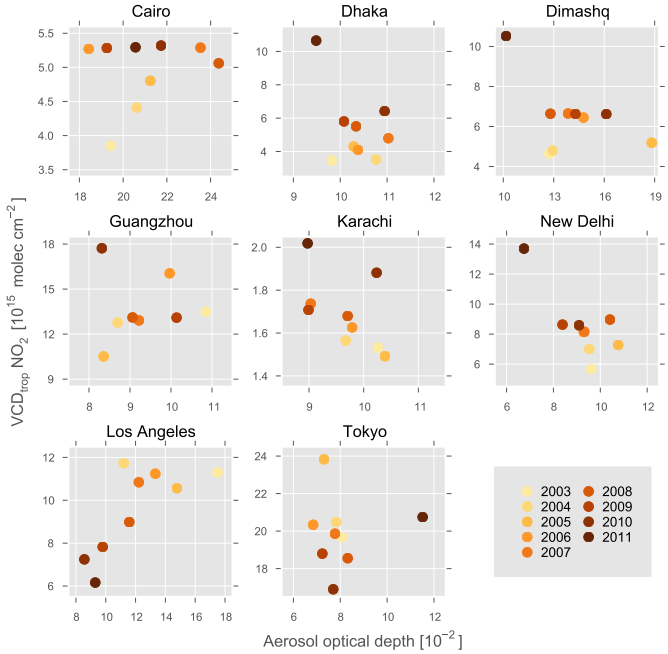

Figure 4.31: VCD_{trop} NO_2 from SCIAMACHY plotted against aerosol optical depth from MISR, for the years 2003–2011. Each data point represents the annual mean of the monthly means of the individual measurements, gridded to 1°×1°.

It is important to note that the visible differences between the NO_2 columns shown here and the trend estimates derived in Sections 4.6 and 4.7 are due to the coarse horizontal gridding of 1°×1°.

4.9.2 *Formaldehyde (HCHO)*

Formaldehyde (HCHO) is an air pollutant with severe impacts on human health. It is mainly produced from natural sources by the oxidation of isoprene and monoterpenes, which are emitted into the troposphere by vegetation in large quantities. In regions dominated by anthropogenic pollution, significant quantities of HCHO originate from

the burning of fossil fuels and biomass; in the extreme, formaldehyde concentrations in these settings (e. g., Mexico City and Los Angeles) can reach significant and harmful levels (Wittrock, 2006, and references therein). The very short lifetime of HCHO of about 5 hours (Arlander et al., 1995) makes it possible to observe the tropospheric HCHO burden close to its sources, enabling the estimation of emission rates.

This short tropospheric lifetime of formaldehyde implies the assumption that any HCHO observed in anthropogenic regions is actually caused by the burning of fossil fuels. Therefore, a comparison of NO_2 with HCHO columns over megacity regions can be hoped to lead to interesting results.

Figure 4.32 compares annual average NO_2 and HCHO columns from the GOME-2 instrument for some selected megacities. As quantitative consistency with other space-borne NO_2 measurements is not as important here compared to trend calculations in chapter 4.7, I use the improved GOME-2 NO_2 retrieval, as described in Richter et al. (2011). The HCHO columns have been derived at the Belgian Institute for Space Aeronomy (BIRA-IASB; De Smedt et al., 2012).

Hong Kong and Singapore both show strongly increasing formaldehyde during the observed period 2007–2012, while the NO2 signals in both cities are diverging: decreasing and increasing for Hong Kong and Singapore, respectively. In Baghdad and Madrid, however, a strong increase/decrease in NO_2 columns is accompanied by a stagnating HCHO signal. Formaldehyde columns over Los Angeles, finally, show large scatter. So obviously, it is not easy to draw any conclusions about possible co-evolution patterns of NO_2 and HCHO. One probable reason for this is that formaldehyde can have strong natural sources from the biosphere, which cannot be distinguished from a possible anthropogenic signal in a straightforward way.

4.9.3 *Carbon dioxide (CO_2)*

A naive comparison of tropospheric NO_2 columns to dry-column-averaged carbon dioxide measurements does not yield meaningful results.

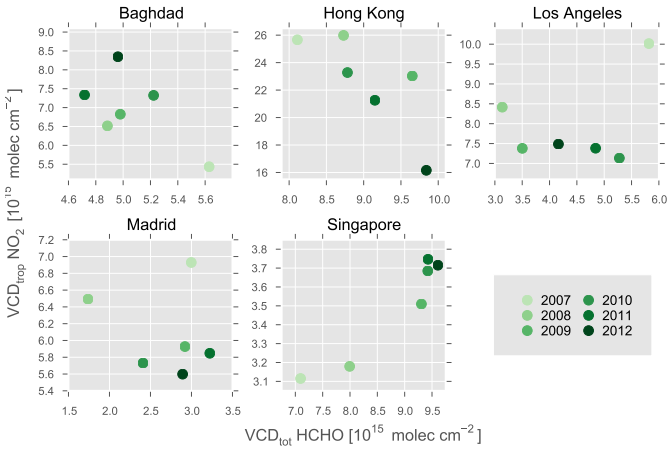

Figure 4.32: VCD_{trop} NO_2 from GOME-2 plotted against VCD_{tot} HCHO from GOME-2, retrieved at the Belgian Institute for Space Aeronomy (BIRA-IASB), for the years 2007–2012. Each data point represents the average of the monthly means of the individual measurements, gridded to $1° \times 1°$.

As an example, Fig. 4.33 shows a comparison of the summer months June/July/August, between VCD_{trop} NO_2 and XCO_2 (using the BESD algorithm; Reuter et al., 2011) from SCIAMACHY measurements. The summer months have been chosen because XCO_2 concentrations show a strong seasonal variation, which is significantly larger than the anthropogenic signal which can be expected to be seen in the measurements. Since the long atmospheric lifetime of CO_2 leads to high atmospheric background levels, it is very challenging to retrieve a possible signal from megacities in the column averages.

Fig. 4.33 reflects the continuous increase in atmospheric CO_2 concentrations; the individual time series do not show significant signs of deviation from this general background increase.

One way to handle this challenge would be to consider each individual megacity as source region and define a background region for it, approximately of the same size, at the same latitude, and opposite to the predominant wind direction. On the basis of monthly means, one could compute the time series of $\Delta XCO_2 = XCO_2^{\text{source}} - XCO_2^{\text{background}}$,

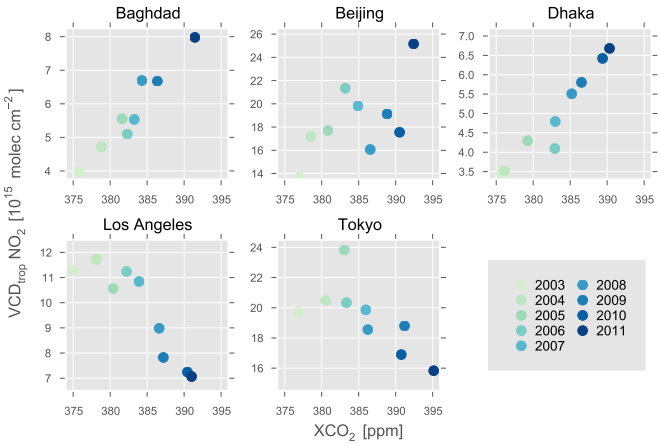

Figure 4.33: VCD_{trop} NO_2 from SCIAMACHY plotted against XCO_2 from SCIAMACHY, retrieved with the BESD algorithm, for the years 2003–2011. Each data point represents the average of the monthly means of the individual measurements for the summer months JJA, gridded to $1° \times 1°$.

which should in principle contain the anthropogenic XCO_2 signal for the megacity. This could then be compared to the observed NO_2 columns, is however out of scope for this study.

4.9.4 *Carbon monoxide (CO)*

Carbon monoxide (CO) can be measured from satellite in the near and thermal infrared spectral regions. The best long-term dataset currently available comes from the MOPITT instrument on board the Terra satellite. While the combined near infrared / thermal infrared retrieval has the greatest sensitivity to lower tropospheric CO, this retrieval shows relatively large random errors and bias drift (Deeter et al., 2013). Therefore, here I compare CO total columns measured in the thermal infrared range (dataset *MOP03TM*, version 5[1]), to tropospheric NO_2 from the GOME-2 instrument. As the retrieval of CO columns is performed

[1]see https://eosweb.larc.nasa.gov/project/mopitt/mop03tm_table

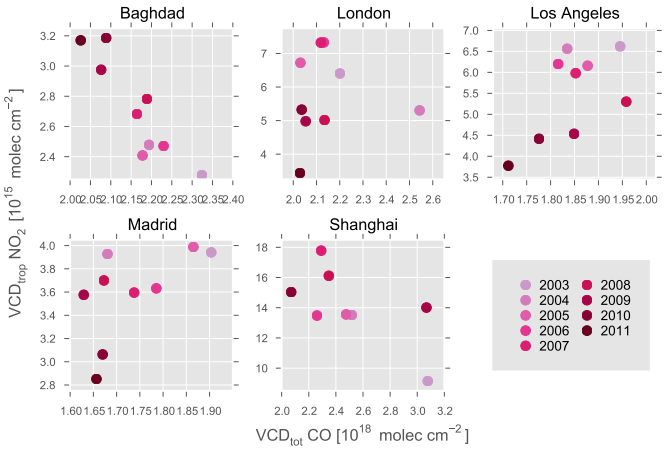

Figure 4.34: VCD_{trop} NO_2 from SCIAMACHY plotted against VCD_{tot} CO from MOPITT, for the years 2003–2011. Each data point represents the average of the summer (JJA) monthly mean values for one year, gridded to $1° \times 1°$.

in the thermal infrared spectral region, it is most reliable over warm surfaces. Figure 4.34 shows the comparison of the seasonal summer (JJA) averages for the years 2003–2011. Voulgarakis et al. (2010) report that "emissions variability makes the largest contributions [to the inter-annual variability] for CO, both in the tropics and in the extratropics". Therefore, in principle, it should be possible to analyze the co-evolution with NO_2. On the other hand, the tropospheric lifetime of the CO molecule is approx. 2 months (Seinfeld and Pandis, 2006, p. 205), so that transported CO can be expected to significantly influence the CO columns measured at any location. Furthermore, the detection of possible linkages between the NO_2 and CO burden is especially difficult because satellite observations have shown that the atmospheric CO burden seems to decline by approx. 1% per year since more than a decade (Yurganov et al., 2010; Worden et al., 2013). This change is partly attributed to decreasing emissions from biomass burning, but not yet fully understood. Therefore, it is challenging to detect any pos-

sible co-evolution effect on top of the general downward trend in CO columns.

As expected, all megacity time series shown in Fig. 4.34 show continuously declining CO columns over the full 2003–2011 period, independently of the observed NO_2 trend. The situation is similar to the comparison of NO_2 and CO_2, so in principle a similar strategy as proposed in Sect. 4.9.3 (comparing source and background regions to extract a possible anthropogenic signal) could lead to interesting results.

4.9.5 *Ozone (O_3)*

The retrieval of tropospheric ozone (O_3) from satellite measurements is challenging, mainly because its main absorption bands lie in the ultraviolet spectrum, which means that Rayleigh scattering in the lower atmosphere considerably interferes with the extraction of an absorption signal from the Earthshine scpectrum. Therefore, the sensitivity to lower-troposheric ozone is usually low in satellite retrievals, and the estimation of the stratospheric O_3 content is very important. Here, I compare VCD_{trop} O_3 from the OMI and MLS instruments (Ziemke et al., 2006) to VCD_{trop} NO_2 from OMI (see Sect. 4.7). As ozone pollution is exceptionally important in summer months, Figure 4.35 shows seasonal averages (JJA).

It is clearly visible that the scatter in the seasonal ozone averages is quite large in most cases. Only Cairo and Mumbai show comparatively clear upward trends for the 2005–2012 time period. While the data for Cairo suggest that indeed it is possible to see the expected positive correlation of O_3 and NO_2 columns, the data for Mumbai should not be trusted too much due to the monsoon season influencing meteorology and the number of available measurements in an unpredictable way. Los Angeles has slightly increasing trop. ozone columns, while the available data do not show any clear trends in the other cities.

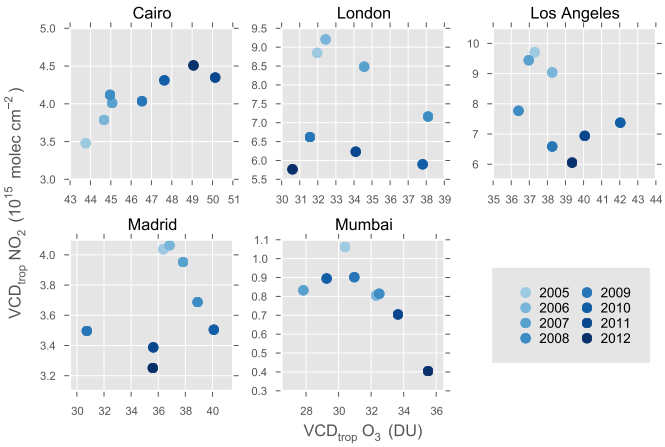

Figure 4.35: VCD_{trop} NO_2 from OMI plotted against VCD_{trop} O_3 from OMI/MLS, for the summer months (JJA) of the years 2005–2012. Each data point represents the average of the summer (JJA) monthly mean values for one year, gridded to 1.25°×1° longitude×latitude.

4.10 SUMMARY*

This present study investigates the temporal evolution of tropospheric NO_2 columns retrieved from satellite observations during the 1996–2011 time period. For the first time, instrumental differences in ground pixel size between the used satellite sensors has been explicitly accounted for. To assess the robustness of this approach and the reliability of the linear changes or trends derived, two additional complementary strategies for the derivation of instrumental and multiple instrumental trends in tropospheric NO_2 were introduced.

Firstly, SCIAMACHY spectra were spatially averaged to be comparable in ground pixel size to GOME measurements. Then, regular DOAS fits were performed on these spectra, and a resolution correction factor from the down-scaled and the regular SCIAMACHY measurements

*Parts of this section have been previously published as part of Hilboll et al. (2013a).

was calculated. These correction factors were shown to represent the spatial distribution of the NO_2 signal measured at a given point on the Earth, as they very well repeat the patterns observed in NO_2 emissions. The GOME measurements were then multiplied with these correction factors. While this can lead to an over-correction in some cases, generally, the corrected NO_2 time series from GOME measurements over individual city regions are shown to be brought into very good agreement with SCIAMACHY values during the time period of parallel measurements, facilitating trend analyses on a spatial resolution appropriate for SCIAMACHY observations.

Secondly, a trend model similar to that developed by Mieruch et al. (2008) for the study of H_2O trends was applied to the combined GOME/SCIAMACHY time series, explicitly accounting for a spatially varying additive offset between the two instruments. The spatial pattern of these offsets was shown to be very similar to that of the resolution correction.

Annual change rates of tropospheric NO_2 columns were calculated for a number of large urban agglomerations (see Tab. 4.7). Compared to previous studies, the results show considerably lower uncertainties of the retrieved trend estimates, most probably due to the longer study period 1996-2011. The trend model was then evolved to be able to include measurements from GOME-2 and OMI, and to account for a trend in the amplitude of the seasonal cycle.

The results show for the period of observation that NO_2 columns over the industrialized countries (U.S., Europe, Japan, Australia) have been steadily decreasing, with significant trends of up to $-6\%\,\mathrm{yr}^{-1}$. On the other hand, Chinese and Indian megacities, as well as many urban centers in the Middle East, show very strong upward trends of up to $+20\%\,\mathrm{yr}^{-1}$. Trends calculated with data from all four instruments agree well with those derived from GOME and SCIAMACHY measurements alone, highlighting the consistency of the satellite observations in spite of differences in sampling, spatial resolution, and overpass time. On the other hand, trends derived from the GOME and SCIAMACHY time series independently show systematic differences. These are attributed to changes in emission trends between the two time periods,

e.g. the accelerated development in China or the recent emission reductions in the U.S. due to improved technology and economic crises.

These strong and significant changes in tropospheric NO_2 columns over megacities show the ongoing need for further instruments, which are able to continue appropriate measurements. When assessing the temporal evolution, it is imperative that instrumental differences are being considered. This is especially true for the upcoming Sentinel-5 Precursor mission, as the proposed TROPOMI instrument will have a very high spatial resolution of $7 \times 7\,km^2$ (Veefkind et al., 2012; see Sect. 2.10.5). With the increasing length of the NO_2 time series available for analysis, the potential to understand the relationship between NO_2 emissions and their atmospheric abundances becomes better than ever. However, as the available time series become longer, the the assumption of uniform linear changes over the whole period gets more unrealistic. Therefore, non-linear trend analysis should be improved in future studies. Likewise, possible co-evolution effects of NO_2 and other air pollutants should be studied in more detail. However, as each trace gas has different emission, evolution, and retrieval characteristics, these studies necessitate careful setup and require deep knowledge of all involved species.

5

CONCLUSIONS AND OUTLOOK

This present thesis dealt with the improvement and the interpretation of space-borne measurements of tropospheric nitrogen dioxide columns using the DOAS technique. As one of the key anthropogenic air pollutants, NO_2 is an important species to be monitored, and this thesis was focused on combining all available satellite measurements of tropospheric NO_2 into one consistent dataset.

IMPROVEMENT OF THE STRATOSPHERIC CORRECTION

Satellites provide a great opportunity to apply consistent measurement conditions around the globe. However, measurements performed in nadir geometry have to be corrected for the influence of stratospheric NO_2, which dominates the total column in cases without significant tropospheric pollution.

Using the unique limb-mode measurements of stratospheric NO_2 provided by the SCIAMACHY instrument, the stratospheric correction of the total column measurements performed in nadir geometry could be significantly improved compared to the commonly used reference sector method. This improvement was made possible by the chosen interpolation scheme for matching limb and nadir measurements; one stratospheric NO_2 column is calculated for each pixel measured in nadir geometry, using all limb measurements from the same orbit and the measurement geometry.

The stratospheric NO_2 fields measured by SCIAMACHY were validated against results from the Oslo CTM2 and Bremen 3d CTM chemistry transport models. After accounting for a systematic bias between the two datasets, measured and modeled NO_2 fields are mostly in excellent agreement. This offset was shown depend on both latitude and season. The stratospheric correction scheme has been further improved by

calculating accurate stratospheric air mass factors from the measured NO_2 profiles and by accounting for the temperature dependence of the NO_2 absorption cross-section. Together, these two effects can cause an error of more than 10% in the climatological mean stratospheric NO_2 fields when not accounted for.

Altogether, the quality of the resulting tropospheric NO_2 fields could be considerably improved. The reference sector method often lead to both unphysical negative tropospheric NO_2 columns over remote regions and significantly reduced NO_2 over urban centers, especially in North America. Using SCIAMACHY limb measurements for stratospheric correction yields significantly better tropospheric NO_2. It could be shown that the thus retrieved tropospheric columns are almost never significantly lower than zero, and that artifacts, which the reference sector method introduced into the data over many regions, could be removed. As a result, the stratospheric correction scheme developed in this thesis leads to the arguably most accurate representation of tropospheric NO_2 slant columns measured from satellite to date.

INVESTIGATION OF THE EFFECT OF INSTRUMENT SPATIAL RESOLUTION ON TROPOSPHERIC NO_2 COLUMN MEASUREMENTS

When simultaneously analyzing measurements of tropospheric NO_2 columns by the GOME, SCIAMACHY, OMI, and GOME-2 satellite sensors, the differences between the individual instruments pose considerable challenges in arriving at a consistent dataset. Especially the differing ground pixel size leads to inconsistent spatial sampling between the instruments, resulting in considerable differences in the retrieved NO_2 columns, particularly over small, localized sources such as megacities. The influence of the instrument spatial resolution on the retrieved NO_2 columns was shown to strongly depend on the geographic conditions of the investigated region. In places where the pollution cannot spread unhindered and is confined to a small region such as, e. g., in mountain regions, the actual NO_2 fields show strong spatial gradients, leading to a strong dependence of the retrieved signal on the instrument's ground pixel size.

In this thesis, the climatological fine-scale structure of tropospheric NO_2 columns was retrieved from SCIAMACHY measurements and subsequently superimposed on the coarser measurements by the GOME instrument. This was achieved using spatially averaged SCIAMACHY spectra and the computation of a 'resolution correction factor'. The 'resolution-corrected' GOME measurements were compared to original SCIAMACHY measurements during the 11 month overlap period in 2002/2003. While in some cases, especially over cities located in arid, desert-like areas, the developed resolution correction yields too high NO_2 columns, the method generally proves to work very well on continental, regional, and megacity scales. This for the first time allows to investigate the temporal changes of small, localized tropospheric NO_2 signals over the 1996–2012 time period using GOME and SCIAMACHY measurements.

ANALYSIS OF INTER-ANNUAL TROPOSPHERIC NO_2 CHANGES OVER MEGACITIES

This thesis analyzed temporal changes of tropospheric NO_2 columns over megacities using space-borne measurements from the 1996–2011 period. Three methods to account for the differences between the individual instruments have been applied, based on (a) the resolution correction factor developed in this thesis, and (b) the explicit inclusion of instrumental differences, called 'levelshifts', into a trend model accounting for the seasonally varying NO_2 amounts measured by GOME and SCIAMACHY, and (c) by GOME, SCIAMACHY, OMI, and GOME-2. The spatial patterns of the resolution correction factor and the levelshifts were shown to agree very well.

For the period of observation, tropospheric NO_2 columns over the industrialized countries (U.S., Europe, Japan, Australia) were shown to be strongly decreasing, with statistically significant trends of up to -6 $\%\,\mathrm{yr}^{-1}$. On the other hand, most megacities in the developing world, especially in China, India, and the Middle East, were shown to exhibit strongly increasing, statistically significant trends of up to +20 $\%\,\mathrm{yr}^{-1}$.

The trends derived from GOME and SCIAMACHY alone were shown to agree very well with those derived from all four instruments, highlighting the consistency of the satellite observations in spite of differences in sampling, spatial resolution, and overpass time. On the other hand, the trends derived from GOME and SCIAMACHY measurements alone show significant differences in several regions, pointing towards changes in NO_2 emissions during the course of the full observation period, and showing the need for non-linear trend analysis. In summary, this thesis for the first time analyzed the temporal change of tropospheric NO_2 abundances by consistently combining measurements from different satellite platforms. The proposed method allows for the inclusion of an arbitrary number of future sensors into the analysis and leads to a high-quality dataset of tropospheric NO_2 time series over megacities.

SUGGESTIONS FOR FURTHER STUDIES

Starting from the work presented in this thesis, numerous studies show potential for interesting results.

Investigation of non-linear changes in tropospheric NO_2

As the available time series of tropospheric NO_2 becomes longer, the assumption of linear changes over the whole available period becomes stronger. Therefore, non-linear changes should be investigated. By combining the multi-instrument trend model presented in Sect. 4.7 with the breakpoint regression technique (see Sect. 4.8), it should in principle be possible to determine both (a) change rates and (b) potential changes of these change rates by the same trend model, while still accounting for the instrumental differences and the seasonality of the observed NO_2 columns.

Co-evolution with other air pollutants

In Section 4.9, the possibility of investigating the temporal co-evolution of tropospheric NO_2 with other air pollutants was introduced. Such an analysis needs careful consideration of many factors, and a thorough treatment was out of scope for this thesis. For the co-evolution with CO_2, for example, one should compare tropospheric NO_2 columns to CO_2 column anomalies, by considering the difference of CO_2 over a source region and CO_2 over an upwind background region. Using this technique, it should in principle be possible to detect changes in the relative contribution of different emission sources, providing a means to validate emission inventories.

Temporal changes in the driving factors for tropospheric NO_2 abundances

Zhou et al. (2012) used a general additive model (GAM) to investigate the relative influence of various factors (e. g., meteorological conditions, seasonal, and weekly cycles) on tropospheric NO_2 columns. This framework could be considerably expanded in various ways. As an example, one could introduce an instrument-dependent factor into this GAM to account for the differences between the different datasets. Following this approach, it would become possible to quantify the biases between the different instruments on a regional basis, which would open up possibilities for even better understanding of the chemical processes determining the tropospheric NO_2 load. A further possibility would be to run the GAM on seasonal subsets of the full time series (i. e., only on those measurements from a specific season or even month) to derive the seasonal variability of the relative importance of the various factors.

Correlations with socio-economic data

While it is hard to get reliable economic data at high temporal resolution (i. e., annual or even monthly) for individual megacity regions,

this might be possible for certain cities, especially in the developed world and in India. Correlation analysis of these economic data (e. g., gross regional product, industrial production, energy consumption, to name a few) with measurements of tropospheric NO_2 (or even also with other air pollutants, see above) could yield valuable insight in the processes underlying the emissions of air pollutants and their relative importance for megacity air quality.

OUTLOOK

As shown by this thesis, satellite measurements are an invaluable tool to observe the tropospheric NO_2 burden over megacities. The numerous approximations and a-priori assumptions made in the retrieval still provide manifold possibilities to improve the already high quality of the datasets. Especially, ongoing effort has to be invested into deriving a high-quality stratospheric correction scheme which does not rely on any relative offsets, as future geostationary missions (e. g., the European Sentinel-4 mission) do not provide measurements over clean background regions at a global scale. In this respect, the concept of limb/nadir matching as implemented by the SCIAMACHY instrument and carried out within this thesis was the optimum, as it provided independent measurements of the stratosphere with the same instrument.

The methods presented in this thesis open up the path for meaningful interpretation of the available long-term, high-quality, multi-instrument dataset. The possibility to include measurements from future missions (GOME-2 / Metop-B, TROPOMI) into the analysis in a consistent manner assures that the analysis of current and future data can profit from and extend the heritage laid out by GOME and SCIAMACHY.

APPENDIX:
ADDITIONAL MATERIAL

A

STRATOSPHERIC CORRECTION

A.1 COMPARISON SCIAMACHY LIMB / OSLO CTM2

Expanding on Figures 3.12 and 3.13, the climatological comparison between SCIAMACHY limb measurements and Oslo CTM2 and Bremen 3d CTM simulations for the years 2003–2007 and 2003–2010, respectively, for all months, is shown in Figs. A.1 and A.2. To be able to compare to SCIAMACHY nadir measurements, the climatological differences between VCD'^{nadir}_{strat} and the stratospheric columns from SCIAMACHY limb and Oslo CTM2 are shown in Figs. A.3 and A.4, respectively. The large positive values in these two Figures can be associated with tropospheric pollution.

A.2 DAILY MAPS OF TROPOSPHERIC SLANT COLUMNS

Expanding on Fig. 3.25, global maps of daily SCD_{trop} NO_2 for the additional days already shown by Beirle et al. (2010) are presented in Fig. A.5.

A.3 ZONAL VARIABILITY OF STRATOSPHERIC VERTICAL COLUMNS

Expanding on Figs. 3.7 and 3.15–3.18, the zonal variation of stratospheric NO_2 for all global 5° latitude bands for Jan and Aug 2006 is shown in Figs. A.6 and A.7, respectively. As in the main manuscript, the plots show the actual stratospheic NO_2 load, i.e. limb measurements and model simulations are adjusted to the level of the nadir measurements over the Pacific Ocean, and all three datasets are subsequently corrected for a tropospheric influence on the nadir measurements in that meridional band. Details can be found in Sect. 3.4.4.

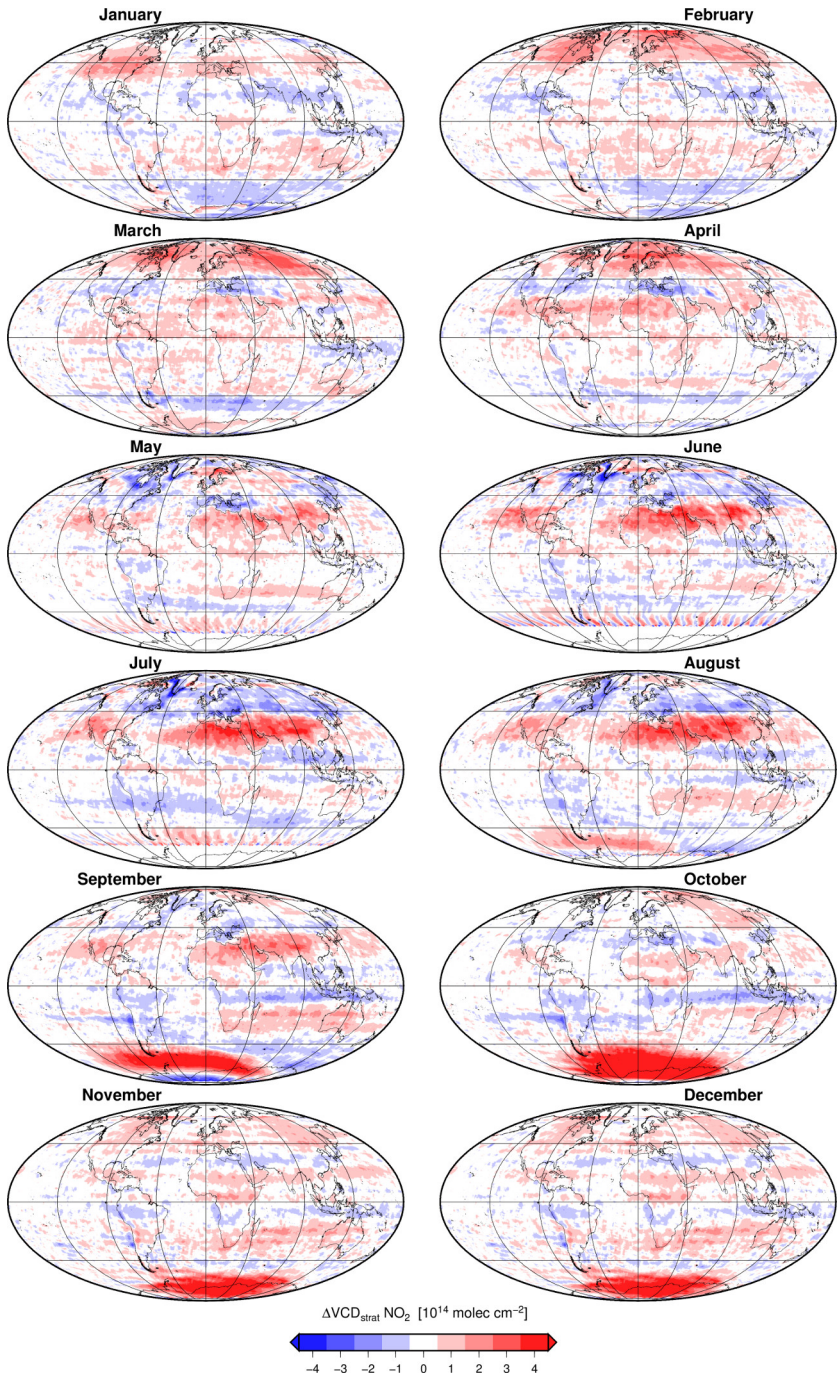

Figure A.1: Climatological differences ΔVCD_{strat} NO_2 between SCIAMACHY limb measurements and Oslo CTM2 simulations, for the years 2003-2007, offset to vanish over the Pacific Ocean (from Hilboll et al., 2013c).

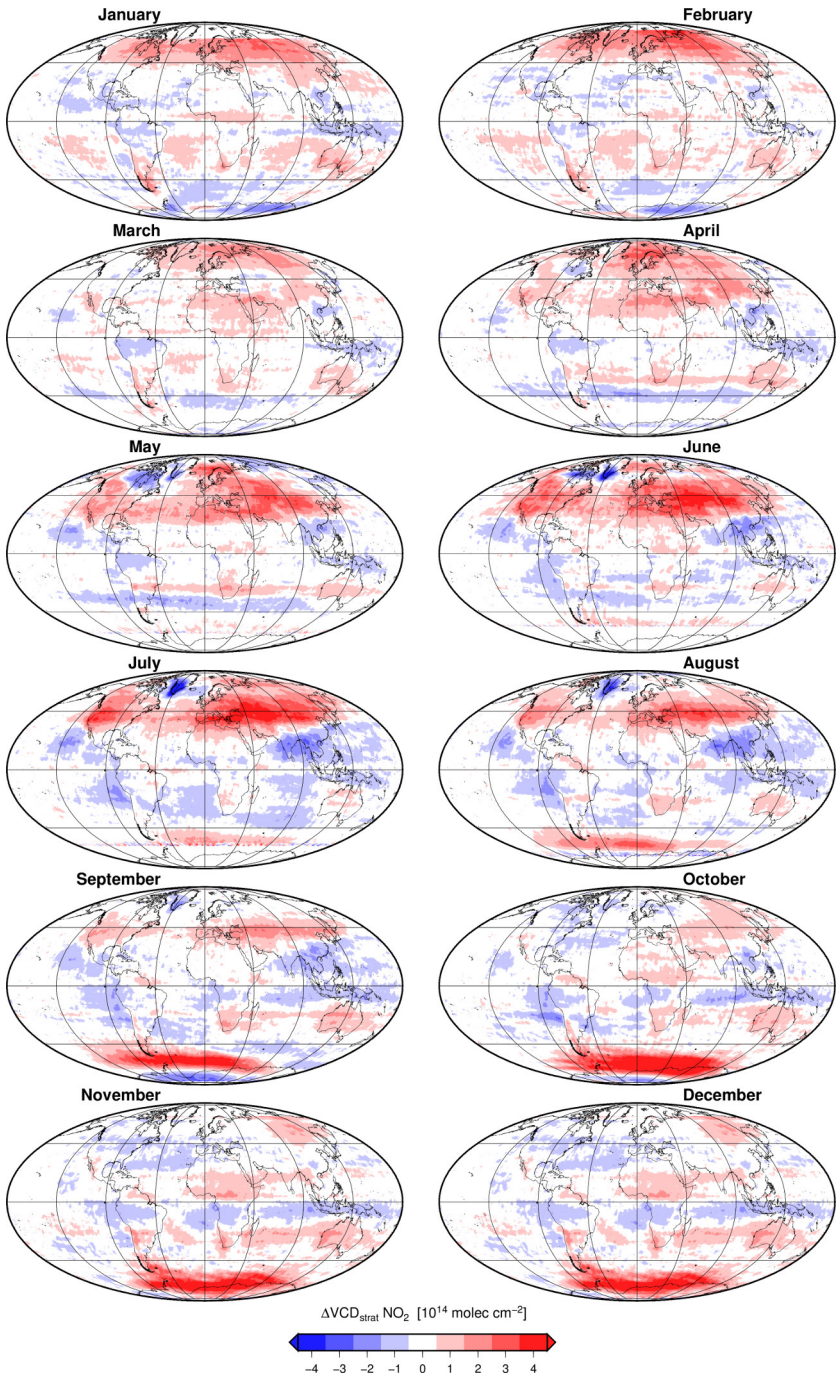

Figure A.2: Climatological differences ΔVCD_{strat} NO_2 between SCIAMACHY limb measurements and Bremen 3d CTM simulations, for the years 2003-2010, offset to vanish over the Pacific Ocean.

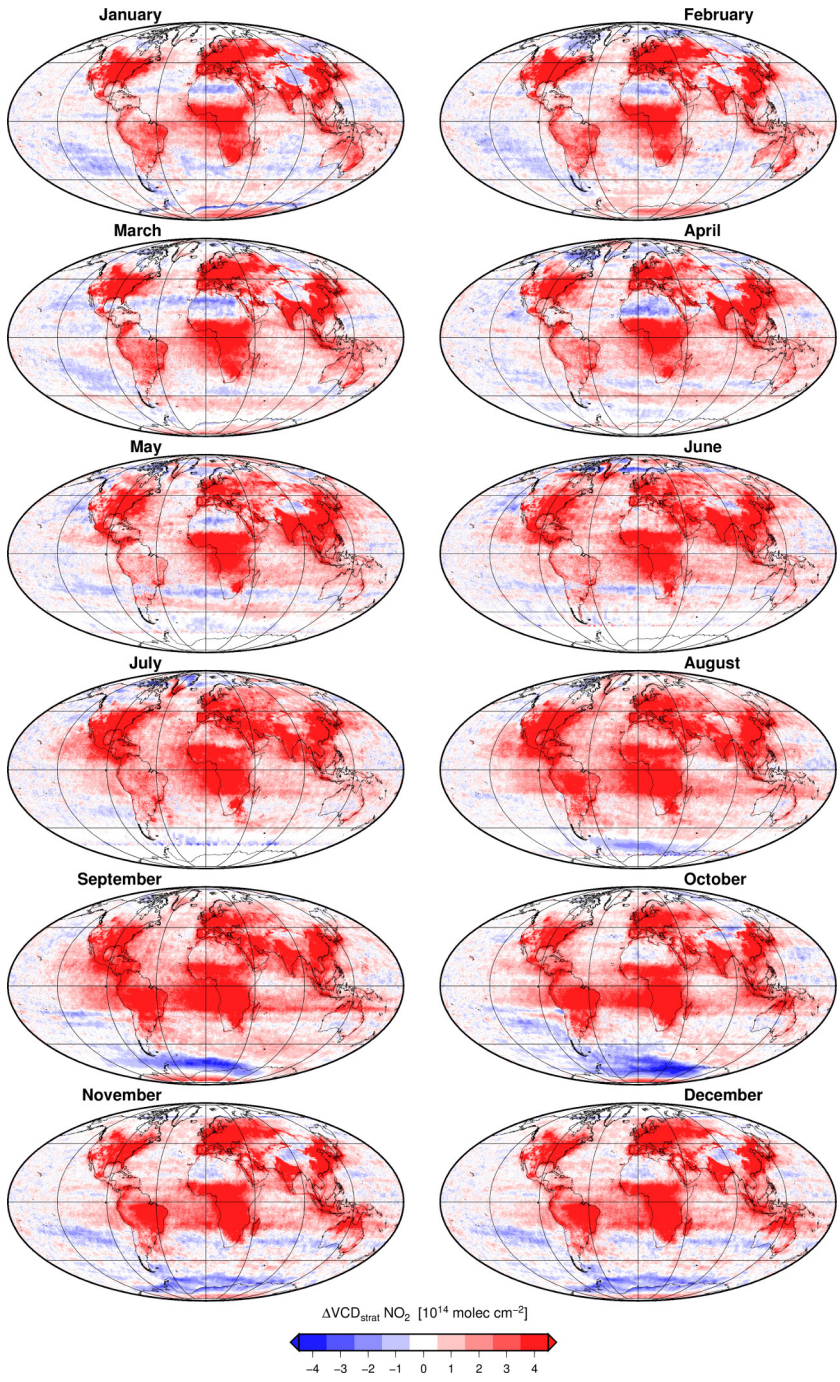

Figure A.3: Climatological differences $\Delta VCD_{strat}\,NO_2$ between stratospheric NO_2 columns from SCIAMACHY nadir and limb measurements, for the years 2003–2007 (from Hilboll et al., 2013c).

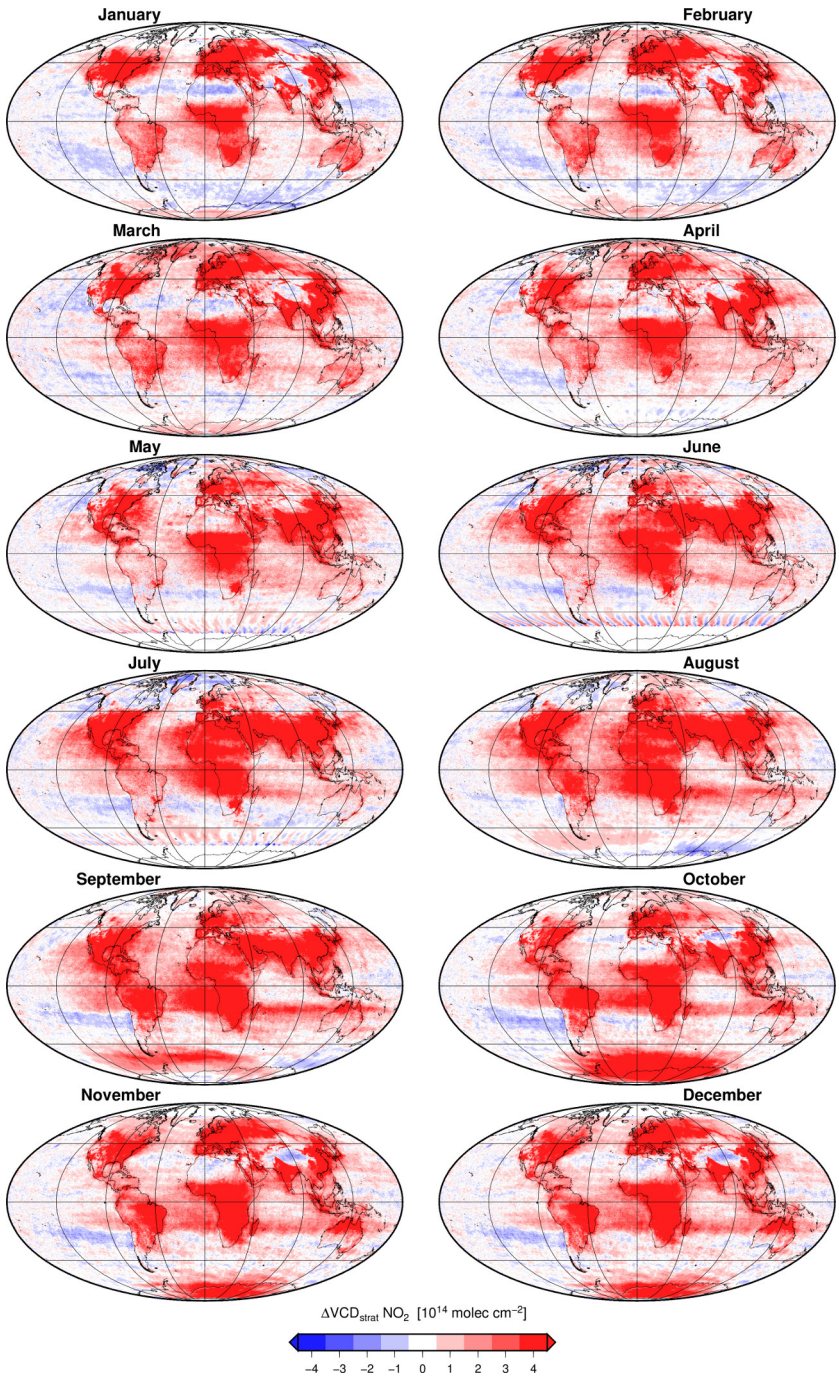

Figure A.4: Climatological differences ΔVCD_{strat} between stratospheric NO_2 columns from SCIAMACHY nadir measurements and Oslo CTM2 simulations, for the years 2003–2007 (from Hilboll et al., 2013c).

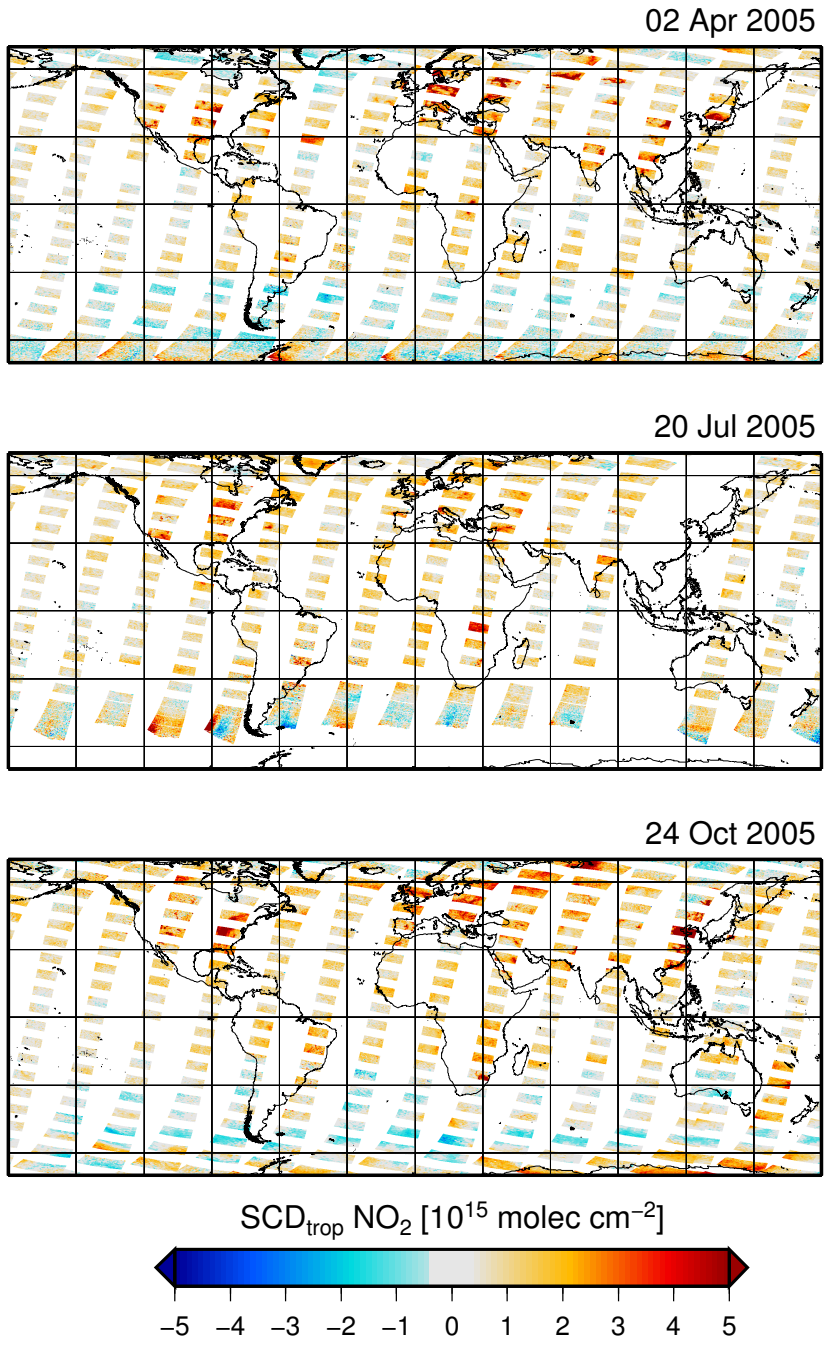

Figure A.5: SCD_{trop} NO_2 using SCIAMACHY limb measurements as stratospheric correction, for the three days 02 Apr 2005 (top), 20 Jul 2005 (center), and 24 Oct 2005 (bottom). These are the days which are shown in Beirle et al. (2010) (from Hilboll et al., 2013c).

Figure A.6: Zonal variation of stratospheric NO_2 columns from SCIAMACHY nadir (black), SCIAMACHY limb (red), Oslo CTM2 (blue), and Bremen 3d CTM (green) for January 2006 (after Hilboll et al., 2013c).

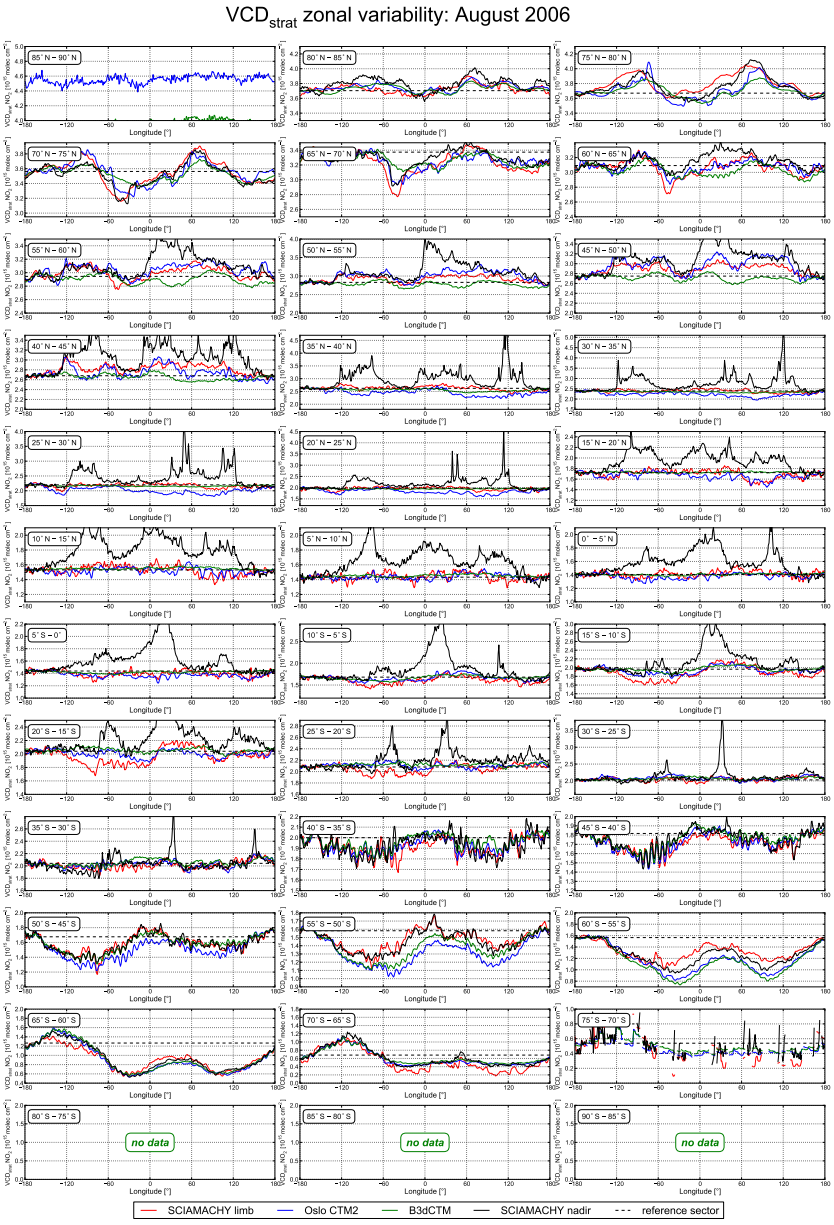

Figure A.7: Zonal variation of stratospheric NO_2 columns from SCIAMACHY nadir (black), SCIAMACHY limb (red), Oslo CTM2 (blue), and Bremen 3d CTM (green) for August 2006 (after Hilboll et al., 2013c).

B

TROPOSPHERIC NO_2 TRENDS

This chapter contains results of trend calculations for the levelshift method applied to resolution-correctd GOME and regular SCIAMACHY measurements (Tables B.1 and B.4), the levelshift method for the reduced time period 1996–2006, to allow better comparison to the results of van der A et al. (2008) (Tables B.2 and B.5), and of the multi-instrument fit with linearly changing seasonality component (Eq. 4.11, Tables B.3 and B.6).

Table B.1: Annual growth rate ΔVCD_{trop} NO_2 from the levelshift model (Eq. 4.3) applied to original and resolution-corrected GOME data, for the time period 1996–2011, for the regions shown in Fig. 4.5. The relative trends have been computed relative to the 1996 annual mean. Values for original GOME data are reproduced from Table 4.6 and given here for better comparison.

Region	Levelshift-model (orig. GOME data)		Levelshift-model (rescorr. GOME data)	
	[10^{14} molec cm^{-2} yr^{-1}]	[% yr^{-1}]	[10^{14} molec cm^{-2} yr^{-1}]	[% yr^{-1}]
Continental U.S.	-0.82 $\pm$ 0.14	-1.72 $\pm$ 0.30	-0.81 $\pm$ 0.15	-1.62 $\pm$ 0.30
Central-Eastern U.S.	-2.94 $\pm$ 0.38	-2.96 $\pm$ 0.38	-2.94 $\pm$ 0.39	-2.92 $\pm$ 0.39
Western Europe	-2.94 $\pm$ 0.63	-2.61 $\pm$ 0.56	-2.96 $\pm$ 0.65	-2.56 $\pm$ 0.56
Japan	-0.49 $\pm$ 0.13	-1.24 $\pm$ 0.33	-0.49 $\pm$ 0.14	-1.17 $\pm$ 0.33
Middle East	+0.779 $\pm$ 0.082	+4.00 $\pm$ 0.42	+0.785 $\pm$ 0.081	+4.01 $\pm$ 0.42
East Central China	+10.1 $\pm$ 1.1	+20.5 $\pm$ 2.2	+10.1 $\pm$ 1.1	+20.3 $\pm$ 2.2
North Central India	+1.30 $\pm$ 0.27	+4.05 $\pm$ 0.84	1.08 $\pm$ 0.27	+4.6 $\pm$ 1.1

Table B.2: Annual growth rate ΔVCD_{trop} NO_2 from the levelshift model (Eq. 4.3) applied to original and resolution-corrected GOME data, for the time period 1996–2006, for the regions shown in Fig. 4.5. The relative trends have been computed relative to the 1996 annual mean.

Region	Levelshift-model (orig. GOME data)		Levelshift-model (rescorr. GOME data)	
	[10^{14} molec cm^{-2} yr^{-1}]	[% yr^{-1}]	[10^{14} molec cm^{-2} yr^{-1}]	[% yr^{-1}]
Continental U.S.	*+0.01 ± 0.17*	*+0.02 ± 0.38*	*+0.03 ± 0.18*	*+0.07 ± 0.39*
Central-Eastern U.S.	-1.54 ± 0.47	-1.63 ± 0.50	-1.54 ± 0.48	-1.61 ± 0.50
Western Europe	-3.6 ± 1.1	-3.11 ± 0.98	-3.6 ± 1.2	-3.08 ± 0.99
Japan	*-0.17 ± 0.23*	*-0.45 ± 0.59*	*-0.16 ± 0.24*	*-0.40 ± 0.58*
Middle East	+0.59 ± 0.11	+2.94 ± 0.54	+0.62 ± 0.11	+3.05 ± 0.53
East Central China	+5.85 ± 0.85	+9.2 ± 1.3	+5.86 ± 0.85	+9.2 ± 1.3
North Central India	+1.18 ± 0.43	+3.7 ± 1.3	*+0.64 ± 0.36*	*+2.6 ± 1.4*

Table B.3: Annual growth rate ΔVCD_{trop} NO_2 from the levelshift model (Eq. 4.3) and the multi-instrument fit (Eq. 4.8) for the regions shown in Fig. 4.5. The relative trends have been computed relative to the 1996 annual mean. Values for constant seasonality are reproduced from Table 4.6 and given here for better comparison.

Region	Multi-instrument fit (const. seasonality)		Multi-instrument fit (var. seasonality)		
	$\hat{\omega}$ [10^{14} molec cm^{-2} yr^{-1}]	[% yr^{-1}]	$\hat{\omega}$ [10^{14} molec cm^{-2} yr^{-1}]	[% yr^{-1}]	$\hat{\xi}$ [% yr^{-1}]
Continental U.S.	-0.78 ± 0.20	-1.66 ± 0.42	-0.77 ± 0.19	-1.64 ± 0.40	*-2.27 ± 0.97*
Central-Eastern U.S.	-2.65 ± 0.47	-2.69 ± 0.48	-2.62 ± 0.44	-2.37 ± 0.44	-3.29 ± 0.66
Western Europe	-2.63 ± 0.85	-2.35 ± 0.76	-2.61 ± 0.84	-2.34 ± 0.75	*-2.8 ± 1.2*
Japan	-0.49 ± 0.17	-1.24 ± 0.42	-0.49 ± 0.17	-1.23 ± 0.42	*-1.3 ± 1.1*
Middle East	+0.727 ± 0.093	+3.70 ± 0.47	+0.725 ± 0.087	+3.69 ± 0.44	+7 ± 65
East Central China	+8.7 ± 1.2	+16.3 ± 2.2	+8.6 ± 1.1	+16.1 ± 2.0	+23 ± 14
North Central India	+1.05 ± 0.32	+3.23 ± 0.98	+1.01 ± 0.31	+3.08 ± 0.95	+9.0 ± 7.0

Table B.4: Annual growth rate ΔVCD_{trop} NO_2 from the levelshift model (Eq. 4.3) applied to original and resolution-corrected GOME data, for the time period 1996–2011, for a list of megacities. The relative trends have been computed relative to the 1996 annual mean. Non-significant trends (see Eq. 4.6) are shown *in italics*. The relative trends have been computed relative to the 1996 annual mean. Values for original GOME data are reproduced from Table 4.7 and given here for better comparison.

Region	Levelshift-model (orig. GOME data)		Levelshift-model (rescorr. GOME data)	
	[10^{14} molec cm^{-2} yr^{-1}]	[% yr^{-1}]	[10^{14} molec cm^{-2} yr^{-1}]	[% yr^{-1}]
Algiers	+0.74 ± 0.14	+3.64±0.69	+0.83±0.17	+2.62±0.53
Athens	-2.33 ± 0.70	-4.1±1.2	-2.10±0.87	-1.72±0.71
Baghdad	+3.54 ± 0.33	+20.7±1.9	+3.91±0.34	+10.1±0.87
Beijing	+8.8 ± 2.5	+6.7±1.9	+9.4±2.7	+4.8±1.4
Buenos Aires	+1.14 ± 0.48	+3.9±1.6	*+0.85±0.73*	*+1.11±0.94*
Cairo	+1.91 ± 0.25	+7.21±0.93	+2.12±0.27	+4.35±0.55
Chicago	-6.7 ± 1.8	-4.1±1.1	-7.0±2.0	-2.46±0.68
Dhaka	+3.66 ± 0.52	+27.2±3.9	+3.94±0.50	+12.7±1.6
Dimashq	+3.44 ± 0.54	+10.2±1.6	+3.90±0.60	+6.03±0.92
Guangzhou	*+1.2 ± 2.0*	*1.3±2.0*	+3.0±2.6	+1.6±1.4
Hong Kong	*-2.6 ± 1.8*	*-2.3±1.6*	*-0.8±2.2*	*-0.4±1.2*
Istanbul	*-0.5 ± 1.1*	*-0.7±1.5*	*-0.5±1.3*	*-0.4±1.0*
Jakarta	-1.45 ± 0.42	-3.9±1.1	-1.57±0.55	-2.58±0.91
Jeddah	+1.30 ± 0.29	+4.07±0.92	+1.64±0.38	+2.31±0.53
Karachi	+0.94 ± 0.22	+6.8±1.6	+1.07±0.29	+3.8±1.0
Kolkata	+0.75 ± 0.22	+2.98±0.89	+0.76±0.23	+2.03±0.61
Lagos	+0.41 ± 0.10	+3.41±0.83	+0.40±0.11	+2.63±0.73
Lima	+0.99 ± 0.40	+7.1±2.9	+1.22±0.48	+3.0±1.2
London	-4.4 ± 1.3	-2.40±0.71	-4.5±1.4	-2.24±0.68
Los Angeles	-13.7 ± 1.7	-6.00±0.72	-14.1±1.9	-3.14±0.43
Manila	-1.13 ± 0.18	-5.32±0.85	-1.43±0.31	-3.56±0.76
Mexico City	*-0.65 ± 0.83*	*-1.2±1.5*	*-0.30±0.98*	*-0.22±0.72*
Moscow	*-0.2 ± 1.5*	*-0.3±1.9*	*+0.3±1.7*	*+0.2±1.2*
Mumbai	+0.82 ± 0.17	4.31±0.91	+0.91±0.20	+2.46±0.53
New Delhi	+3.07 ± 0.53	+9.3±1.6	+3.07±0.56	+5.5±1.0
New York	-5.3 ± 1.7	-2.45±0.80	-5.2±2.3	-1.45±0.64
Osaka	-1.94 ± 0.98	-1.74±0.88	-2.1±1.1	-1.23±0.61
Paris	-4.6 ± 2.0	-3.0±1.3	-5.8±2.6	-2.3±1.0
Riyadh	+2.01 ± 0.39	+6.7±1.3	+2.51±0.49	+3.49±0.68
São Paolo	*+0.52 ± 0.46*	*-1.3±1.2*	*+0.53±0.58*	*+0.62±0.69*
Seoul	*+0.6±1.7*	*0.4±1.1*	*+0.6±2.1*	*+0.21±0.72*
Shanghai	+11.9 ± 3.1	+12.8±3.3	+12.8±3.2	+9.5±2.4
Shenzhen	*-2.4 ± 1.6*	*-1.9±1.3*	-1.8±1.7	-1.2±1.1
Tehran	+2.08 ± 0.68	+5.7±1.9	+2.49±0.74	+2.84±0.84
Tokyo	-5.2 ± 1.1	-3.61±0.79	-5.5±1.4	-2.21±0.54

Table B.5: Annual growth rate ΔVCD_{trop} NO_2 from the levelshift model (Eq. 4.3) applied to original and resolution-corrected GOME data, for the time period 1996–2006, for a list of megacities. The relative trends have been computed relative to the 1996 annual mean. Non-significant trends (see Eq. 4.6) are shown *in italics*. The relative trends have been computed relative to the 1996 annual mean.

Region	Levelshift-model (orig. GOME data)		Levelshift-model (rescorr. GOME data)	
	[10^{14} molec cm^{-2} yr^{-1}]	[% yr^{-1}]	[10^{14} molec cm^{-2} yr^{-1}]	[% yr^{-1}]
Algiers	+0.64 ± +0.17	+3.1 ± 0.81	+0.87 ± 0.23	+2.75 ± 0.74
Athens	*+1.16 ± 0.83*	*+2.6 ± 1.9*	*+2.0 ± 1.2*	*+1.9 ± 1.1*
Baghdad	+1.81 ± 0.35	+7.9 ± 1.5	+2.82 ± 0.45	+6.7 ± 1.1
Beijing	+8.8 ± 3.6	+6.7 ± 2.8	+10.2 ± 4.0	+5.3 ± 2.1
Buenos Aires	*+0.06 ± 0.73*	*+0.2 ± 2.2*	*-0.7 ± 1.3*	*-0.8 ± 1.5*
Cairo	+1.46 ± 0.41	+5.2 ± 1.5	+2.00 ± 0.46	+4.08 ± 0.93
Chicago	*-3.8 ± 3.0*	*-2.5 ± 2.0*	*-5.0 ± 3.4*	*-1.8 ± 1.2*
Dhaka	+1.39 ± 0.48	+6.5 ± 2.2	+2.00 ± 0.55	+5.3 ± 1.5
Dimashq	+2.93 ± 0.63	+8.3 ± 1.8	+4.12 ± 0.78	+6.4 ± 1.2
Guangzhou	+7.8 ± 2.7	+10.6 ± 3.6	+13.6 ± 3.8	+9.2 ± 2.6
Hong Kong	+7.0 ± 2.2	+8.7 ± 2.7	+12.4 ± 3.0	+8.5 ± 2.0
Istanbul	*+1.6 ± 1.6*	*+2.5 ± 2.5*	*+1.5 ± 2.1*	*+1.3 ± 1.7*
Jakarta	*-0.23 ± 0.63*	*-0.7 ± 1.9*	*-0.61 ± 0.93*	*-1.1 ± 1.6*
Jeddah	+0.83 ± 0.38	+2.5 ± 1.1	+1.71 ± 0.58	+2.42 ± 0.81
Karachi	*+0.21 ± 0.29*	*+1.3 ± 1.7*	*+0.56 ± 0.47*	*+1.9 ± 1.6*
Kolkata	*+0.35 ± 0.34*	*+1.3 ± 1.3*	*+0.39 ± 0.37*	*+1.00 ± 0.94*
Lagos	*+0.03 ± 0.15*	*+0.2 ± 1.1*	*-0.03 ± 0.18*	*-0.2 ± 1.1*
Lima	*+0.63 ± 0.55*	*+4.2 ± 3.7*	*+1.27 ± 0.74*	*+3.1 ± 1.8*
London	*-2.9 ± 2.1*	*-1.6 ± 1.2*	*-3.2 ± 2.3*	*-1.6 ± 1.2*
Los Angeles	*-3.9 ± 2.4*	*-2.0 ± 1.2*	*-4.7 ± 3.1*	*-1.13 ± 0.76*
Manila	-0.99 ± 0.30	-4.8 ± 1.5	-1.74 ± 0.57	-4.2 ± 1.4
Mexico City	*+0.8 ± 1.2*	*+1.6 ± 2.4*	*+1.7 ± 1.6*	*+1.3 ± 1.2*
Moscow	*+2.1 ± 2.2*	*+3.1 ± 3.2*	*+3.8 ± 2.5*	*+3.4 ± 2.2*
Mumbai	+0.48 ± 0.23	+2.4 ± 1.1	+0.69 ± 0.30	+1.84 ± 0.81
New Delhi	+2.67 ± 0.76	+7.9 ± 2.2	+2.80 ± 0.87	+5.0 ± 1.6
New York	*+2.0 ± 2.2*	*+1.0 ± 1.1*	*+2.3 ± 3.5*	*+0.7 ± 1.1*
Osaka	*+0.13 ± 1.3*	*+0.1 ± 1.2*	*-0.2 ± 1.5*	*-0.13 ± 0.90*
Paris	*-4.3 ± 3.4*	*-2.8 ± 2.2*	*-7.7 ± 4.6*	*-3.0 ± 1.8*
Riyadh	+1.29 ± 0.45	4.0 ± 1.4	+2.60 ± 0.75	+3.6 ± 1.0
São Paolo	*+0.08 ± 0.65*	*+0.2 ± 1.6*	*+0.16 ± 0.93*	*+0.2 ± 1.1*
Seoul	*-1.3 ± 2.6*	*-0.8 ± 1.6*	*-1.4 ± 3.5*	*-0.5 ± 1.2*
Shanghai	+10.0 ± 3.9	+9.9 ± 3.8	+12.1 ± 4.0	+8.8 ± 2.9
Shenzhen	*+3.2 ± 2.0*	*+3.0 ± 1.9*	+4.9 ± 2.2	+3.6 ± 1.7
Tehran	+1.94 ± 0.82	+5.2 ± 2.2	+3.05 ± 0.95	+3.6 ± 1.1
Tokyo	*-0.9 ± 1.7*	*-0.7 ± 1.3*	*-1.9 ± 2.3*	*-0.78 ± 0.96*

Table B.6: Annual growth rate ΔVCD_{trop} NO_2 from the levelshift model (Eq. 4.3) and the multi-instrument fit (Eq. 4.8) for a list of megacities. The relative trends have been computed relative to the 1996 annual mean. Non-significant trends (see Eq. 4.6) are shown *in italics*. Values for constant seasonality are reproduced from Table 4.7 and given here for better comparison.

Region	Multi-instrument fit (const. seasonality)		Multi-instrument fit (var. seasonality)		
	$\hat{\omega}$ [10^{14} molec cm^{-2} yr^{-1}]	[% yr^{-1}]	$\hat{\omega}$ [10^{14} molec cm^{-2} yr^{-1}]	[% yr^{-1}]	$\hat{\xi}$ [% yr^{-1}]
Algiers	+0.60 ± 0.18	+2.89 ± 0.88	+0.60 ± 0.18	+2.89 ± 0.87	*-1.7 ± 4.2*
Athens	-2.09 ± 0.83	-3.7 ± 1.5	-2.08 ± 0.82	-3.7 ± 1.5	*-2.8 ± 1.6*
Baghdad	+3.24 ± 0.37	+18.0 ± 2.1	+3.23 ± 0.38	+17.8 ± 2.1	+17 ± 75
Beijing	+9.5 ± 2.9	+7.3 ± 2.2	+9.4 ± 2.7	+7.2 ± 2.1	+7.4 ± 6.3
Buenos Aires	*+0.55 ± 0.51*	*+1.7 ± 1.6*	*+0.55 ± 0.51*	*+1.7 ± 1.6*	*-1.2 ± 6.7*
Cairo	+1.73 ± 0.28	+6.4 ± 1.0	+1.72 ± 0.28	+6.4 ± 1.0	+10 ± 94
Chicago	-6.2 ± 2.2	-3.9 ± 1.4	-6.3 ± 2.2	-3.9 ± 1.4	*+1 ± 23*
Dhaka	+3.41 ± 0.54	+24.0 ± 3.8	+3.35 ± 0.53	+23.0 ± 3.6	+22 ± 61
Dimashq	+2.62 ± 0.53	+7.2 ± 1.4	+2.60 ± 0.51	+7.1 ± 1.4	+13 ± 78
Guangzhou	*+0.2 ± 2.6*	*+0.2 ± 2.6*	*+0.3 ± 2.6*	*+0.3 ± 2.6*	-1 ± 12
Hong Kong	*-1.1 ± 2.3*	*-1.0 ± 2.1*	*-1.0 ± 2.2*	*-1.0 ± 2.0*	*-2.1 ± 1.9*
Istanbul	*-0.4 ± 1.1*	*-0.5 ± 1.5*	*-0.4 ± 1.1*	*-0.5 ± 1.5*	*+1 ± 16*
Jakarta	-1.19 ± 0.41	-3.3 ± 1.1	-1.20 ± 0.41	-3.3 ± 1.1	*+1 ± 16*
Jeddah	+1.4 2± 0.36	+4.5 ± 1.2	+1.41 ± 0.35	+4.5 ± 1.1	+30 ± 350
Karachi	+0.85 ± 0.25	+6.0 ± 1.8	+0.84 ± 0.25	+5.9 ± 1.8	+6 ± 24
Kolkata	+0.80 ± 0.26	+3.2 ± 1.0	+0.80 ± 0.25	+3.2 ± 0.99	*+2.9 ± 2.2*
Lagos	+0.33 ± 0.12	+2.68 ± 0.95	+0.33 ± 0.12	+2.67 ± 0.96	*+0.4 ± 2.6*
Lima	+1.06 ± 0.36	+7.9 ± 2.7	+1.06 ± 0.36	+7.9 ± 2.7	+1 ± 190
London	*-3.0 ± 1.6*	*-1.66 ± 0.91*	*-3.0 ± 1.6*	*-1.68 ± 0.89*	*+7.1 ± 7.7*
Los Angeles	-13.2 ± 2.6	-5.8 ± 1.2	-13.1 ± 2.6	-5.8 ± 1.1	*-3.0 ± 1.3*
Manila	-1.03 ± 0.20	-4.93 ± 0.95	-1.04 ± 0.21	-5.0 ± 1.0	*-4.0 ± 9.8*
Mexico City	*+0.51 ± 0.82*	*+1.0 ± 1.6*	*+0.51 ± 0.82*	*+1.0 ± 1.6*	*+0.1 ± 7.4*
Moscow	*-1.4 ± 1.6*	*-1.6 ± 1.9*	*-1.4 ± 1.6*	*-1.7 ± 1.9*	*-2 ± 16*
Mumbai	+0.70 ± 0.21	+3.6 ± 1.1	+0.68 ± 0.21	+3.5 ± 1.0	*+2.1 ± 1.7*
New Delhi	+2.57 ± 0.60	+7.4 ± 1.7	+2.47 ± 0.55	+6.9 ± 1.6	+24 ± 62
New York	-5.7 ± 2.3	-2.6 ± 1.0	-5.7 ± 2.3	-2.6 ± 1.0	+1.1 ± 5.1
Osaka	-2.54 ± 0.98	-2.23 ± 0.86	-2.52 ± 0.98	-2.21 ± 0.86	*-1.7 ± 2.3*
Paris	*-5.2 ± 2.5*	*-3.3 ± 1.6*	-5.1 ± 2.4	-3.3 ± 1.6	*-2.0 ± 3.6*
Riyadh	+2.05 ± 0.38	+6.9 ± 1.3	+2.06 ± 0.39	+7.0 ± 1.3	*-3.3 ± 1.9*
São Paolo	*+0.37 ± 0.52*	*+0.9 ± 1.3*	*+0.36 ± 0.51*	*+0.9 ± 1.3*	-3.45 ± 0.92
Seoul	*+1.0 ± 1.8*	*+0.7 ± 1.2*	*+1.0 ± 1.8*	*+0.7 ± 1.2*	*+2.3 ± 3.4*
Shanghai	+9.4 ± 3.0	+9.2 ± 2.9	+9.3 ± 2.9	+9.1 ± 2.8	+12 ± 57
Shenzhen	*-2.2 ± 1.7*	*-1.8 ± 1.3*	*-2.2 ± 1.7*	*-1.7 ± 1.3*	*-2.6 ± 2.2*
Tehran	+2.68 ± 0.93	+7.8 ± 2.7	+2.66 ± 0.92	+7.7 ± 2.7	*+1.6 ± 6.3*
Tokyo	-5.4 ± 1.4	-3.77 ± 0.97	-5.3 ± 1.3	-3.72 ± 0.93	-2.97 ± 0.97

BIBLIOGRAPHY

Air Science Group, Environmental Protection Department, The Government of Hong Kong Special Administrative Region: Air Quality in Hong Kong 2011, Tech. Rep. EPD/TR 2/12, Hong Kong, 2012. (Cited on page 146.)

Alpert, P., Shvainshtein, O., and Kishcha, P.: AOD Trends over Megacities Based on Space Monitoring Using MODIS and MISR, American Journal of Climate Change, 1, 117–131, 2012. (Cited on page 162.)

Anderson, B., Bartlett, K., Frolking, S., Hayhoe, K., Jenkins, J., and Salas, W.: Methane and Nitrous Oxide Emissions From Natural Sources, Tech. rep., United States Environmental Protection Agency, Washington, D.C., 2010. (Cited on page 14.)

Arlander, D. W., Brüning, D., Schmidt, U., and Ehhalt, D. H.: The tropospheric distribution of formaldehyde during TROPOZ II, Journal of Atmospheric Chemistry, 22, 251–269, 1995. (Cited on page 164.)

Bauer, R., Rozanov, A., McLinden, C. A., Gordley, L. L., Lotz, W., Russell III, J. M., Walker, K. A., Zawodny, J. M., Ladstätter-Weißenmayer, A., Bovensmann, H., and Burrows, J. P.: Validation of SCIAMACHY limb NO2 profiles using solar occultation measurements, Atmospheric Measurement Techniques, 5, 1059–1084, 2012. (Cited on pages 48 and 88.)

Beirle, S., Platt, U., Wenig, M. O., and Wagner, T.: Weekly cycle of NO2 by GOME measurements: a signature of anthropogenic sources, Atmospheric Chemistry and Physics, 3, 2225–2232, 2003. (Cited on page 99.)

Beirle, S., Platt, U., Wenig, M. O., and Wagner, T.: Highly resolved global distribution of tropospheric NO2 using GOME narrow swath mode data, Atmospheric Chemistry and Physics, 4, 1913–1924, 2004a. (Cited on pages 34, 116, 120, 122, 123, and 128.)

Beirle, S., Platt, U., Wenig, M. O., and Wagner, T.: NOx production by lightning estimated with GOME, Advances in Space Research, 34, 793–797, 2004b. (Cited on page 13.)

Beirle, S., Kühl, S., Pukite, J., and Wagner, T.: Retrieval of tropospheric column densities of NO2 from combined SCIAMACHY nadir/limb measurements, Atmospheric Measurement Techniques, 3, 283–299, 2010. (Cited on pages 45, 47, 52, 62, 82, 83, 90, 92, 181, and 186.)

Berntsen, T. K. and Isaksen, I. S. A.: A global three-dimensional chemical transport model for the troposphere 1. Model description and CO and ozone results, Journal of Geophysical Research, 102, PP. 21,239–21,280, 1997. (Cited on page 50.)

Bertram, T. H., Heckel, A., Richter, A., Burrows, J. P., and Cohen, R. C.: Satellite measurements of daily variations in soil NOx emissions, Geophysical Research Letters, 32, L24 812, 2005. (Cited on page 13.)

Bian, H. and Prather, M. J.: Fast-J2: Accurate Simulation of Stratospheric Photolysis in Global Chemical Models, Journal of Atmospheric Chemistry, 41, 281–296, 2002. (Cited on page 50.)

Boersma, K. F., Eskes, H. J., and Brinksma, E. J.: Error analysis for tropospheric NO2 retrieval from space, Journal of Geophysical Research, 109, D04 311, 2004. (Cited on pages 32, 46, 56, 57, 87, and 88.)

Boersma, K. F., Eskes, H. J., Veefkind, J. P., Brinksma, E. J., van der A, R. J., Sneep, M., van den Oord, G. H. J., Levelt, P. F., Stammes, P., Gleason, J. F., and Bucsela, E. J.: Near-real time retrieval of tropospheric NO2 from OMI, Atmospheric Chemistry and Physics, 7, 2103–2118, 2007. (Cited on pages 44, 45, 92, and 115.)

Bogumil, K., Orphal, J., Homann, T., Voigt, S., Spietz, P., Fleischmann, O., Vogel, A., Hartmann, M., Kromminga, H., Bovensmann, H., Frerick, J., and Burrows, J. P.: Measurements of molecular absorption spectra with the SCIAMACHY pre-flight model: instrument characterization and reference data for atmospheric remote-sensing in the 230–2380 nm region, Journal of Photochemistry and Photobiology A: Chemistry, 157, 167–184, 2003. (Cited on page 105.)

Bohren, C. F. and Clothiaux, E. E.: Fundamentals of Atmospheric Radiation, Wiley-VCH, Weinheim, 2006. (Cited on pages 25, 26, and 28.)

Bovensmann, H., Noël, S., Monks, P., Goede, A., and Burrows, J.: The geostationary scanning imaging absorption spectrometer (GeoSCIA) mission: requirements and capabilities, Advances in Space Research, 29, 1849–1859, 2002. (Cited on page 37.)

Bovensmann, H., Eichmann, K., Noël, S., Flaud, J., Orphal, J., Monks, P., Corlett, G., Goede, A., von Clarmann, T., Steck, T., Rozanov, V., and Burrows, J.: The geostationary scanning imaging absorption spectrometer (GeoSCIA) as part of the geostationary tropospheric pollution explorer (GeoTROPE) mission: requirements, concepts and capabilities, Advances in Space Research, 34, 694–699, 2004. (Cited on page 37.)

Brasseur, G. P. and Solomon, S.: Aeronomy of the Middle Atmosphere, Springer, Dordrecht, 3 edn., 2005. (Cited on pages 20 and 41.)

Brasseur, G. P., Orlando, J. J., and Tyndall, G. S.: Atmospheric Chemistry and Global Change, Oxford University Press, New York, 1999. (Cited on pages 14 and 17.)

Bucsela, E. J., Celarier, E. A., Wenig, M. O., Gleason, J. F., Veefkind, J. P., Boersma, K. F., and Brinksma, E. J.: Algorithm for NO2 vertical column retrieval from the ozone monitoring instrument, IEEE Transactions on Geoscience and Remote Sensing, 44, 1245–1258, 2006. (Cited on page 44.)

Bucsela, E. J., Krotkov, N. A., Celarier, E. A., Lamsal, L. N., Swartz, W. H., Bhartia, P. K., Boersma, K. F., Veefkind, J. P., Gleason, J. F., and Pickering, K. E.: A new stratospheric and tropospheric NO_2 retrieval algorithm for nadir-viewing satellite instruments: applications to OMI, Atmospheric Measurement Techniques Discussions, 6, 1361–1407, 2013. (Cited on page 45.)

Bühlmann, P. and Künsch, H. R.: Block length selection in the bootstrap for time series, Computational Statistics & Data Analysis, 31, 295–310, 1999. (Cited on page 149.)

Burrows, J., Bovensmann, H., Bergametti, G., Flaud, J., Orphal, J., Noël, S., Monks, P., Corlett, G., Goede, A., von Clarmann, T., Steck, T., Fischer, H., and Friedl-Vallon, F.: The geostationary tropospheric pollution explorer (GeoTROPE) mission: objectives, requirements and mission concept, Advances in Space Research, 34, 682–687, 2004. (Cited on page 37.)

Burrows, J. P., Hölzle, E., Goede, A., Visser, H., and Fricke, W.: SCIAMACHY - scanning imaging absorption spectrometer for atmospheric chartography, Acta Astronautica, 35, 445–451, 1995. (Cited on pages 34 and 45.)

Burrows, J. P., Dehn, A., Deters, B., Himmelmann, S., Richter, A., Voigt, S., and Orphal, J.: Atmospheric remote-sensing reference data from GOME—1. Temperature-dependent absorption cross-sections of NO2 in the 231–794 nm range, Journal of Quantitative Spectroscopy and Radiative Transfer, 60, 1025–1031, 1998. (Cited on page 56.)

Burrows, J. P., Weber, M., Buchwitz, M., Rozanov, V. V., Ladstätter-Weiß enmayer, A., Richter, A., DeBeek, R., Hoogen, R., Bramstedt, K., Eichmann, K.-U., and Eisinger, M.: The Global Ozone Monitoring Experiment (GOME): Mission Concept and First Scientific Results, Journal of the Atmospheric Sciences, 56, 151–175, 1999. (Cited on pages 3, 34, 41, and 96.)

Byrd, R. H., Lu, P., Nocedal, J., and Zhu, C.: A Limited Memory Algorithm for Bound Constrained Optimization, SIAM Journal on Scientific Computing, 16, 1190–1208, 1995. (Cited on page 159.)

Callies, J., Corpaccioli, E., Eisinger, M., Hahne, A., and Lefebvre, A.: GOME-2 – Metop's Second-Generation Sensor for Operational Ozone Monitoring, ESA Bulletin, 102, 28–36, 2000. (Cited on page 36.)

Castellanos, P. and Boersma, K. F.: Reductions in nitrogen oxides over Europe driven by environmental policy and economic recession., Scientific Reports, 2, 265, 2012. (Cited on page 98.)

Center for International Earth Science Information Network, Columbia University, International Food Policy Research Institute, The World Bank, and Centro Internacional de Agricultura Tropical: Global Rural-Urban Mapping Project, Version 1 (GRUMPv1): Population Density Grid., Socioeconomic Data and Applications Center, Columbia University, Palisades, NY, 2011. (Cited on pages 152 and 153.)

Chance, K.: Analysis of BrO measurements from the Global Ozone Monitoring Experiment, Geophysical Research Letters, 25, pp. 3335–3338, 1998. (Cited on page 105.)

Chauhan, A. J., Krishna, M. T., Frew, A. J., and Holgate, S. T.: Exposure to nitrogen dioxide (NO2) and respiratory disease risk, Reviews on environmental health, 13, 73–90, 1998. (Cited on page 14.)

Chipperfield, M. P.: Multiannual simulations with a three-dimensional chemical transport model, Journal of Geophysical Research, 104, 1781–1805, 1999. (Cited on page 49.)

Cleveland, R. B., Cleveland, W. S., McRae, J. E., and Terpenning, I.: STL: A Seasonal-Trend Decomposition Procedure Based on Loess, Journal of Official Statistics, 6, 3–73, 1990. (Cited on pages 157 and 158.)

Cook, P. A. and Roscoe, H. K.: Variability and trends in stratospheric NO2 in Antarctic summer, and implications for stratospheric NOy, Atmospheric Chemistry and Physics, 9, 3601–3612, 2009. (Cited on pages 39 and 40.)

Crutzen, P. J.: The influence of nitrogen oxides on the atmospheric ozone content, Quarterly Journal of the Royal Meteorological Society, 96, 320–325, 1970. (Cited on page 19.)

Crutzen, P. J. and Stoermer, E. F.: The "Anthropocene", Global Change Newsletter, 41, 17–18, 2000. (Cited on page 1.)

de Ruyter de Wildt, M., Eskes, H., and Boersma, K. F.: The global economic cycle and satellite-derived NO2 trends over shipping lanes, Geophysical Research Letters, 39, 2–7, 2012. (Cited on pages 98 and 122.)

De Smedt, I., Van Roozendael, M., Stavrakou, T., Müller, J.-F., Lerot, C., Theys, N., Valks, P., Hao, N., and van der A, R.: Improved retrieval of global tropospheric formaldehyde columns from GOME-2/MetOp-A addressing noise reduction and instrumental degradation issues, Atmospheric Measurement Techniques, 5, 2933–2949, 2012. (Cited on page 164.)

Dee, D. P., Uppala, S. M., Simmons, A. J., Berrisford, P., Poli, P., Kobayashi, S., Andrae, U., Balmaseda, M. A., Balsamo, G., Bauer, P., Bechtold, P., Beljaars, A. C. M., van de Berg, L., Bidlot, J., Bormann, N., Delsol, C., Dragani, R., Fuentes, M., Geer, A. J., Haimberger, L., Healy, S. B., Hersbach, H., Hólm, E. V., Isaksen, L., Kållberg, P., Köhler, M., Matricardi, M., McNally, A. P., Monge-Sanz, B. M., Morcrette, J.-J., Park, B.-K., Peubey, C., de Rosnay, P., Tavolato, C., Thépaut, J.-N., and Vitart, F.: The ERA-Interim reanalysis: configuration and performance of the data assimilation system, Quarterly Journal of the Royal Meteorological Society, 137, 553–597, 2011. (Cited on page 49.)

Deeter, M. N., Martínez-Alonso, S., Edwards, D. P., Emmons, L. K., Gille, J. C., Worden, H. M., Pittman, J. V., Daube, B. C., and Wofsy, S. C.: Validation of MOPITT Version 5 thermal-infrared, near-infrared, and multispectral carbon monoxide profile retrievals for 2000–2011, Journal of Geophysical Research: Atmospheres, p. n/a–n/a, 2013. (Cited on page 166.)

Diner, D., Beckert, J., Reilly, T., Bruegge, C., Conel, J., Kahn, R., Martonchik, J., Ackerman, T., Davies, R., Gerstl, S. A. W., Gordon, H., Muller, J.-P., Myneni, R., Sellers, P., Pinty, B., and Verstraete, M.: Multi-angle Imaging SpectroRadiometer (MISR) instrument description and experiment overview, IEEE Transactions on Geoscience and Remote Sensing, 36, 1072–1087, 1998. (Cited on page 162.)

Dirksen, R. J., Boersma, K. F., Eskes, H. J., Ionov, D. V., Bucsela, E. J., Levelt, P. F., and Kelder, H. M.: Evaluation of stratospheric NO2 retrieved from the Ozone Monitoring Instrument: Intercomparison, diurnal cycle, and trending, Journal of Geophysical Research, 116, 22 PP., 2011. (Cited on pages 20, 40, and 92.)

Doney, S. C., Mahowald, N., Lima, I., Feely, R. A., Mackenzie, F. T., Lamarque, J.-F., and Rasch, P. J.: Impact of anthropogenic atmospheric nitrogen and sulfur deposition on ocean acidification and the inorganic carbon system, Proceedings of the National Academy of Sciences, 104, 14 580–14 585, 2007. (Cited on page 2.)

Ebojie, F., von Savigny, C., Ladstätter-Weißenmayer, A., Rozanov, A., Weber, M., Eichmann, K.-U., Bötel, S., Rahpoe, N., Bovensmann, H., and Burrows, J. P.: Seasonal variability of tropospheric ozone derived from SCIAMACHY limb-nadir matching observations. (Cited on page 49.)

Efron, B. and Tibshirani, R. J.: An Introduction to the Bootstrap, Chapman & Hall, New York, 1993. (Cited on pages 148 and 149.)

Elbern, H., Hendricks, J., and Ebel, A.: A Climatology of Tropopause Folds by Global Analyses, Theoretical and Applied Climatology, 59, 181–200, 1998. (Cited on pages 18 and 73.)

Encyclopædia Britannica: modernization :: Population change, http://www.britannica.com/EBchecked/topic/387301/modernization/12022/Population-change (last access: 2013-07-17). (Cited on page 1.)

Environmental Protection Department, The Government of the Hong Kong Special Administrative Region‘: Key Points of the Pearl River Delta Regional Air Quality Management Plan, 2004. (Cited on page 147.)

Environmental Protection Department, The Government of the Hong Kong Special Administrative Region‘: Pearl River Delta Regional Air Quality Management Plan Enhanced Control Measures of Hong Kong Special Administrative Region - Annex A, 2012. (Cited on page 147.)

ESA Earthnet Online: ERS-2 Low Rate Mission Availability, https://earth.esa.int/web/guest/missions/esa-operational-eo-missions/ers/news/-/asset_publisher/T7aX/content/ers-2-low-rate-mission-availability-3183 (last access: 2013-06-26), 2003. (Cited on page 34.)

ESA Earthnet Online: Implementation of Envisat extension orbit in October 2010, http://earth.esa.int/object/index.cfm?fobjectid=6999 (last access: 2013-03-21), 2010. (Cited on page 34.)

ESA Earthnet Online: ERS-2 decommissioning completed, https://earth.esa.int/web/guest/missions/esa-operational-eo-missions/ers/news/-/asset_publisher/T7aX/content/ers-2-decommissioning-completed-7875 (last access: 2013-06-24), 2011. (Cited on page 34.)

EUMETSAT: Metop Mission Overview, http://www.eumetsat.int/Home/Main/Satellites/Metop/MissionOverview/index.htm (last access: 2013-06-24), 2012. (Cited on page 37.)

European Commission, Joint Research Centre and Netherlands Environmental Assessment Agency: Emission Database for Global Atmospheric Research (EDGAR), version 4.2, 2011. (Cited on pages 13, 107, 123, 124, 152, and 153.)

European Space Agency: GlobCover 2009 v2.3 Global Land Cover Map, 2009. (Cited on page 126.)

European Space Agency: MetOp Second Generation instruments, http://www.esa.int/Our_Activities/Observing_the_Earth/The_Living_Planet_Programme/Meteorological_missions/MetOp/MetOp_Second_Generation_instruments (last access: 2013-08-16), 2011. (Cited on page 38.)

European Space Agency: Sentinel-4 Copernicus Geostationary Atmospheric Mission, http://esamultimedia.esa.int/docs/S4-Data_Sheet.pdf (last access: 2013-08-16), 2013a. (Cited on page 38.)

European Space Agency: Sentinels -4/-5 and -5P, http://www.esa.int/Our_Activities/Observing_the_Earth/Copernicus/Sentinels_-4_-5_and_-5P (last access: 2013-08-16), 2013b. (Cited on page 38.)

Finlayson-Pitts, B. J. and Pitts, James N., J.: Chemistry of the Upper and Lower Atmosphere: Theory, Experiments, and Applications, Academic Press, San Diego, 6th edn., 1999. (Cited on pages 2 and 19.)

Franke, K., Richter, A., Bovensmann, H., Eyring, V., Jöckel, P., Hoor, P., and Burrows, J. P.: Ship emitted NO2 in the Indian Ocean: comparison of model results with satellite data, Atmospheric Chemistry and Physics, 9, 7289–7301, 2009. (Cited on pages 98 and 122.)

Ganzeveld, L. N., Lelieveld, J., Dentener, F. J., Krol, M. C., Bouwman, A. J., and Roelofs, G.-J.: Global soil-biogenic NOx emissions and the role of canopy processes, Journal of Geophysical Research: Atmospheres, 107, ACH 9–1–ACH 9–17, 2002. (Cited on page 13.)

Ghude, S. D., Fadnavis, S., Beig, G., Polade, S. D., and van der A, R. J.: Detection of surface emission hot spots, trends, and seasonal cycle from satellite-retrieved NO2 over India, Journal of Geophysical Research, 113, D20 305, 2008. (Cited on pages 97 and 98.)

Gordley, L. L., Russell, J. M., Mickley, L. J., Frederick, J. E., Park, J. H., Stone, K. A., Beaver, G. M., McInerney, J. M., Deaver, L. E., Toon, G. C., Murcray, F. J., Blatherwick, R. D., Gunson, M. R., Abbatt, J. P. D., Mauldin, R. L., Mount, G. H., Sen, B., and Blavier, J.-F.: Validation of nitric oxide and nitrogen dioxide measurements made by the Halogen Occultation Experiment for UARS platform, Journal of Geophysical Research: Atmospheres, 101, 10 241–10 266, 1996. (Cited on page 41.)

Gottwald, M. and Bovensmann, H., eds.: SCIAMACHY - Exploring the Changing Earth's Atmosphere, Springer Netherlands, Dordrecht, 2011. (Cited on pages 35, 36, 47, and 48.)

Granier, C., Lamarque, J.-F., Mieville, A., Müller, J.-F., Olivier, J., Orlando, J., Peters, J., Petron, G., Tyndall, G., and Wallens, S.: POET, a database of surface emissions of ozone precursors, http://www.aero.jussieu.fr/projet/ACCENT/POET.php (last access: 2013-03-22), 2005. (Cited on page 50.)

Granier, C., Bessagnet, B., Bond, T., D'Angiola, A., Denier van der Gon, H., Frost, G. J., Heil, A., Kaiser, J. W., Kinne, S., Klimont, Z., Kloster, S., Lamarque, J.-F., Liousse, C., Masui, T., Meleux, F., Mieville, A., Ohara, T., Raut, J.-C., Riahi, K., Schultz, M. G., Smith, S. J., Thompson, A., Aardenne, J., Werf, G. R., and Vuuren, D. P.: Evolution of anthropogenic and biomass burning emissions of air pollutants at global and regional scales during the 1980–2010 period, Climatic Change, 109, 163–190, 2011. (Cited on pages 12, 50, and 138.)

Greenblatt, G. D., Orlando, J. J., Burkholder, J. B., and Ravishankara, A. R.: Absorption measurements of oxygen between 330 and 1140 nm, Journal of Geophysical Research, 95, 18 577–18 582, 1990. (Cited on page 105.)

Gurjar, B., Butler, T., Lawrence, M., and Lelieveld, J.: Evaluation of emissions and air quality in megacities, Atmospheric Environment, 42, 1593–1606, 2008. (Cited on page 23.)

Gurjar, B. R., Molina, L. T., and Ojha, C. S. P.: Air Pollution: Health and Environmental Concerns, in: Air Pollution: Health and Environmental Impacts, CRC Press, Boca Raton, 2010. (Cited on page 9.)

Haken, H. and Wolf, H. C.: Atom- und Quantenphysik, Springer, Berlin, 7. auflage edn., 2001. (Cited on page 25.)

Haken, H. and Wolf, H. C.: Molekülphysik und Quantenchemie, Springer-Lehrbuch, Springer, Berlin, 2006. (Cited on page 25.)

Hastings, D. A., Dunbar, P. K., Elphingstone, G. M., Bootz, M., Murakami, H., Holland, P., Bryant, N. A., Logan, T. L., Muller, J.-P., Schreier, G., and MacDonald, J. S., eds.: The Global Land One-kilometer Base Elevation (GLOBE) Digital Elevation Model, Version 1.0, National Oceanic and Atmospheric Administration, Boulder, 1998. (Cited on pages 152 and 153.)

Hayn, M., Beirle, S., Hamprecht, F. A., Platt, U., Menze, B. H., and Wagner, T.: Analysing spatio-temporal patterns of the global NO2-distribution retrieved from GOME satellite observations using a generalized additive model, Atmospheric Chemistry and Physics, 9, 6459–6477, 2009. (Cited on pages 99 and 109.)

He, Y., Uno, I., Wang, Z., Ohara, T., Sugimoto, N., Shimizu, A., Richter, A., and Burrows, J. P.: Variations of the increasing trend of tropospheric NO2 over central east China during the past decade, Atmospheric Environment, 41, 4865–4876, 2007. (Cited on pages 97 and 98.)

Heckel, A.: Limb Nadir Matching, Presentation given at the workshop "Tropospheric NO2 measured by satellites" in De Bilt, Netherlands, 2007. (Cited on page 35.)

Heckel, A., Kim, S.-W., Frost, G. J., Richter, A., Trainer, M. K., and Burrows, J. P.: Influence of low spatial resolution a priori data on tropospheric NO2 satellite retrievals, Atmospheric Measurement Techniques, 4, 1805–1820, 2011. (Cited on pages 88 and 113.)

Hegglin, M. I., Brunner, D., Wernli, H., Schwierz, C., Martius, O., Hoor, P., Fischer, H., Parchatka, U., Spelten, N., Schiller, C., Krebsbach, M., Weers, U., Staehelin, J., and Peter, T.: Tracing troposphere-to-stratosphere transport above a mid-latitude deep convective system, Atmos. Chem. Phys., 4, 741–756, 2004. (Cited on page 18.)

Hendrick, F., Mahieu, E., Bodeker, G. E., Boersma, K. F., Chipperfield, M. P., De Mazière, M., De Smedt, I., Demoulin, P., Fayt, C., Hermans, C., Kreher, K., Lejeune, B., Pinardi, G., Servais, C., Stübi, R., van der A, R., Vernier, J.-P., and Van Roozendael, M.: Analysis of stratospheric NO2 trends above Jungfraujoch using ground-based UV-visible, FTIR, and satellite nadir observations, Atmospheric Chemistry and Physics, 12, 8851–8864, 2012. (Cited on pages 19, 39, and 40.)

Hesstvedt, E., Hov, Ö., and Isaksen, I. S. A.: Quasi-steady-state approximations in air pollution modeling: Comparison of two numerical schemes for oxidant prediction, International Journal of Chemical Kinetics, 10, 971–994, 1978. (Cited on page 50.)

Hilboll, A., Richter, A., and Burrows, J. P.: Long-term changes of tropospheric NO2 over megacities derived from multiple satellite instruments, Atmospheric Chemistry and Physics, 13, 4145–4169, 2013a. (Cited on pages 96, 100, 101, 104, 106, 107, 108, 110, 113, 114, 115, 116, 118, 121, 122, 125, 127, 128, 129, 131, 133, 136, 137, 138, 139, 140, 141, 142, 145, 147, 148, 151, 152, 153, 154, and 169.)

Hilboll, A., Richter, A., and Burrows, J. P.: NO2 pollution trends over megacities 1996-2010 from combined multiple satellite data sets, in: Earth System Sciences: Bridging the gaps between disciplines. Perspectives from a Multi-Disciplinary Helmholtz Research School., edited by Lohmann, G., Grosfeld, K., Wolf-Gladrow, D., Unnithan, V., Notholt, J., and Wegner, A., pp. 9–15, Springer, Heidelberg, doi: 10.1007/978-3-642-32235-8_2, 2013b. (Cited on page 147.)

Hilboll, A., Richter, A., Rozanov, A., Hodnebrog, Ø., Heckel, A., Solberg, S., Stordal, F., and Burrows, J. P.: Improvements to the retrieval of tropospheric NO2 from satellite – stratospheric correction using SCIAMACHY limb/nadir matching and comparison to Oslo CTM2 simulations, Atmospheric Measurement Techniques, 6, 565–584, 2013c. (Cited on pages 40, 43, 47, 49, 50, 51, 52, 53, 54, 55, 56, 58, 59, 60, 61, 62, 63, 64, 65, 67, 69, 70, 71, 72, 73, 76, 77, 78, 79, 80, 81, 82, 84, 86, 87, 91, 182, 184, 185, 186, 187, and 188.)

Hoinka, K. P.: Statistics of the Global Tropopause Pressure, Monthly Weather Review, 126, 3303–3325, 1998. (Cited on page 49.)

Holtslag, A. A. M., De Bruijn, E. I. F., and Pan, H.-L.: A High Resolution Air Mass Transformation Model for Short-Range Weather Forecasting, Monthly Weather Review, 118, 1561–1575, 1990. (Cited on page 50.)

Horowitz, L. W., Walters, S., Mauzerall, D. L., Emmons, L. K., Rasch, P. J., Granier, C., Tie, X., Lamarque, J.-F., Schultz, M. G., Tyndall, G. S., Orlando, J. J., and Brasseur, G. P.: A global simulation of tropospheric ozone and related tracers: Description and evaluation of MOZART, version 2, Journal of Geophysical Research, 108, 4784, 2003. (Cited on page 105.)

Houghton, J. T., Ding, Y., Griggs, D. J., Noguer, M., Linden, P. J. v. d., Dai, X., Maskell, K., and Johnson, C. A.: Climate Change 2001: The Scientific Basis: Contribution of Working Group I to the Third Assessment Report of the Intergovernmental Panel on Climate Change, Cambridge University Press, 2001. (Cited on pages 14 and 20.)

Huang, J., Zhou, C., Lee, X., Bao, Y., Zhao, X., Fung, J., Richter, A., Liu, X., and Zheng, Y.: Impact of rapid urbanization on changes in tropospheric nitrogen dioxide and ozone over East China, in preparation. (Cited on page 112.)

Hudson, R. D. and Thompson, A. M.: Tropical tropospheric ozone from total ozone mapping spectrometer by a modified residual method, Journal of Geophysical Research: Atmospheres, 103, 22 129–22 145, 1998. (Cited on page 41.)

Huijnen, V., Eskes, H. J., Poupkou, A., Elbern, H., Boersma, K. F., Foret, G., Sofiev, M., Valdebenito, A., Flemming, J., Stein, O., Gross, A., Robertson, L., D'Isidoro, M., Kioutsioukis, I., Friese, E., Amstrup, B., Bergstrom, R., Strunk, A., Vira, J., Zyryanov, D., Maurizi, A., Melas, D., Peuch, V.-H., and Zerefos, C.: Comparison of OMI NO2 tropospheric columns with an ensemble of global and European regional air quality models, Atmospheric Chemistry and Physics, 10, 3273–3296, 2010. (Cited on page 151.)

InfoMine Inc.: Mine Sites - Major Mining Operations Around the World, 2012. (Cited on page 123.)

International Monetary Fund: World Economic Outlook Database, 2012. (Cited on page 157.)

Irie, H., Sudo, K., Akimoto, H., Richter, A., Burrows, J. P., Wagner, T., Wenig, M. O., Beirle, S., Kondo, Y., Sinyakov, V. P., and Goutail, F.: Evaluation of long-term tropospheric NO 2 data obtained by GOME over East Asia in 1996–2002, Geophysical Research Letters, 32, 2–5, 2005. (Cited on pages 96 and 104.)

Isaksen, I., Granier, C., Myhre, G., Berntsen, T., Dalsøren, S., Gauss, M., Klimont, Z., Benestad, R., Bousquet, P., Collins, W., Cox, T., Eyring, V., Fowler, D., Fuzzi, S., Jöckel, P., Laj, P., Lohmann, U., Maione, M., Monks, P., Prevot, A., Raes, F., Richter, A., Rognerud, B., Schulz, M., Shindell, D., Stevenson, D., Storelvmo, T., Wang, W.-C., van Weele, M., Wild, M., and Wuebbles, D.: Atmospheric composition change: Climate–Chemistry interactions, Atmospheric Environment, 43, 5138–5192, 2009. (Cited on pages 21 and 22.)

Jones, E., Oliphant, T., and Peterson, P.: SciPy: Open source scientific tools for Python, http://www.scipy.org (last access: 2013-03-22), 2001. (Cited on page 159.)

Kanter, D., Mauzerall, D. L., Ravishankara, A. R., Daniel, J. S., Portmann, R. W., Grabiel, P. M., Moomaw, W. R., and Galloway, J. N.: A post-Kyoto partner: Considering the

stratospheric ozone regime as a tool to manage nitrous oxide, Proceedings of the National Academy of Sciences, 2013. (Cited on page 14.)

Kim, J. H., Hudson, R. D., and Thompson, A. M.: A new method of deriving time-averaged tropospheric column ozone over the tropics using total ozone mapping spectrometer (TOMS) radiances: Intercomparison and analysis using TRACE A data, Journal of Geophysical Research: Atmospheres, 101, 24 317–24 330, 1996. (Cited on page 41.)

Kim, S.-W., Heckel, A., McKeen, S. A., Frost, G. J., Hsie, E.-Y., Trainer, M. K., Richter, A., Burrows, J. P., Peckham, S. E., and Grell, G. A.: Satellite-observed U.S. power plant NOx emission reductions and their impact on air quality, Geophysical Research Letters, 33, L22 812, 2006. (Cited on pages 98, 122, and 138.)

Kim, S.-W., Heckel, A., Frost, G. J., Richter, A., Gleason, J. F., Burrows, J. P., McKeen, S. A., Hsie, E.-Y., Granier, C., and Trainer, M. K.: NO2 columns in the western United States observed from space and simulated by a regional chemistry model and their implications for NOx emissions, Journal of Geophysical Research, 114, D11 301, 2009. (Cited on page 99.)

Koelemeijer, R. B. A., de Haan, J. F., and Stammes, P.: A database of spectral surface reflectivity in the range 335–772 nm derived from 5.5 years of GOME observations, Journal of Geophysical Research, 108, 4070, 2003. (Cited on page 105.)

Koninklijk Nederlands Meteorologisch Instituut: Background information about the Row Anomaly in OMI, http://www.knmi.nl/omi/research/product/rowanomaly-background.php (last access: 2013-06-24), 2012. (Cited on page 36.)

Konovalov, I. B., Beekmann, M., Richter, A., and Burrows, J. P.: Inverse modelling of the spatial distribution of NOx emissions on a continental scale using satellite data, Atmospheric Chemistry and Physics, 6, 1747–1770, 2006. (Cited on pages 96, 104, and 115.)

Konovalov, I. B., Beekmann, M., Richter, A., Burrows, J. P., and Hilboll, A.: Multi-annual changes of NOx emissions in megacity regions: nonlinear trend analysis of satellite measurement based estimates, Atmospheric Chemistry and Physics, 10, 8481–8498, 2010. (Cited on pages 99, 104, 109, 142, 158, and 160.)

Kosmopoulos, P., Kaskaoutis, D., Nastos, P., and Kambezidis, H.: Seasonal variation of columnar aerosol optical properties over Athens, Greece, based on MODIS data, Remote Sensing of Environment, 112, 2354–2366, 2008. (Cited on page 112.)

Lamsal, L. N., Martin, R. V., Padmanabhan, A., Donkelaar, A. v., Zhang, Q., Sioris, C. E., Chance, K., Kurosu, T. P., and Newchurch, M. J.: Application of satellite observations for timely updates to global anthropogenic NOx emission inventories, Geophysical Research Letters, 38, L05 810, 2011. (Cited on page 109.)

Lee, D. S., Köhler, I., Grobler, E., Rohrer, F., Sausen, R., Gallardo-Klenner, L., Olivier, J. G. J., Dentener, F. J., and Bouwman, A. F.: Estimations of global NOx emissions and their uncertainties, Atmospheric Environment, 31, 1735–1749, 1997. (Cited on page 13.)

Leitão, J., Richter, A., Vrekoussis, M., Kokhanovsky, A., Zhang, Q. J., Beekmann, M., and Burrows, J. P.: On the improvement of NO2 satellite retrievals – aerosol impact on the airmass factors, Atmospheric Measurement Techniques, 3, 475–493, 2010. (Cited on pages 31, 88, and 113.)

Lelieveld, J., Barlas, C., Giannadaki, D., and Pozzer, A.: Model calculated global, regional and megacity premature mortality due to air pollution, Atmos. Chem. Phys., 13, 7023–7037, 2013. (Cited on page 24.)

Lerot, C., Stavrakou, T., De Smedt, I., Müller, J.-F., and Van Roozendael, M.: Glyoxal vertical columns from GOME-2 backscattered light measurements and comparisons with a global model, Atmospheric Chemistry and Physics, 10, 12 059–12 072, 2010. (Cited on page 73.)

Leue, C., Wenig, M. O., Wagner, T., Klimm, O., Platt, U., and Jähne, B.: Quantitative analysis of NOx emissions from Global Ozone Monitoring Experiment satellite image sequences, Journal of Geophysical Research, 106, 5493–5505, 2001. (Cited on pages 43 and 96.)

Levelt, P. F., Hilsenrath, E., Leppelmeier, G. W., van den Oord, G. H., Bhartia, P. K., Tamminen, J., de Haan, J. F., and Veefkind, J. P.: Science objectives of the ozone monitoring instrument, IEEE Transactions on Geoscience and Remote Sensing, 44, 1199– 1208, 2006. (Cited on page 36.)

Levy, R. C., Remer, L. A., Kleidman, R. G., Mattoo, S., Ichoku, C., Kahn, R., and Eck, T. F.: Global evaluation of the Collection 5 MODIS dark-target aerosol products over land, Atmospheric Chemistry and Physics, 10, 10 399–10 420, 2010. (Cited on page 162.)

Liang, Q., Rodriguez, J. M., Douglass, A. R., Crawford, J. H., Olson, J. R., Apel, E., Bian, H., Blake, D. R., Brune, W., Chin, M., Colarco, P. R., da Silva, A., Diskin, G. S., Duncan, B. N., Huey, L. G., Knapp, D. J., Montzka, D. D., Nielsen, J. E., Pawson, S., Riemer, D. D., Weinheimer, A. J., and Wisthaler, A.: Reactive nitrogen, ozone and ozone production in the Arctic troposphere and the impact of stratosphere-troposphere exchange, Atmos. Chem. Phys., 11, 13 181–13 199, 2011. (Cited on page 18.)

Liley, J. B., Johnston, P. V., McKenzie, R. L., Thomas, A. J., and Boyd, I. S.: Stratospheric NO2 variations from a long time series at Lauder, New Zealand, Journal of Geophysical Research: Atmospheres, 105, 11 633–11 640, 2000. (Cited on page 40.)

Lin, J. and McElroy, M. B.: Detection from space of a reduction in anthropogenic emissions of nitrogen oxides during the Chinese economic downturn, Atmospheric Chemistry and Physics, 11, 8171–8188, 2011. (Cited on page 98.)

Liou, K.-N.: An Introduction to Atmospheric Radiation, vol. 84 of *International Geophysics Series*, Academic Press, San Diego, 2nd edn., 2002. (Cited on page 27.)

Ma, J. Z., Beirle, S., Jin, J. L., Shaiganfar, R., Yan, P., and Wagner, T.: Tropospheric NO2 vertical column densities over Beijing: results of the first three years of ground-based MAX-DOAS measurements (2008–2011) and satellite validation, Atmospheric Chemistry and Physics, 13, 1547–1567, 2013. (Cited on page 125.)

Mage, D., Ozolins, G., Peterson, P., Webster, A., Orthofer, R., Vandeweerd, V., and Gwynne, M.: Urban air pollution in megacities of the world, Atmospheric Environment, 30, 681–686, 1996. (Cited on page 24.)

Martin, R. V., Chance, K., Jacob, D. J., Kurosu, T. P., Spurr, R. J. D., Bucsela, E., Gleason, J. F., Palmer, P. I., Bey, I., Fiore, A. M., Li, Q., Yantosca, R. M., and Koelemeijer, R. B. A.: An improved retrieval of tropospheric nitrogen dioxide from GOME, Journal of Geophysical Research, 107, 4437, 2002. (Cited on pages 41, 43, 59, and 96.)

Mieruch, S., Noël, S., Bovensmann, H., and Burrows, J. P.: Analysis of global water vapour trends from satellite measurements in the visible spectral range, Atmospheric Chemistry and Physics, 8, 491–504, 2008. (Cited on pages 4, 134, 135, and 170.)

Mijling, B., A, R. J. v. d., Boersma, K. F., Roozendael, M. V., Smedt, I. D., and Kelder, H. M.: Reductions of NO2 detected from space during the 2008 Beijing Olympic Games, Geophysical Research Letters, 36, L13 801, 2009. (Cited on pages 115 and 125.)

Mohr, P. J., Taylor, B. N., and Newell, D. B.: CODATA recommended values of the fundamental physical constants: 2010, Reviews of Modern Physics, 84, 1527–1605, 2012. (Cited on page 25.)

Molina, M. J. and Molina, L. T.: Megacities and Atmospheric Pollution, Journal of the Air and Waste Management Association, 54, 644–680, 2004. (Cited on pages 2 and 24.)

Moore, J. C., Grinsted, A., and Jevrejeva, S.: New tools for analyzing time series relationships and trends, Eos, Transactions American Geophysical Union, 86, 226–232, 2005. (Cited on page 158.)

Mudelsee, M.: {C}limate {T}ime {S}eries {A}nalysis, no. 42 in Atmospheric and Oceanographic Sciences Library, Springer, Dordrecht, 2010. (Cited on pages 148, 149, 155, and 158.)

Mudelsee, M. and Alkio, M.: Quantifying effects in two-sample environmental experiments using bootstrap confidence intervals, Environmental Modelling & Software, 22, 84–96, 2007. (Cited on page 149.)

Murphy, D. M., Fahey, D. W., Proffitt, M. H., Liu, S. C., Chan, K. R., Eubank, C. S., Kawa, S. R., and Kelly, K. K.: Reactive nitrogen and its correlation with ozone in the lower stratosphere and upper troposphere, Journal of Geophysical Research: Atmospheres, 98, 8751–8773, 1993. (Cited on page 19.)

Noxon, J. F.: NOx in the mid-Pacific troposphere, Geophysical Research Letters, 8, 1223–1226, 1981. (Cited on page 42.)

Nüß, H., Richter, A., Valks, P., and Burrows, J. P.: Improvements of the NO2 Total Column Retrieval for GOME-2, O3M SAF visiting scientist activity, final report, Universität Bremen, 2006. (Cited on page 57.)

Nüß, J. H.: Improvements of the retrieval of tropospheric NO2 from GOME and SCIAMACHY data, PhD thesis, Universität Bremen, Bremen, 2005. (Cited on pages 31, 59, 105, and 113.)

O3M SAF - EUMETSAT Satellite Application Facility on Ozone and Atmospheric Chemistry Monitoring: Information on Metop-b/GOME-2 products and measurement configurations of GOME-2 instruments onboard Metop-A and B satellites, http://o3msaf.fmi.fi/metopB_info.html (last access: 2013-07-18), 2013. (Cited on page 37.)

O'Donnell, M. A.: Shenzhen population statistics, 1979-2011, 2011. (Cited on page 146.)

Office Of Air Quality Planning And Standards and Office Of Air And Radiation: Compilation of Air Pollutant Emission Factors. Volume I: Stationary Point and Area Sources, Tech. rep., United States Environmental Protection Agency, Research Triangle Park, 1995. (Cited on page 11.)

Palmer, P. I., Jacob, D. J., Chance, K., Martin, R. V., Spurr, R. J. D., Kurosu, T. P., Bey, I., Yantosca, R., Fiore, A., and Li, Q.: Air mass factor formulation for spectroscopic measurements from satellites: Application to formaldehyde retrievals from the Global Ozone Monitoring Experiment, Journal of Geophysical Research, 106, PP. 14,539–14,550, 2001. (Cited on page 32.)

Pennington, D., Potting, J., Finnveden, G., Lindeijer, E., Jolliet, O., Rydberg, T., and Rebitzer, G.: Life cycle assessment Part 2: Current impact assessment practice, Environment International, 30, 721–739, 2004. (Cited on page 9.)

Peters, E.: MAX-DOAS instrumental improvement and observations of trace gas profiles focusing on the marine troposphere, Ph.D. thesis, Universität Bremen, Bremen, 2013. (Cited on page 73.)

Peters, E., Wittrock, F., Großmann, K., Frieß, U., Richter, A., and Burrows, J. P.: Formaldehyde and nitrogen dioxide over the remote western Pacific Ocean: SCIAMACHY and GOME-2 validation using ship-based MAX-DOAS observations, Atmos. Chem. Phys., 12, 11 179–11 197, 2012. (Cited on page 42.)

Platt, U. and Stutz, J.: Differential Optical Absorption Spectroscopy, Physics of Earth and Space Environments, Springer, Berlin, 2008. (Cited on pages 29 and 105.)

Prather, M. J.: Numerical Advection by Conservation of Second-Order Moments, Journal of Geophysical Research, 91, 6671–6681, 1986. (Cited on pages 49 and 50.)

Price, C., Penner, J., and Prather, M.: NOx from lightning 1. Global distribution based on lightning physics, Journal of Geophysical Research, 102, PP. 5929–5941, 1997. (Cited on page 50.)

Pukite, J., Kühl, S., Deutschmann, T., Dörner, S., Jöckel, P., Platt, U., and Wagner, T.: The effect of horizontal gradients and spatial measurement resolution on the retrieval of global vertical NO2 distributions from SCIAMACHY measurements in limb only mode, Atmospheric Measurement Techniques, 3, 1155–1174, 2010. (Cited on pages 52, 88, and 89.)

Raes, F., Liao, H., Chen, W.-T., and Seinfeld, J. H.: Atmospheric chemistry-climate feedbacks, Journal of Geophysical Research, 115, 14 PP., 2010. (Cited on pages 21 and 22.)

Ravishankara, A. R., Daniel, J. S., and Portmann, R. W.: Nitrous Oxide (N2O): The Dominant Ozone-Depleting Substance Emitted in the 21st Century, Science, 326, 123–125, 2009. (Cited on page 14.)

Reinsel, G. C., Weatherhead, E., Tiao, G. C., Miller, A. J., Nagatani, R. M., Wuebbles, D. J., and Flynn, L. E.: On detection of turnaround and recovery in trend for ozone, Journal of Geophysical Research: Atmospheres, 107, ACH 1–1–ACH 1–12, 2002. (Cited on page 158.)

Reinsel, G. C., Miller, A. J., Weatherhead, E. C., Flynn, L. E., Nagatani, R. M., Tiao, G. C., and Wuebbles, D. J.: Trend analysis of total ozone data for turnaround and dynamical contributions, Journal of Geophysical Research: Atmospheres, 110, n/a–n/a, 2005. (Cited on page 158.)

Reuter, M., Bovensmann, H., Buchwitz, M., Burrows, J. P., Connor, B. J., Deutscher, N. M., Griffith, D. W. T., Heymann, J., Keppel-Aleks, G., Messerschmidt, J., Notholt, J., Petri, C., Robinson, J., Schneising, O., Sherlock, V., Velazco, V., Warneke, T., Wennberg, P. O., and Wunch, D.: Retrieval of atmospheric CO2 with enhanced accuracy and precision from SCIAMACHY: Validation with FTS measurements and comparison with model results, Journal of Geophysical Research: Atmospheres, 116, n/a–n/a, 2011. (Cited on page 165.)

Revell, L. E., Bodeker, G. E., Smale, D., Lehmann, R., Huck, P. E., Williamson, B. E., Rozanov, E., and Struthers, H.: The effectiveness of N2O in depleting stratospheric ozone, Geophysical Research Letters, 39, L15 806, 2012. (Cited on page 14.)

Richter, A.: Absorptionsspektroskopische Messungen stratosphärischer Spurengase über Bremen, 53°N, Ph.D. thesis, University of Bremen, 1997. (Cited on page 30.)

Richter, A.: Line of sight correction in PGlobal, Technical note, Universität Bremen, 2004. (Cited on page 57.)

Richter, A. and Burrows, J. P.: Tropospheric NO2 from GOME measurements, Advances in Space Research, 29, 1673–1683, 2002. (Cited on pages 41, 43, 96, and 105.)

Richter, A., Wittrock, F., Eisinger, M., and Burrows, J. P.: GOME observations of tropospheric BrO in northern hemispheric spring and summer 1997, Geophysical Research Letters, 25, 2683–2686, 1998. (Cited on page 87.)

Richter, A., Eyring, V., Burrows, J. P., Bovensmann, H., Lauer, A., Sierk, B., and Crutzen, P. J.: Satellite measurements of NO2 from international shipping emissions, Geophysical Research Letters, 31, L23 110, 2004. (Cited on pages 98 and 122.)

Richter, A., Burrows, J. P., Nüß, H., Granier, C., and Niemeier, U.: Increase in tropospheric nitrogen dioxide over China observed from space, Nature, 437, 129–132, 2005. (Cited on pages 3, 44, 96, 97, 100, 104, 106, 107, and 131.)

Richter, A., Begoin, M., Hilboll, A., and Burrows, J. P.: An improved NO2 retrieval for the GOME-2 satellite instrument, Atmospheric Measurement Techniques, 4, 1147–1159, 2011. (Cited on pages 63, 131, and 164.)

Ritchie, E., Barros, A., Bell, R., Braun, A., Houghton, R., Johnson, B. C., Liu, G., Luo, J., Morrill, J., Posselt, D., Powell, S., Randel, W., Strub, T., and Vandemark, D.: NASA Earth Science Senior Review 2013, Tech. rep., 2013. (Cited on page 36.)

Rothman, L., Gamache, R., Tipping, R., Rinsland, C., Smith, M., Benner, D., Devi, V., Flaud, J.-M., Camy-Peyret, C., Perrin, A., Goldman, A., Massie, S., Brown, L., and Toth, R.: The HITRAN molecular database: Editions of 1991 and 1992, Journal of Quantitative Spectroscopy and Radiative Transfer, 48, 469–507, 1992. (Cited on page 105.)

Rothman, L., Gordon, I., Barbe, A., Benner, D., Bernath, P., Birk, M., Boudon, V., Brown, L., Campargue, A., Champion, J.-P., Chance, K., Coudert, L., Dana, V., Devi, V., Fally, S., Flaud, J.-M., Gamache, R., Goldman, A., Jacquemart, D., Kleiner, I., Lacome, N., Lafferty, W., Mandin, J.-Y., Massie, S., Mikhailenko, S., Miller, C., Moazzen-Ahmadi, N., Naumenko, O., Nikitin, A., Orphal, J., Perevalov, V., Perrin, A., Predoi-Cross, A., Rinsland, C., Rotger, M., Šimečková, M., Smith, M., Sung, K., Tashkun, S., Tennyson,

J., Toth, R., Vandaele, A., and Vander Auwera, J.: The HITRAN 2008 molecular spectroscopic database, Journal of Quantitative Spectroscopy and Radiative Transfer, 110, 533–572, 2009. (Cited on page 95.)

Rozanov, A., Bovensmann, H., Bracher, A., Hrechanyy, S., Rozanov, V. V., Sinnhuber, M., Stroh, F., and Burrows, J. P.: NO2 and BrO vertical profile retrieval from SCIAMACHY limb measurements: Sensitivity studies, Advances in Space Research, 36, 846–854, 2005a. (Cited on pages 41, 51, and 88.)

Rozanov, A., Rozanov, V. V., Buchwitz, M., Kokhanovsky, A. A., and Burrows, J. P.: SCIATRAN 2.0 - A new radiative transfer model for geophysical applications in the 175-2400 nm spectral region, Advances in Space Research, 36, 1015–1019, 2005b. (Cited on pages 48, 56, 59, and 105.)

Rozanov, V. V., Rozanov, A. V., Kokhanovsky, A. A., and Burrows, J. P.: Radiative transfer through terrestrial atmosphere and ocean: Software package SCIATRAN, Journal of Quantitative Spectroscopy and Radiative Transfer, 2013. (Cited on page 28.)

Russell, A. R., Valin, L. C., and Cohen, R. C.: Trends in OMI NO2 observations over the United States: effects of emission control technology and the economic recession, Atmospheric Chemistry and Physics, 12, 12 197–12 209, 2012. (Cited on pages 98, 114, 146, 160, and 161.)

Samet, J. M. and Utell, M. J.: The risk of nitrogen dioxide: what have we learned from epidemiological and clinical studies?, Toxicology and industrial health, 6, 247–262, 1990. (Cited on page 14.)

Saunders, D.: Arrival City, Random House, London, 2010. (Cited on pages 1 and 24.)

Schneider, P. and van der A, R. J.: A global single-sensor analysis of 2002–2011 tropospheric nitrogen dioxide trends observed from space, Journal of Geophysical Research, 117, D16 309, 2012. (Cited on pages 97, 98, 104, 124, and 143.)

Schultz, M. G., Jacob, D. J., Wang, Y., Logan, J. A., Atlas, E. L., Blake, D. R., Blake, N. J., Bradshaw, J. D., Browell, E. V., Fenn, M. A., Flocke, F., Gregory, G. L., Heikes, B. G., Sachse, G. W., Sandholm, S. T., Shetter, R. E., Singh, H. B., and Talbot, R. W.: On the origin of tropospheric ozone and NOx over the tropical South Pacific, Journal of Geophysical Research, 104, 5829–5843, 1999. (Cited on pages 30 and 42.)

Schultz, M. G., Heil, A., Hoelzemann, J. J., Spessa, A., Thonicke, K., Goldammer, J. G., Held, A. C., Pereira, J. M. C., and Bolscher, M. v. h.: Global wildland fire emissions from 1960 to 2000, Global Biogeochemical Cycles, 22, 17 PP., 2008. (Cited on page 50.)

Seinfeld, J. H. and Pandis, S. N.: Atmospheric chemistry and physics: from air pollution to climate change, John Wiley & Sons, Hoboken, 2nd edn., 2006. (Cited on pages 14, 16, 17, and 167.)

Seneca, L. A.: Moral Epistles, vol. 3, Cambridge University Press, Cambridge, Mass., 1917. (Cited on page 9.)

Sierk, B., Richter, A., Rozanov, A., von Savigny, C., Schmoltner, A. M., Buchwitz, M., Bovensmann, H., and Burrows, J. P.: Retrieval And Monitoring of Atmospheric Trace Gas Concentrations in Nadir and Limb Geometry Using the Space-Borne Sciamachy Instrument, Environmental Monitoring and Assessment, 120, 65–77, 2006. (Cited on page 45.)

Sinnhuber, B.-M., Weber, M., Amankwah, A., and Burrows, J. P.: Total ozone during the unusual Antarctic winter of 2002, Geophysical Research Letters, 30, 1580–1584, 2003a. (Cited on page 49.)

Sinnhuber, M., Burrows, J. P., Chipperfield, M. P., Jackman, C. H., Kallenrode, M.-B., Künzi, K. F., and Quack, M.: A model study of the impact of magnetic field structure on atmospheric composition during solar proton events, Geophysical Research Letters, 30, 1818–1821, 2003b. (Cited on page 49.)

Sitnov, S. A.: Analysis of spatial-temporal variability of tropospheric NO2 column over Moscow megapolis using OMI spectrometer (Aura satellite) data, Doklady Earth Sciences, 429, 1511–1517, 2010. (Cited on pages 97 and 160.)

Smith, K. R.: Fuel Combustion, Air Pollution Exposure, and Health: The Situation in Developing Countries, Annual Review of Energy and the Environment, 18, 529–566, 1993. (Cited on page 10.)

Solomon, S. and Keys, J. G.: Seasonal variations in Antarctic NO x chemistry, Journal of Geophysical Research: Atmospheres, 97, 7971–7978, 1992. (Cited on page 20.)

Solomon, S., Qin, D., Manning, M., Marquis, M., Averyt, K., Tignor, M. M. B., LeRoy Miller, H. J., and Chen, Z.: Climate Change 2007: Working Group I: The Physical Science Basis, Tech. rep., Intergovernmental Panel on Climate Change, Geneva, 2007. (Cited on pages 12, 21, and 22.)

Søvde, O. A., Gauss, M., Smyshlyaev, S. P., and Isaksen, I. S. A.: Evaluation of the chemical transport model Oslo CTM2 with focus on arctic winter ozone depletion, Journal of Geophysical Research, 113, 26 PP., 2008. (Cited on page 50.)

Sprenger, M. and Wernli, H.: A northern hemispheric climatology of cross-tropopause exchange for the ERA15 time period (1979–1993), Journal of Geophysical Research, 108, 8521, 2003. (Cited on pages 18 and 73.)

Stavrakou, T., Müller, J.-F., Boersma, K. F., de Smedt, I., and van der A, R. J.: Assessing the distribution and growth rates of NOx emission sources by inverting a 10-year record of NO2 satellite columns, Geophysical Research Letters, 35, L10 801, 2008. (Cited on pages 97, 104, 109, and 111.)

Stolarski, R. S., Krueger, A. J., Schoeberl, M. R., McPeters, R. D., Newman, P. A., and Alpert, J. C.: Nimbus 7 satellite measurements of the springtime Antarctic ozone decrease, Nature, 322, 808–811, 1986. (Cited on page 3.)

Stordal, F., Isaksen, I. S. A., and Horntveth, K.: A Diabatic Circulation Two-Dimensional Model With Photochemistry: Simulations of Ozone and Long-Lived Tracers With Surface Sources, Journal of Geophysical Research, 90, PP. 5757–5776, 1985. (Cited on page 50.)

Tiao, G. C., Reinsel, G. C., Xu, D., Pedrick, J. H., Zhu, X., Miller, A. J., DeLuisi, J. J., Mateer, C. L., and Wuebbles, D. J.: Effects of Autocorrelation and Temporal Sampling Schemes on Estimates of Trend and Spatial Correlation, Journal of Geophysical Research, 95, 20 507–20,517, 1990. (Cited on page 134.)

Tiedtke, M.: A Comprehensive Mass Flux Scheme for Cumulus Parameterization in Large-Scale Models, Monthly Weather Review, 117, 1779–1800, 1989. (Cited on page 50.)

Trenberth, K. E., Fasullo, J. T., and Kiehl, J.: Earth's Global Energy Budget, Bulletin of the American Meteorological Society, 90, 311–323, 2009. (Cited on page 21.)

Ummel, K.: CARMA Revisited: An Updated Database of Carbon Dioxide Emissions from Power Plants Worldwide, Tech. Rep. Working Paper 304, Center for Global Development, Washington, D.C., 2012. (Cited on page 123.)

United Nations Children's Fund: The State of the World's Children 2012, Tech. rep., United Nations, New York, 2012. (Cited on page 23.)

United Nations, Department of Economic and Social Affairs, Population Division: World Urbanization Prospects, the 2011 Revision. Highlights., Tech. rep., United Nations, New York, 2012. (Cited on pages 23 and 24.)

U.S. Census Bureau: U.S. Primary Roads, Tech. rep., 2012. (Cited on page 123.)

U.S. Environmental Protection Agency: Nitrogen Oxides (NOx), Why and How They Are Controlled, Tech. Rep. EPA 456/F-99-006a, 1999. (Cited on page 11.)

U.S. Environmental Protection Agency: Terms of Environment: Glossary, Abbreviations, and Acronyms, http://iaspub.epa.gov/sor_internet/registry/termreg/searchandretrieve/glossariesandkeywordlists/search.do?details= (last access: 2013-07-03), 2009. (Cited on page 9.)

U.S. Geological Survey: Landsat Enhanced Thematic Mapper Plus (ETM+). (Cited on page 126.)

U.S. Geological Survey: Global Digital Elevation Model (GTOPO30), 2004. (Cited on page 123.)

U.S. Government Printing Office: U.S. Standard Atmosphere, 1976, U.S. Government Printing Office, Washington, D.C., 1976. (Cited on pages 8 and 79.)

Valks, P. J. M., Koelemeijer, R. B. A., van Weele, M., van Velthoven, P., Fortuin, J. P. F., and Kelder, H.: Variability in tropical tropospheric ozone: Analysis with Global Ozone Monitoring Experiment observations and a global model, Journal of Geophysical Research: Atmospheres, 108, n/a–n/a, 2003. (Cited on page 95.)

Vallero, D.: Fundamentals of Air Pollution, Elsevier, Oxford, 4th edn., 2007. (Cited on page 10.)

van der A, R. J., Eskes, H. J., Boersma, K. F., van Noije, T. P. C., van Roozendael, M., de Smedt, I., Peters, D. H. M. U., and Meijer, E. W.: Trends, seasonal variability and dominant NOx source derived from a ten year record of NO2 measured from space, Journal of Geophysical Research, 113, D04 302, 2008. (Cited on pages 4, 97, 98, 104, 107, 142, 145, 146, and 189.)

van der Werf, G. R., Randerson, J. T., Giglio, L., Collatz, G. J., Kasibhatla, P. S., and Arellano Jr., A. F.: Interannual variability in global biomass burning emissions from 1997 to 2004, Atmospheric Chemistry and Physics, 6, 3423–3441, 2006. (Cited on page 50.)

Veefkind, J., Aben, I., McMullan, K., Förster, H., de Vries, J., Otter, G., Claas, J., Eskes, H., de Haan, J., Kleipool, Q., van Weele, M., Hasekamp, O., Hoogeveen, R., Landgraf, J., Snel, R., Tol, P., Ingmann, P., Voors, R., Kruizinga, B., Vink, R., Visser, H., and Levelt, P.: TROPOMI on the ESA Sentinel-5 Precursor: A GMES mission for global observations of the atmospheric composition for climate, air quality and ozone layer applications, Remote Sensing of Environment, 120, 70–83, 2012. (Cited on pages 37 and 171.)

Velders, G. J. M., Granier, C., Portmann, R. W., Pfeilsticker, K., Wenig, M., Wagner, T., Platt, U., Richter, A., and Burrows, J. P.: Global tropospheric NO2 column distributions: Comparing three-dimensional model calculations with GOME measurements, Journal of Geophysical Research: Atmospheres, 106, 12 643–12 660, 2001. (Cited on pages 42 and 43.)

von Hoyningen-Huene, W., Yoon, J., Vountas, M., Istomina, L., Rohen, G., Dinter, T., Kokhanovsky, A. A., and Burrows, J. P.: Retrieval of spectral aerosol optical thickness over land using ocean color sensors MERIS and SeaWiFS, Atmospheric Measurement Techniques, 4, 151–171, 2011. (Cited on page 112.)

Voulgarakis, A., Savage, N. H., Wild, O., Braesicke, P., Young, P. J., Carver, G. D., and Pyle, J. A.: Interannual variability of tropospheric composition: the influence of changes in emissions, meteorology and clouds, Atmospheric Chemistry and Physics, 10, 2491–2506, 2010. (Cited on pages 99, 109, 156, and 167.)

Vountas, M., Rozanov, V. V., and Burrows, J. P.: Ring effect: Impact of rotational Raman scattering on radiative transfer in Earth's atmosphere, Journal of Quantitative Spectroscopy and Radiative Transfer, 60, 943–961, 1998. (Cited on pages 30 and 105.)

Vountas, M., Richter, A., Wittrock, F., and Burrows, J. P.: Inelastic scattering in ocean water and its impact on trace gas retrievals from satellite data, Atmospheric Chemistry and Physics, 3, 1365–1375, 2003. (Cited on page 73.)

Vrekoussis, M., Richter, A., Hilboll, A., Burrows, J. P., Gerasopoulos, E., Lelieveld, J., Barrie, L., Zerefos, C., and Mihalopoulos, N.: Economic Crisis Detected from Space: Air Quality observations over Athens/Greece, Geophysical Research Letters, 40, 458–463, 2013. (Cited on pages 98, 114, and 159.)

Vyushin, D. I., Fioletov, V. E., and Shepherd, T. G.: Impact of long-range correlations on trend detection in total ozone, Journal of Geophysical Research: Atmospheres, 112, n/a–n/a, 2007. (Cited on page 158.)

Wallace, J. M.: Atmospheric Science: an introductory survey, vol. 92 of *International Geophysics Series*, Academic Press, 2nd edn., 2006. (Cited on pages 7 and 8.)

Wang, P., Stammes, P., A, R. J. v. d., Pinardi, G., and Roozendael, M. v.: FRESCO+: an improved O2 A-band cloud retrieval algorithm for tropospheric trace gas retrievals, Atmospheric Chemistry and Physics, 8, 6565–6576, 2008. (Cited on pages 68, 75, and 105.)

Wayne, R., Barnes, I., Biggs, P., Burrows, J., Canosa-Mas, C., Hjorth, J., Le Bras, G., Moortgat, G., Perner, D., Poulet, G., Restelli, G., and Sidebottom, H.: The nitrate radical: Physics, chemistry, and the atmosphere, Atmospheric Environment. Part A. General Topics, 25, 1–203, 1991. (Cited on pages 17 and 19.)

Weatherhead, E. C., Reinsel, G. C., Tiao, G. C., Meng, X.-L., Choi, D., Cheang, W.-K., Keller, T., DeLuisi, J., Wuebbles, D. J., Kerr, J. B., Miller, A. J., Oltmans, S. J., and Frederick, J. E.: Factors affecting the detection of trends: Statistical considerations and applications to environmental data, Journal of Geophysical Research, 103, 17 149–17 161, 1998. (Cited on pages 134, 135, and 158.)

Wenig, M. O., Kühl, S., Beirle, S., Bucsela, E. J., Jähne, B., Platt, U., Gleason, J. F., and Wagner, T.: Retrieval and analysis of stratospheric NO2 from the Global Ozone Monitoring Experiment, Journal of Geophysical Research, 109, 11 PP., 2004. (Cited on pages 79 and 87.)

Wheeler, D. and Ummel, K.: Calculating CARMA: Global Estimation of CO2 Emissions from the Power Sector, Tech. Rep. Working Paper 145, Center for Global Development, Washington, D.C., 2008. (Cited on page 123.)

Wild, O., Zhu, X., and Prather, M. J.: Fast-J: Accurate Simulation of In- and Below-Cloud Photolysis in Tropospheric Chemical Models, Journal of Atmospheric Chemistry, 37, 245–282, 2000. (Cited on page 50.)

Williams, E. J., Hutchinson, G. L., and Fehsenfeld, F. C.: NOx And N2O Emissions From Soil, Global Biogeochemical Cycles, 6, 351–388, 1992. (Cited on page 12.)

Winkler, H., Sinnhuber, M., Notholt, J., Kallenrode, M.-B., Steinhilber, F., Vogt, J., Zieger, B., Glassmeier, K.-H., and Stadelmann, A.: Modeling impacts of geomagnetic field variations on middle atmospheric ozone responses to solar proton events on long timescales, Journal of Geophysical Research, 113, D02 302, 2008. (Cited on page 49.)

Wittrock, F.: The retrieval of oxygenated volatile organic compounds by remote sensing techniques, Ph.D. thesis, Universität Bremen, 2006. (Cited on page 164.)

Worden, H. M., Deeter, M. N., Frankenberg, C., George, M., Nichitiu, F., Worden, J., Aben, I., Bowman, K. W., Clerbaux, C., Coheur, P. F., de Laat, A. T. J., Detweiler, R., Drummond, J. R., Edwards, D. P., Gille, J. C., Hurtmans, D., Luo, M., Martínez-Alonso, S., Massie, S., Pfister, G., and Warner, J. X.: Decadal record of satellite carbon monoxide observations, Atmos. Chem. Phys., 13, 837–850, 2013. (Cited on page 167.)

World Health Organization: Health Aspects of Air Pollution with Particulate Matter, Ozone and Nitrogen Dioxide, Report on a WHO working group, World Health Organization, Bonn, 2003. (Cited on pages 10 and 15.)

World Meteorological Organization: Scientific Assessment of Ozone Depletion: 2006, Tech. Rep. 50, Geneva, Switzerland, 2007. (Cited on pages 10, 39, and 50.)

Yoon, J., Burrows, J. P., Vountas, M., von Hoyningen-Huene, W., Chang, D. Y., Richter, A., and Hilboll, A.: Changes in atmospheric aerosol loading retrieved from space based measurements during the past decade, Atmospheric Chemistry and Physics Discussions, 13, 26 001–26 041, 2013. (Cited on page 162.)

Yurganov, L., McMillan, W., Grechko, E., and Dzhola, A.: Analysis of global and regional CO burdens measured from space between 2000 and 2009 and validated by ground-based solar tracking spectrometers, Atmospheric Chemistry and Physics, 10, 3479–3494, 2010. (Cited on page 167.)

Zahn, M. and Storch, H. v.: A long-term climatology of North Atlantic polar lows, Geophysical Research Letters, 35, L22 702, 2008. (Cited on page 74.)

Zhang, J. and Reid, J. S.: A decadal regional and global trend analysis of the aerosol optical depth using a data-assimilation grade over-water MODIS and Level 2 MISR aerosol products, Atmospheric Chemistry and Physics, 10, 10 949–10 963, 2010. (Cited on page 162.)

Zhang, Q., Streets, D. G., He, K. B., Wang, Y., Richter, A., Burrows, J. P., Uno, I., Jang, C. J., Chen, D., Yao, Z., and Lei, Y.: NOx emission trends for China, 1995–2004: The view from the ground and the view from space, Journal of Geophysical Research, 112, 18 PP., 2007a. (Cited on page 108.)

Zhang, Q., Streets, D. G., and He, K. B.: Satellite observations of recent power plant construction in Inner Mongolia, China, Geophysical Research Letters, 36, L15 809, 2009a. (Cited on pages 97 and 122.)

Zhang, X., Zhang, P., Zhang, Y., Li, X., and Qiu, H.: The trend, seasonal cycle, and sources of tropospheric NO2 over China during 1997–2006 based on satellite measurement, Science in China Series D: Earth Sciences, 50, 1877–1884, 2007b. (Cited on page 97.)

Zhang, Y., Dubey, M. K., Olsen, S. C., Zheng, J., and Zhang, R.: Comparisons of WRF/Chem simulations in Mexico City with ground-based RAMA measurements during the 2006-MILAGRO, Atmospheric Chemistry and Physics, 9, 3777–3798, 2009b. (Cited on page 115.)

Zhou, Y., Brunner, D., Boersma, K. F., Dirksen, R., and Wang, P.: An improved tropospheric NO_2 retrieval for OMI observations in the vicinity of mountainous terrain, Atmospheric Measurement Techniques, 2, 401–416, 2009. (Cited on page 113.)

Zhou, Y., Brunner, D., Hueglin, C., Henne, S., and Staehelin, J.: Changes in OMI tropospheric NO2 columns over Europe from 2004 to 2009 and the influence of meteorological variability, Atmospheric Environment, 46, 482–495, 2012. (Cited on pages 99, 104, and 177.)

Zhu, C., Byrd, R. H., Lu, P., and Nocedal, J.: Algorithm 778: L-BFGS-B: Fortran subroutines for large-scale bound-constrained optimization, ACM Trans. Math. Softw., 23, 550–560, 1997. (Cited on page 159.)

Ziemke, J. R., Chandra, S., Duncan, B. N., Froidevaux, L., Bhartia, P. K., Levelt, P. F., and Waters, J. W.: Tropospheric ozone determined from Aura OMI and MLS: Evaluation of measurements and comparison with the Global Modeling Initiative's Chemical Transport Model, Journal of Geophysical Research: Atmospheres, 111, n/a–n/a, 2006. (Cited on page 168.)

COLOPHON

This thesis was typeset with XeTEX, using the LYX editor. The typographical look-and-feel is based on `classicthesis` developed by André Miede; the style was inspired by Robert Bringhurst's seminal book on typography *"The Elements of Typographic Style"*. Philipp H. Poll's *Linux Libertine* is used as type face. The "typewriter" text is typeset in Raph Levien's *Inconsolata*. Maps were produced by *Generic Mapping Tools (GMT)*, using mostly the Albers and Mollweide projections for regional and global maps, respectively. All other figures were produced with *matplotlib* and *Inkscape*.